Optimisation of DC cast microstructure of Aluminium alloys containing immiscible elements

A thesis submitted for the degree of

Doctor of Philosophy

by

Paula Camean Queijo

BCAST
Brunel University
Uxbridge, UB8 3PH
United Kingdom

Dedicated to my family and in particular to my little

daughter, who made me smile in the most difficult

moments throughout the completion of this thesis

Abstract

Free machining alloys containing soft immiscible phases in the aluminium (Al) matrix, like lead (Pb) and bismuth (Bi), are of great industrial interest. Typical applications in automotive industry are components requiring very high machinability, such as braking pistons and anti-blocking system (ABS) housings. Presence of soft immiscible phases is giving their machining properties to this class of alloys. These phases melt due to localised heat build-up generated by machining process and induce chips breaking. Such type of alloys offers best in class performance when the soft phase is uniformly distributed in the Al matrix.

The main objective of this work was to develop a method to tailor the distribution of the immiscible phase particles in the final solidified structure of DC cast billets in order to provide enhanced machinability while keeping low levels of Pb and/or Bi additions. As a consequence, another objective of this study was to improve recyclability of such alloys as well as to reduce their environmental impact.

Three categories of Al-Pb alloys and different solidification paths were studied: hyper-monotectic Al-3Pb, monotectic Al-1.2Pb and industrial hypo-monotectic free machining alloy containing both Pb and Bi.

A newly developed melt conditioning combines mechanical, thermal and chemical treatments to obtain a very fine and uniform distribution of the immiscible phase droplets and eliminate compositional heterogeneities.   The effect of these new melt treatments on microstructure was evaluated. For the soft phase droplets size was reduced and distribution becomes finer and more homogeneous under the individual effect of each of the treatments and optimum results obtained with the combination of them.

These new melt treatments affect not only the nucleation of the Pb/Bi droplets, enhancing their heterogeneous nucleation but reduces considerably the Marangoni motion and Stokes sedimentation reducing therefore the droplet coalescence and restricting their growth. As a consequence of this improved microstructure, mechanical properties and machining performance were enhanced considerably.

The results from this study provide a promising new microstructure with a fine and uniform distribution of droplets.

Preface

This thesis is a description of work that I performed in the Brunel Centre for Advanced Solidification Technology, Brunel University, West London from April 2012 to October 2015. To the best of my knowledge, this work is original, except where suitable references are made to previous work. Neither this, nor any substantially similar dissertation has been submitted to any other institution. It is the result of my own work. The content of the dissertation does not exceed 60,000 words.

Conferences

- National Student Conference in Metallic Materials, Manchester University, June 2012.
- National Student Conference in Metallic Materials, Brunel University, June 2013, oral presentation.
- Specialist research Institutes and Graduate School Research Conference, Brunel University, November 2012, poster.
- Light Metals Technology Workshop (Lime), Brunel University, April 2013.
- The 6th International Conference on Solidification and Gravity, Hungary, September 2013, oral presentation.
- 6th International Light Metals Technology Conference, Lime, UK, July 2013.

Acknowledgements

Nomenclature

A list of symbols and a short description of each of them is provided here.

Al: Aluminium

Bi: Bismuth

CPAl: Commercial purity aluminium

Θ_{SL2}:   Contact angle (°) between solid inoculant particles and liquid droplets of the minority phase

Cu: Copper

DC casting: Direct chill casting

$\rho 1, \rho 2$ Density of phases 1 and 2 respectively (g/cm^3)

D: Diffusion coefficient ($m^{-2} s^{-1}$)

DSC: Differential scanning calorimetry

E_b: Brownian motion of particles and droplets (N)

$f(\Theta)$:   Catalytic factor

Fe: Iron

G: Temperature gradient (˚C/mm)

ΔG_{het}:   Energy barrier for heterogeneous nucleation (J/m^2)

ΔG_{hom}:   Energy barrier for homogeneous nucleation (J/m^2)

ΔG_{remove}:   Energy to remove the particles from the surface of the minority phase droplets

ΔG_v: Change in Gibbs free energy of the system (J/m^2)

HB: Brinell hardness

I_{hom}:   Homogeneous nucleation rate

I_{het}:   Heterogeneous nucleation rate

σ, σ_{L1L2}:   Interfacial tension at L_1–L_2 interface (J/m^2)

k: Partition coefficient

K: Capillary number, dimensionless

L_1, L_2:   Liquid 1, liquid 2 (minority phase)

m: Liquidus slope

MC-DC: Melt conditioning direct chill casting

Mn: Manganese

OPS: Oxide particle suspension

Pb: Lead

Q: Growth restriction parameter

r: Droplet diameter (µm)

R: Cooling rate (˚C/sec)

SDAS (λ_2):   Secondary dendritic arm spacing

SEM: Scanning electron microscopy

SHT: Solution heat treatment

Si: Silicon

s/l: Solid/liquid

Sn: Tin

Sr: Strontium

TEM: Transmission electron microscopy

UTS: Ultimate tensile Strength

V: Growth velocity (mm/sec)

µ, μ_d, μ_m: Viscosity, droplet viscosity, matrix viscosity (Pa.s)

Λ: Viscosity ratio, dimensionless

V_s: Stokes sedimentation velocity in mm/sec.

V_m: Marangoni velocity (m/sec)

XRD: X-ray diffraction

Contents

Chapter 1

Introduction

1.1 Background

The 2XXX series of Al alloys are usually binary alloys containing up to 6% Cu, and other alloying elements only in small proportions. Their extruded products are nowadays used for various automotive applications, including as row material in automated machining processes. Within the 2XXX series, 2011 alloy is a free-machining alloy containing Pb and Bi; which form an eutectic that melts at 175˚C, providing the alloy with excellent chipping and cutting characteristics, suitable for high-speed production parts on CNC machines (I. Duplancic et al.,2007).

Recycling of scrap is a highly efficient way of reintroducing valuable materials into the economy, and avoid harming the environment and health. Energy savings of up to 95% can be achieved from the use of recycled Al compared to its primary production, contributing to significant reductions in CO_2 emission.   Recycled Al alloys represent 35% of the total Al used in EU (European Association of Metals, 2013 Survey).

Therefore the reasons for the presence of Pb in Al products are twofold, as nearly 80% of the scrap used in recycling contains an average Pb content of 0.20-0.40 %, as a non-intentionally added impurity. Alloys with a higher content of Pb cannot be used for recycling. Pb is considered as a hazard for the health, as its grinding dust and/or fumes can be inhaled causing serious lung disorders (European Association of Metals, 2013 Survey).

Historically Environmental and Health Directives have been pushing to reduce or eliminate the amounts of Pb permitted in industrial products and scrap for recycling, therefore it is expected that this trend will continue in the future. Complete elimination of Pb/Bi would reduce the machining efficiency of the alloys, as no other element additions have been proven as efficient or as economically feasible. Hence reduction of Pb contents in free machining alloys could be critical for future recyclability of alloys containing this metal. Understanding Pb behaviour in Al alloys is critical to reduce its content.

Alloys containing immiscible elements like Pb and Bi offer the best performance when the soft phase is completely and homogeneously dispersed, as very fine particles, in the Al matrix (Budai, Kaptay, 2009). However, optimum droplet size and droplet size distribution for best machining performance is not known. These fine dispersions of immiscible particles are difficult to achieve due to component separation. The Al–Bi and Al–Pb systems are characterized by a wide miscibility gap in the liquid state (Ratke, 1998). Above the critical temperature, both components are completely miscible, on cooling the homogeneous liquid decomposes originating 2 separate liquid phases. The separation begins with the nucleation of minority phase droplets, and continues with their growth and coalesce via diffusion and Marangoni motion; when the droplets are big enough, they sink down to the bottom of the sample, due to Stokes motion and finally a layered liquid structure can appear (J. Wang et al., 2013).   Therefore, coarse dispersions are normally obtained with immiscible alloys.

As the melting temperature and density difference between Al and Pb, is bigger and its enthalpy of mixing is more positive, Al-Pb system is the most difficult to obtain a uniform distribution of the soft phase. Hence the selection of Pb as the element of study in this work; if homogeneous dispersion of Pb in Al is achieved we can assume that the learning from this binary system can be used to achieve the same uniform microstructure in other immiscible systems like Al-Bi (Fan et al., 2006).

This thesis reviews monotectic solidification of Al-Pb, covering the three composition dependant categories in which the binary system is divided, that is:

- hypo-monotectic or compositions bellow monotectic, represented by the industrial 2011 alloy in which the Pb content is 0.4 %
- exact monotectic, corresponding to 1.2 % Pb
- hyper-monotectic, for which liquid-liquid separation takes place, and which will be represented by an Al-3Pb binary alloy.

Many methods were attempted to fabricate the homogeneous immiscible alloys in the last decade. The desired microstructure, however, was difficult to obtain by the normal solidification technology (J. He et al., 2008).

Therefore, in order to explore the microstructural refinement, for each of the three categories differentiated from the phase diagram, the effect of melt conditioning by shearing, inoculant additions and melt superheat was analysed. The influence of Al-Ti and Al-B additions and melt conditioning on the nucleation and growth of Al-Pb of monotectic composition will be discussed.

1.2 Objective

The main objectives of this study are:

- To study the effect of superheat, shearing and inoculant additions on the size and distribution of the soft immiscible phases, mainly Pb, in the Al matrix.
- To reach an appropriate level of understanding of the effect of these parameters on phase separation and final microstructure.
- To develop new DC casting practices, which provide improved distributions of Pb droplets in the Al matrix, from a very fine and uniform distribution to a coarser one, to understand the effect of droplet size and their distribution on machining performance.
- To identify possible means for reducing the amount of second phase additions, mainly Pb, in DC cast 2011 alloy, maintaining or improving the current machining performance.

1.3 Thesis outline

Following the "Introduction" and "Objectives" chapters of this thesis, Chapter 2 is a review of literature relevant to this research project. It starts with an introduction to solidification and casting and goes on to describe the concept of machinability and free machining alloys, including attempts to replace Pb with other elements in alloys for machining applications. Melt conditioning by shearing using the rotor stator high shear device, will also be discussed. And finally the main focus of the literature review is to go through the information available on immiscible monotectic systems, including a general introduction, description of the main forces involved in the droplet coalescence and growth, and a review

of the techniques that have been used to obtain a well dispersed homogeneous structure, including the three categories of alloys mentioned and studied in the current work.

The experimental work in Chapter 3 focuses on the development of the new DC casting practices (considering the 3 previously mentioned techniques) to obtain a fine and uniform distribution of Pb particles in the Al matrix. The procedure for the preparation of the binary and 2011 alloys and main inoculants such as Al-Ti and Al-B master alloys, Al-5Ti-B, TiB_2 synthetic powders, under different casting conditions will be explained. Furthermore the characterisation including metallographic analysis and mechanical property measurement techniques will be presented. Experiments to try to understand the effect of shearing, superheat and chemical additions on morphologies and size of Pb particles are described. Other techniques that have been applied to get an understanding of monotectic systems, like DSC, in situ solidification on the synchrotron facilities are also presented and discussed.

In Chapter 4 the metallographic studies on the effect of shearing, superheat and inoculant on Pb particle sizes and morphologies are presented and quantitatively compared for the different casting conditions. The results of new DC casting practices, employed to obtain different levels of refinement of the soft phase particles, are investigated in detail for each of the three chosen alloy compositions. Chapter 5 offers a detailed discussion of the effect of the mentioned parameters and casting practices on the refinement of Pb particles on the solidification of hypo, monotectic and hyper-monotectic alloys. The possible mechanism underlying the refinement provided by each of the individual factors will also be analysed in detail. The main conclusions and suggestions for future work, based on the findings and learnings from this work, are presented in Chapter 6 and Chapter 7, respectively. Finally the bibliographic references are presented in Chapter 8, which is the chapter that concludes the work presented in this thesis.

Chapter 2

Literature review

2.1 Solidification and casting

2.1.1 Solidification

Al is a crystalline solid, composed of a collection of many small crystals or grains. Grain boundaries are formed between crystals of different orientations. Sometimes these are called high angle grain boundaries to distinguish them from the low angle boundaries that result from small imperfections. They are mechanically more reactive than the grain itself (Porter et al., 2009).

Nucleation is the first step for solidification. At full equilibrium, thermodynamics predicts that solidification is not possible. For nucleation to be initiated, the liquid has to be in an undercooled state in metastable equilibrium (ASM Metal Handbook, Volume 2. Properties and Selection: Nonferrous Alloys and Special-Purpose Materials (1990)).

For homogeneous nucleation there is a critical radius for a stable particle to form, both this critical radius and activation energy decreases as temperature decreases (undercooling). The degree of undercooling for homogeneous nucleation is usually quite large, but in practice, due to the presence of foreign particles a range of heterogeneous nucleation temperatures is possible. The more effective the foreign particle the less undercooling will be required for nucleation (Campbell, 2003, Chapter 5).

Furthermore, the thermal history of the melt has a big influence on the transformation kinetics, from one phase to another, and therefore on the microstructure of the solidified alloys (Campbell, 2003, Chapter 5).

When metal enters in a mould, which is normally much cooler, huge amounts of nucleation takes place; the number of nuclei formed during this state depends on the effectiveness of

the nucleant particles present, rate of heat extraction and volume of chilled liquid. If these nucleants can make the alloy nucleate at very low undercooling, the crystal will grow slowly and the number of nuclei that form increases (Campbell, 2003, Chapter 5).

After nucleation, growth is the next step in solidification. Growth starts when an embryo exceeds a critical radius and becomes a stable nucleus. The driving force for growth is the reduction in the total free energy (Porter et al., 2009).

There are 3 modes of growth (planar, cellular and dendritic growth) which can be similarly present during solidification. When solidification starts there is a planar front moving at a certain velocity, causing a diffusion profile of the rejected species in the liquid. The increase in under-cooling causes instability in the advancing front, which changes first to form cells and with further instability it can advance as dendrites. The driving force for instability is the presence of an extra concentration of alloying elements ahead of the solidification front which can reduce the melting point of the liquid below the liquidus temperature of the alloy (constitutional under-cooling)(Kostorz, 2001).
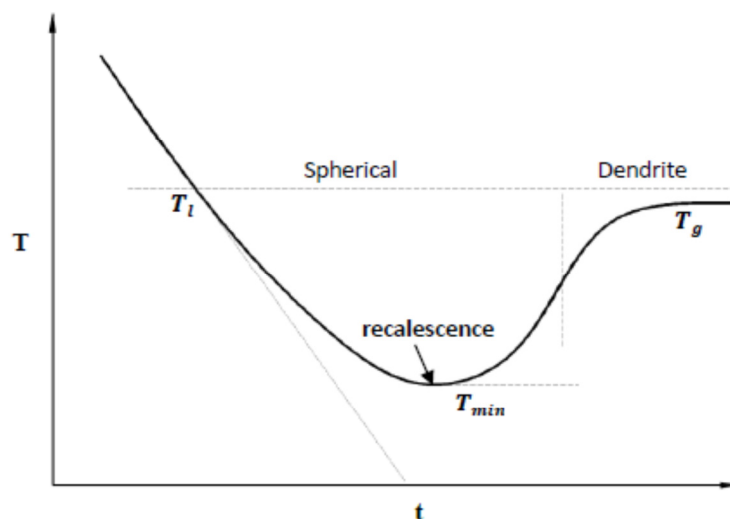
Figure 2-1 Schematic illustration of a cooling curve during solidification, T_l the liquidus temperature, T_{min} the minimum temperature during recalescence, T_g the growth temperature after recalescence. During transformation, growth starts from spherical growth to then become dendritic growth at a further stage (Maxwell and Hellawell, 1975).

The dendritic destabilization can be inhibited with high purity Al and under a strong thermal gradient or cooling rate (less time for diffusion), in which case a columnar solidification will take place. Columnar growth is rejecting only solutes at the front (Dantzig, 2009).

On the other hand the tendency to form dendrites increases as the solidification range increases, with the additions of solute. Due to the solute rejection on the solidification front, solute concentration gradients are established across the grain (micro-segregation). These concentration gradients depend on the value of the partition coefficient:

- When the partition coefficient is smaller than one, the centre of the grain will be richer in the high melting point element and the concentration of the low melting point elements increases with the distance from the centre of the grain.
- When the partition coefficient is bigger than one, that solute will have a peritectic reaction with Al and the center of the grain will be rich in solute (Campbell, 2003).

Partition coefficients close to 1 indicate little tendency toward segregation; whilst very small partition coefficients indicate a strongly partitioning of alloying element.

2.1.2 Al-Cu system

Most of the industrial alloys on the basis of Al-Cu systems belong to the group called "Solid solution type". These alloys are characterised by the presence of an eutectic reaction.

In Al-Cu systems, Al will always be in equilibrium with Al_2Cu (52% Cu) phase which is always present in the structure (see **Figure 2-2**).

Additions of copper can result not only in a solid solution strengthening effect, but also in substantial dispersion hardening after solid solution heat treatment (SHT), quenching, and aging as its solubility in Al dramatically decreases with temperature. Therefore Al–Cu alloys generally have high Yield Strength and Ultimate Tensile Strength (UTS). Unfortunately, copper reduces corrosion resistance of Al alloys. The phase diagram of the Al–Cu system is characterized by large solidification range, which makes castability of Al–Cu-based alloys very low. The solidification range of process of these alloys is quite big, therefore they

normally require to be cast at lower speeds during the DC cast process. This normally results in the formation of coarse dendrites as well as significant micro segregation (Mondolfo, 1976).
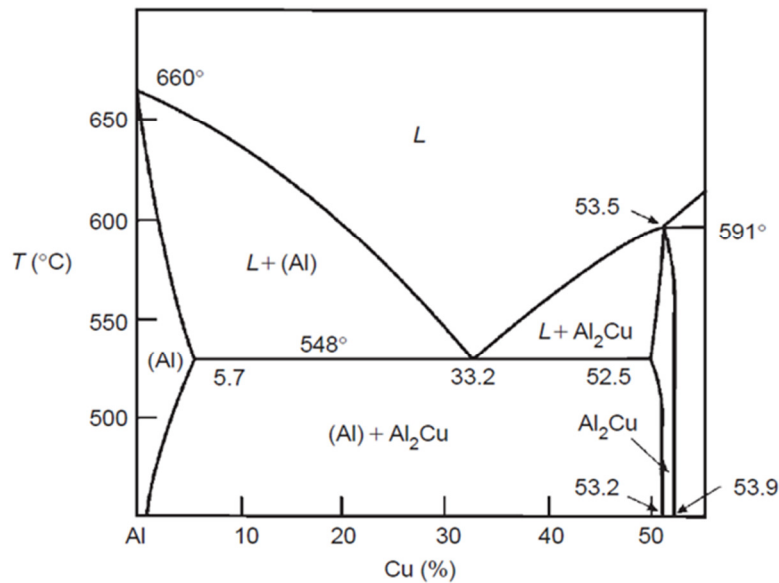
Figure 2-2 Schematic of a binary phase diagram of the eutectic type Al-Cu (Zolotoreski et al., 2007).

Enrichment of Cu in the alloy from 2% results in prominent grain refinement but has virtually no effect on dendritic arm spacing (Jamly et al., 2012).

2.1.3 Casting

In the structure of a cast metal we have to consider the following factors:

- Metallographic structure: size, shape, orientation and perfection of the crystals. It is important to consider, extent of columnar zone and grain size of the equiaxed region.

- Distribution of the different chemical elements in the melt (macro and micro-segregation)

- Internal and external topography of the metal: porosity, surface shape, surface finish.

The different structures obtained in casting depends basically on two different factors, on one hand chemical composition of the melt, including gases created during the process, impurities, nucleant present; and on the other hand on the solidification rate (different part of the melt will solidify at different rates), mould characteristics, like thermal properties, temperature, geometry.

There are three possible zones in solidified alloy ingots (Zolotorevskij, 2007):

- Chill zone: the material in contact with the mould wall cools rapidly and many solid nuclei will form. Under the influence of turbulence in the melt, these crystals will be swept into the melt, if pouring temperature is low these crystals may continue to grow in the melt and this can produce an equiaxed structure. If pouring temperatures are too high the liquid in the center will be above liquidus and these crystals may remelt. When turbulent convection (due to temperature differences) is absent the chill zone will not exist.

- Columnar zone: after pouring the temperature gradient with the mould wall decreases and the crystals start to grow dendritically in some particular crystallographic directions (100) for cubic metals, perpendicular to the mould wall. The region between the tip of the dendrites and the point where the last drop of liquid is solidifying is known as the mushy zone. The length of this zone depends on the temperature gradient and the non-equilibrium freezing range of the alloy.

- Equiaxed zone: consists of equiaxed grains randomly oriented in the centre of the ingot. As one of the reasons for this equiaxed zone, it is believed that these grains could form from melted-off dendrite side-arms. These side arms may partially remelt and detached from the main dendrite, if the temperature is low enough. Constitutional undercooling has also an important contribution to the creation of these small equiaxed grains.

This work will be based on wrought Al alloys, whose domain over casting alloys is represented in the phase diagram in **Figure 2-3**. Wrought Al alloys are cast following a semi-continuous direct chill casting process (DC casting).
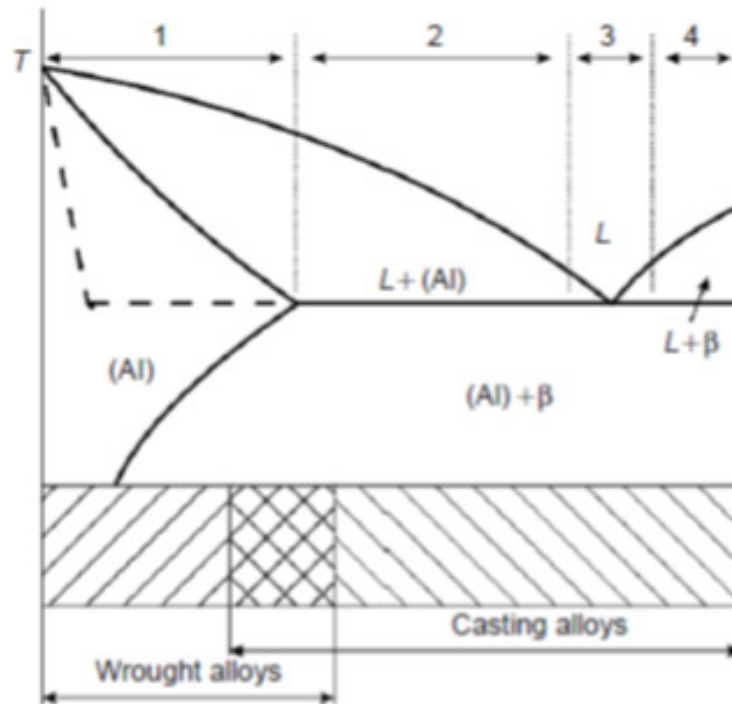
Figure 2-3 Schematic of a binary phase diagram Al-B (2nd component) of the eutectic type: domain of wrought and casting alloys (Zolotorevskij, 2007).

2.2 DC Casting

2.2.1 Introduction

The production of a uniform ingot structure is desirable and this is promoted by direct-chill (DC), semi-continuous processes. DC casting is the main technology for wrought Al alloys since 1950s.

Round ingots for extrusion are now being DC cast with diameters from 0.1 to 2 m. Several ingots can be produced at the same time (Porter and Easterling, 1992).

Most commonly, ingots are cast by the vertical process in which the molten alloy is poured into one, or more fixed, water-cooled moulds (see **Figure 2-4**) (Polmear, 2005).
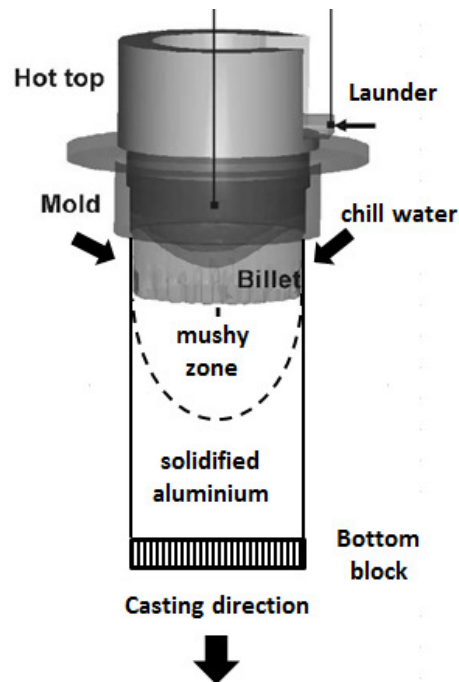
Figure 2-4 Schematic representation of a DC cast unit.

The DC unit (see **Figure 2-4**) consists of a launder, hot top mould fitted into a water box and a moving retractable base to extract the ingot. Melt is poured from the top in an open, short, water-cooled mould that at the beginning is closed by a dummy block connected to a lowering system. After the melt in the mould reaches a certain level, the ram is lowered and the solid part of the billet is extracted downward. The melt flow rate is adjusted in such way to keep constant the level in the mould. As soon as the solid emerges through the bottom water is applied to the surface in form of a film or water spray. This process is semi-continuous, as soon as the ram reaches the lowest position in the pit the process is stopped and the billet is removed (Eskin, 2008).

The process of solidification in DC casting is accomplished in two stages: formation of solid metal at the chilled mould wall and solidification of the remainder of the billet cross section by the removal of heat by sub-mould, spray cooling. The heat is extracted mainly through the solid part of the casting. As a result the sump will be shallow and the solidification profile flat (Eskin, 2008).

A characteristic feature of the process of DC casting is that, the solidification parameters, which influence the solidified microstructure are not constant across the thickness of the ingot. Each elementary volume of the cast metal is solidified with different rate. Its

magnitude depends on the parameters used in the casting process (like the temperature of the melt, the casting speed, the amount of cooling water), and on the position in relation to the mould walls and the axis of the ingot being cast (Jaradeh, 2006).

The finest DAS (dendritic arm spacing) is found in the region with faster cooling, where water impinges the surface of the metal. The dendritic arms are coarser in the centre of the billet and in the region where the air gap is formed.

However, in the metallurgy of wrought alloys is usually the grain size the important structural feature. For purer alloys in the subsurface region the grains are fine and equiaxed, further inside columnar grains are found and in the centre of the billet coarser, equiaxed grains are found (Nadella et al., 2006). In Industrial production of Al alloys the development of small grains during the solidification of the casting is generally an advantage. When the grain size is small, the area of grain boundary is large, leading to a lower concentration of impurities in the boundaries. The practical consequences that generally follow from a finer grain size are:

- Improved resistance to hot tearing during solidification.
- Reduced micro-segregation
- Reduced anisotropy
- Improved resistance to cracking when welding
- Improved resistance to grain boundary corrosion
- Higher yield strength (because of Hall-Petch relationship).
- Higher ductility and toughness, which can also allow for shorter or more beneficial heat treatments.
- Improved fatigue resistance
- Reduced porosity and reduced size of pores.
- Improved hot workability of material cast as ingots (Campbell, 2003).

The main drawback of DC casting is the high thermal gradient between the surface and the interior of the billet (0.3-5 K/mm), which can give rise to surface cracking. Another problem is bleed-outs when the solid shell is fractured bellow the mould and the melt goes through.

On the other hand the high cooling rates achieved by DC casting are beneficial for structure formation, producing fine and homogeneous structure across the billet.

2.2.2 Casting conditions

The main rules to determine the correct casting recipe are as follows:

- Melt level in the mould should be low, in order to avoid high thermal stresses, a wide transition region and a large air gap within the mould. Due to thermal contraction of the solidified shell, it withdraws from the mould surface, reheats and may remelt. The melt can then penetrate through the remelt shell and cause segregation bands or bleed outs. A region of very low cooling rates is observed in the mould when casting with a high melt level and is absent, when casting with low level. Moritz proposed a solution by simply isolating the higher part of the mould with a heat-isolating material. The effective mould length could be controlled by the sizes of the insert. As a result the effective mould length decreased while the real melt level could be maintained as high as suitable for the casting control. What matters is the distance between the lower edge of the refractory insert and the lower edge of the water-cooled mould (Moritz, 1962).
- The water should be applied to the billet surface as close as possible to the end of the mould, and at the minimum angle to the billet axis.
- Melt should be evenly feed into the sump.
- Use the correct casting speed and melt temperature.

Effect of casting speed:

The sump is directly proportional to the casting speed, which means that changes in casting speed will considerably affect the structure and characteristics of the cast billet. Shallower sump and flatter solidification front provides considerably reduced centreline segregation and more homogeneous structure with correspondently improved mechanical properties. When the sump is deepened, by an increase in casting speed, the distance between liquidus and solidus will be bigger, which will increase the mushy zone thickness and consequently an overall acceleration of solidification. For each billet size and alloy there is a maximum

solidification rate that can't be improved by increasing the casting speed; this being lower for larger billet diameters (Suyitno et al., 2004).

Although an increase in casting speed results in some refinement of the grains, their internal structure and the diametric distribution are only slightly affected. The increase of speed enhances only slightly the tendency of grain coarsening towards the centre of the billet.

Casting speed is believed to be the most important parameter that affects hot tearing defects, while pouring temperature and cooling water flow rate are only of minor importance (Eskin, 2005).

Effect of casting temperature:

Temperature is another parameter which can influence billet structures. Evidence has also been provided, by different studies, that a melt superheat increases the probability of bleed-outs during casting, deepens the sump and affects strongly the subsurface positive macro-segregation. On the contrary the macrosegregation throughout the cross section of the billet remains virtually the same, irrespective of the melt superheat (Eskin, 2005). Although not much information was found on the effect of superheat on DC cast solidified microstructure, studies suggested that melt superheat creates a coarser microstructure (Zolotorevskij et al., 2007; Suyitno et al., 2004). However, the findings from the present work suggest completely the opposite for Al-Cu alloys; superheat reduces not only the grain size but also the SDAS.

Grain refinement by inoculation:

Due to the need for small grains in DC cast wrought Al alloys, it is usual to add small amounts of master alloys of Al-Ti, Al-Ti-C or Al-Ti-B to the melt before casting to promote grain refinement. Al-Ti-B is the most widely used alloy with Ti:B ratios varying from 1:1, 3:1 to 5:1, although Al-5Ti-B is now the favoured composition. These grain refiners used to be introduced to the melt in the form of tablets made from titanium and boron salts. Now they are prepared as rods which are fed automatically into the launder and dissolved by the molten metal as it passes from the furnace to the casting station. This is the preferred

method because less time is available for the effects of the grain refiner to fade before the ingots have solidified (Polmear, 2005).

Effective grain refinement by the Al–5Ti–1B grain refiner is directly attributed to the enhanced potency of TiB_2 particles, with a mono-layer of Al_3Ti. The presence of Al_3Ti on the surface of TiB_2 lowers the interfacial energy between Al/TiB_2 (Fan et al., 2015). Furthermore, sufficient free Ti solute in the melt helps to achieve the columnar-to-equiaxed transition, segregate at the solid liquid interface to restrict its growth, allowing for a slower heat release resulting in larger undercooling for nucleation. Solute additions can slow down the heat realease TiB_2 particles without an Al_3Ti monolayer are not potent substrates for heterogeneous nucleation.

2.2.3 Homogenisation

Before DC ingots are transformed into semi-finished products it is necessary to homogenize them at a temperature below solidus, commonly in the range of 450-600 °C, during which diffusion takes place. This treatment has the following objectives:

- Reduction of the effects of micro-segregation that takes place during DC casting
- Removal of non-equilibrium, low melting point eutectics that may cause cracking during subsequent working.
- Controlled precipitation of excess concentrations of elements that are dissolved during solidification.

Homogenization mainly involves diffusion of alloying elements from grain boundaries and other solute-rich regions to grain centres (**Figure 2-5**). The time required depends on diffusion distances, and is reduced as grain size (or dendritic arm spacing) decreases or as rate of diffusion increases for each of the alloying elements (Polmear, 2005). As a rough guide, increasing the homogenisation temperature by 50 °C reduces the furnace time to approximately one third of that needed at the lower temperature. In practice, homogenization times usually vary from 6-24 h depending upon casting conditions and the alloy system.
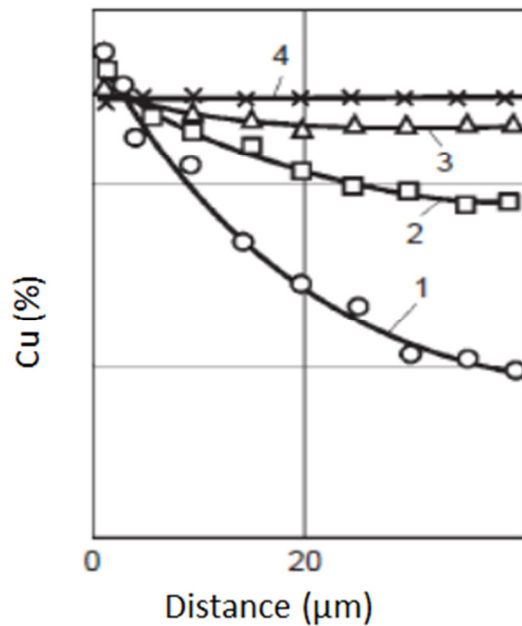
Figure 2-5 Cu distribution across the dendrite cells in Al-5Cu alloy as a function of the homogenisation time, at 540˚C; 1 corresponds to as cast, 2-4 corresponds to heat treatment at 540˚C for 0.2, 1.5 and 2 h respectively (Zolotorevsky, 2007).

Homogenisation is particularly important for high strength alloys as it helps to precipitate and redistribute submicron intermetallic compounds, which will help to control grain structure during subsequent fabrication and heat treatment (Polmear, 2005).

2.2.4 Extrusion

Extrusion is second to rolling for making semi-fabricated products from Al and its alloys. Essentially, the process involves holding a round, pre-heated ingot in a container in a hydraulic press and forcing the ingot through a steel die opening to form elongated shapes or tubes with constant cross-sections. It is of high importance to avoid forming coarse, recrystallized grains which tend to form around the periphery of sections, where the alloy flows through the edges of the die. This effect predominates at the back end of an extruded length because of the nature of flow during extrusion, and is detrimental for mechanical properties. However, in general, the heavy deformation associated with the process of extrusion is beneficial in producing a highly refined microstructure elsewhere in a section.

During high temperature deformation of Al alloys, the main microstructural feature is a network of constantly changing sub-grains. The size of these sub-grains depends on the deformation conditions (strain rate and temperature). Grains and sub-grains can have a strengthening effect in Al.

During extrusion the centre of the billet is extruded first and the peripheral part flows latter. The temperature distribution of billets during extrusion depends on several factors such as billet properties, friction conditions at container and die interface, ram speed, extrusion ratio and die design (see also **Chapter 3, Section 3.4**). Due to the changes in friction conditions during extrusion, the distribution of microstructure cross and along the extrudate can vary considerably under the condition of constant ram speed (Duan and Shepard, 2003).

2.2.5 Ageing

The strength and hardness of some metal alloys may be enhanced by the formation of extremely small uniformly dispersed particles of a second phase; this must be accomplished by phase transformations that are induced by appropriate heat treatments. The process is called precipitation hardening or age hardening. Al-Cu alloys, including 2011 alloy, are part of those alloys which can be hardened by precipitation treatments (Calister, 2007).

Two requisite features must be displayed by the phase diagrams of alloy systems for precipitation hardening: an appreciable maximum solubility of one component in the other; and a solubility limit that rapidly decreases with temperature reduction (Calister, 2007).

Precipitation hardening is accomplished by two different heat treatments. The first is a solution heat treatment in which all solute atoms are dissolved to form a single phase solid solution. The treatment consists of heating the alloy to a temperature at which all the phases present are completely dissolved. This procedure is followed by rapid cooling or quenching to prevent diffusion. For the second or precipitation heat treatment, the supersaturated solid solution is heated to an intermediate temperature within the two-phase region, at which temperature diffusion rates become appreciable. The precipitate phase begins to form as finely dispersed particles. After the appropriate aging time the alloy

is cooled to room temperature. The strength and hardness of the alloy, depend on both the precipitation temperature and the aging time at this temperature (Calister, 2007).

2.3 Melt Conditioning by shearing

Several examples can be found in literature where external forces have been applied to induce fluid flow during solidification to get a grain refinement effect. Some examples are sonic and ultrasonic vibrations, mould rotation and mechanical stirring. These methodologies have been proven to change grain structures from columnar-dendritic to equiaxed-dendritic.

The method described in more detail in this thesis is melt conditioning by shearing employing the high shear device. The efficiency of this method depends on the alloy composition; they are more efficient when alloying elements are present, and some alloying elements are more beneficial than others (Wilson et al., 1988).

The initial technique developed by BCAST consisted of a twin screw Melt Conditioner, in which liquid metal is delivered into a twin screw, and after intensive melt shearing, the conditioned liquid metal is poured for casting. The result of this process is a fine and uniform microstructure achieved by exploiting solidification under high shear stress and rate. This technique has demonstrated an alternative method for producing billets at below liquidus temperature (Zhang et al., 2006). However this process is not suitable for treatment of wrought alloys.

Therefore, a new technology for liquid metal treatment through intensive melt shearing was developed recently to improve the melt quality for wrought Al alloys. The new technology uses a rotor-stator unit to provide intensive melt shearing (Li et al., 2011). This high shear device can provide not only a macro flow for distributive mixing, but intensive shear of the melt next to the tip of the device. A high dispersive and a high shear action are provided simultaneously by the shear unit. The rotor sucks the melt, below the high shear device, into the stator and forces it to leave at high speed, through the openings on the wall of the stator. The escaping liquid will create a macroscopic flow pattern, providing a mixing action in the sump, which homogenises not only the temperature but the chemical composition of

the melt. This macroscopic melt flow will be stronger next to the tip of the high shear device, and weak near the surface of the melt, which will prevent the gas entrapment from the melt surface. The shear rate provided by this device is many orders of magnitude higher than that provided by electromagnetic stirring (Scamans et al.,2012) (Fan et al., 2011). In the absence of fluid flow the dendrite growth is controlled by the diffusion of heat and/or solute. On the other hand under turbulent flow, although initially the growth rate is relatively high due to faster transport of solvent atoms by convection, it decreases with time being finally much lower than with pure laminar or pure diffusive flow (Das et al., 2002).

The intensity of shearing affects the solidification structure by affecting the nature of the fluid flow (Doherty, 200). Under the flow pattern created by the shear device, the liquid atoms are allowed to impinge upon the solid from all directions. The sheared liquid will penetrate inside the diffusion boundary layer of the growing solid particles promoting a destabilizing effect on the solid-liquid interface, liquid will enter the interdendritic spacing avoiding any constitutional undercooling, promoting a planar stable solidification interface, thus producing rosette type morphology (Das et al., 2002).

The key functions of the high-shear device include effective forced wetting of solid particles by the melt, enhanced kinetic conditions for any chemical reaction involving the liquid phase, effective dispersion of particle agglomerates and the uniform distribution of the dispersed solid particles in the melt (Fan et al., 2015). Without shearing nucleation was triggered by thermal undercooling through the mould wall.

Intensive melt shearing does not change the starting nucleating temperature, but it does increase the finishing nucleating temperature. Consequently the temperature homogenization induced by intense shearing, allows the whole of the liquid to be undercooled prior to initiation of solidification. Increasing the survival chance of nuclei throughout the entire melt and nucleation can occur instantaneously throughout the entire volume of the liquid though heterogeneously. This will increase the number of particles nucleating without provoking changes in the nucleation characteristics of the melt (Li et al., 2011). Heterogeneous nucleation will take place throughout the whole volume of the liquid metal, and all the nuclei created will have a chance to survive which allows for a finer grain size and a more uniform distribution through the entire sample (Li et al., 2011). Melt

shearing creates a sharp decrease in melt temperature around the head of the unit, which helps to reduce the remelt rate of the nuclei. By contrast, with the conventional casting process, where most of the nuclei created in the first place may be remelt when they are transferred to regions where the temperature is higher than the alloy liquidus.

However, there is no agreement on the mechanism underlying this effect of shearing on the cast structure, on some other authors, like Helawell et al. divided grain refinement induced by fluid flow by melt conditioning in 5 steps (Helawell, 1996):

- Dendrite branches detach due to local remelt of necks.
- Fragments are transported through the mushy zone by interdendritic convection,
- Fragments avoid remelting, growing and sedimenting
- Fragments block the growth of columnar dendrites.

Furthermore other publications, suggest that under shear conditions primary arms would disappear and growth happens through arm thickening, leading to a near spherical crystal (Kumar et al., 2011). This is directly related to the shear rate, as higher shear rates will give higher arm bending. The bending angle is a function of the cross flow and growth Peclet number. On one hand, the tip rotation increases linearly with flow Peclet number, which is given directly by the shear rate. On the other hand it decreases non-linearly with growth Peclet number, which is determined by the solidification rate. The authors deduce that the maximum dendritic crystal size before spheroidization would decrease with increasing shear rate or decreasing solidification rate (Kapranos, D.H. Kirkwood, 1996; Li et al., 2012).

The main advantages of this unit, are generally agreed in the publications, and include well dispersed and uniform particle distribution, improved chemical composition (reduced macrosegregation), and hot tearing, small equiaxed grains (Fan et al., 2011). Furthermore it is reducing considerably casting defects such as porosity and cracks.

The combination of melt conditioning by the shear device on DC casting has been named Melt conditioned Direct Chill Casting (MC-DC casting). It has been demonstrated that the MC-DC process was capable of producing light alloy billets with fine and uniform microstructure, uniform chemistry and reduced cast defects without the addition of grain

refiner. Grains grow as compact rosettes under intensive convection (Xia et al., 2013). However there is no literature linking the effect of shearing on the DC cast structure with mechanical properties. During the present research it is found that the microstructure created by shearing includes coarser and less numerous intermetallic particles, which finally have a negative effect on mechanical properties of the extruded and thermos-mechanically treated profiles (Li et al., 2011; Zuo et al., 2012).

Melt shearing has proven to have an effect on the oxides that are naturally occurring in Al. Al-Ti-B master alloys are commonly added to DC ingots for wrought alloy production. However, only 1% of the added particles nucleate Al grains. The addition of refiners is undesirable mainly for cost reasons but also because refiner particles may be detrimental for the microstructure, specially for extrusion, deep drawing and high performance structural applications (Li et al., 2012).

The high shear rate provided by the rotor-stator disperses the inclusions and oxide films into individual particles. These individual particles are useful for grain refinement (Scamans et al., 2012; Fan et al., 2011), as they can act as nucleus for Al_3Ti, provided that there are a good crystallographic matching between the oxides and the Al_3Ti particles. Both Zn-spinel and Mg-spinel, could be good substrates for the nucleation of the Al_3Ti phase. Al_3Ti particles will then nucleate on oxide particles (which are existent in sufficient number and with favourable particle size and distribution) at relatively low undercooling (Li et al., 2011). This theory of nucleation has been also supported by the fact that Al_3Ti had formed before the melt was poured into the MCAST unit at 650°C, so that intensive melt shearing had no influence on the formation of Al_3Ti, when shearing at this temperature.

Contrary to the faceted morphology exhibited by the $TiAl_3$ particle in the non-sheared melt, with melt conditioning these particles will be equiaxed and with a narrow size distribution.

Melt shearing can be used to wet, disperse and distribute synthetic TiB_2 particles in Al, and to enhance the kinetic condition for the interaction between solute Ti and TiB_2 particles. This will help to create a monolayer of Al_3Ti on TiB_2, which then act as a potent nucleant for Al (Fan et al., 2015).

2.4 Machinability

2.4.1 Introduction

The application of Al to automobile parts has been greatly increased. Machining is a usual way to make parts of metallic materials. Therefore extruded sections are often machined to produce value-added finished components. Machining process produces the required shape by removal of selected areas of the work piece. Most machining is accomplished by straining a local region of the work piece to fracture by the relative motion of the tool with respect to the work piece (Dieter, 1987). Machining is usually employed to produce pieces with high dimensional tolerance, good surface finish and often complex geometry. The machining process is represented in **Figure 2-6**.
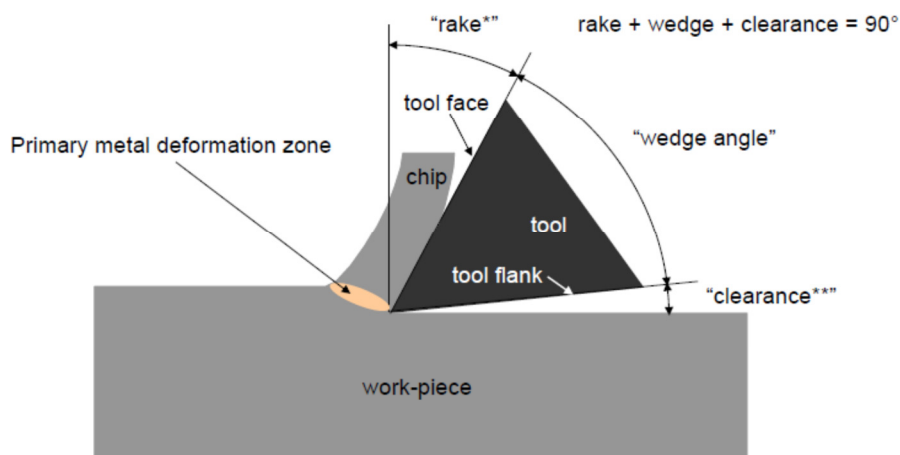
Figure 2-6 Schematic representation of the machining (chip breaking process).

Machining productivity is a function of several process parameters such as cutting speed, feed rate, depth of cut, tool radius, rake angle, cutting fluid and others. The alloy plays also a very crucial role (Parsons, 2012).

2.4.2 Machinability indicators

Machinability is a term which combines different factors, including productivity and cost of the machining process (Kouam et al., 2012). There are several indicators to measure the machining performance, between them are cutting force and moment, tool life (normally

calculated as number of holes drilled up to the point of tool breakage) (Elgallad et al., 2010) and quality of the machined part.   The ability to form discontinuous and short chips to facilitate their removal from automated machining lines is the primary requirement for a machining. Grade "A" machinability performance, which is characterised by short and broken chips, is desired in order to guarantee high tool feed rates in connection with low cycle times and reduced machine downtimes for cleaning (Duplancic et al), and long machining tool life.

Chips are one of the major waste stream components of machining. They are formed as unwanted material is cut away from a work piece, and can be continuous or discontinuous. Continuous chips have a uniform amount of shear strain throughout their length. For discontinuous chips intense shearing is concentrated in narrow bands, causing slippage of planes and a discontinuous surface. As the chip is forced into the work piece, it develops a bending moment which ultimately causes fracture. Small, well broken, chips which are easier to handle and dispose of (specially in automated machining lines) and they are a primary requirement for machinability. Long unbroken chips may damage the machine or work piece, and can even be dangerous to the machine tool operator (Campbell et al., 2006).

The chip formation process is highly complex and is governed by mechanisms which are not yet fully understood. It is deformed plastically and sheared adiabatically away from the remaining metal. Although the deformation region goes to extremely elevated temperature, it is transferring little (or no) heat to its surroundings while the material deforms in shear parallel to the shear plane angle (Wang et al., 1987).

Several solute additions can have an influence in machinability. Functions of some of the alloying elements present in 2011 alloy in machinability are:

- Copper: in most cases is distributed between the Al and Al_2Cu phase. Chip breakability was proved to be also related to the cracking of the second-phase particles, and a direct relationship between volume of second phase intermetallics (Al_2Cu) and machinability has been found (Kamiya and Yakou, 2008).   Medium Cu contents provide a good compromise between high strength and good machinability. Noticeable influence of Cu in chip sizes can only be observed at concentrations higher than 4%.

- Low melting point additions (Pb, Bi, In) improve machinability when they meet the following criteria
  - Insoluble in solid Al
  - The phases formed partially melt during machining.

However, the exact contribution of each of those factors to machinability is not completely clear from the information contained in the literature. Furthermore, there is no description of the type and morphology, including exact chemical composition (when Fe is present it will also appear on the Al-Cu intermetallics), of the intermetallics for enhanced machinability. Alloys like 2011 containing Pb and Bi are designated as free machining alloys (see section 2.4.1).

2.5 Free machining alloys

2.5.1 Introduction

Standard Al alloys are of inferior machinability, due to the fragility of the produced chips. Therefore, free-machining Al alloys have been developed, in which the fragility of the chip is improved by the addition of these low melting point elements like Pb, Bi. These low melting point phases not only expand, and create the surface tension necessary to allow the chips to break away; but they are melted due to the increased temperature during machining, generating chips easily. They provide a soft and ductile dispersed phase in a hard and strong matrix, producing alloys with optimum machining performances. Free-machining alloy are considered as the benchmark in machinability and provide an "A" rate in machinability.

The alloys formed between Al and these soft phases are called monotectic immiscible systems, which are explained in detail in **Section 2.6.**

For this type of alloys, the machining performance of the final product is determined by microstructure, which in turn, is largely dependent on the complex phenomena taking place during the cooling and solidification of these immiscible monotectic systems (Ratke and Diefenbach, 1994; Tegze et al., 2005).

The studied 2011 alloy belongs to the group of Al-Cu-Pb-Bi alloys, which is the most common series of free machining alloys (Mohamed et al., 2009). In 2011 alloy the soft phases Pb and Bi are present, as low melting Pb_3Bi (125˚C) eutectic. When Mg is present, Mg_2Pb and Bi_2Mg_3 phases will form instead of the eutectic Bi-Pb, these phases melt at 248°C and 271°C respectively. Due to these higher melting points the phases are more stable at a higher temperature, and as a consequence they produce bigger chips and are more abrasive to the tooling (Spillard, 1998).

It is believed that the size, shape and distribution of the soft particles are very important to the machining properties. These low melting point particles must be of a very small size and in uniform distribution in the alloy structure (Wang et al., 1987). However, there is no information about optimum phase size and distribution, for best machining results, and no direct link between particle size and machinability has been shown.

Over the past decades, there has been a global movement to restrict Pb and Pb containing products due to their toxicity. Consequently, by the 1st of July, 2008, Al for machining purposes with a Pb content of more than 0.4 wt.% by weight was prohibited by the European Union.

Also the European Union endeavours to reduce environmental Pb contaminations in a large scale through the RoHS (Reduction of Hazardous Substances 2002/95/EC) and the ELV (End of Life Vehicles 2000/53/EC). Disposal of Pb chips is problematic and during the machining process Pb can be released as smoke and/or dust.

Therefore, the industry is seeking alternative alloy formulations with machinability approaching that of alloys containing Pb and Bi (Kouam et al., 2012).

2.5.2 Machinability improvement techniques replacing Pb additions

Several approaches were taken to try to replace Pb additions in Al alloys while maintaining optimum machinability results. The present chapter will be focussed on the effect of different alloying additions to replace Pb, trying to keep an optimum machining performance. The effect of Sn, Si, Mn and Cu additions, together with refinement of Fe/Mn intermetallics, and relationship between hardness and machinability will be considered.

Spillard analyses the replacement of both Pb and Bi with Sn, in Mg containing alloys, suggesting that it would give a greater volume of low meting phases (Spillard, 1998). DSC scans show a dissolution reaction in the region between 195 – 208 °C, which indicates a low melting eutectic of β-Sn + Mg_2Sn (S. Koch et al., 2008). Since the melting area is situated at such low temperatures, the machining performance of the investigated alloys can be assumed as "A" rated (Koch et al., 2008). However Sn additions are not suitable for a number of alloys due to different reasons, for example for Al-Si-Cu-Mg alloys, Sn prevents the formation of Mg_2Si, and Sn and Pb prevent the formation of Al-4Cu-5Mg-4Si, decreasing therefore the alloy mechanical properties (Mohamed et al., 2009; Koch et al., 2010).

Best machinability defined by Asano and Fujiwara (Asano and Fujiwara, 1971) is when the number of chips in 100 g is a $10^4 < N < 10^5$. They found that the alloys that provide the best machinability are the ones which contain the following 2nd phase particles: Al_2Cu, Si, Mg_2Si and Al-Fe-Si. Within those particles only Al_2Cu and Si particles could be easily cracked during machining. The fracture of Mg_2Si particles could not be observed, they are also believed to have an effect as a cause of chip breaking (Kamiya and Yakou, 2008). The precipitation of Al_2Cu phase particles, when adequate amount of Cu is added, can improve the homogeneity of the matrix. This improvement leads to a reduction in cutting force during machining, but also to an improvement on the surface finish and reduction of build up on the edge of the cutting tool (Tash et al., 2006).

The improvement in machinability with additions of Si was also described in several publications. Si containing second phase compounds were found on the origin of the chip fracture. It is believed that Si lowers the friction coefficient against the cutting face, this will increase the bending strain and make the curl radius of the chip decrease, facilitating therefore the rupture of the chip (Yoshihara and Osaki, 2002).

For the same depth of cut, Si additions change the chip morphology from continuous to broken, chips become thinner as Si quantities are increased. Shear strain also decreases with Si additions.

Other results confirm a direct relationship between the surface roughness of the matrix and the force employed during machining. Surface roughness was found to improve as Si phase

was increased and space between Si compounds reduced (Grum and Kisin, 2003, part I and part II).

Despite the previously mentioned advantages of using Si additions to improve machinability, Si has a negative effect on the alloy thermal stability, which is one of the most interesting properties of these alloy series, and therefore cannot be used on 2xxx series alloys. Furthermore, Yoshihara et al suggested that Si additions reduce mechanical properties when added to alloys like 6061.

In the case of 6XXX, Mn, Fe contents around 2% increase the number of secondary particles and improve lightly machinability for 6XXX alloy (Sato et al., 1998). Two main types of iron intermetallics are formed in these Al-Si-Mg alloys, the platelet or needle-like βFe (Al-5Fe-Si) phase that is detrimental to the alloy properties, and the αFe Al-15(Fe,Mn)-3Si phase which is less harmful. The formation of the latter phase is promoted by additions of neutralizing elements such as Sr in the presence of Mn, and higher Mn/Fe ratios (from 0.4 to 0.75) (Tash et al., 2006).

Hardness and its relationship to machinability have also been studied. The optimum machining results (considering optimum cutting force, moment and build up edge) were obtained at medium hardness levels (100HB). Considerably higher values of hardness showed an increase in cutting force, and although the build-up was decreased, general machinability was not improved. Therefore heat treatment, after alloying, is one of the most important controlling factors that can be used to enhance the mechanical properties and machinability for Al-Si alloys (M. Tash et al., 2006). However, it is found that small changes in hardness, on values around 100HB, have no direct link with machinability. On the other hand, Yoshihara et al suggested that the increase of machinability with hardness depends on the additions made to the alloy (Yoshihara and Hirano, 1998).

Furthermore, Tash et al explain that Al alloys differ from many other metals in that the machinability of Al generally improves as the hardness increases. However this results are only linking hardness to machining characteristics like build up edge and cutting force but no to size and morphology of the resulting chips; the current study on Al-Cu alloys suggest no direct relationship has been found between machining performance, measured as number of chips per 100 g, and hardness (Tash et al., 2006).

It is explained by Tash and co-workers that heat treatment is one of the most important controlling factors used to enhance the machinability of cast Al–Si alloys, through optimization of both the solution and aging heat treatments given to such alloys.

Chip size and morphology was also found to be directly dependent on alloy temper. For 2011 machined, chips were long after quenching on the press; whereas chips become considerably smaller after treatment to get to T6 and T8 Tempers. However, there is no information on the difference in machinability obtained from profiles treated to T6 and T8 tempers, which would be the most relevant industrially.

Some results on the role of dendrite arm spacing and heat treatment on machinability have also been reported by Yamada and Tanaka (Yamada and Tanka, 1977). These results showed that by refining the dendrite arm spacing it is possible to reduce tool wear.

2.6   Immiscible alloys

2.6.1   Introduction

The latent heat, evolving during mixing of two constituents, is related to the interatomic interactions between atoms. Depending on whether the interatomic energies in the alloy are stronger or weaker than in the unmixed components, there is a tendency towards compound formation or towards phase separation (preferred neighbourhood of the same atoms). Immiscible alloys are characterized generally by positive enthalpies of mixing, this occurs for liquid alloys if the atomic radii differences of the components are large and the differences in electronegativity are small, and it practically means that immiscible systems the tendency is towards phase separation (Andrews et al., 1993) . These radii differences, between the metals, are also related to the critical temperature for demixing. Bigger radii differences will give a higher critical demixing temperature, and a more positive enthalpy of mixing; which in turn means smaller solubility of the components in each other (Prebel, 1997). This is the case for Al-Pb, which has the biggest radii difference within the Al based immiscible systems.

 Another characteristic of these immiscible systems is that the liquid/liquid interfacial energies are lower than the surface tensions by about one order of magnitude (I. Budai et

al., 2010). For instance at 700°C the surface tension of pure liquid Al and Bi are about 880 and 350 mJ/m, respectively, while the liquid/liquid interfacial energy is only about 50 mJ/m (Budai et al., 2010).

The wide miscibility gap in the liquid state that characterise the Al-Pb system, is shown in the phase diagram (Kaban et al., 2011) in **Figure 2-7 (b).** The miscibility–immiscibility phase boundary is named the binodal line. Above the so-called critical temperature, indicated by the binodal line, both components are completely miscible to every amount or proportion in the liquid state. But on cooling the homogeneous liquid decomposes in 2 liquids when crossing the binodal line, originating 2 separate liquid phases.

On further cooling, when the monotectic temperature is reached, one liquid phase adjusts its composition to the monotectic one and solidification then occurs as for exact monotectic, with the additional microstructure set during cooling through the miscibility gap. The first liquid decomposes at the monotectic temperature into a solid and a liquid phase (Silva et al., 2009).

The solidification of immiscible alloys can be divided into three categories depending on alloy composition (Ratke et al., 1996):

- Composition below the monotectic, i.e. hypo-monotectic: the solidification of these alloys can be treated as the classical solidification of miscible alloys. The primary phase occurring during solidification is a nearly perfectly pure phase, i.e. the partition coefficient is very small, of the order 10^{-4}.
- Monotectic.
- Compositions above the monotectic, i.e. hyper-monotectic composition: prior to the occurrence of a solid phase liquid-liquid decomposition and spatial microstructure evolution takes place.
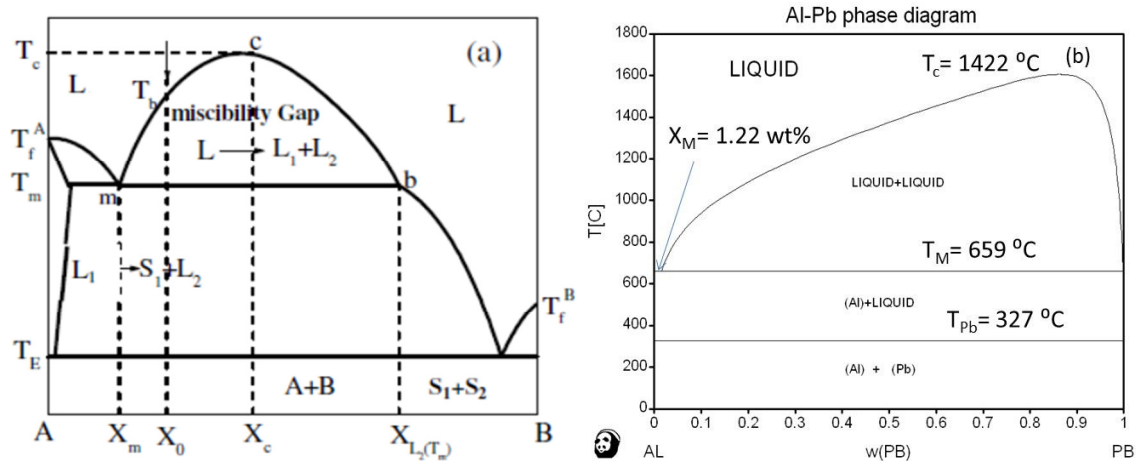
Figure 2-7 (a) Schematic diagram (Kotadia, 2010) of a typical binary phase diagram with a miscibility gap in the liquid state. Tc – critical temperature; Tf $_A$ – melting temperature of component A; Tf$_B$ – melting temperature of component B; Tb – melting temperature at X0 composition; Tm - monotectic temperature; Xm – monotectic composition; X0 – gross composition of the alloy considered; (b) phase diagram of Al-Pb binary alloy, where the Tc is 1422 ^{o}C, XM corresponds to 1.22 wt% Pb, TM is 659 ^{o}C, and Pb melting temperature (T$_{Pb}$) is 327°C. L1, L2 designate the two different liquids being in equilibrium below the critical temperature and (b) binary phase diagram for AlPb

Monotectic solidification could be treated similarly to eutectic solidification; alloys of monotectic composition can be solidified directionally such that a fibrous microstructure is observed (as in some eutectics) (Soecker and Ratke, 1999). Silva and co-workers have seen that the Pb morphology depends on the growth rate and the critical value of growth rate in which the morphology changes depends on the Pb content of the alloy. If the rate of solidification is faster than the droplets growth, the droplets are trapped by the advancing front (Silva et al., 2009). The regime of fibrous composite growth is only restricted to small velocities and high temperature gradients ahead of the solid/liquid interface. Two fundamental differences can be considered between monotectic and eutectic solidification (Ratke et al., 1996):

- One of the products of the monotectic reaction is a liquid phase. Normally the melting temperatures of the components differ considerably; the second liquid stays liquid far behind the monotectic reaction.
- The liquid-liquid interface will be a low-energy interface with high mobility and a high diffusivity.

2.6.2 Collision and coalescence or coagulation

The previously mentioned phase separation, which is relevant even under microgravity conditions (Ratke, 1988), takes place in three steps. When passing through the miscibility gap, at first a finely dispersed precipitation occurs with tiny droplets nucleating on the Al matrix. The driving force for phase transformation, which is the reduction in the Gibbs free energy of the system ΔGv, (calculated by multiplying the enthalpy of reaction by the undercooling) dictates the nucleation. The Gibbs free energy is partially consumed to overcome the barrier for nucleation (Zhao et al., 2002). Ideally, the shape of a liquid droplet is determined by the surface tension. The molecules exposed at the surface and in contact with the other liquid do not have neighbour molecules in all directions to provide a balanced net force. Instead they are pulled inward by neighbouring molecules, creating an internal pressure. As a result the liquid tries to maintain the lowest surface free energy, therefore the droplets are spherical, which gives the minimum surface area for a fixed volume (Yuan et al., 2013).

After the critical level of supersaturation is reached and nucleation starts, the growth of the formed droplet will take place. The droplets formed during the phase separation will start to approach each other, influenced by several forces mainly Marangoni and Stokes.

 The diffusion coefficient in liquid alloys is generally very high (up to 10^{-8} m^2 s^{-1}, 10 orders of magnitude higher than the one in solid, typical of 10^{-18} m2 s^{-1}); therefore once nucleated, the minority liquid droplets can grow very rapidly to become large droplets. Diffusion and convection phenomena induce droplet coalescence and segregation (Ratke, 1988), and are influenced by several forces mainly Marangoni and Stokes.

Ratke found experimentally that the diffusion coefficient for immiscible systems is related to temperature by the following formula:

$$D(T) = D_0 T^2 \qquad\qquad (2\text{-}1)$$

Where $D(T)$ is the diffusion coefficient as a function of temperature (m^{-2} s^{-1}), D_0 is a constant (m^{-2} s^{-1} K^{-2}) and T temperature (K).

This same power relation for the diffusivity in relation to temperature has been confirmed for Al-Bi and Al-In alloys.

For the Al-Pb system D_0 is 5.747x10-15 and therefore the diffusion coefficient was estimated as 5 x10–9 m^{-2} s^{-1} at monotectic temperature (J. Zhao, L. Ratke, 2004; L. Ratke et al., 1996).

$$Pe = vr/D \qquad\qquad (2\text{-}2)$$

 Where Pe is the Peclet number, D is diffusivity (m^{-2} $s^{-1}$$K^2$), v is particle velocity (m s^{-1}) and r is the particle diameter (m).

The Peclet number (**Equation 2-2**) determines the dominant mechanism on droplet growth. Although the diffusional growth of the minority phase takes place during the whole separation process, this process dominates only when the diameter of the droplets is smaller than 1 µm and mainly in the absence of melt flow (Pe<<1). In the presence of melt flow, Tegze and co-workers (G. Tegze et al., 2005) found hydro dynamically driven coalescence to be several orders of magnitude faster than the diffusion, and therefore the Pe>>1.

Subsequently, when the supersaturation reaches very low levels, coarsening will take place. The driving force for coarsening is the reduction in interfacial energy, as the exposed surface of a big droplet is smaller than that of a dispersion of small ones therefore the interfacial energy of the system will also be smaller (Ratke, 1988).   Droplets will therefore, collide with each other and coalesce to reduce their surface energy by forming a single one and reducing the exposed surface. When two droplets are sufficiently close they interact to each other due to hydrodynamic disturbances. The large droplet overtakes the small one and they combine with each other to form a new one (Schauffer et al., 2009; H. Tang et al., 2005). Coalescence depends on droplet motion, which in turn is directly influenced by Stokes and Marangoni forces, but it also depends on the volume fraction of droplets of the soft phase existing in the system (Kotadia et al., 2011).

Another important parameters affecting droplet coalescence is Brownian motion (L. Chen et al.,2014), which can be easily calculated with the following formula:

$$E_b = Tk/2 \qquad (2\text{-}3)$$

Where E_b is the Brownian motion *(*m^2 kg s^{-2}), k is the Boltzmann constant (1.3806503 × 10^{-23} m^2 kg s^{-2} K^{-1}) and T is the absolute temperature of the system (K). Brownian motion is only relevant for droplets sizes around 1.5 μm and smaller.

On the third step, of phase separation, as the denser phase sinks to the bottom, layers are formed with the denser phase at the bottom, lowering the centre of gravity, which results in a potential energy gain, dependent on the concentrations (see section 2.5.4). Although this layer formation results in a very small decrease in free Gibbs energy, the decrease in potential energy is enough to create in a 10 cm height sample a complete phase separation in less than 10 sec, for an Al-Pb alloy. The cooling needed to avoid this effect was calculated to be on values around 106 K/s (Zhao et al., 2005).

2.6.3   Marangoni motion

The high temperature gradient during casting generally induces severe thermo-capillary forces that push the droplets to the hotter region.

These thermo-capillary forces, drive the droplets with a velocity proportional to the radius of the drop and the temperature gradient. This motion is a surface-driven convection, which takes place trying to reduce the interfacial tension between the 2 phases, making the droplets move towards hotter areas of the sample, as surface tension is reduced with temperature increase (Nester et al., 2000). Therefore any temperature gradient will induce a fluid motion. The velocity of a drop caused by Marangoni motion can be described with the following (Dai et al., 2011) equation:

$$V_m = \frac{-2r}{3(3\mu_d + 2\mu_m)} \cdot \frac{\delta\sigma}{\delta T} \cdot \frac{\delta T}{\delta x} \qquad (2\text{-}4)$$

Where V_m is the Marangoni velocity (ms^{-1}), R is the droplet diameter (m), μd: droplet viscosity (Pa.s), μm: matrix viscosity (Pa.s), x: distance, g: gravity, δσ: interfacial tension gradient (Jm^{-2})

Marangoni motion is therefore increasing with droplet diameter, temperature and interfacial tension gradients, and is inversely proportional to the viscosity of the 2 liquids. The lower the viscosity the larger the repulsive force. If homogeneous temperature can be created along the molten metal during solidification, it should contribute to a significant reduction or elimination of the Marangoni motion. When the temperature is completely uniform Marangoni forces will not apply.

Marangoni motion can lead to undesirable spatial separation of the phases both on the Earth and in low-gravity environments (Kotadia, 2010). The types of microstructure that can be obtained under microgravity, including a well dispersed structure, and the conditions to obtain them are reviewed by Andrews and co-workers (Andrews et al., 1993).

Marangoni effect causes convection at the interface of the liquid L2 phase. This convection induces a flow field in front of the solidification front and has a strong influence on the solute transport. The influence of the surface convection could be estimated by the Marangoni number. Typical values of this dimensionless quantity are Ma=10. When Ma<1 the surface convection cannot be neglected.

Marangoni motion starts to become significant with droplets sizes bigger than 1 μm. At this point the droplets are big enough to produce a surface tension difference between the hot and the cold area to create a Marangoni migration (Wang et al. 2013).

Some of the main parameters that contribute to Marangoni motion are explained in the following paragraphs.

Viscosity is the measurement of fluid resistance to motion, under applied stress. The viscosity of liquids is related to internal friction and defined by Newton's law as the proportionality coefficient between a shear stress (ϕ) acting on a fluid and the related velocity gradient (dv/dx) (Ratke and Diefenbach, 1994):

$$\mu = \phi \cdot \frac{dv}{dx} \qquad\qquad (2\text{-}5)$$

The viscosity is temperature dependent and can be expresses in an Arrhenius type equation (Fan et al., 2001):

$$\mu = C\ exp\left(\frac{E}{RT}\right) \qquad (2\text{-}6)$$

Where μ is the viscosity (Pas), C (Pa s) and E (Jmol^{-1}) are constants and R the ideal gas constant (Jmol^{-1}K^{-1}).

The value of these constants has been previously determined and is shown within the following formulas (Nuclear Energy Agency, 2007; Zhao and Ratke, 2004):

$$\mu_d = 0.0001492 exp\left(\frac{1986.9}{T}\right) \qquad (2\text{-}7)$$

Where μ_d is the viscosity of the Pb droplets (Pas)

$$\mu_{dd\prime} = 0.000494 exp\left(\frac{754.1}{T}\right) \qquad (2\text{-}8)$$

Where μ_{dd} is the viscosity of the Pb-Bi eutectic droplets (Pas)

$$\mu_m = 0.0004636 exp\left(\frac{1036.7}{T}\right) \qquad (2\text{-}9)$$

Where μ_m is the viscosity of the Pb-Bi eutectic droplets (Pas)

The other important parameter to determine the Marangoni motion is the interfacial tension. Interfacial tension is of high importance for the phase separation process in immiscible alloys. It determines the possible undercooling below the equilibrium binodal line and therefore the barrier for nucleation and the rate of nucleation (Ratke and Diefenbach, 1995). The interfacial tension between 2 phases is the force acting normal to the interfacial plane, and it is direct measure of intermolecular forces. It is essential to understand processes like nucleation, growth and chemical reactions. Chadwick (Chadwick, 1965) proposed that for an alloy of monotectic composition the interfacial energies between the phases could control the final structure obtained after solidification.

$$\sigma = \sigma_0\left(1 - \frac{T}{T_c}\right)^{1.26} \qquad (2\text{-}10)$$

The interface tension is related to temperature using **Equation 2-10** (J. Zhao et al., 1998).

Where σ is the interfacial tension (Jm^{-2}), σ$_0$ is a constant (Jm^{-2}), T is the absolute temperature of the system (K), T$_c$ the critical temperature (K), which for the Al-Pb binary system was calculated from the phase diagram with a value of 1695.4K.

σ$_0$ a constant that can be determined from the value of the interfacial tension at the monotectic temperature, measured in J/m^2. This constant was calculated for the Al-Pb system and has a value of 0.328 J/m2 (Zhao and Ratke, 2004). Interfacial tension Al-Pb and Al-Bi decreases considerably with temperature increase.

2.6.4 Droplet sedimentation (Stokes motion)

Nucleated and grown droplets are exposed to gravity-induced sedimentation, due to the different densities of the phases. Stokes motion can be described by the following equation (Dai et al., 2011).

$$V_S = \frac{2g\Delta\rho r^2}{3\mu_m} \cdot \frac{\mu_d + \mu_m}{3\mu_d + 2\mu_m}$$
(2-1)

Where Vs is the Stokes sedimentation velocity (ms^{-1}), g is the gravity force (N) and Δρ is the density difference between both phases (Kgm^{-3}). This gravitational force is an increasing function of the drop diameter and an inverse function of its viscosity.

Settling velocity increases mainly as the size of the droplets increases and as the density difference between the 2 phases is bigger (assuming that droplet density is higher than that of the parent liquid). For a particular casting, in which the rest of the parameters are constant, the smaller the droplet radius the less sedimentation will take place.

When the droplets sediment they coalesce into a segregated layer of liquid phase. This layer grows if solidification is slow enough until all the dispersed droplets have coalesced into it (Kotadia, 2010). The Stokes sedimentation takes place mainly when the droplet diameter is bigger than 10 µm.

Depending on the size and volume fraction of droplets this process can be very fast, even more rapid than growth by diffusion.

To summarise, both Stokes and Marangoni are the biggest barriers to produce a dispersed and fine microstructure, but additional factors, like contact angles between phases at the growth front, the miscibility gap height, the ratio of liquidus slopes and the degree of undercooling at the solidification front, are known to have an influence on the type of structures obtained during solidification of immiscible alloys (Ratke et al., 1996).

In summary, the various processes that explain droplet coalescence and growth are (Tegze et al., 2005):

- Diffusion-related and convection processes
- Hydrodynamic effects
  - Marangoni motion, thermo-capillary forces move the droplets due to thermal gradients. Trying to reduce their interfacial tension the droplets will move toward hotter areas of the sample, facilitating the coalescence.
  - gravity-dependent effects, Stokes motion: settling of the second phase droplets due to density differences with the Al matrix.

As seen from the Marangoni and Stokes sedimentation velocities formulas, for manufacturing of immiscible alloys fluid flow properties, like density, viscosity, surface tension, have a critical importance (Wilson et al., 1988; Akagwu et al., 2000)

A description of monotectic growth was presented by Coriell and co-workers and Nestler and co-workers (Nestler et al., 2000; Coriel et al., 1997). The latter have also included convection in their face field model.

2.6.5 Techniques to produce a well dispersed homogeneous structure in immiscible systems

The present work is based on the hypothesis that the size, shape and distribution of the soft particles are very important to the machining properties of the previously described free machining alloys (**see Section 2.4.1**). However, no information has been found, on the reviewed literature, about optimum droplet size and droplet size distribution for enhanced machining performance of Al free machining alloys containing immiscible elements.

Under conventional casting conditions, serious segregation and quick phase separation in immiscible systems, is leading to layered structures and coarse dispersions; making the production of monotectic alloys with a finally dispersed minority phase nearly impossible (Ratke et al. 1996). Therefore immiscible alloys can't be casted using conventional casting methods

Several preparation technologies such as powder metallurgy, directional solidification, casting under microgravity conditions, stir casting, controlled casting, and rapid solidification, etc. have been applied for the processing of immiscible alloys (Tang 2004). None of them has been completely successful to produce a very fine and completely uniform distribution of the soft phase in the Al matrix.

Several authors have proved that the effect of the gravity field on earth, can be partially compensated with magnetic and electric cross-fields as well as by ultrasonic vibration, to produce a homogeneous distribution of the Pb phase in the Al matrix (Kotadia, 2010).

Some of the techniques that have been employed as means of trying to have the optimum soft phase droplet size and distribution and can be easier applied in industry, can be summarised as follows:

1. Stir casting, which is of a special importance in this study. The dispersion of the minority droplets, through vigorous stirring, depends on processing parameters like temperature, viscosity of the phases, density and interfacial tension. Dispersion of the minority particles also depends on the type of stirrer used for mixing and other parameters like stirring speed, time and temperature.

    a. Mechanical stirring.

    Mechanical stirring promotes droplet break up and dispersion of the minority phase droplets in the Al matrix, but also helps to reduce droplet coagulation and sedimentation, due to the temperature uniformity created along the solidifying melt. Several experiments have been performed applying mechanical stirring on immiscible systems. The higher the stirring speed the finer the distribution of the second phase droplets in the Al matrix. These results are confirmed by Kotadia and co-workers (Kotadia et al., 2009), who applied different stirring speeds (200,

400, 600, 880 and 1000 rpm) before casting. The stirring technique chosen in this research is the rotor stator high shear device developed by BCAST to overcome segregation problem, on immiscible alloys during DC casting. However, this work is only based on immiscible alloys of hyper-monotectic compositions, and no information was found on the effect of shearing on hypo- and exact monotectic compositions, which are the most relevant in industrial applications.

b. Ultrasonic and magnetic vibration: and ultrasonic and magnetic vibration which mainly act avoiding particle coagulation

c. Physical stirring: degassing also has an effect on refining the Pb-Bi particles. The longer the bubbling time the finer the Pb-Bi particles. There is a critical time, which when exceeded, reduces or inverts the refining tendency.

2. Fast cooling rates (rapid solidification): fast cooling rate gives finer structure and finer particles also.

3. Addition of inoculants

Some of these techniques will be explained in more detail in the following sections of this chapter.

2.6.5.1. _Effect of Shearing on immiscible systems_

The working principle and benefits of the rotor-stator unit for melt conditioning of Al and magnesium alloys, have been explained elsewhere (Fan et al., 2011). This section is focussed only on the applicability and effect of stirring (particularly focussed on twin screw and rotor stator units) on immiscible systems. The shear flow, created by stirring an immiscible alloy, can have a direct effect on its microstructure (Kotadia et al., 2009). Shearing employing adequate parameters can induce the rupture of the liquid droplets (Scardovelli et al., 1999) and disperse them in the Al matrix (Fan, Z. Fan, 2005). This will create a fine and homogeneous liquid dispersion within the miscibility gap. The final size of liquid droplets will be dictated by the intensity of shear mixing action and the thermo-physical properties of the system, such as viscosity and interfacial tension (Callister, 2007).

This deformation and rupture in a simple shear flow is the most common feature in emulsions, and occurs widely in various industrial processes, including materials processing. Appropriate temperature and enough external force are required to break up and refine the structure but also to avoid further coalescence (Kotadia et al., 2009).

When an initially spherical Newtonian liquid droplet of radius r and a viscosity μ_d is suspended in another Newtonian liquid of a viscosity μ_m and subjected to shear stresses, it will deform and the droplets will be broken up into smaller ones (Fan, 2001).

The process of breaking a droplet can be classified into two mechanisms - that of binary break-up and that of capillary break-up, as previously reported (Zhao et al., 1998; Tegze et al., 2005).

Binary break-up is the simpler mechanism, droplets continuously break up into two fragments, which is cascaded until the droplet gets small enough to survive the hydrodynamic conditions (Briscoe et al., 2006).

The second process is the capillary break-up mechanism where the droplet is stretched to produce a long filament that will fragment by the action of capillary waves into a relatively large number of droplets. Low viscosity droplets, like Pb droplets, will require higher strain rates to be broken. This second process is the one that can be affected by the shear device.

The shear strain rate required to produce droplet break-up in steady laminar flow has been shown to depend on:

- the dispersed and continuous phase viscosities
- the initial droplet radius, r
- the interfacial tension between the 2 liquids σ_{L1L2} (Briscoe et al., 2006).

Taylor concluded that the degree of deformation of the droplet on the presence of shear flow can be expressed by two dimensionless parameters, the capillary number (k) and the viscosity ratio (Λ). The capillary number (see **Equation 2-12**) is defined as the ratio between the viscous shear of the matrix, which causes drop deformation and characteristic Laplace pressure in which interfacial tension forces tend to resist the deformation and keep the droplet spherical.

$$K = \frac{2\mu_m r \dot{\gamma}}{\sigma_{L1L2}}$$ (2-12)

where K is the capillary number, σ_{L1L2} is the interfacial tension between two liquids (Jm^{-2}), $\dot{\gamma}$ is the shear rate (s^{-1}), r is the droplet radius (m) and μ_d and μ_m are the viscosities of the droplets and matrix respectively (Pas).

$$\Lambda = \frac{\mu_d}{\mu_m}$$ (2 -13)

Where Λ is the viscosity ratio, μ_d is the viscosity of the liquid droplets (Pas) and μ_m is the viscosity of the matrix (Pas).

For droplet break up k has to be bigger than a critical value. This value is determined when the interfacial tension force can no longer balance the viscous force, and depends therefore on the viscosity ratio between the droplets and the Al matrix. It has also been experimentally confirmed that breakup of liquid droplet is easiest when the viscosity ratio is within 0.3<Λ<1.5 (Fan, 2001).

Figure 2-8 Capillary number and viscosity ratio: droplet stability under shearing.

As seen on **Figure 2-8** below the curve the droplet is stable and when the capillary number is increased to a value above the critical condition the droplet will stretch, become unstable and break up due to the capillary waves created (Briscoe et al., 1998).

52

It has also been pointed out that the dynamic behaviour of droplets in flows with different viscosity ratio is very different. With viscosity ratios close to 1, a quick break up takes place and fine droplets are produced. Decreasing the viscosity ratio to 0.5 implies that the viscosity of the matrix increases considerable with respect to droplet viscosity, leading to a delay in the formation of the first droplets and an increase in the final size of droplets. However coalescence of droplets is highly reduced when the viscosity of the matrix is high (Tang et al., 2006).

However, it is important to highlight that such a fine liquid suspension will become unstable and will demix rapidly under the effect of Stokes' and Marangoni motions once the shear deformation field is removed. Therefore initially is important to shear above the monotectic temperature, to enhance turbulent flow to break droplets quicker and obtain a smaller droplet size distribution. Finally, just before complete solidification of the α-Al, shearing below the monotectic temperature increases viscosity of the matrix and reduces the coalescence (H. Tang et al., 2006). It is important to keep viscous forces high enough to help counterbalance the gravity force, reduce agglomeration and slow down diffusion. Therefore it is critical to select correctly the processing temperature range to optimise the effect obtained from shearing on immiscible alloys (Kotadia et al., 2009).

This effect of shearing to achieve a homogeneous distribution of the soft phase in the Al matrix was also described by Kotadia and co-workers. Shearing increases the number of droplets as a result of a decrease in droplet size. Concluding that, the final microstructures of alloys are strongly influenced by the viscosity, shear forces, turbulence and processing parameters such as shearing time and speed.

Budai and Kaptay also observed this effect of mechanical stirring on immiscible systems, comparing it to organic immiscible systems. Stirring creates a emulsion between the 2 immiscible liquid metals. The formation of this emulsion determines the optimum speed to achieve a uniform and fine distribution (Budai and Kaptay, 2009).

The rupturing and dispersion of the droplets is one of the main mechanism of the shearing process on immiscible systems, but there is another important microscopic effect created by shearing on this immiscible systems, which is the reduction of the Marangoni and Stokes motion (see **Figure 2-9**, **Equation 2-4** and **Equation 2-11).**

Figure 2-9 Schematic representation of the change of Marangoni and Stokes velocities with droplet size, as well as a curve representing the difference between the 2 of them and the critical radius where they take the same value.

The effect of shearing on immiscible systems during DC casting has not been previously studied. However, its effect on the microstructure of DC cast ingots for Mg and Al, specially 6XXX series alloys has been analysed in detail in several publications. Xia and co-workers (Xia et al., 2013) demonstrate that the shearing creates a uniform temperature in the sump, which is just a few degrees below the alloy liquidus. Therefore shearing offers the possibility to reduce to a minimum the effect of the Marangoni forces through mastering the heat flow by providing this constant temperature in the sump (Kotadia, 2010).

2.6.5.2. Effect of Particle additions on immiscible systems

Several authors have observed and explain the efficiency of certain solid particles to create a uniform distribution of the soft phase in the Al matrix for immiscible systems. These particles help to decrease the maximum size of the solidified soft phase particles and increase their number. The specific characteristics and sizes of these particles have been described elsewhere.

Two different possibilities have been proposed in literature about the mechanism behind this refining effect of certain particles on the soft phase in the Al matrix.

The first approach, proposed and explained in several publications (Kaban et al., 2011) (Kaban et al., 2007), is based on the idea that those particles enhance the heterogeneous nucleation of the liquid soft phase droplets in the Al matrix, therefore this particles have been named as inoculants. They refer particularly to the Al-Pb and Al-Bi systems, which are the ones chosen in this thesitation. The minority phase will be referred to as L_2 and the Al matrix as L_1. The idea is to catalyse the nucleation of minority liquid phase droplets on inoculant particles and to trap the droplets in the solidifying Al matrix, preventing their growth and coagulation (Kaban et al., 2011).

Initially it was believed that the L-L nucleation in immiscible systems could be described as an homogeneous nucleation process. (In the classical theory the homogeneous nucleation rate of L2 in an immiscible alloy can be expressed as:

$$I_{hom} = I_0 exp\left(-\frac{\Delta G_{hom}}{kT}\right) \qquad (2\text{-}14)$$

Where I_{hom} is the homogeneous nucleation rate, *K is a constant (JK^{-1}),* *T* is the temperature (K). And ΔG_{hom} is the energy barrier for homogeneous nucleation (J), which can be calculated as:

$$\Delta G_{hom} = \frac{16\pi}{3}\frac{\sigma_{L1L2}^3}{\Delta G_v^2} \qquad (2\text{-}15)$$

ΔGv is the Gibbs free energy change per unit area associated with formation of the L_2 phase (in the case of nucleation for immiscible systems) or between the undercooled liquid and the solid in the case of Al solidification. $\sigma^3{}_{L1L2}$ is the interfacial tension (Jm^{-2}) between the liquid and liquid in nucleation of Pb in Al and between solid and liquid in the solidification of Al.

However, it was later found that the nucleation of the immiscible phase droplets takes places heterogeneous on insoluble melt particles and can be enhanced by adding certain potent inoculant particles.

The heterogeneous nucleation rate can be calculated using **Equation 2-16**. The relationship between homogeneous and heterogeneous nucleation can be found considering **Equation 2-17.**

$$I_{het} = X_v I_0 exp\left(-f(\theta)\frac{\Delta G_{hom}}{kT}\right) \qquad (2\text{-}16)$$

Where I_{het} is the heterogeneous nucleation rate,

$$I_{het} = I_{hom} X_v exp\left(-f(\theta)\right) \qquad (2\text{-}17)$$

Where X_v concentration of the nucleating agent

In the heterogeneous nucleation the energy barrier is reduced by the catalytic factor which can be calculated with the following formula (Kaban et al., 2011):

$$\Delta G_{het} = \Delta G_{hom} f(\theta) \qquad (2\text{-}18)$$

Where ΔG_{het} is the *e*nergy barrier for heterogeneous nucleation, f(θ) is the catalytic factor, which can be calculated considering the contact angle between the inoculant and the droplets of the minority phase (θ), and can be calculated using **Equation 2-19.**

$$f(\theta) = (2 - 3cos\theta + cos^3\theta)/4 \qquad (2\text{-}19)$$

Figure 2-10 Schematic illustration of interfacial energies and contact angles for enhanced heterogeneous nucleation of liquid droplets on a solid substrate.

The contact angle can be calculated using Young's equation (**Equation 2-20, Figure 2-10).**

$$\gamma_{l1l2} COS\,\theta_{Sl2} = \gamma_{Sl1} - \gamma_{sl2} \qquad\qquad (2\text{-}20)$$

Due to complexity of contact angle phenomena, the experimentally observed contact angle might or might not be equal to Young's contact angle.

Tensiometry was the technique applied to measure the contact angle between the liquid Pb and TiB$_2$ (Kaban et al., 2005). The force exerted on a cylindrical probe is determined as a function of its immersion depth during an immersion–emersion process. The contact angles can be calculated at the emersion depth in which the contact line is sliding the vertical line of the probe (capillary force is constant and measured force is used to determine angles). When the contact line is at the bottom edge of the probe the interfacial tension can be calculated (meniscus is described by the Young-Laplace equation) from there knowing the value of the capillary constant the interfacial tension can also be determined (Kaban et al., 2011).

To reduce the barrier for nucleation and act as inoculants, these particles should provide a catalytic factor smaller than 1, being the catalytic factor directly dependent on the contact angle. The dependency of the catalytic factor with wetting angle is shown in **Figure 2.11.**

Figure 2-11 Catalytic factor $f(\theta)$ for heterogeneous nucleation in an immiscible system with inoculant additions represented as a function of the wetting angle(θ), which is the angle at the contact line inoculant/L_1/L_2 (Kaban et al., 2011).

The inoculant particles must be preferably wetted by the soft phase in the presence of the Al matrix. A small contact angle is observed when the liquid spreads on the surface while a big contact angle is observed when the liquid beds on the surface. More specifically a contact angle lower than 90° indicates that the wetting of the surface is favourable, and the liquid will spread on the surface. Wetting angles between 0 and 40° provide a perfect wetting of the inoculants by the minority phase for Al-Pb and Al-Bi alloy, providing a very small catalytic factor and therefore reducing significantly the barrier for nucleation and increasing the nucleation efficiency (Kaban et al., 2010). However, angles greater than 90° the wetting of the surface is generally unfavourable, so the fluid will minimise its contact with the surface and form a compact liquid droplet.

The main difficulty is to find an appropriate nucleating agent. From theoretical calculations, of wetting angles between the minority phase and the particles, it is been found that Al_2O_3 provides the optimum contact angle. However during experimental observation other inoculants like ZrO_2 or TiB_2 particles proved more efficient; this could be explained due to the rapid oxidation of Al, which makes very hard to control the amount of oxide in the melt.

Kavan and co-workers concluded that TiB_2 can be used as inoculant in Al-Pb system, being the contact angle 22-25 in a wide temperature range, but not for Al-Bi system in which TiB_2 provides a contact angle with the minority phase of 180, giving a catalytic factor of 1 (Kavan, 2011).

The second approach, to understand the effect of particle additions on immiscible systems, has been mainly proposed by Kaptay and his team, who have also observed the efficiency of certain solid particles to improve microstructure of monotectic alloys, but propose a different explanation for the mechanism responsible for this refinement. They suggested that the presence of those particles will promote emulsification (Budai and Kaptay, 2010), lower the interfacial tension and provide the interface with viscoelastic properties, reducing coalescence events. The droplets are not able to coalesce due to the fact that they are surrounded by those particles.

This approach differs fundamentally from the previous one as it is proposing that these particles reduce the coalescence and coagulation of the particles but do not affect their nucleation process. It is suggested that one of the factors to be considered when choosing these particles is their size, as large inoculants may not migrate quickly enough to the surface of the droplet. Other key factors, to achieve a homogeneous and fine distribution of the minority phase, are the inoculant concentration and its distribution within the matrix (Briscoe, 1999).

Wetting angles are also considered as a key factor, but in this case to control the stability of this liquid metallic emulsions. The calculated contact angles for Al-Bi systems (Kaptay, 2006) are in accordance with those calculated by Kaban and co-workers but contrary to them, Kaptay concluded that:

- If the contact angle is below 15∘ particles are not able to stabilize liquid emulsions.
- If contact angle is between 15∘ and 165∘ the stabilization of emulsions by solid particles becomes possible. Budai and Kaptay (Budai and Kaptay, 2010) found that Al_2O_3 particles could were perfectly wetted by the Bi-rich phase in a solidified Al–Bi alloy. Hence, Al_2O_3 could be used as the inoculant in Al-Bi alloys.

Further analysis following the same approach has been done by Chen et al (Chen, 2014). They suggested that after phase nucleation of Al-Bi systems, nanoparticles (TiC $_{0.7}$N$_{0.3}$) can rapidly be absorbed to the interface resulting in a reduction of the interfacial energy (reduction of interfacial area) and blocking diffusional transport. The interfacial energy will retain the particles on the interface as long as the energy required to remove the particles is considerably bigger than the Brownian motion (see **Equation 2-22)** of these particles:

$$\Delta G_{remove} = \pi r^2 \sigma (1 - cos(\theta))^2 \qquad (2\text{-}21)$$

Where ΔG_{remove} is the energy to remove the particle from the interface of the droplet (J), r is the average radius of the particles (μm), σ is the interfacial tension (Jm^{-2}) and θ is the wetting angle

$$E_b = \frac{kT}{2} \qquad (2\text{-}22)$$

E_b is the brownian motion of the droplets (J), K is the Boltzmann constant which has a value of 1.38065 10^{-23} (m^{2}kgs^{-2} K^{-1}) and T is the absolute temperature of the liquids (K).

The nanoparticles also supress coalescence between droplets and control the phase growth, by increasing the pressure needed to break the thin film between 2 approaching droplets. Apart from blocking the growth of nucleated droplets it also enables a continuous formation of new droplets, contrary to the system without particle additions were the nuclei can only form at the beginning of the phase separation. These particles limit the consumption of super saturated solute by the nucleated droplets, reducing latent heat released and allowing sufficient undercooling for new droplets to nucleate. The decrease of super saturation results in a quick decrease of the nucleation rate. The opposite is also true, the enhancement of super saturation leads to an increase on the nucleation rate, and for the nucleation to occur the supersaturation has to arrive to a critical value (Zhao et al., 2005).

Applicability of some solid particle additions has also been proven as an efficient way to improve phase distribution and miscibility, with other immiscible systems, like Fe-Sn. DSC scans performed on Fe-Sn system (Lu et al., 2014) show how Cu additions can reduce or even avoid the liquid phase separation for Fe-Sn alloy. The critical temperature of the binary system is also found to decrease with Cu additions. Furthermore, according to the authors

the phase separation is also described by the curvature of the Gibbs free energy. The curvature inflexions indicate the existence of a miscibility gap in the liquid estate. With Cu the Gibbs free energy gets more negative and the inflexions disappear, implying that there is no demixing at the studied temperatures.

In summary, several mechanisms have been proposed in the literature as responsible for the refinement of immiscible systems in the presence of certain solid particles; however, none of them has been fully validated and the exact mechanism underlying this refinement remains unclear, hence the importance of the work presented in this thesis. Furthermore, the effect of inoculant additions on hypo- and exact monotectic compositions has not been previously studied.

2.6.5.3. Effect of Superheat

2.6.5.3.1 Effect of superheat in the solidified structure

It has been concluded in several studies that melt superheat has an important effect on the solidified microstructure of different alloys. The conclusion from several of these studies agreed that superheat reduces considerably the SDAS. This reduction is accompanied by a refinement in the structure of intermetallic phases. This is the case for Ni based alloys (Yin et al., 2003), Si or Mg containing alloys and Al-Fe-Mn alloy.

Several hypothesis have been made trying to explain the mechanism behind this micro structural refinement, however, so far it has not been fully clarified or understood. Furthermore, several publications suggest that for some particular alloys the effect of superheat is to coarsen the microstructure rather than refine it.

With superheat the melt becomes much more homogeneous and the average size of atom cluster becomes much smaller, for Al-Fe-Mn alloys. These fewer and smaller heterogeneities will become solidification nucleus during quenching, increasing as a consequence the undercooling. The increase in undercooling increases the free energy change from the liquid to the solidifying crystals, providing therefore a bigger crystallization driving force. This leads to an increase in the nucleation rate, which in turn gives place to finer dendrites, and less dendritic segregation. A more uniform microstructure will therefore be obtained.

An study on Al containing Mg alloys shows a decrease in grain size with superheat of between 180°C to 300°C, the degree of superheat required and holding time is dependent on the alloy composition, and in general the more superheat the greater the refinement until the solubility limit of the impurities has been reached. Superheat makes the nucleant particles more potent by dissolving the impurity layer which surrounds them. For these alloys superheat increases the solidification undercooling, which is in accordance with previous publications on Al alloys (Cao et al., 2007).

Fu et al conclude that superheat refines not only the dendritic arm spacing but the intermetallic phases which also become much finer (Wang et al., 2009).

These results have also been confirmed by Wang et al. Furthermore they suggest that the stability of the solid liquid interface is enhanced after melt superheat and increases the critical velocity at which the interface becomes unstable (Wang et al., 2011). However this would not have a significant effect on DC casting, as the velocities employed are far from the low velocities at which the destabilisation of the front would occur. Wang and co-workers also suggested that there is a turning point and when the melt superheat exceeds a particular value the effect is opposite and the solidifying interval and solidification undercooling increase again (and therefore the nucleation rate decreases).

It is generally known that diffusion coefficient has an effect not only on the distribution of elements contained in a particular alloy, but on crystal growth rate and segregation in the solidification process. Diffusion is related to temperature exponentially (F. Yin et al., 2003; Li et al., 2002).

Furthermore it was observed that melt treatment by superheat makes the alloy microstructure much more independent on cooling rate (Li et al., 2002).

Finally the increase in superheat has been related by Dahlborg and co-workers to an increase of yield strength, tensile strength and ductility in those samples whose melt has been conditioned by superheat (Dalhborg et al., 2013). They also show evidence that some particles are dissolved after a certain value of superheat (Taha et al., 1992).

2.6.5.3.2 Effect of superheat on the soft phase particle distribution and size

The effect of superheat on the dendritic structure has been explained previously in section a). He et al found that the reduction in dendritic arm spacing associated with superheat is directly related to the reduction in droplet size for Al-Bi alloys. The entrapment of the soft phase droplets, which enhances the microstructural refinement of these soft immiscible phases, is related to the dendritic structure. When the dendrite tip radius is small enough the droplets are entrapped in the inter-dendritic space, particularly in the triple junctions. The trapped droplets will therefore be much smaller. However, with big radius of the dendrite tip the repulsion region is much higher than with small tip radius, and all the rejected droplets will accumulate and grow. The size of the repelled spheres will be larger than that of the trapped ones (He et al., 2008). **Figure 2-12** shows the change in dendritic arm spacing and droplet size with melt superheat. It is clearly seen that both SDAS and droplet size decrease linearly with melt superheat.

Figure 2-12 Bi droplet diameter and primary dendritic arm spacing (PDAS) as a function of the temperature (He et al., 2008)

With the increase of the MS temperature, the volume fraction of the soft phase droplets (Bi, Pb) in the solidified structure increases, while the amount of the spheres congregated at the solidifying front decreases.

It has also been suggested that melt superheat has a direct effect on droplet size of immiscible systems Al-Pb and Al-Bi. The cluster number and size of potential nucleating

particles are smaller as melt superheat increases, reducing therefore the size and number of sites available for nucleation of the minority phase droplets, which in turn will increase the undercooling required for nucleation (He et al., 2009; Wang et al., 2009). The increase in undercooling will therefore increase the nucleation rate of the minority phase. As the temperature at which the separation takes place is lower than equilibrium binodal temperature, this will also result in the reduction of the miscibility gap and therefore a reduction in the time available for droplet growth and coagulation, resulting in a decrease of the average droplet size.

The change in undercooling is related to the composition of the binary alloy, in other words, to the distance from the position on the phase Al-Pb or Al-Bi. The phase diagram Al-Pb (**Figure 2-7**) is not symmetrical with respect to the critical concentration, which is a direct reflexion of the free energy vs concentration curves. According to the homogeneous nucleation theory the gain on Gibbs free energy on nucleation depends on slopes of the energy–concentration curves and when those curves are asymmetric the necessary undercooling required for nucleation will also vary across as we move along the binodal line, and therefore the critical undercooling required for the nucleation to start depends on alloy composition (Ratke, 1988).

It is nevertheless important to point out here that the nucleation theories analysed to date had always fail to predict nucleation at regimes of high levels of undercooling (Arnberg et al., 2009). The Binder–Stauffer model (Stauffer et al., 1974; Binder et al., 1976; Binder, 1975) predicts a significant reduction in the nucleation site density at large undercooling compared with results from Cahn–Hilliard and classical nucleation models, and provides qualitatively a better approximation for the high undercooling nucleation regime.

Ratke et al. have related the nucleation of immiscible droplets with undercooling. They suggested that the critical level of undercooling defines the critical level of super saturation. When this critical level of supersaturation is reached the nucleation will start. The nucleation barrier is inversely proportional to the square of supersaturation, a high level of supersaturation means that there is no competitive growth and no decrease in the density of drops. The first effect of cooling into the miscibility gap is an increase in the

supersaturation. The nucleation barrier will increase as cooling continues and the level of supersaturation decreases (Zhao et al., 2004).

All the mentioned studies have been made on hyper-monotectic immiscible systems and therefore the effect of superheat on immiscible alloys of hypo- and exact monotectic compositions is not known. Furthermore, there is no definitive proof to fully explain the changes that superheat induces in the final solidified microstructure for immiscible alloys.

2.6.5.4. Effect of other alloying additions on immiscible systems

It has been suggested in previous studies that (Kaban et al., 2010) the addition of elements like Zn, Si, Cu or Sn, changes the wetting angle, modifying the catalytic efficiency of the inoculants particles previously mentioned.

Within those we highlight the importance of Cu. Cu addition increases the liquid-liquid interfacial tension. I. Kaban, W. Hoyer found that when Cu is added to the binary Al-Bi alloy, it increases highly the binodal temperature, which means an increase in the size of the miscibility gap. This also means that the liquid-liquid separation is enhanced by Cu additions. An equation is proposed to calculate the temperature dependency of interfacial tension.

Kavan and co-workers suggested that the knowledge of the liquid-liquid interfacial tension and its temperature dependency is of high importance for monotectic systems (Kaban et al., 2007).

The temperature dependences of the interfacial tension in binary Al-Bi and ternary Al-Bi-Cu monotectic alloys are accurately described by the power function as shown in **Equation 2-10.**

$$\sigma = \sigma_0 \left(1 - \frac{T}{T_c}\right)^{1.26} \qquad (2\text{-}23)$$

Where σ is the interfacial tension as a function of alloy temperature (Jm^{-2}), σ_0 is a constant (Jm^{-2}), T actual temperature (K) and T_c is the critical temperature (K).

Considering **Equation 2-23** the interfacial tension increase can be partially compensated with temperature increase, however 300°C increase in temperature are necessary to compensate 5wt% Cu additions (Grum et al., 2003).

Figure 2.13 shows the effect of Cu additions on the interfacial tension between Al and Bi. Cu increases from 2 to 20 % increase the interfacial tension linearly from 60 to 110 10^{-3} Nm^{-1}.

Figure 2-13 Dependency of liquid-liquid interfacial tension, for Al-Bi with Cu additions, at 660°C (Kaban et al., 2007).

2.6.6 Effect of cooling on soft phase droplet size

Most of the results in the literature, concerning steady and unsteady regimes, for hypoeutectic alloys, indicate a decrease in SDAS with increasing cooling rate for a given alloy composition and with increasing solute content for a given cooling rate. Primary arm spacing is found to be independent of composition but also decreases as tip cooling rate increases (Rocha et al., 2003)   This decrease has previously been related to a proportional decrease in droplet size for immiscible systems (see **Section 2.6.3 b).**

Kaban et al demonstrated that by increasing cooling rate we can decrease the average size of solid particles of soft alloying additions (Pb, Bi), and reduce or even supress

sedimentation of the second phase. However, if no further treatment is applied to these alloys the soft particles will not be uniformly distributed and their sizes will vary considerably (Kaban et al., 2012).

Zhao et al found that droplet radius (R) to decrease with increasing cooling rate proportional to $(dT/dt)^{-1/2}$ (Zhao et al., 1998).

The number density of nucleated droplets and their radius depends on the nucleation rate and nucleation time (Zhao et al., 2002), and therefore is increased with cooling rate. A melt cooled at a higher cooling rate should lead to a dispersion with a higher droplet density and smaller average droplet radius for any binary alloy composition.

 Number of nucleated droplets can be related to the cooling rate (T.) by:

$$n = C_1 \frac{dT^x}{dt} \qquad\qquad (2\text{-}24)$$

Where n is the number of nucleated droplets, C_1 ($K^{-1}s$) and x are constants, x is approximately 1.44 and does not change with composition while C_1 is composition dependent.

Number density of particles does not change significantly with alloy composition, while average droplet radius is more dependent on composition.

This strong dependency on cooling rate represents and high cooling rates required to avoid the coarsening of the soft phase microstructure is an important disadvantage for the production of immiscible alloys.

Chapter 3

Experimental

In this chapter, the procedure for preparation and processing of the binary and quaternary Al alloys, under different casting conditions and with different inoculant additions, will be presented. Casting procedures, characterisation and analysis techniques, in situ

solidification experiments, thermal analysis, processing and preparation for mechanical testing and mechanical properties measurement are explained in this chapter.

3.1 Alloy preparation

Different Al-Pb alloys were prepared to understand the effect of melt conditioning and inoculant additions on the solidification behaviour of both binary immiscible systems Al-Pb and industrial Al copper 2011 alloy containing both Bi and Pb. The mechanisms behind the second phase refinement of both binary systems and 2011 alloy, in the presence of inoculant and melt conditioning were also investigated.

For the study of binary systems both exact monotectic and hyper-monotectic compositions were employed. The base alloys were prepared in an electrical resistance furnace by melting commercial purity Al (99.99 %) and Pb of 99.9 % purity to get monotectic (1.2 %) and a 3 % hyper-monotectic concentration. For the industrial alloys Al-40Cu master alloy was diluted to 6 % Cu, with commercial purity Al at 740 °C for 3 h in a 6.5 kg clay-graphite crucible. Subsequently pure Pb and Bi powder with a purity of 99.99 % were added to get a nominal composition of 0.4 and 0.6 % respectively. The compositions of the raw materials are listed in **Table 3-1** and a summary of the composition of the final alloys prepared for the experiments is found in **Table 3-2.** The composition presented on these tablets are all measured after the alloy has been cast.

Table 3-1 Composition of the master alloys alloy raw materials.

Alloy	Cu	Mg	Si	Fe	Mn	Ni	Zn	Al
LM0	0.002	0.003	0.082	0.043	0.000	0.004	0.010	Bal.
Al-40Cu	46.600	0.006	0.240	0.840	0.130	0.000	0.030	Bal.

Table 3-2 Composition of binary and quaternary alloys used in the experiments.

Alloy	Cu	Si	Fe	Pb	Bi
2011	5.900	0.2400	0.300	0.390	0.000

Al-1.2Pb	0.002	0.082	0.043	1.180	0.000
Al-3Pb	0.002	0.082	0.043	3.080	0.000

3.2   Casting processes

Several casting processes were used to produce the billets and samples for subsequent analysis. The types of casting employed to obtain the different samples include, for binary Al-Pb alloys, DC simulator and DC casting, which are explained in **Section 3.2.3** and **Section 3.2.4**, in this chapter. Solidification in the crucible and filtering were also carried out to isolate the in situ created inoculants containing TiB_2. For the Al-3Pb alloy cylindrical steel mould described later was employed to test different inoculant additions before DC casting.

For industrial 2011 alloy samples were cast in a cylindrical shaped steel mould and DC cast unit. The casting experiments were performed with and without melt conditioning by shearing.

3.2.1   Steel mould casting

Samples were taken, from the bottom and towards the top (both on the centre of the cast piece), by using a steel mould, showed in **Figure 3-1**, preheated to 200°C. The measured cooling rate is aproximately 3 K/sec at the central region of the sample. This mould was used to test different inoculant on binary Al-3Pb system and to study the effect of superheat on the microstructure of 2011 alloy, as explained in **Section 3.2.1.1**.
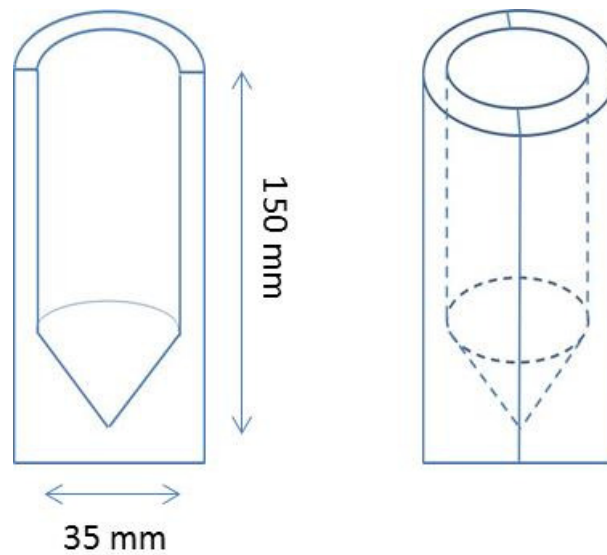
Figure 3-1 Cylindrical steel mould used in the experiments .

3.2.1.1   Optimisation of inoculant additions on Al-Pb and 2011 alloys.

A number of different inoculants were added, to the Al-3Pb binary alloy, to study their effect on the nucleation of liquid Pb droplets in the presence of Al, these are presented in **Table 3-2**. The chemicals and master alloys listed here were wrapped in Al foil and added at 740°C to the melt with gentle mixing every 5-10 min.

The selected casting temperature was 820°C, chosen to cast above the binodal line indicated in the phase diagram.

Table 3-3 Properties and quantities of inoculants added to the melt.

Material	Properties	Wt.% added	experiment
ZrO_2		0.4	Steel mould for Al-3Pb
TiB_2	Powder (99.9% and 1-3 μm in size)	0.1, 0.4, 1	Steel mould for Al-3Pb
Al-5Ti-B	rod	2.0 (to get 0.1% Ti and 0.05% B) for Al-1.2Pb; 5.0 (to get 0.25% Ti and 0.%2 B) for Al-3Pb and 0.2 (to get 0.01% Ti and 0.005% B) for industrial 2011	DC casting for Al1.2, Al-3Pb and 2011 alloy
Al-10Ti+Al-5B	Master alloy	2 Al-10Ti (to get 0.1% Ti) and 1 Al-5B (slight excess of B for TiB_2) for Al-1.2Pb; 8 and 4 Al-10Ti (to get 0.4 %Ti and 0.2%) and 4 and 2 Al-5B (slight excess of B for TiB_2) for Al-3Pb and 0.2 Al-10Ti (to get 0.01% Ti) and 0.1 Al-5B (slight excess of B for TiB_2) for 2011 alloy	For hyper-monotectic the higher percentage were used for steel mould experiments and the smaller percentages for DC casting

3.2.1.2 Effect of superheat on microstructure of 2011 alloy

The previously mentioned steal mould was used to understand the effect of superheat with and without inoculant additions on the microstructure of 2011 alloy. For each experiment, 2011 alloy, previously prepared (see **Section 3.1**), was heated up the 3 different temperatures and then cooled down to the experiment pouring temperature of 720°C prior to casting. The procedure can be summarised as follows:

The alloy was heated to 740°C, the melt was hold at that temperature for 20 minutes, and then cast.

- The alloy was heated to 820°C, the melt was hold at that temperature for 20 minutes, cool outside the furnace and then cast at 740°C.

- The alloy was heated to 920°C, the melt was hold at that temperature for 20 minutes, cool outside the furnace and then cast at 740°C.

3.2.2 Crucible experiments and filtering

In order to understand the mechanism behind the Pb particle refinement in the presence of TiB$_2$, samples had to be prepared for TEM analysis. To obtain a significant particle density and be able to observe them in the TEM, after the Al and Pb (3%) were melted as explain in **Section 3.2**, two different subsequent steps were tried, sedimentation in the crucible and pressurised melt filtration:

3.2.2.1 _Sedimentation in the crucible_

The inoculant chosen for these experiments were those containing TiB$_2$. Both Al-Ti and Al-B master alloy and synthetic TiB$_2$ powder were added to the melt (together with the Pb) following 2 different processing routes:

- Inoculant and Pb added at 860°C, above the binodal line for Al-3Pb system and therefore when both metals are completely mixable in each other.
- Inoculant was added at 740 °C, the melt was hold at that temperature for 10 minutes, heated up to 860°C, hold for 30 minutes.

The amount of master alloys added were calculated to get 0.7 %Ti and balanced B and for TiB$_2$ powder 1 %. As seen on annex when the master alloys are added together TiB$_2$ is formed within the melt, which is more stable than any of the Al borides and titanium aluminides, on the working temperature range from 650°C to 950°C.

The later procedure has been proven beneficial to increase the efficiency of the inoculant, all Pb was trapped with the TiB$_2$ particles (see Chapter 4). When the inoculant is added at 860°C a considerable amount of Pb is sediments as a continuous layer, instead of being surrounded by the particles. Therefore the later was the methodology chosen for the inoculant additions on DC casting, for both binary systems and 2011 alloy.

Once the additions were made and the melt reached the 860C and soaked for the indicated times, the furnace was switched off and the melt is left to solidify inside the crucible at a

cooling rate of approximately 0.5 k/min, therefore there is enough time for the TiB_2 particles and the Pb to concentrate on the bottom of the sample.

When TiB_2 powder was added melt conditioning by shearing was employed to try to get the TiB_2 wetted by the molten Al. However this process did not prove successful as only a very small amount of TiB_2 was found when examining the sample, despite the experiment being repeated several times.

Solidification in crucible was also use to measure the solidification profile of 2011 alloy. The temperature was recorded during the cooling of the alloy from 700°C until the alloy has completely solidified. Temperature is represented against time. The liquidus and recalescence temperature have been calculated from the recorded cooling curves. Maximum undercooling is the difference between the theoretical liquidus temperature and the temperature on onset of recalescence. Liquidus temperature is calculated with the derivative of the temperature with time and plotted against time, the value of the liquidus temperature is taken at the point where the slope of the derivative changes and from there a straight vertical line is drawn, the point where this line intersects with the derivative curve itself the liquidus temperature can be read. The temperature of the onset of recalescence, *TI,* was determined as that temperature at which the slope of the cooling curve became zero.

3.2.2.2   *Melt filtration*

A pressurized melt filtration technique showed in **Figure 3-2** and **Figure 3-3,** was employed to collect the inclusions (TiB_2 particles) contained in the melt. During the filtration process, the melt is forced through a micro-porous ceramic filter. In order to provide pressure to force the liquid Al through the ceramic filter, argon gas was fluxed in the system. Most of the melt is filtered thorough and collected from the bottom of the unit, but some will solidify on the crucible which is placed just on top of the filter. The inoculant inclusions contained in the melt can be collected from the metal solidified in the crucible. The surface above the filter will contain a high density of inoculant particles, therefore this area was sectioned and prepared for SEM/TEM examination.
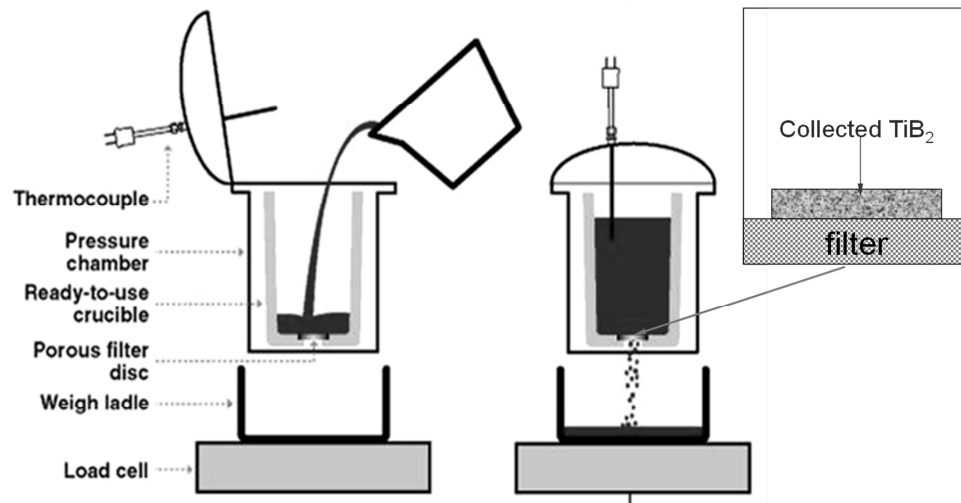
Figure 3-2 Schematic representation of the filtering unit (Enright et al., 2003).

Figure 3-3 Photograph of the filtering unit.

In both cases the area with the biggest accumulation of inoculant particles was cut from the solidified melt in the crucible and examined in TEM as seen in **Section 4.3.1.**

3.2.3 DC Simulator

The DC simulator is similar to DC cast (see **Section 3.2.4**) but a steel cylindrical mould is holding the solidified metal so that the metal is not in direct contact with the water. The water cools the mould, which in turn will cools down and solidifies the melt. The cooling rate achieved was around 6-8 °C/sec. Due to the miscibility dependency with temperature

for hyper-monotectic systems, the melt heating and casting temperature and the melt shearing temperature are critical to get the desired solidified microstructure. Therefore the DC simulator was used to determine the optimum casting and shearing temperature range for the Al-3Pb hyper-monotectic system, which later be applied on the DC casting of binary systems Al-3Pb.

The DC simulator unit is shown in **Figure 3-3**, **Figure 3-4** and **Figure 3-5**.

Figure 3-3 General picture of the DC Simulator unit used in the experiments.

Figure 3-4 Top of the DC simulator, where the melt is poured into.

Figure 3-5 Picture of the heating elements in which the steel mould is inserted and cooling water chamber.

3.2.4   DC casting

DC unit consists of a launder, a hot top mould fitted into a water box and a moving mechanism for the billet (see **Figure 3-6**). Melt is poured in an open, water-cooled mould that is initially closed from the bottom side by a dummy block connected to a lowering system. After the melt reaches a certain level in the mould, the ram is lowered and the solid part of the billet is extracted downward. The melt flow rate is adjusted in such way to keep constant the level in the mould. As soon as the solid appears through the bottom, water is applied to the surface in form of a film or water spray. This is a semi-continuous process and as soon as the ram reaches the slowest position in the pit the process is stopped and the billet removed (Eskin, 2008).
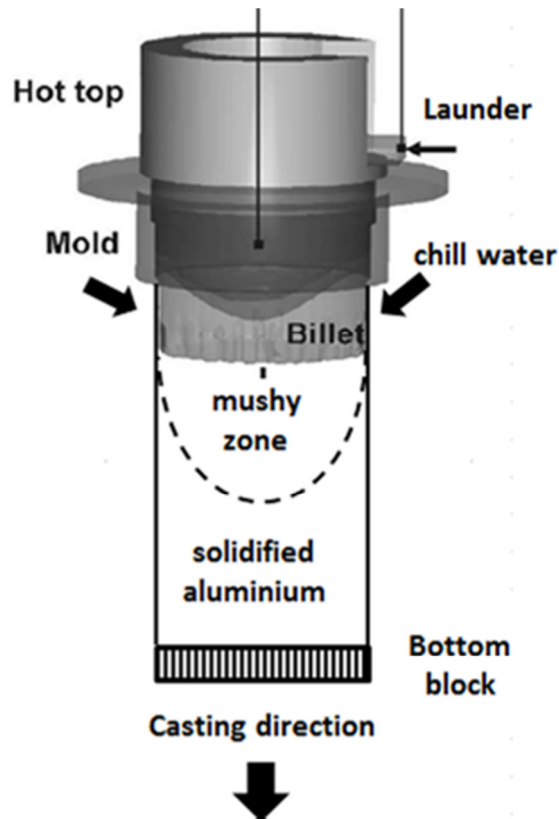
Figure 3-6 Schematic representation of a DC casting unit.

The procedure for melt heating and preparation is displayed in fig for hyper-monotectic alloys, with a casting temperature of 820°C, which differs to the hypo- (2011) and monotectic alloys on the casting temperature, which is set to 720°C.

DC casting was the casting procedure chosen to understand the effect of inoculant additions and melt conditioning by shearing on both binary monotectic systems Al-Pb and 2011 alloy.

For the sample preparation each cast log was sectioned longitudinally into two halves. **Figure 3-7** shows a schematic representation of the two halves of the log, the first half indicating the position were the chemical composition was checked and the second longitudinal section indicating the positions in which samples were taken for metallographic analysis (see **Figure 3-7**).
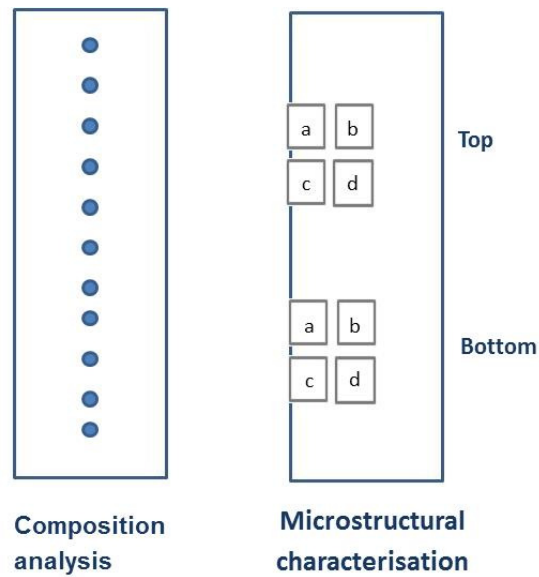
Figure 3-7 Schematic representation of the two halves of the billet.

Different casting conditions and different inoculant additions (see **Table 3-3**) were tested for both the binary systems (monotectic and hyper-monotectic) and 2011 alloy.

For binary monotectic and hyper-monotectic systems:

- No shear no inoculant
- Shear at 6000 rpm, no inoculant
- Shear at 6000 rpm, Al-5Ti-B
- Shear at 6000 rpm, Al-Ti and Al-B
- Shear at 6000 rpm, Al-Ti and Al-B, superheated to 860°C

For monotectic systems the casting temperature was 720 °C and for Al-3Pb was 820 °C. The amount of inoculant added was adjusted depending on the alloy and is detailed on the results chapter.

For 2011 alloy the casting variants are as follows:

- Al-Ti (0.02 % Ti)+Al-B(0.05 %), heat to 860°C, sheared at 6000 rpm. (The number assignated to reffer to this cast is 156 A and B).
- Al-Ti (0.02 % Ti)+Al-B(0.05 %), heat to 860°C, non sheared (157 A and B).
- Al-5Ti-B (0.02 %), no shear, heat to 740°C (158 A and B).

- Al-Ti (0.02 % Ti)+Al-B(0.05 %), Shear, heat to740°C (159A).
- No refiner, heat to 860°C, sheared at 6000 rpm (180A).

3.3 Melt conditioning by shearing

For melt conditioning, a new technology based on intensive melt shearing was employed; this technology has been developed by BCAST to improve the melt quality for wrought Al alloys (Zuo et al, 2011).

The combination of DC casting and melt shearing is called MC-DC (Melt Conditioned Direct Chill) casting unit. This novel technology is represented schematically in **Figure 3-8.**
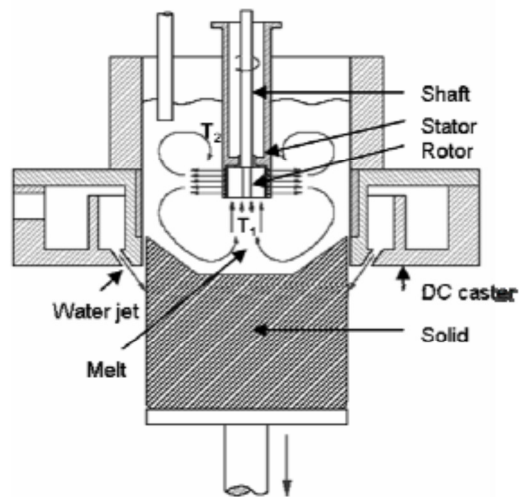
Figure 3-8 Schematic of the MC-DC process (Xia et al., 2013).

It uses a rotor-stator unit to achieve intensive melt shearing. A motor drives the rotor to shear the liquid metal in the gap between the rotor and the stator and forced through the holes of the stator at high velocities. The high shear device is submerged in the sump of a conventional DC cast unit. It can not only provide a macro flow for distributive mixing (in the lower part of the sump) but intensive shear of the melt next to the tip of the device.

The shear device can operate at rotation speeds between 2000 and 7000 rpm providing a shear rate of up to 10^5 s^{-1}, depending on the rotation speed and gap size. Two different speeds were tested 2000 and 6000 rpm.

3.4 Characterisation methods

3.4.1 Preparation of samples

After cutting to the correct sizes, samples are mounted in Bakelite, during this process they are heated up to 180°C for 4 min and cooled down to room temperature, until the resin is cured and ready for the grinding process. Grinding is performed automatically for 2 min each step, using SiC papers 120, 320, 800 and 1200 grit, until the surface is completely flat and free from scratches. Polishing is the final step before microstructural observation; it is performed in the same machine as the grinding and also automatically. The polishing solution used was 1µm OPS and it was taking from 20 to 30 min depending on the alloy, to get a shiny, clean surface, free from scratches and external contamination.

3.4.2 Chemical Composition Analysis

In this work it is essential to check if the prepared alloys have the targeted composition all along the cast samples and billets. A "Worldwide analysis system (WAS) AG Foundry Master" has been used to check the Chemical Composition. This is a quick, reproducible and reliable technique, which gives an accurate value of the elements present in the sample. The sample surface is spark to produce a burnt, photons will be emit by this surface, and will be detected by the optical spectrometer. Photons emitted by different elements have their own specific wavelengths; the spectrometer will measure these wavelengths and their intensity and produce spectral lines. Different elements have different emission spectrums. The values obtained are compared with the standards, which have been previously acquired by the system during calibration.

The results are given in wt.% of chemical composition. Several sparks should be collected in the same sample, in several positions. It is important to check both that the results are concordant and that the composition is close to target and constant along the sample. This would help to identify possible macrosegregation. Recalibration was performed on alloy change. All samples produced were chemical analysed as described here.

3.4.4 Optical microscopy

A Zeiss Axioscope Optical Microscope was used to check grain sizes and Pb and intermetallic particle size and distribution within the sample. Both contrast modes available in the microscope were used, bright field and polarised light.

3.4.4.1 *Sample microstructure*

Bright field is the standard mode, it collects only directly reflected/diffracted light, that is reflected back towards the objective from reflective surfaces, making them to appear bright (Smallman, 1999, page 124). It gets the contrast from absorption and diffraction of light. It shows the real colour of inclusions and is very good for high contrast details. In bright field mode the surface irregularities such as intermetallics can be observed because they appear dark in contrast, while the Al matrix in a polished sample appears bright in contrast. For each sample, a significant amount of micrographs were taken to cover the whole section.

3.4.4.2 *Grain size measurement*

Metals with cubic structure will appear uniformly dark under cross polar, unless they are etched to show the artificial anisotropy. One of the main uses of polarised light is to distinguish between areas of varying orientation, as they are revealed as differences of intensity (Smallman, 1999, page 125). Polarisation needs a separate analyser filter in the optical path.

Electro etching was used after grinding and polishing, to reveal the grain boundaries. Barker's etching reagent was used (7 ml HBF_4 48%, 93 ml H_2O) at 20V for 45 seconds, using a stainless steel cathode.

After electro etching a grain contrast effect is observed under cross polars, as a variation of colour and brightness with crystal orientation. Plain polarised light is therefore used for quantitative metallographic analysis, to check the grain sizes.

The intercept method is used to measure the grain sizes, following DIN EN ISO 643, 10 vertical, 10 horizontal lines have been drawn on the 5x and 10x magnification micrographs to count intercepts with grain boundaries. The number of intercepts and the total length of the measurement gives the grain sizes, which is calculated averaging several values from the same sample and same position.

$$GS = \frac{total\ measured\ length}{length\ of\ scale\ bar\ (mm)} \frac{value\ of\ scale\ bar\ (\mu m)}{counts} \quad \text{(3-1)}$$

Grain size measurement was only employed on both binary and 2011 alloy.

Another employed technique, i.e. macro-etching provides information on variations and type of structure, such as grain morphology (columnar, dendritic, globular), flow lines, segregation, coring and inclusions, that can be a qualitative indication of variations in chemical composition composition.

For macro-etching the sample is immersed for 10-15 secs in Tucker's solution (45 ml HCl concentrated, 15 ml HNO_3 concentrated, 15 ml HF at 48% and 25 ml water). For safety reasons this procedure has to be done under a fume hood. Macro-etching was performed in both binary systems and 2011 alloy.

3.4.5 Scanning electron microscopy

Some of the samples used for optical microscopy were subsequently used for SEM (scanning electron microscopy) examination.

The advantage of SEM over optical microscopy is the large depth of field and higher resolution, thus producing high resolution images at high magnification (up to 50,000 times). A modern SEM provides an image resolution between 1 nm and 10 nm, and the images produce have a relative large depth of focus. SEM provides important information for sample analysis and characterisation, including topography or surface structure, elemental content, microstructures, crystallographic phases and their orientation. SEM microscopes can resolve easily below the submicron scale (Dieter, 2007).

A SEM is provided with an electron beam scanning over the sample. When the electron beam hits the sample several interactions take place, some of the incident beam is back-

scattered and some penetrate the sample, both generating useful structural information. Interaction of the beam with the atoms in the sample leads to the ejection of low energy electrons (secondary electrons) which can be used to characterise the material.

The SEM used for the present was is a Zeiss Supra 35 FEG, equipped with a primary electron imaging, secondary electron imaging or back scattered electron imaging (BSE) and Energy dispersive X-ray analysis (XRD) operation modes. The microscope was operated at an accelerating voltage of 20 kV.

3.4.6 Phase size and number density of different phases

The average particle size, and number density of primary Pb particles and Al_2Cu intermetallics (the latter only for 2011 alloy) were quantified for more than 500 particles per sample. This calculation was performed with the image analysis software available on the optical microscope and with Imagej software to ensure reproducibility and accuracy of the measurements. ImageJ software is an image processing program designed for scientific multidimensional images. The program has thousands of plugins and macros for performing a wide variety of tasks, and a strong, established user base. Based on colour contrasts the different phases can be identified and individually selected. Then different parameters (like diameter, number of particles, area occupied by a particular phase, shape factor) can be measured for each phase.

3.4.7 SDAS (secondary dendritic arm spacing) measurements

SDAS was measured for the 2011 alloy samples cast in the steel mould. The SDAS for the melt heated to 740˚C, 840˚C, 920˚C, with and without Al-Ti and Al-B additions, was analysed and compared.
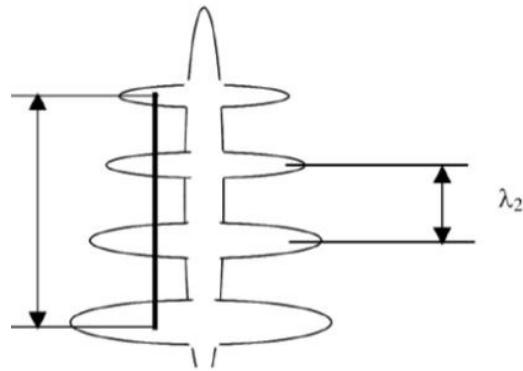
Figure 3-9 Schematic representation of SDAS measurements

Values of λ_2 were measured by calculating the distance between adjacent side branches on the longitudinal section of a primary dendrite as seen in **Figure 3-9.**

3.4.8 TEM analysis

The samples used for the TEM were melted in a crucible and after the melt was filtered using a pressure filtration technique, as seen in **Section 3.2.2.2**. The initial step to prepare the samples for TEM examination, is to obtain thin foils. For that, slices of 500-600 μm were cut from the as cast sample. These slices were mechanically ground using grinding paper from 120 to 1200 grit, to prepare the surface for the subsequent process steps and to get a thickness of 150 μm. Finally to obtain, the final round sample the thin foil was punched to create 3mm diameter discs. These discs were then ground to a thickness of less than 100 μm and finally ion-beam thinned on a Gatan Precision Ion Polishing System (PIPS) at a voltage of 5.0 kV and an incident angle of 4~6°. PIPS was used as final step before TEM examination as it thins down one side of the specimen. This system combines a high powered ion gun, ensuring reasonable thinning rates and a low angle of incidence, which removes any surface roughness with minimum damage to the sample (Williams and Carter New York 2009, page 181).

In a Transmission Electron Microscope (TEM) electrons penetrate thin sample and are subsequently imaged by appropriate lenses. TEM resolution can be around 0.2 nm and it is possible to image individual atom planes or columns of atoms. Jeol-2100F field emission

TEM was used for the microstructure examination at 200 kV accelerating voltage. And, FEI Titan G2 80-200 scanning transmission electron microscope (S/TEM) with ChemiSTEM™ technology was used for the interface analysis.

TEM samples were produce to determine if absorption of Pb was taking place on the surface of the TiB$_2$ particles as initially expected.

3.4 Differential Scanning Calorimetry (DSC)

Chemical reactions and many physical transitions are connected with the production or consumption of heat, calorimetry is therefore a useful method to investigate those processes.

DSC is a thermal analysis method, which helps to quickly measure, on small sample masses, characteristic temperatures of reaction, heat of transition from one state to another, heat flow rates and their changes at specific temperatures. It also measures partial heats developed in a selected temperature range, which are important for kinetic evaluations. These measurements can be performed very accurately and over a big temperature range (Smallman, 1999).

When a difference in temperature develops between the sample and the reference an automatic control loop heats the cooler of the two until the temperature difference is eliminated. DSC measures the heat flow rate necessary to stablish a zero temperature difference between the evaluated substance and the reference material, while they are subjected to identical temperature programs. The energy required to equal out the samples is plotted against temperature, and are expressed as energy per unit mass. A peak from an endothermic change is plotted upwards (Smallman, 1999, page 165-168).

In the case of immiscible alloys, when reaching the monotectic temperature the whole material melts via the monotectic reaction, then both liquids continuously change their composition as well as their relative volume concentrations, which creates a deviation from the baseline. When reaching the binodal line there is only one liquid left and the DSC signal turns back to the baseline. During cooling the nucleation occurs at a particular undercooling temperature (which gives an idea of the height of the energy barrier for nucleation), which

can be calculated as the difference between the miscibility temperature during heating and the decomposition temperature during cooling (Ratke, Diefenbach, 1995.

Phase transitions of 2011 alloy were measured using a DSC NETZSCH STA 409PC instrument. The temperature ranges in which the alloys were analysed ranged from 100 to 960˚C, and two different final heating temperatures were tested, i.e. 740 and 920°C. The aim of these experiments is to determine the effect of superheat on the solidification of the described 2011 alloy. Various scanning rates from 1-20K/min were employed, being the cooling or solidification process of particular interest for this study.

The sample masses ranged from 9.5 to 10 mg. They were placed in an alumina crucible, with the following dimensions 12.5 mm outer diameter and 7.5 mm height. Argon air flow was used to avoid oxidation. Chips from 2011 alloy were used on the experiments, to obtain those chips the previously described process was followed, the 2011 melt was prepared and cast in the DC cast unit, the billets were homogenised and extruded, and the obtained cylindrical bars were SHT, stretch, aged and machined. The sample used was produced under the following conditions: melt heated to 740˚C and cast at 720˚C with a speed of 120 mm/min.

3.5 In situ solidification experiments (radiography)

In situ synchrotron X-ray diffraction imaging (radiography) studies of the solidification of an Al–1.2 % Pb alloy were carried out using the B16 beamline at the Diamond Light Source, in Didcot UK. The set up used is shown in **Figure 3-18**.
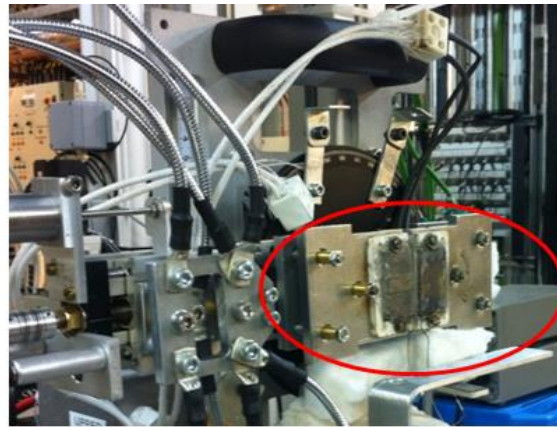
Figure 3-18 Pictures from the experimental set up in the synchrotron.

The two plate heaters were positioned on the area indicated as "furnace" as shown in **Figure 3-18 (a).** The heaters were aligned vertically and separated by an adjustable gap, which allows X-rays to pass though the sample. The position of the heaters did not allow for the top and the bottom of the sample to be observed.

The various temperatures, heater powers, etc. were controlled and data recorded at 10 Hz through a variety of analog and digital input/output modules under computer control using National Instruments LabView software. A common trigger signal was used to synchronize these data with corresponding video files so that specific events observed in the video files could be attributed directly to thermal data (Liotti et al., 2014).

Radiographic imaging of solidification was performed and digital video recorded for each experiment. The beamline was used in monochromatic mode and tuned to an energy of 18 keV using an Ru/B4C double multilayer monochromator in order to obtain the highest flux available (Sawhney et al., 2010). The X-ray signal passing through the sample was collected by a 150 lm thick single crystal cadmium tungstate (CdWO4) scintillator, focused into an Optique Peter Lens module and recorded with a high-speed Phantom 7.3 CMOS camera. The camera had an area of 800 x600 pixels and, at the selected magnification used for all the experiments, provided a field of view, in the centre of the sample, of 4.4 mm x 3.3 mm with a resolution of 5.5 lm/pixel. The video was recorded at a constant frame rate of 10 fps. The distance from the detector to the sample was 17 cm (Liotti et al., 2014).

The Al-1.2Pb foil samples were prepared by melting and homogenizing commercial-purity Al (99.98%) and Pb (99.99%) in an electrical resistance furnace. Samples were prepared to have a target concentration of 1.2 % Pb, but accurate Pb concentration cannot be exactly known, due to high Pb segregation experienced during casting of binary Al-Pb alloys.

From the cast sample sections of 8X20 mm X 300 μm plates were cut; which were thinned and polished on both sides to approximately 200 μm thickness, using a 1μm cloth. The thin foils were then coated with a thin layer of boron nitride spray, and subsequently enclosed between two 100 μm quartz plates that were welded together at the side edges. During the experiments the sample was then positioned in contact with the 2 heaters.

To allow isothermal conditions, the temperature on the top and bottom heaters was set to the same value. However, in practice, we could see that is not possible to work isothermally, and the temperature gradient from top to bottom was changing slightly from one experiment to the next. The real thermal gradient was therefore calculated for each experiment. The temperature accuracy of the heater control was estimated as ±0.5 °C. Two different temperatures, both above the alloy melting temperature, were selected for these

experiments, i.e. 740°C and 830°C. Extra heater and wool isolation was used to try to reach the higher temperatures.

Raw images were processed using custom MatLab scripts: each image underwent a flat-field correction and minor image artefacts were removed for both low and high pixel values. The raw images also had a superimposed vertical periodicity in intensity that was caused by surface imperfections in the multilayer monochromator used to select the X-ray wavelength used for the experiment. These intensity bands were removed by normalizing each pixel, with the mean pixel intensity taken from a 101 pixel horizontal window centred on the pixel in question. Finally, the intensity range of an image was scaled according to the maximum and minimum pixel intensities from the image; however, if multiple images were used to reconstruct a video sequence, then the global maximum and minimum pixel intensities across all images were used (Rack et al., 2010).

2 samples were used and several experiments performed on each sample as explain below:

1st *sample: Al + Al-Ti (0.2 %Ti) + Al-B (0.11 %B) + 1.2 %Pb*

- Test 1 (47): Heat up to 720°C and cool down at 2.5°C/sec.

- Test 2 (48): Heat up to 720°C and cool down at 0.7°C/sec.

- Test 3 (49): Heat up to 830°C and cool down at 2.5°C/sec.

- Test 4 (51): Heat up to 830°C and cool down at 0.7°C/sec.

2nd *sample: Al-no inoculant-1.2 %Pb*

- Test 1 (56): Heat up to 720°C and cool down at around 2.5°C/sec.

- Test 2 (54): Heat up to 720°C and cool down at 0.7°C/sec.

- Test 3 (57): Heat up to 720°C and cool down at 0.2°C/sec.

- Test 4 (58, 59): Heat up to 830°C and cool down at around 2.5°C/sec.

- Test 5 (60): Heat up to 830°C and cool down at 0.2°C/sec.

Chapter 4

Results

In this chapter the results obtained from each of the relevant experiments are presented. Experiments were carried out to understand the effect of casting practices and melt conditioning by shearing on alloys containing a miscibility gap in the liquid state. The effect of superheat before casting, inoculant additions and shearing on the morphology and distribution of Pb and Bi in Al were studied. Optical micrographs, SEM and TEM images as well as EBSD and EDS mapping and tables and graphs plotting the results will be displayed.

4.1 Solidification in the immiscible system Al-Pb at monotectic compositions

To study the solidification of Al-Pb immiscible alloys, in situ synchrotron X-ray diffraction imaging (radiography) studies of the solidification of an Al–1.2 %Pb alloy were carried out using the B16 beamline at the Diamond Light Source.

Samples illustrated in **Figure 4-1** shows a sequence of images recorded during the melting of an Al-Pb alloy of monotectic composition. The behaviour of Pb (black particles) behaves in the Al matrix, in which it is immiscible, can be summarised as follows:

- In order to reduce their exposed surface to Al, and decrease therefore their surface tension, elongated Pb shapes convert into particles (see points 1, 3, 4 in the images).

- As the exposed surface of a big particle is smaller than that of the several small ones, particles approach each other and coalesce (see points 4, 5, 6 in the images).

- Due to important density differences, considerable sedimentation and/or segregation are taking place despite working with monotectic compositions (particles are observed moving very fast towards the bottom of the sample). It is important to highlight that the area under observation is in the centre of the prepared sample, therefore the exact amount of sedimentation that takes place cannot be observed, during the in situ solidification.

- Around the particles horizontal white strikes can be observed. It is believed that they are aluminium depleted areas after the nucleation of the liquid Pb droplets.
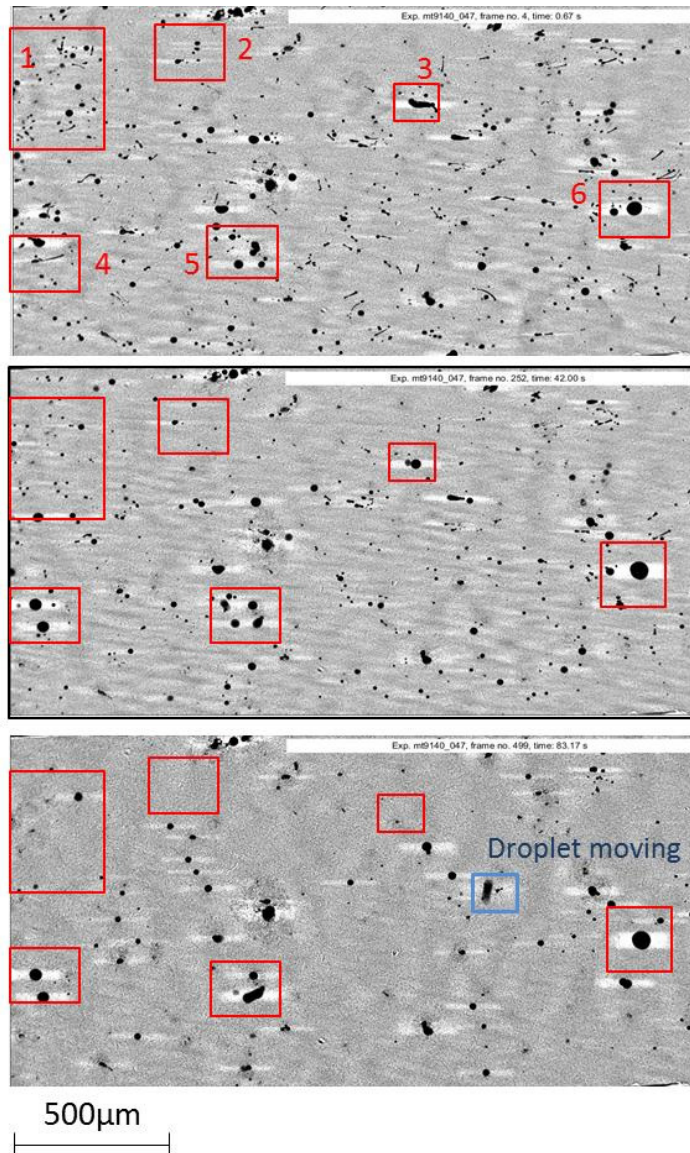
Figure 4-1 Sequence of original synchrotron images obtained during the heating of Al-1.2Pb alloy, Pb is represented by the black particles in the grey Al matrix.

Figure 4-2 shows the alloy at 720°C, Al-Pb have become a single phase and most of the Pb is dissolved within the Al or sediment to the bottom of the sample.

Exp. mt9140_047, frame no. 1051, time: 175.17 s

500µm
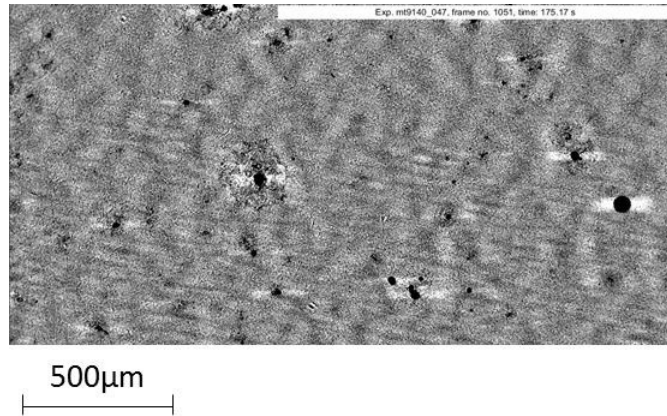
Figure 4-2 Original synchrotron image of Al-1.2Pb alloy in the final stage of melting when both liquids become miscible and only one phase is observed.

The formation of the α-Al was not detected during the experiments. Therefore the initiation of the Pb nucleation and movement of the droplets (rejected, enfulged) between the dendrites can not be observed. This makes the interpretation of the results more complicated.

All the synchrotron images with the Al matrix represented in black and Pb particles in white correspond to images treated and cleaned with imagej. The colour code was chosen for similitude with SEM back scattered images, in which the heavy metals appear white in contrast and the lighter metals appear in dark.

Figure 4-3 shows images corresponding to the solidification of Al-1.2Pb alloy. **Figure 4-3 (a)** corresponds to the first steps of the solidification, where the Pb starts to separate from the matrix, by nucleating as very small particles (represented in white, contrary to previous images these images have been cleaned and treated). **Figure 4-3 (b)** corresponds to the end of solidification, at which point more Pb has nucleated and the nucleated particles have approach each other and coalesce, due to the effect of Marangoni and other hydrodynamic forces. As a result of this processes a coarse distribution of the Pb particles is observed in the final solidified microstructure.

500μm
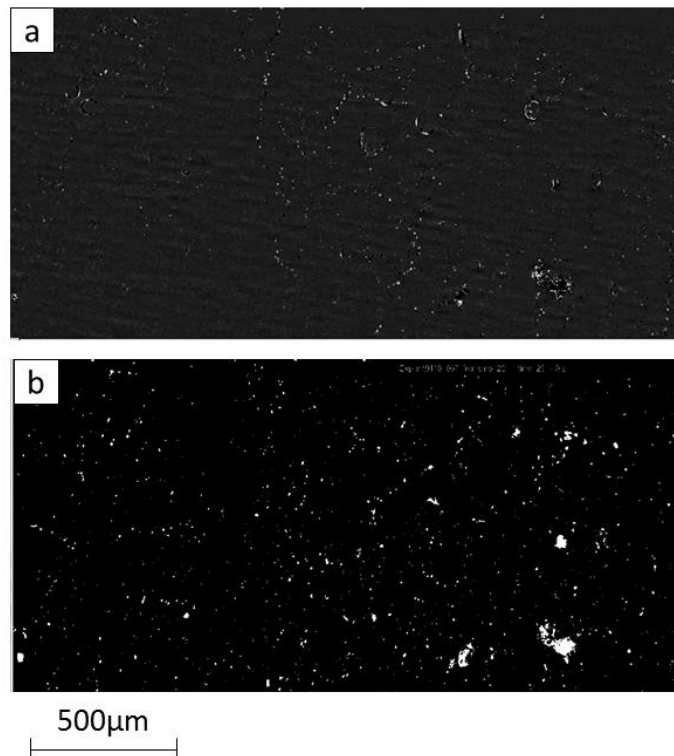
Figure 4-3 Treated synchrotron images for Al-1.2Pb alloy, solidified at 2 °C/sec, after being heated to 720°C, corresponding (a) to the beginning and (b) to the end of solidification.

4.2 Effect of shearing on the microstructure of immiscible systems

The effect of shearing on hyper-, exact monotectic immiscible Al-Pb systems and 2011 alloy containing Pb/Bi was investigated. The microstructural evolution and quantitative analysis of Pb particle size and distribution, in the Al matrix, are presented in this chapter. A consistent casting and sampling procedure was followed for consistent measurement and evaluation. Samples were taken on 4 different positions on the top and 4 positions on the bottom section of the ingot, as shown in **Figure 3-7.** The casts were repeated 3 times to ensure reproducibility.

4.2.1 Hyper-monotectic binary alloys

Figure 4-4 shows the phase diagram of an Al-Pb binary alloy, with the composition (3 % Pb) and binodal or decomposition temperature (760°C) corresponding to the alloy studied in this chapter.
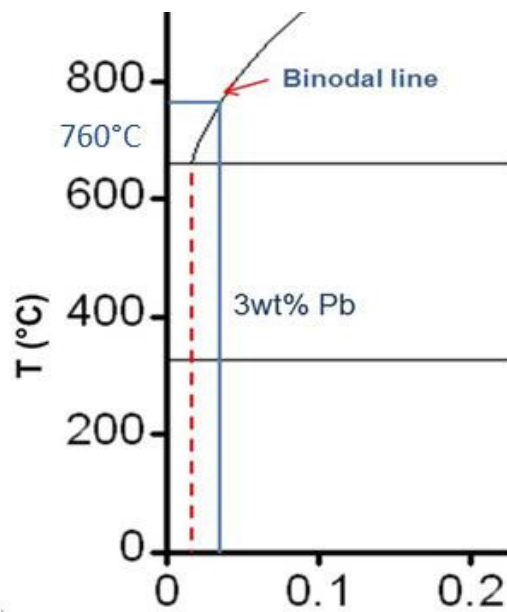
Figure 4-4 Schematic representation of part of the phase diagram Al-Pb showing an hyper-monotectic Al-3Pb alloy.

4.2.1.1 DC simulator

The first experiments were perform on DC simulator unit, described in Chapter 2, to identify the optimum casting and shearing conditions for the hyper-monotectic Al3-Pb alloy, before starting the trials on the DC caster. All billets were cast at the same speed of 140 mm/min.

Figure 4-5, Figure 4-7 and **Figure 4-8** comprise SEM back scattered images showing the distribution and size of Pb particles in the Al matrix for an Al3-Pb alloy. A pouring temperature of 790°C was chosen for the experiments and the mould temperature was set to 820°C for the samples showed in **Figure 4-5** and **Figure 4-7** and 860°C for both pouring temperature and mould temperature on **Figure 4-8** .

SEM back scattered images show the phases with lower atomic number in the darker scale of greys, the heavier the element the lighter the colour, hence Al matrix is black, and Pb white. The previous applied to all the SEM images showed throughout the results chapter.

It is clear from **Figure 4-5** that there is a severe segregation and sedimentation towards the bottom of the billet. Pb particles are very small on the top region of the billet and big

agglomeration and a continuous Pb layer are observed on the bottom-centre of the billet. **Figure 4-6** shows this sedimentation of Pb on the central part of the billet. The image is obtained by etching the billet to reveal macrostructure as explained in Chapter 2, Section 2.4.3.

When the melt is sheared in the temperature range 720°C-665°C, as seen on **Figure 4-7,** segregation/sedimentation is reduced and the number of Pb particles distributed along the billet increased consequently.

 Figure 4-8 shows the effect of shearing in the temperature range 800°C-665°C, i.e. from above the binodal line to the monotectic temperature of the alloy. It is clear that the distribution and size of Pb particles is significantly more homogeneous along and across the billet. Furthermore, sedimentation is completely supressed.
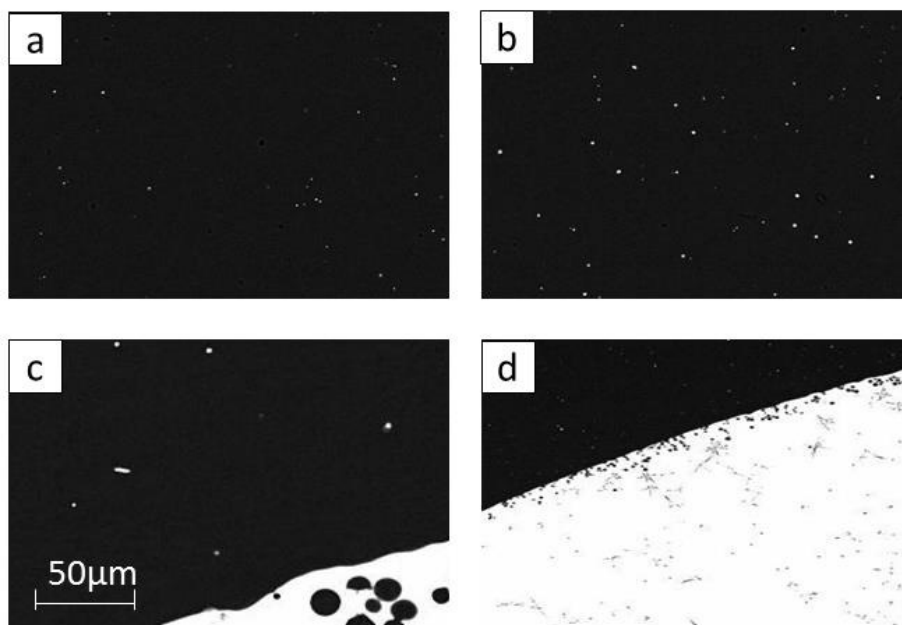
Figure 4-5   SEM images of Al-3Pb DC cast billet, cast at 790°C in a DC simulator at 140 mm/min, corresponding to the cross section, showing the edge (a,c) and centre (b,d) of Al-3Pb alloy: (a, b) top and (c, d) bottom of the billet.

20mm

Figure 4-6 Macro etched section showing the bottom of DC simulator non sheared billet.
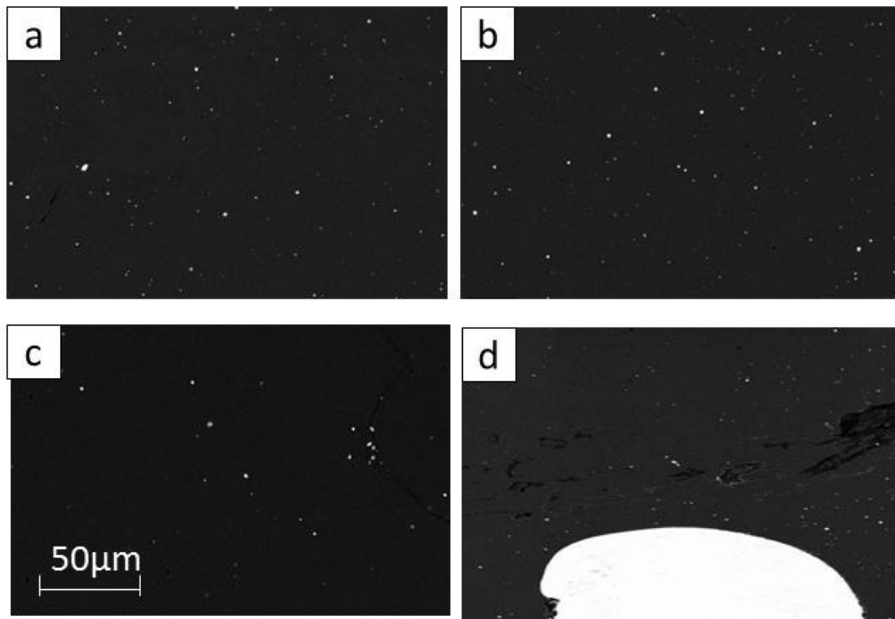
Figure 4-7 SEM images of Al-3Pb DC cast billet, cast at 790°C in a DC simulator at 140 mm/min, sheared between 720°C and 665°C, corresponding to the cross section, showing the edge (a,c) and centre (b,d) of Al-3Pb alloy: (a, b) top and (c, d) bottom of the billet.
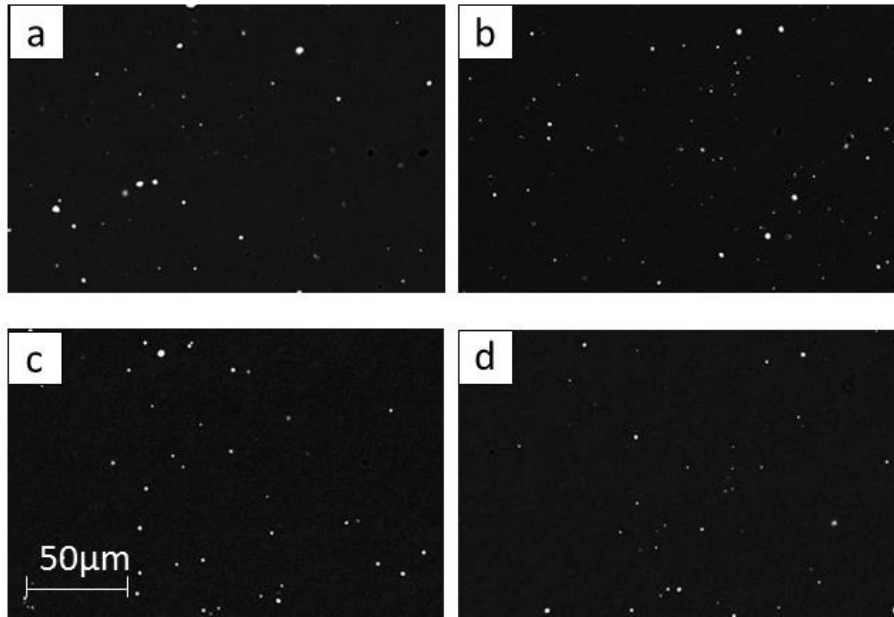
Figure 4-8 SEM images of Al-3Pb DC cast billet, cast at 790°C in a DC simulator at 140 mm/min, sheared between 820°C and 665°C, corresponding to the cross section, showing the edge (a,c) and centre (b,d) of Al-3Pb alloy: (a, b) top and (c, d) bottom of the billet.

From the comparison of **Figure 4-8** with **Figure 4-5** and **Figure 4-7** the importance of shearing on the correct temperature interval is highlighted.

A quantitative analysis of the size and number of particles along and across the billet is shown in **Figure 4-9** and **Table 4-1.** Confirming what was observed in previous micrographs, when shearing is initiated at a temperature below the decomposition temperature, the sedimentation of Pb decreases and the number of Pb particles distributed within the billet increases. However, the distribution of Pb is non-uniform and the average particle size increases from 2.2 to 3.3 μm. When the melt is sheared from above the decomposition temperature, not only sedimentation (as a continuous layer) is highly reduced but the average number of particles increases from 79 to 132.
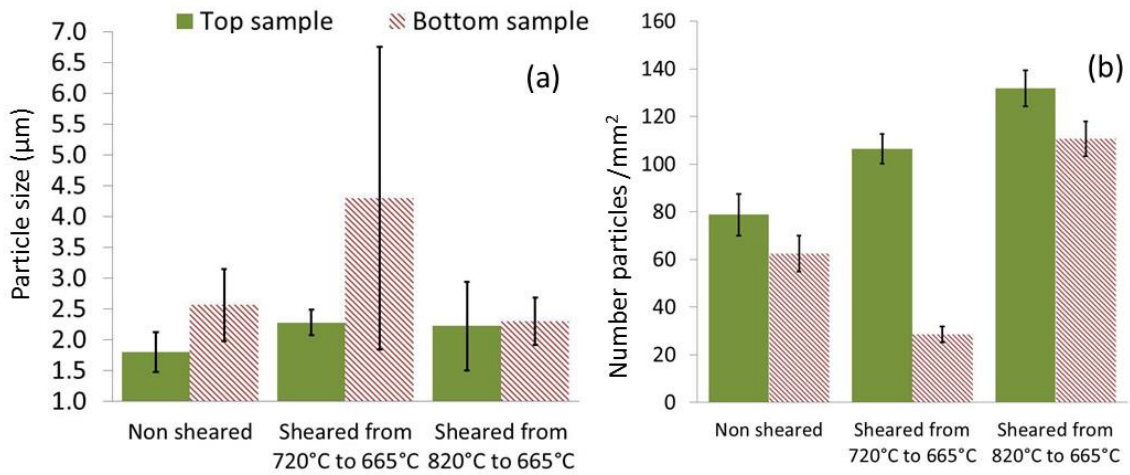
Figure 4-9 Comparison from top to bottom of sheared and non-sheared Al-3Pb DC simulator billets: (a) particle size and (b) number of particles per mm^2.

Table 4-1 Average Pb particle size and number of particles.

Cast	Number particles/mm^2	Particle size (µm)
Non sheared	79	2.2
Sheared from 720°C to 660°C	106	3.3
Shared from 820°C to 660°C	132	2.3

Furthermore the relative Pb particle area (µm^2)/(µm) (calculated as the area occupied by the Pb particles divided the average particle size) increases and becomes more uniform, when shearing on the correct temperature interval (see **Figure 4-10**).
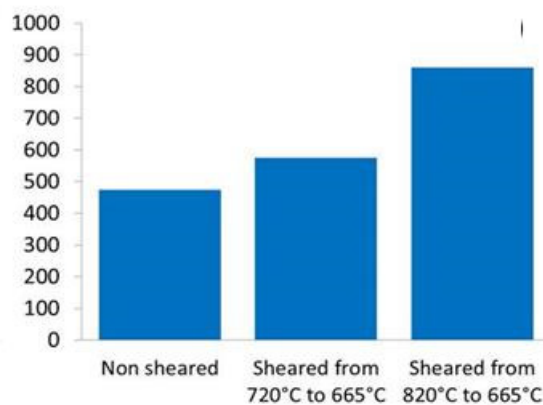
Figure 4-10 Relative Pb particle area per mm^2 for the DC simulator billets.

Figure 4-11 shows the Pb content along the billet for the 3 different casting conditions, on the centre (a) and edge (b) of the cast billets. Shearing from 720°C improves slightly the distribution of Pb along the billet, however, the distribution is very heterogeneous from top to bottom and the content is still far from the nominal of 3 %. When shearing from above the decomposition temperature the content of Pb along the billet is considerably more homogeneous and close to the target of 3%. Composition of Pb, and therefore Pb area fraction, in the billets, varies for each cast depending on the amount of sedimentation that takes place on the crucible before casting and the sedimentation of the cast billet itself. If the temperature falls down before the binodal on the crucible sedimentation will start taking place. Furthermore, even when the casting temperature is higher than the binodal temperature, sedimentation can still take place on the cast billet as a continuous layer of Pb on the bottom.
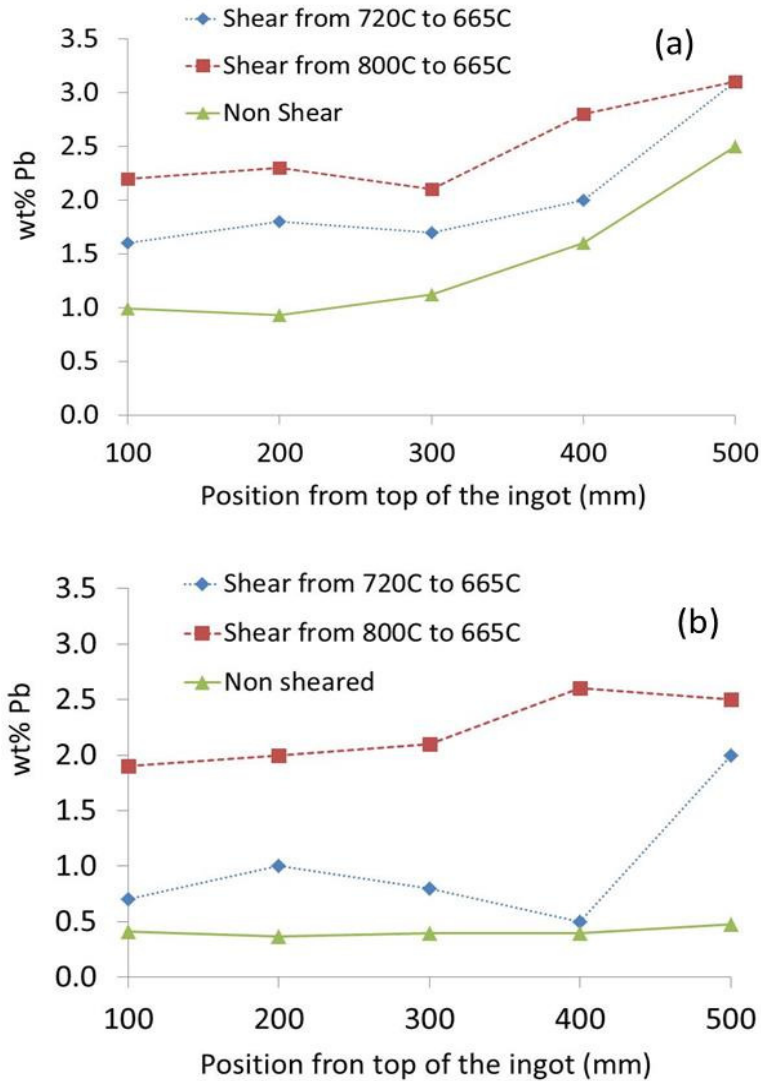
Figure 4-11 Results of the spark analysis, indicating Pb composition in wt% from the top to the bottom of the Al-3Pb DC cast billets, for the 3 different castings: (a) on the centre of the billet (b) on the edge of the billet.

4.2.1.2   DC casting

Once the relevant trials were finalised in the DC simulator, DC casting of hyper-monotectic alloys Al3-Pb was the next experimental step. The aim of the first set of experiments was to determine the effect of shearing on DC cast billets for hyper-monotectic compositions. All billets were cast at 140 mm/min and with a casting temperature of 790°C. Due to the position of the shear with respect to the mould, shearing cannot be done from a temperature above the decomposition.

40mm

Figure 4-12 Macro etched section showing the Pb segregation towards the centre of the billet for an Al-3Pb billet.

It is clear by comparing **Figure 4-6** and **Figure 4-12** that one of the main differences between DC cast and DC simulator billets is that sedimentation, as a continuous layer, is not observed for hyper-monotectic compositions; instead severe segregation of Pb can take place in the centre of the billet.

Figure 4-13 comprises micrographs in which the distribution and size of the Pb particles, in the Al matrix, can be observed. The untreated melt (a) is compared to the melt sheared at 2 different speeds: 2000 rpm (b) and (c) 6000 rpm. The untreated billet shows heavy segregation towards the centreline of the billet. By shearing at 2000 rpm it is possible to improve considerably the Pb distribution, increasing the number of particles and decreasing the average particle size. However, the temperature gradient still allows for a higher concentration of particles on the centre of the billet. For completely homogenous structure from edge to centre a shearing speed of 6000 rpm is required. These results are confirmed

in **Table 4-2**, where quantitative information about particle size and number of particles, from edge to centre, is displayed for the two different shearing conditions.
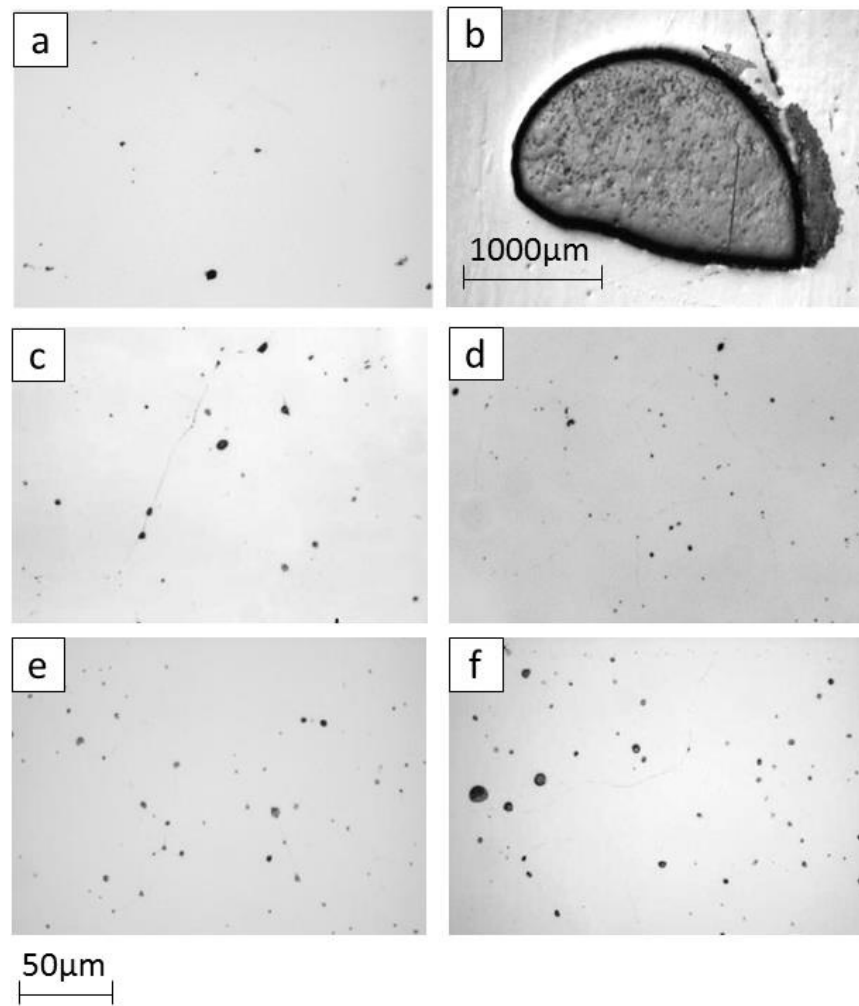
Figure 4-13 Optical micrographs of DC cast Al-3Pb billet, cast at 790°C and 140 mm/min, corresponding to (a,c,e) edge and (b,d,f) centre of the billet: (a,b) non sheared, (c,d) sheared at 2000 rpm (e,f) sheared at 6000 rpm.

Table 4-2 Number of particles from edge to centre, as a function of shear speed for Al-3Pb DC cast billet.

Shear speed	position	Number particles/mm^2
2000 rpm	edge	90
2000 rpm	middle	115
6000 rpm	edge	106
6000 rpm	middle	102

Therefore 6000 rpm was chosen as the rotational shearing speed, and all the experiments from here onwards are based on this value.

Figure 4-14 and **Figure 4-15** comprise SEM back scattered images showing the distribution and size of Pb particles in the Al matrix for an Al-3Pb alloy, on the top and bottom of the billet respectively. It is seen that shearing can decrease the particle size and increase considerably the number of particles. The microstructure created by shearing is more homogeneous across and along the billet, i.e. the number and size of particles remains equal in any position on the billet. **Figure 4-16** and **Figure 4-17** summarise the quantitative analysis on particle size and number of particles from edge to centre and top to bottom of the billet, respectively.
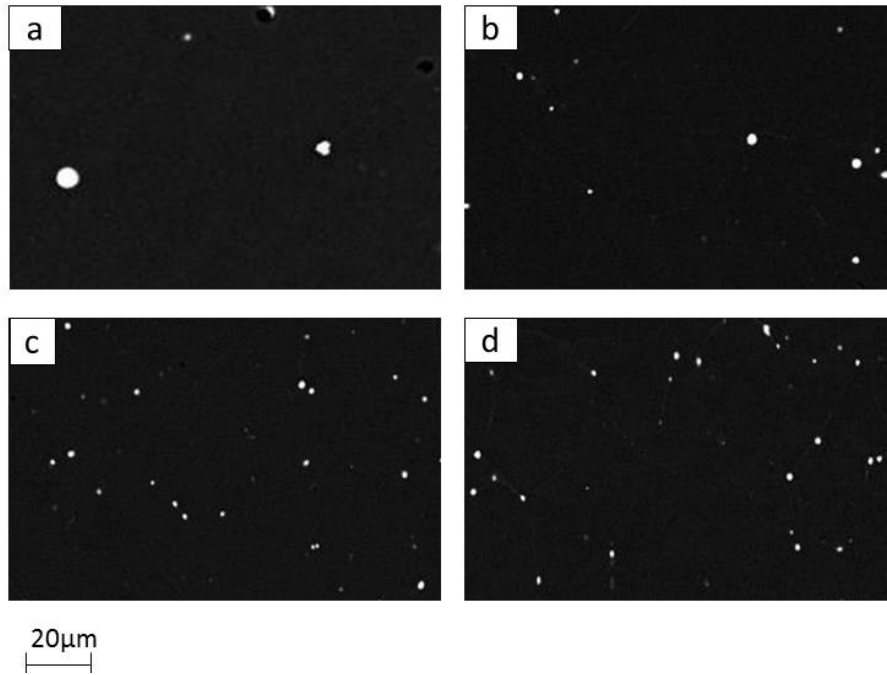
Figure 4-14 SEM back scattered images of Al-3Pb DC cast billet, cast at 790°C and 140 mm/min, corresponding to edge (a,c) and centre (b, d) of the top of the billet: (a,b) non sheared and (c,d) sheared at 6000 rpm.
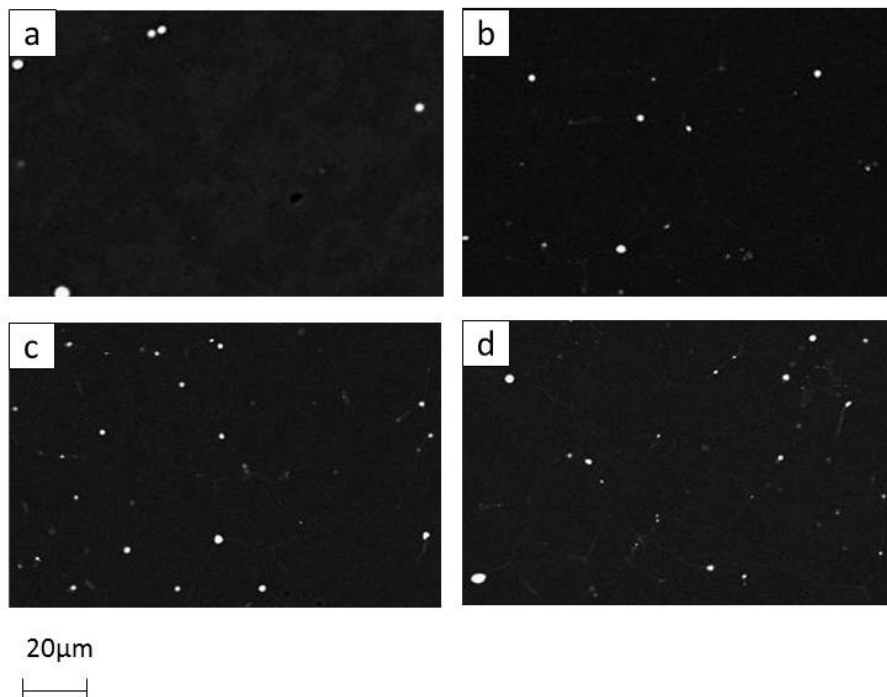
Figure 4-15 SEM back scattered images of Al-3Pb DC cast billet, cast at 790°C and 140 mm/min, corresponding to edge (a,c) and centre (b, d) of the bottom of the billet: (a,b) non sheared and (c,d) sheared at 6000 rpm.

From the analysis of data in **Figure 4-16** it can be seen that shearing leads not only to an increase in the number of Pb particles and reduction of particle size but to a more homogeneous distribution of particles across the billet. For the untreated melt the particle size ranged from a few microns to several mm, as indicated by the high standard deviation seen in **Figure 4-16**. The same can be said when comparing the top and bottom of the billet, as seen on **Figure 4-17.**
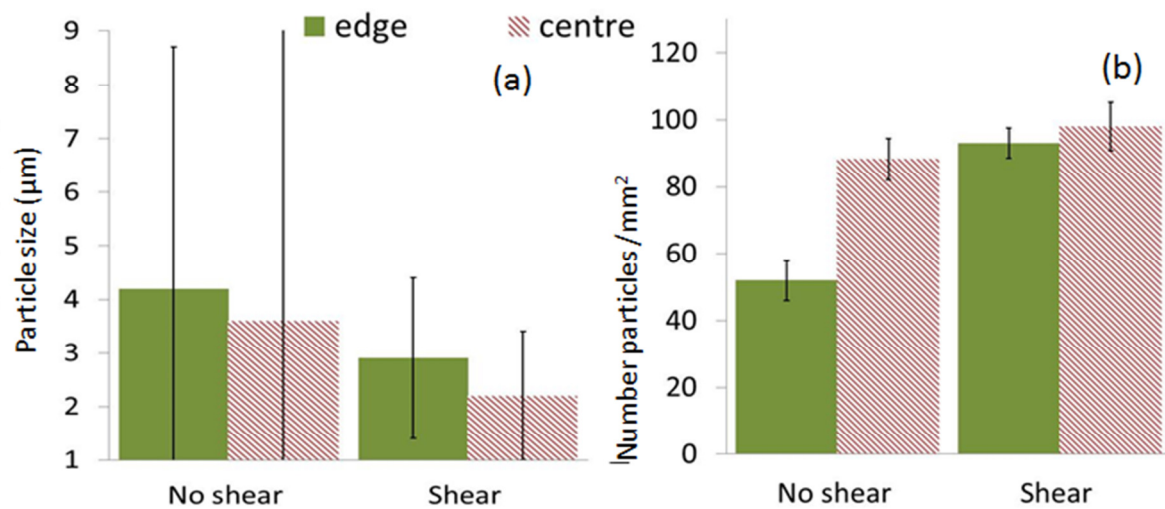
Figure 4-16 Comparison of non-sheared and sheared Al-3Pb billets, (a) Particle size and (b) number of particles from edge to centre of the billet.
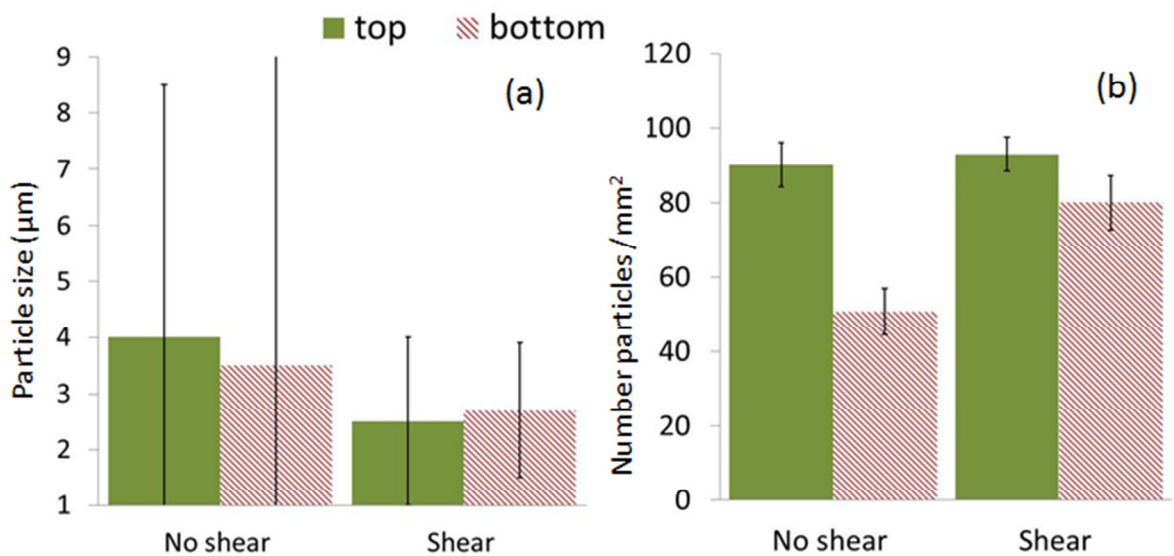
Figure 4-17 Comparison of non-sheared and sheared Al-3Pb billets, (a) Particle size and (b) number of particles from top to bottom of the billet.

Table 4-3 summarises quantitative information about average particle size and number of particles. The data shows that shearing increases the number of particles from 70 to 96, (36% increase). Furthermore, average particle size is reduced from 3.8 to 2.6 µm (30 % reduction).

Table 4-3 Average number of particles and dropelt size for Al-3Pb DC cast billet.

	Number particles/mm²	Particle size (µm)
Non-Sheared	70	3.8
Sheared	92	2.6

As seen on **Figure 4-18** shows the Pb content along the billet for the untreated (a) and the sheared melt (b). It is clearly seen, by comparing (a) and (b) that improve the distribution of Pb along the cast billet. However, severe segregation is still present and the composition is still below nominal values, particularly on the bottom of the billet. Composition of Pb, and therefore Pb area fraction, in the billets, varies for each cast depending on the amount of sedimentation that takes place on the crucible before casting and the sedimentation of the cast billet itself. If the temperature falls down before the binodal on the crucible sedimentation will start taking place. Furthermore, even when the casting temperature is higher than the binodal temperature, sedimentation can still take place on the cast billet as a very big droplet in the centre bottom part.
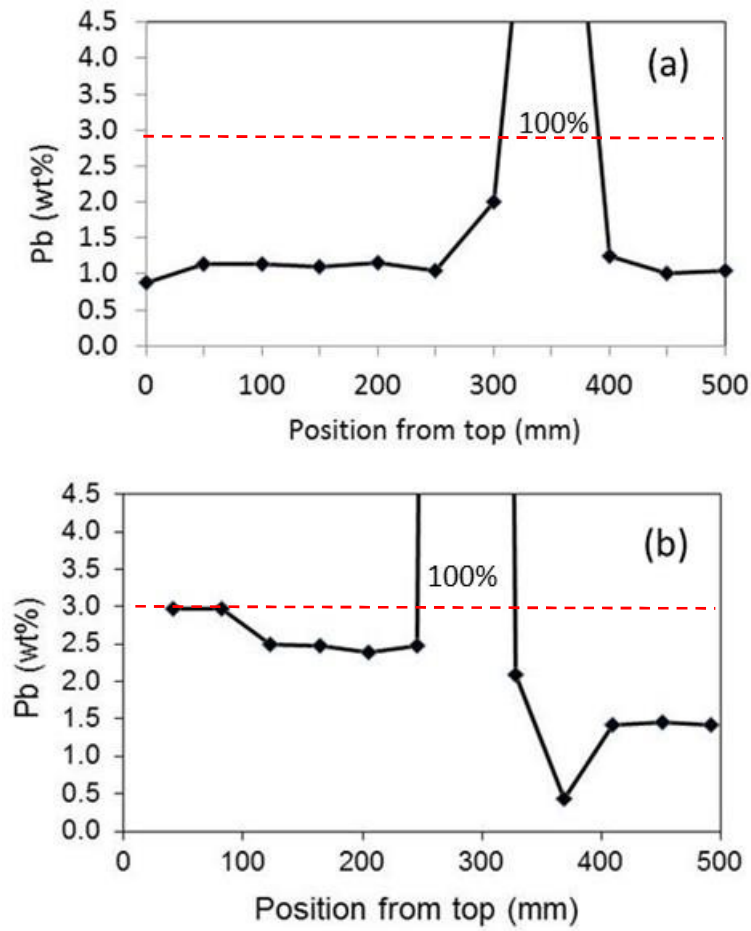
Figure 4-18 Results of the spark analysis, indicating Pb composition in wt% from the top to the bottom of the Al-3Pb billet, for: (a) non sheared (b) sheared at 6000 rpm during casting.

4.2.2 Exact Monotectic binary alloys

The effect of shearing on Al-Pb DC cast billet of exact monotectic (1.2 %) was investigated. All the billets described in this chapter were cast at 740°C and 140 mm/min. The treated melt was sheared at 6000 rpm and in the temperature interval between 720°C and 660°C. **Figure 4-19** shows part of the phase diagram of Al-Pb for the particular Pb content studied in this chapter. The solidification path dictates that the phase separation, i.e. nucleation of Pb as particles, and the solidification of Al take place simultaneously. Furthermore, Pb should be miscible in Al at any temperature in the liquid state.
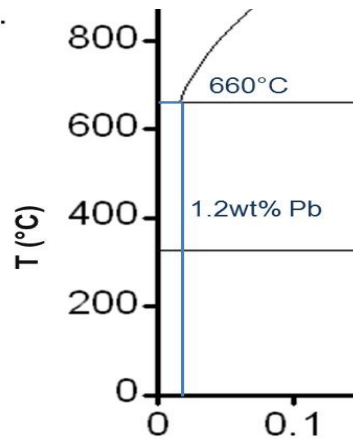
Figure 4-19 Schematic representation of part of the phase diagram Al-Pb for a monotectic Al-1.2Pb alloy.

Figure 4-20 and **Figure 4-21** comprise optical micrographs showing the size and distribution of Pb particles in the Al matrix for the Al-1.2Pb DC cast billets. It can be seen that for the untreated melt Pb shows a tendency to move to the centre of the billet, where bigger particles and Pb segregation are found. When the melt is sheared a more fine and uniform distribution of Pb particles across and along the billet is obtained. The comparison of micrographs (a, b) to (c, d) in both figures and the quantitative analysis from edge to centre and top to bottom, displayed in **Figure 4-22** and

Figure 4-23, respectively, shows that shearing not only leads to an increase in the number of Pb particles but also to their homogeneous distribution, across and along the billet, reducing considerably the segregation of Pb towards the centre.
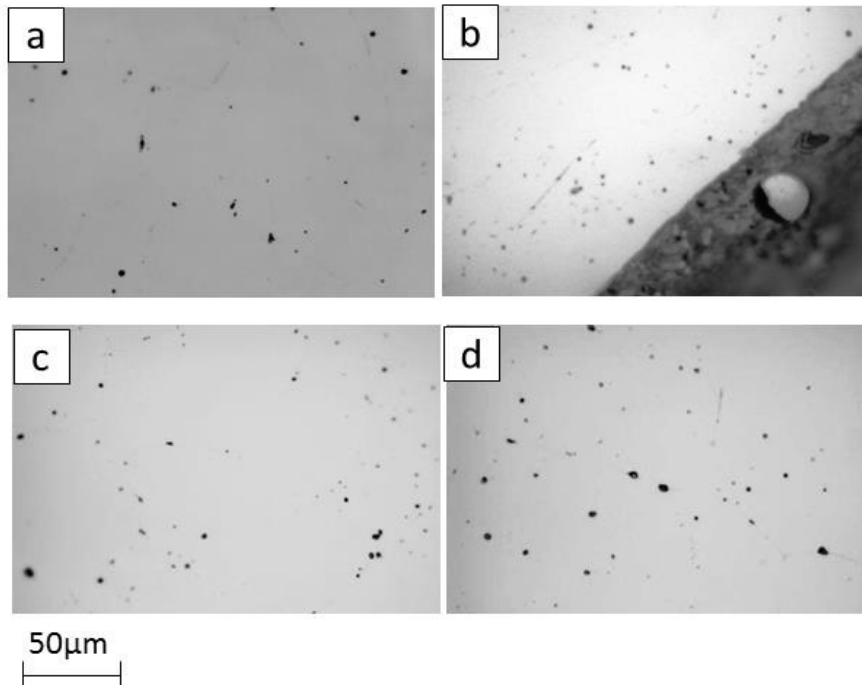
Figure 4-20 Optical micrographs of Al-1.2Pb DC billet, cast at 740°C and 140 mm/min, corresponding to (a, c) edge and (b, d) centre of the top of the billet: (a,b) non sheared (c,d) sheared at 6000 rpm.
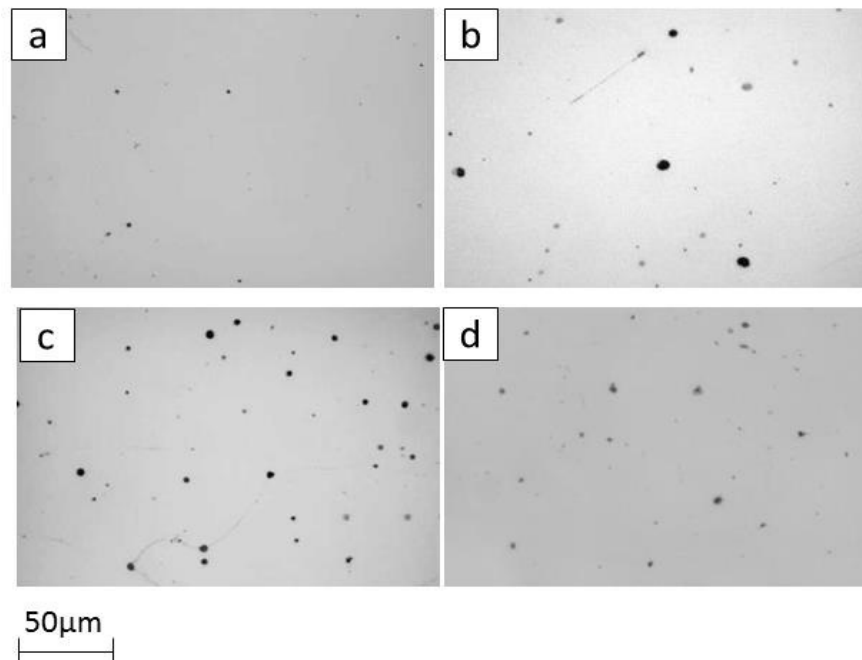
Figure 4-21 Optical micrographs of Al-1.2Pb DC billet, cast at 740°C and 140 mm/min, corresponding to (a, c) edge and (b, d) centre of the bottom of the billet: (a,b) non sheared (c,d) sheared at 6000 rpm.

Figure 4-22 and

Figure *4-23* comprise a quantitative analysis of particle size and number of particles across and along the billet, respectively. It is seen that shearing not only improves the distribution but it increases the number of particles, reducing their size. Furthermore it gets a more homogenous particle size, as indicated by the small standard deviation, compared to the untreated melt. For the untreated melt the particle size ranges from several mm to a few microns.
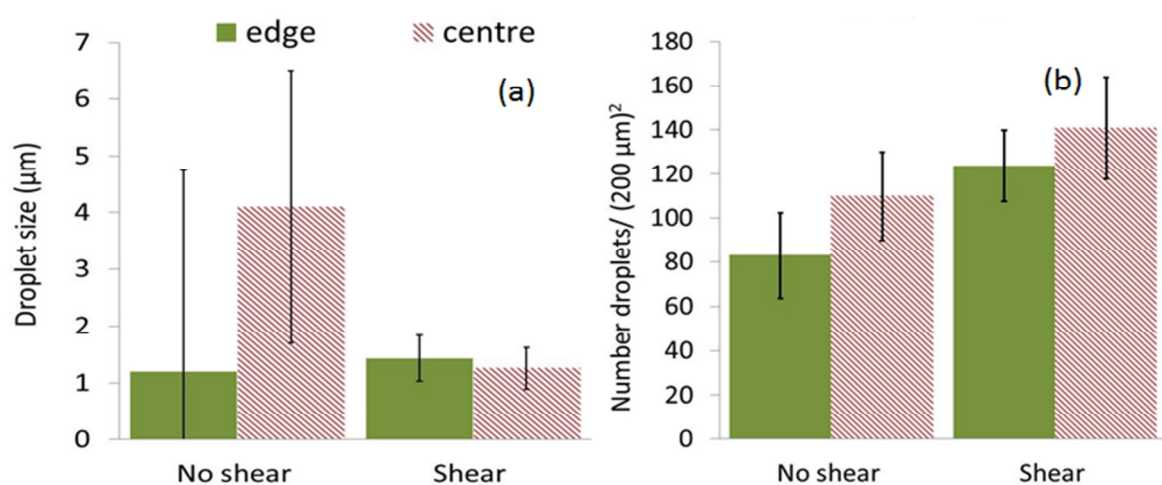
Figure 4-22 Comparison of non-sheared and sheared Al-1.2Pb billets: (a) Particle size and (b) number of particles from edge to centre of the billet.
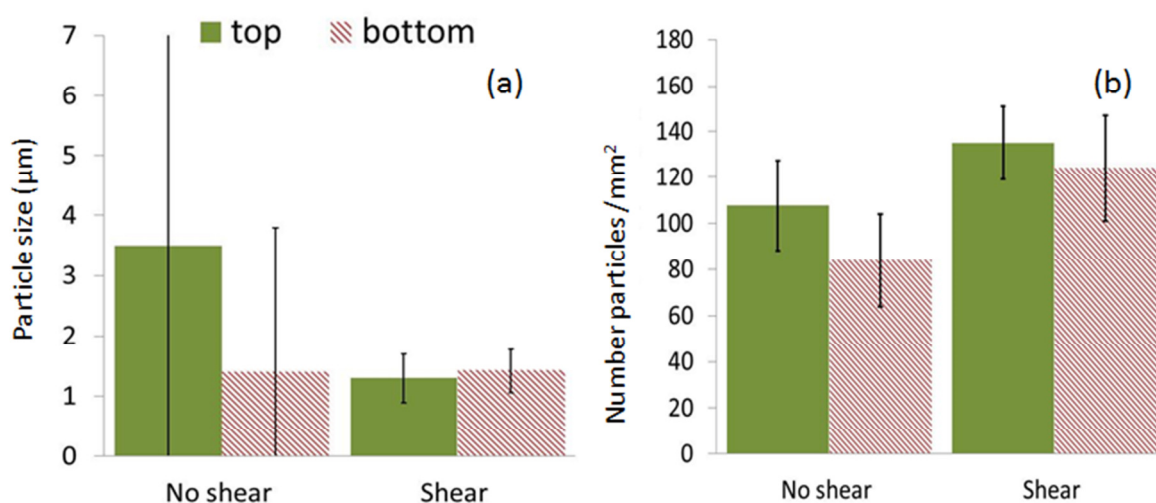
Figure 4-23 Comparison of non-sheared and sheared Al-1.2Pb billets: (a) Particle size and (b) number of particles from top to bottom of the billet.

An average particle size reduction from 2.6 μm to 1.3 μm, comparing untreated with sheared melt, is shown in **Table 4-4**. This particle size reduction is accompanied by an increase in the number of particles from 96 in untreated melt to 130 under shearing conditions (27% increase).

Table 4-4 Average number of particles and particle size for Al-1.2Pb DC cast billet.

	Number particles/mm²	Particle size (μm)
Non-Sheared	96	2.6
Sheared	130	1.3

By comparing **Figure 4-24** (a) and (b) it is clearly seen that shearing reduces considerably the compositional segregation towards the bottom for monotectic compositions in DC casting. However a different Pb content from top (0.8 %) to bottom (1 %). Sedimentation of Pb was also observed on the bottom of the crucible from which the metal was poured.
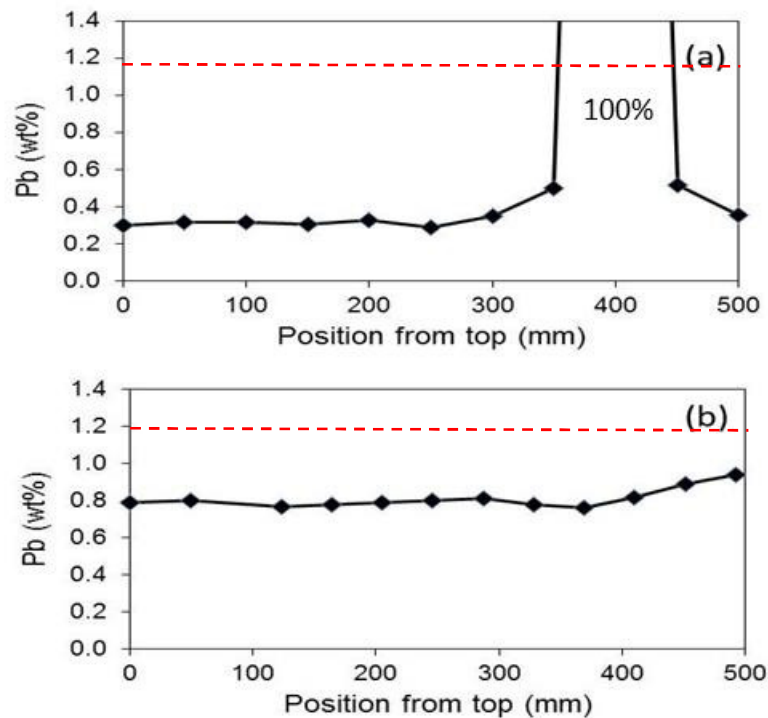
Figure 4-24 Results of the spark analysis, indicating Pb composition in wt% from the top to the bottom of an Al-1.2Pb DC cast billet, for: (a) untreated melt (b) melt sheared at 6000 rpm during casting.

The difference in behaviour between hyper- and exact monotectic alloys can be observed by comparing **Figure 4-18** and **Figure 4-24**. For the sheared melt, the segregation and accumulation of Pb is much more severe for hyper- than for monotectic compositions. Furthermore, from the comparison of **Table 4-3** and **Table 4-4** it is obvious the average particle size increase as we increase the Pb content and we move towards hyper-monotectic compositions.

4.2.3 2011 alloy

The final step to get a complete understand of the effect of shearing on immiscible systems was to test an industrial alloy, in which the concentration of soft phases, is in the hypo-monotectic regime. 2011 alloy, containing Pb and Bi (both immiscible in Al) was the industrial alloy chosen for these trials. The composition of this alloy in detailed Chapter 2.

All the billets were cast at 720°C and with a speed of 140 mm/min. The shearing speed, when applicable, was set 6000 rpm. The heating temperature of the melt (or superheat) was modified for different casting and it will be individually mentioned for each casting. The inoculant added was calculated to get 0.01 % equivalent to Ti, and balanced B for stoichiometric TiB_2, in the case of the Al-Ti and Al-B master alloy additions.

Figure 4-25 and **Figure 4-26** show typical optical images of the microstructure obtained for untreated (a,b) and sheared (c,d) melt, cast at 740°C. **Figure 4-27** and **Figure 4-28** comprise SEM images of the billets for the alloy containing Al-Ti and Al-B and heated to 860°C. The micrographs represent the structures obtained for the untreated (a,b) and sheared (c,d) melt. The grey phases, in the interdendritic spaces, correspond to Al-Cu intermetallics, some of them containing also small amounts of Fe (see **Figure 4-29**) and the black particles correspond to Pb. By comparing micrographs (a,b) with (c,d) in each of the figures, it can be seen that shearing increases the number of particles and decrease their average size across and along the billet independently of other processing conditions of the melt, like refiner additions and superheating. However, with superheat and Al-Ti Al-B additions as the Pb microstructure is already very refined before shearing, the effect of shearing is less pronounced.
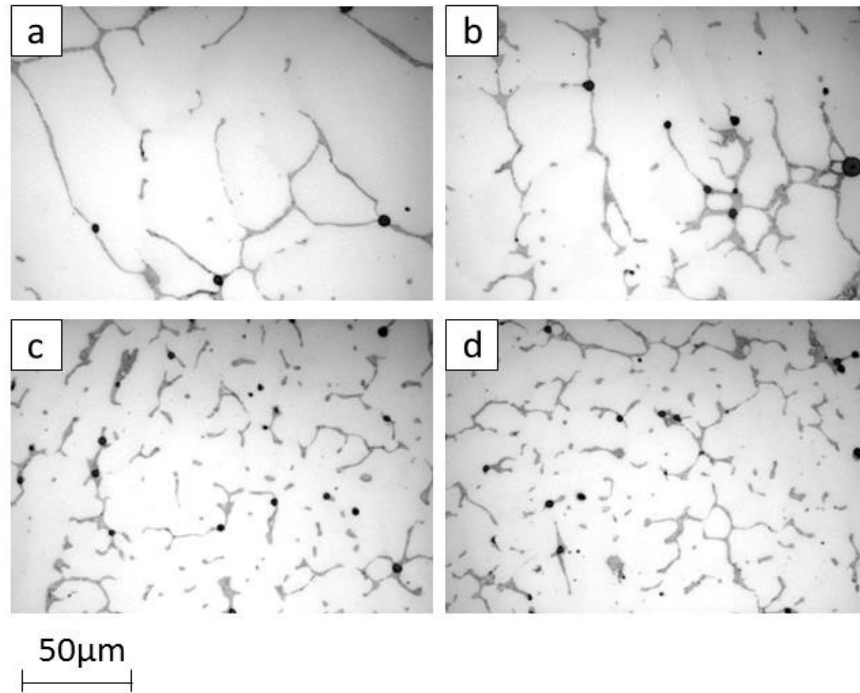
Figure 4-25 Optical micrographs of 2011 DC billets, cast at 740°C and 140 mm/min: (a,b) non sheared (c,d) sheared at 6000 rpm corresponding to edge (a, c) and centre (b, d) on the top of the billet.
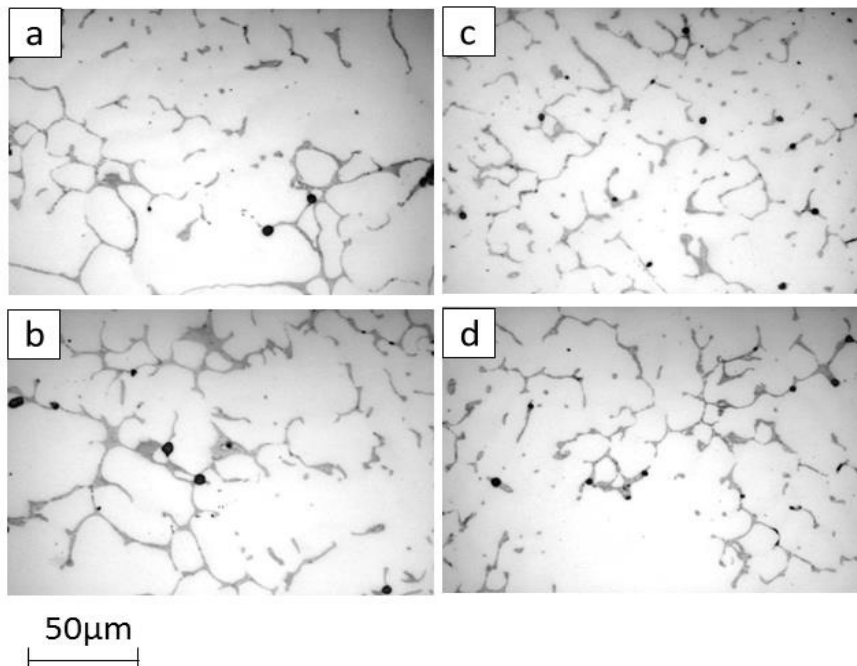
Figure 4-26 Optical micrographs of 2011 DC billets, cast at 740°C and 140 mm/min: (a,b) non sheared (c,d) sheared at 6000 rpm corresponding to edge (a, c) and centre (b, d) on the bottom of the billet.
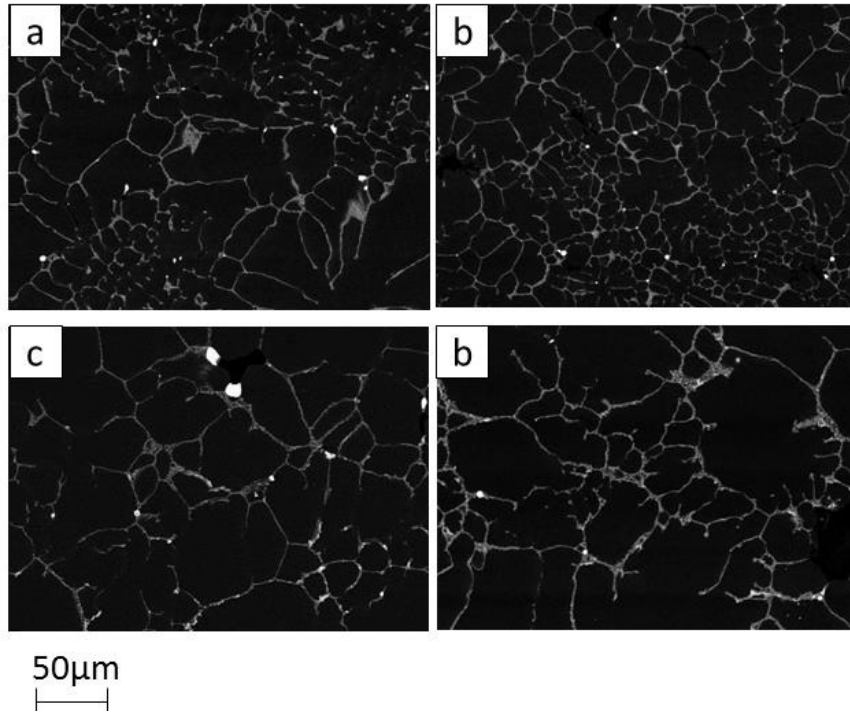
Figure 4-27 Back scattered SEM image of 2011 DC cast billets, containing Al-Ti and Al-B, heated to 860°C, cast at 740°C and 140 mm/min, corresponding to (a, c) edge and (b, d) centre from the top of the billet: (a,b) non sheared (c,d) sheared at 6000 rpm.
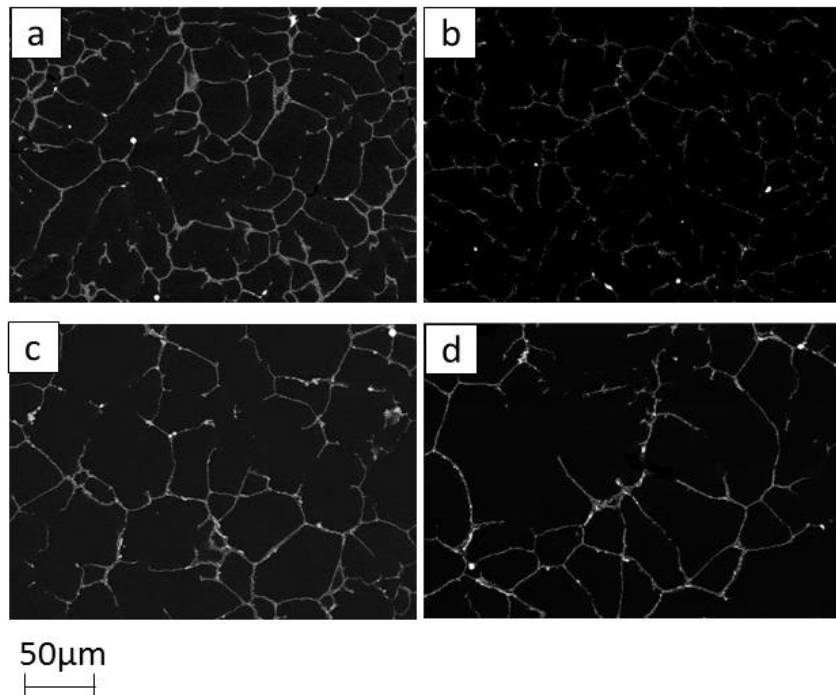
Figure 4-28 Back scattered SEM image of 2011 DC cast billets, containing Al-Ti and Al-B, heated to 860°C, cast at 740°C and 140 mm/min, corresponding to edge (a, c) and centre (b, d) from the bottom of the billet: (a,b) non sheared (c,d) sheared at 6000 rpm.
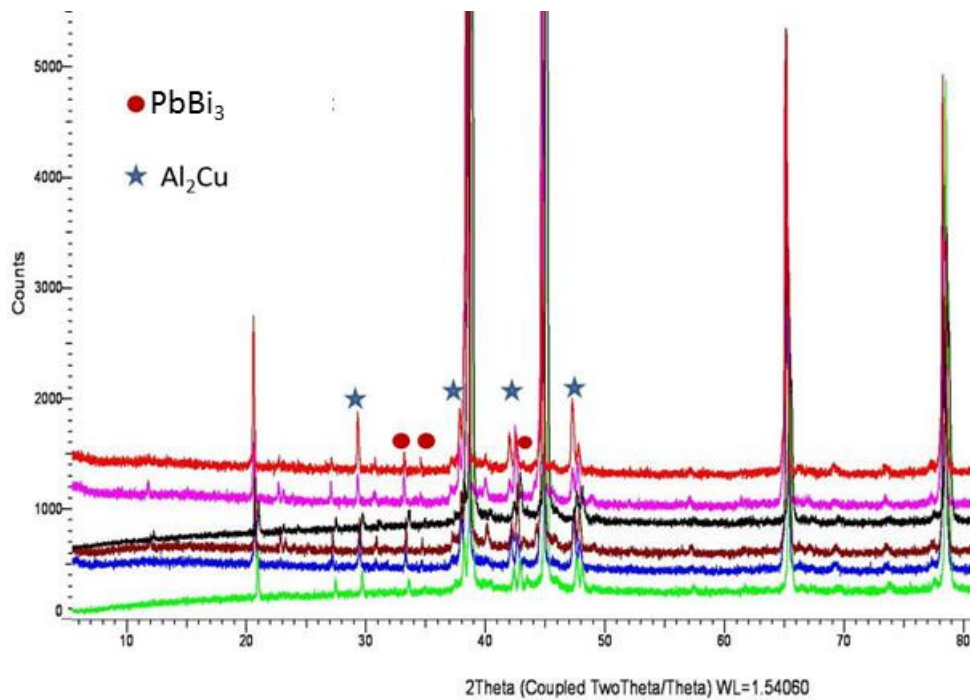
Figure 4-29 XRD mapping of different samples of 2011 where the Al-Cu and Pb-Bi eutectic are detected, the big peaks are corresponding to Al.

A quantitative analysis of particle size and number of particles for the billets from the untreated melt (a,b) and melt sheared at 6000 rpm (c,d), across and along the billet is shown in **Figure 4-30** and **Figure 4-31**, respectively. It is clear that shearing not only leads to an increase in the number of Pb particles but contributes to their homogeneous size and distribution, across and along the billet. Furthermore it reduces the centreline segregation, compared to conventional casting conditions.
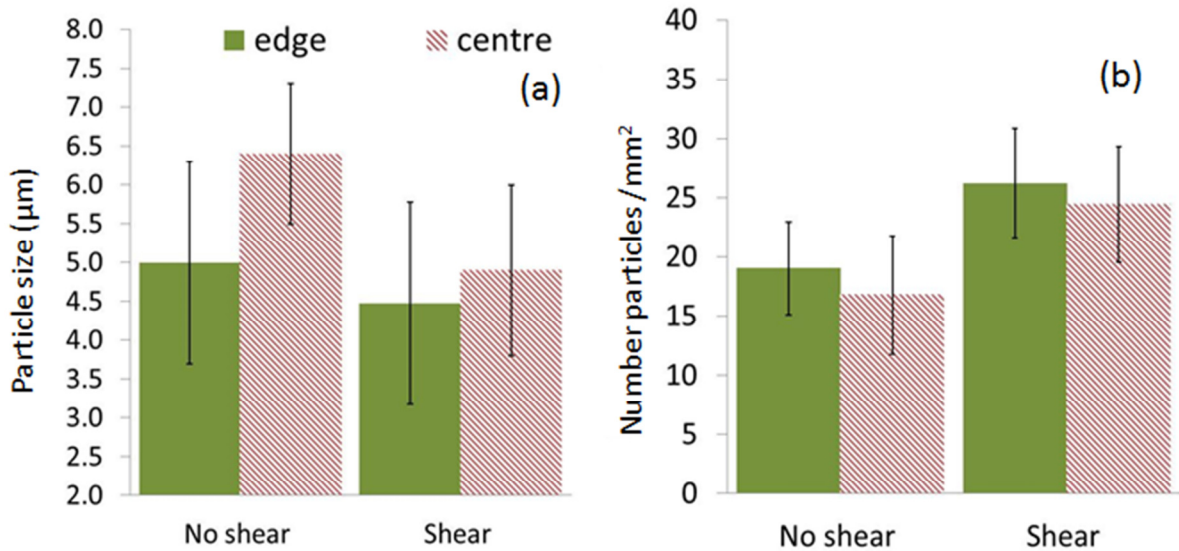
Figure 4-30 Comparison of sheared and non-sheared 2011 billets, (a) Particle size and (b) number of particles from edge to centre of the billet.
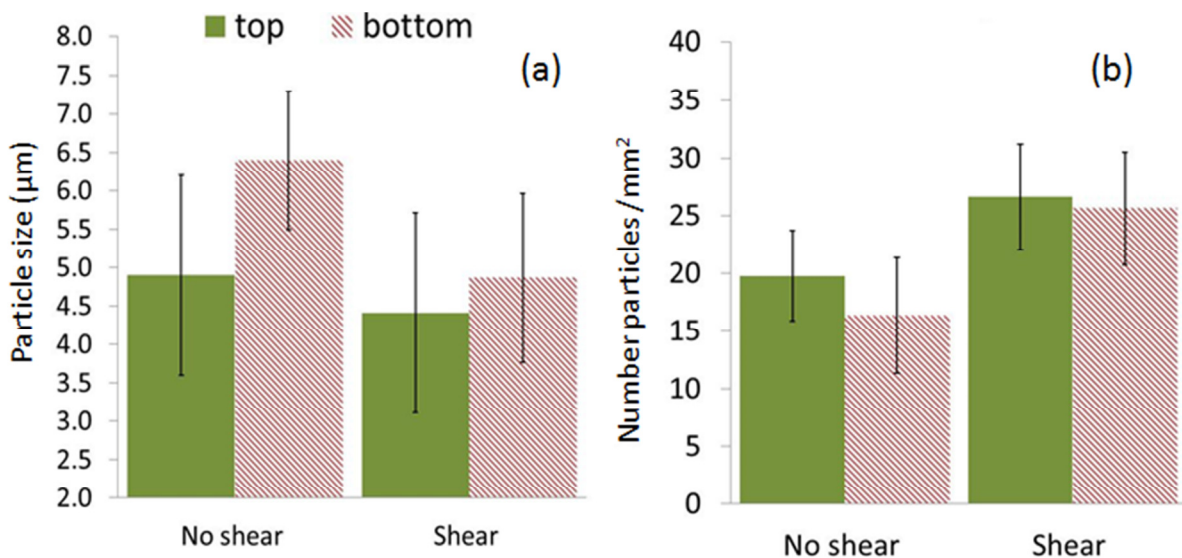
Figure 4-31 Comparison of sheared and non-sheared 2011 billets, (a) Particle size and (b) number of particles from top to bottom of the billet.

Contrary to the alloy of exact monotectic composition (see **Figure 4-22** and

*Figure 4-23***)**, for 2011 alloy (see **Figure 4-30** and **Figure 4-31**) the particle size for the untreated billet, with values between 3.5 and 6.3 µm is much more homogeneous, as indicated by standard deviation.

The effect of shearing on Pb size and distribution is summarised in **Table 4-5** and **Figure 4-32**. **Table 4-5** comprises a quantitative analysis of particle size and number comparing untreated and sheared melt. Shearing can provide a reduction in particle size from 5.7 to 4.7 μm (17% reduction), as well as an increase in their number from 18 to 26 per unit area (37% increase). **Figure 4-32** shows the effect of shearing on the particle size distribution for DC cast 2011 billets. It is clear that shearing has a significant effect on the size distribution of Pb/Bi particles, by increasing considerably the amount of particles smaller than 4 μm, reducing at the same time the quantity of particles bigger than 5 μm.

Table 4-5 Average number of particles and particle size for 2011 DC cast billet.

Cast	Number particles/mm^2	Particle size (μm)
Non-sheared	18	5.7
Sheared	26	4.7
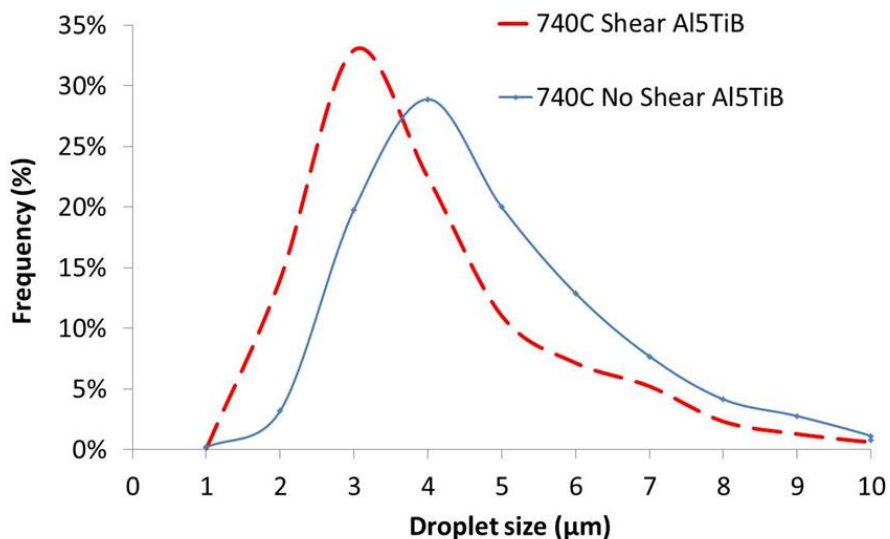
Figure 4-32 Effect of the shearing on particle size distribution: 2011 DC cast billets.

Figure 4-33 and **Figure 4-34** comprise optical images of etched samples, to reveal the grain morphologies and sizes. Samples from non-treated (a,b) and sheared (c,d) billets are compared. The average grain size is significantly reduced and the **Figure 4-33** represents billets whose melt has been heated to 740°C, a reduction in average grain size from 426 µm to 152 µm can be achieved by melt shearing. Similarly, **Figure 4-34** present images for the melt containing Al-Ti and Al-B master alloys and heated to 860°C, where average grain size is reduced, under the effect of shearing, from 239 µm to 140 µm. Furthermore, it is clear, in both cases, that shearing changes the grain morphology from big equiaxed to rosette type structure, as shown in images (a, b) compared to images (c, d).
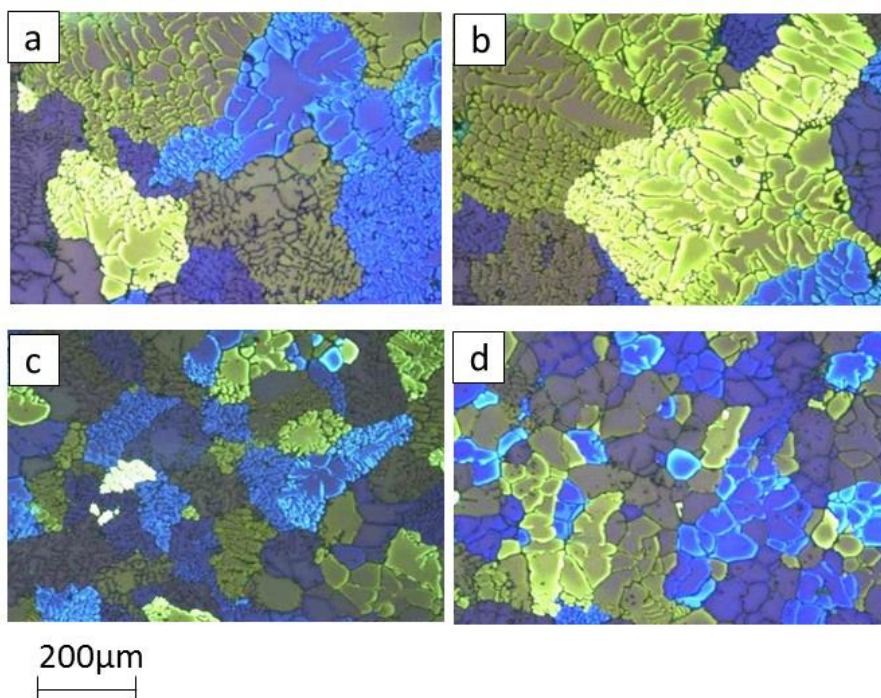
Figure 4-33 Optical images, obtained under polarised light, showing the grain of the 2011 DC cast billets, cast at 740°C and 140 mm/min corresponding to (a, c) edge and (b, d) centre of the billet: (a,b) non sheared (c,d) sheared at 6000 rpm.
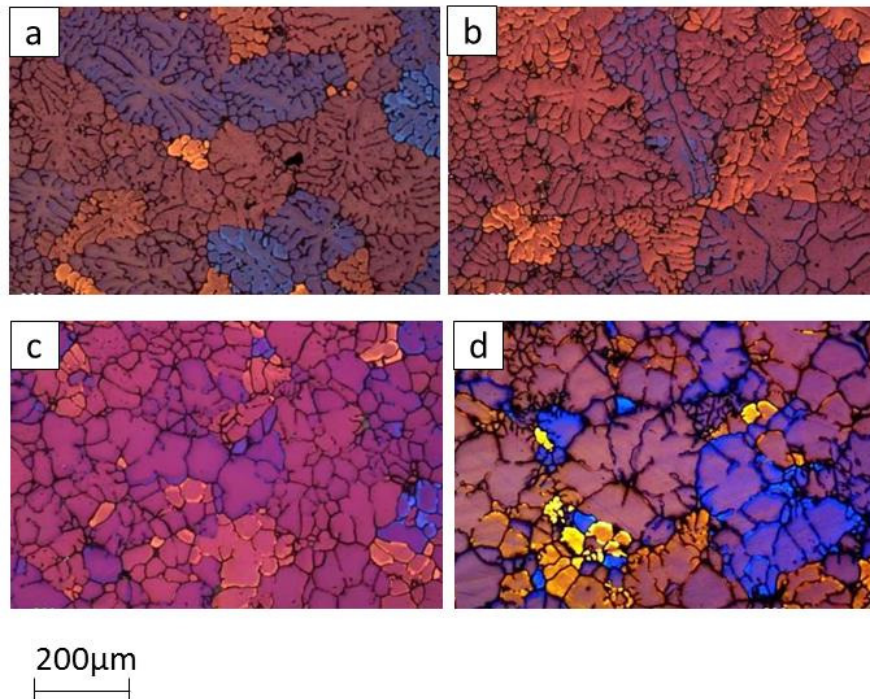
Figure 4-34 Optical images, obtained under polarised light, showing the grain of 2011 DC cast billets containing Al-Ti and Al-B, heated to 860°C, cast at 740°C and 140 mm/min, corresponding to (a, c) edge and (b, d) centre of the billet: (a,b) non sheared (c,d) sheared at 6000 rpm.

4.3 Effect of inoculant additions on microstructure of immiscible systems

As seen on the previous chapter, although shearing provides an important improvement on the microstructure obtained in DC casting for Hypo-, exact and hyper-monotectic Al-Pb alloys, shearing alone cannot create a completely fine and uniform distribution of the soft phase in the Al matrix. Hence the need to continue investigating in possible mechanism to get an optimum particle size and volume fraction for enhanced properties.

All the billets have been cast at 140 mm/min. The inoculant was added as explained in **Chapter 2 Section 2.2**. The amount of inoculant required increases with Pb content, and it will be indicated individually for each of the three selected alloy categories. The casts were repeated 3 times to ensure reproducibility.

4.3.1 Hyper-monotectic binary alloys

4.3.1.1 Steel mould casting with different inoculant additions

Several inoculant particles were initially selected, to try to understand their effect on the microstructure of the immiscible systems Al-Pb. The inoculants chosen are seen in **Figure 4-35**. These inoculants remain solid at the experimental temperatures and theoretically can act as substrates for the nucleation of liquid Pb particles. Al-Ti and Al-B were added in amount required to obtain 0.4 % of Ti, with balanced amount of B for stoichiometric proportion. The inoculants were added after the alloy was molten. The alloy containing the inoculant was heated to 800°C and cast at 790°C.

Figure 4-35 shows SEM images of typical microstructures obtained using the mentioned inoculant additions compared to the reference sample, without inoculant. It is clear from images (c, d, e, f) that both ZrO_2 and TiB_2 improve the distribution of Pb within the Al matrix but the best particle distribution and most refined particle size is obtained with the novel inoculant prepared from mixing Al-Ti and Al-B master alloy.
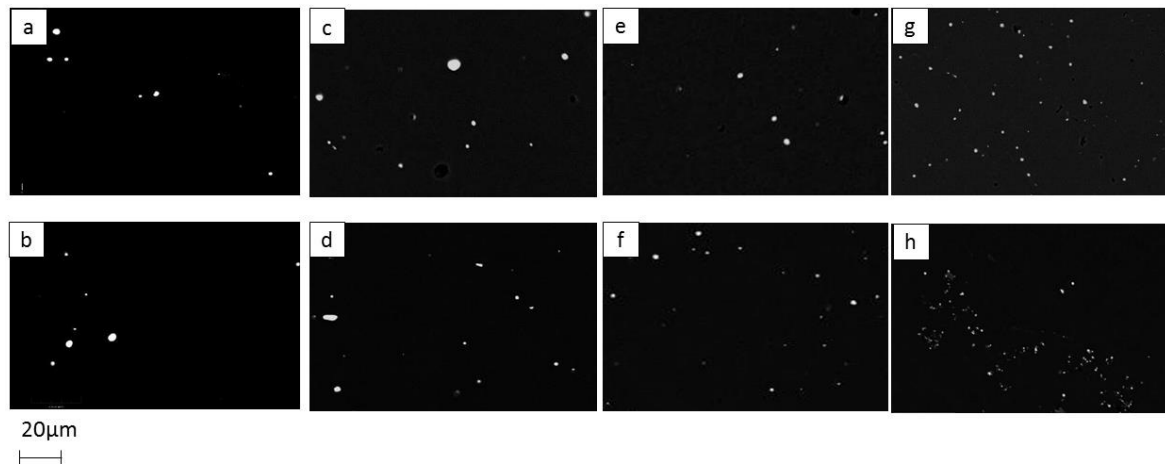
Figure 4-35 Back scattered SEM image of steel mould casting of Al-3Pb sample, heated to 800°C and cast at 790°C corresponding to (a, c, e, g) top and (b, d, f, h) bottom of the billet: (a,b) untreated (c,d) sheared and containing ZrO_2 nanoparticle (e, f) sheared and containing synthetic TiB_2 powder and (g, h) sheared and containing Al-Ti and Al-B .

In **Figure 4-36** a quantitative analysis of particle size and number of particles, for the castings with different inoculant additions, is presented. It is clear that all the inoculants added have an effect on the Pb distribution and refinement. ZrO_2 reduces the particle size by 25% and increases their number by 39%, synthetic TiB_2 decreases particle size by 40% and increases number of particles by 52% and Al-Ti and Al-B reduce particle size by 48% and increase their number by more than 100% with respect to the reference sample. The results confirm therefore that Al-Ti and Al-B master alloy are the most efficient inoculant. The novel inoculant, not only produces the highest amount of particles of the smallest size, but also a more homogeneous distribution and size along the cast billet. Therefore this will be chosen for the DC casting trials for the three different Pb concentrations.
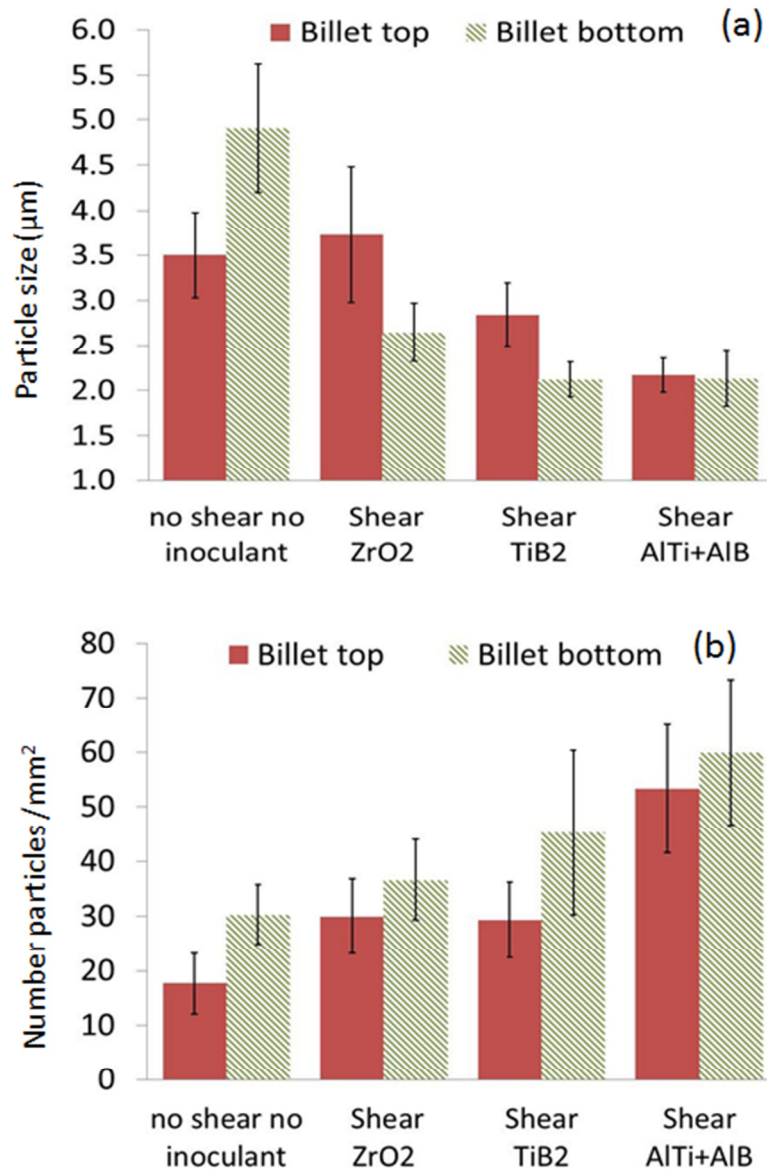
Figure 4-36 Comparison of untreated Al-3Pb alloy melt, and melt sheared with different inoculant additions (a) Particle size and (b) number of particles from top to bottom of the billet.

4.3.1.2 _Effect of inoculant additions on DC casting_

The inoculant made from Al-Ti and Al-B master alloys, due to its efficiency and Al-5Ti-B, due to its importance and presence in industry, were the inoculants chosen for the DC cast trials. The amount of inoculant was added to get a concentration of 0.25 % of Ti for both cases and balanced boron for the case of Al-Ti and Al-B additions. The practice to add the inoculant is

explained in Chapter 2, Section 2.2. The casting temperature was 790°C for each individual casting.

Figure 4-37 and **Figure 4-38** shows optical images of the Pb particles in the Al matrix, across the top and bottom of the billet, respectively. The solidified structure obtained from the melt without inoculant (a,b) is compared to that of the melt containing Al-5Ti-B (c,d) and Al-Ti and Al-B (e,f). It is clear that Al-Ti and Al-B provides an increased number of particles of smaller size. However, the effect of Al-5Ti-B is the opposite, providing an heterogeneous distribution and size and a smaller number of particles.
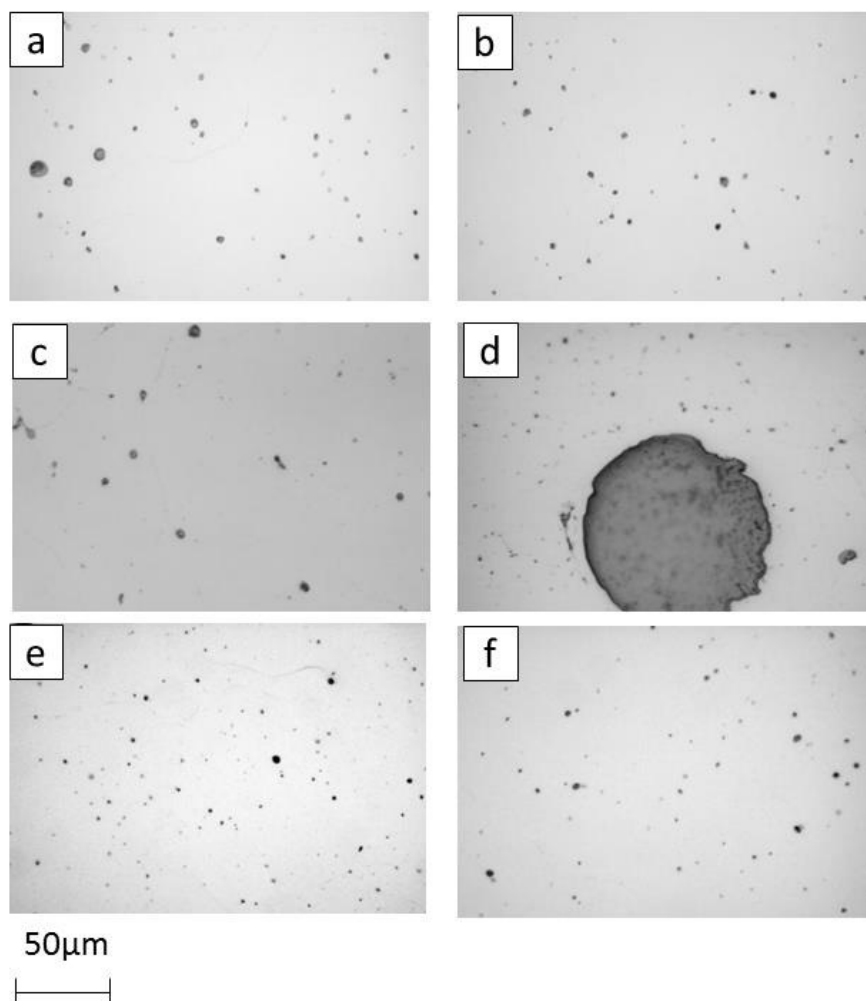
Figure 4-37 Optical micrographs of Al-3Pb DC cast billets, cast at 790°C and 140 mm/min, corresponding to (a, c, e) edge and (b, d, f) centre on top section of the billet: (a,b) without inoculant (c,d) with Al-5Ti-B and (e,f) with Al-Ti and Al-B.
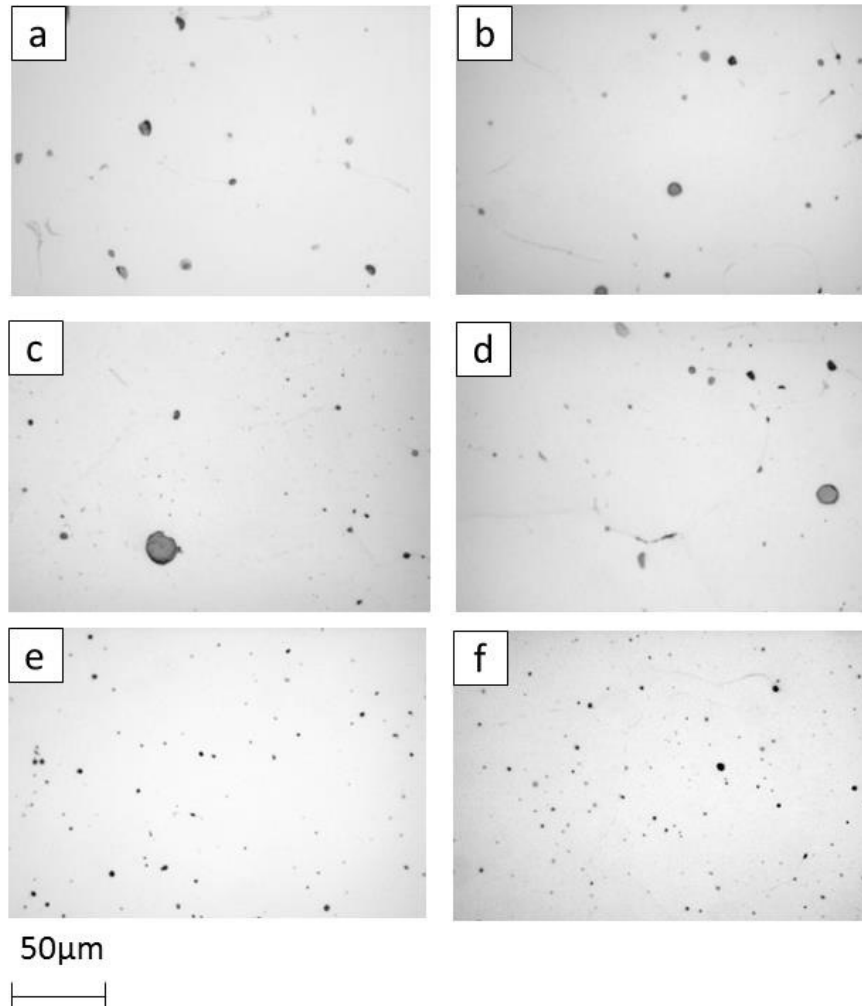
Figure 4-38 Optical micrographs of Al-3Pb DC cast billets, cast at 790°C and 140 mm/min, corresponding to (a, c, e) edge and (b, d, f) centre on the bottom section of the billet: (a,b) without inoculant (c,d) with Al-5Ti-B and (e,f) with Al-Ti and Al-B.

In **Figure 4-39** and **Figure 4-40** quantitative information of average particle size and number of particles, across and along the billet, is displayed. This analysis confirms what is seen on the micrographs. However, Al-5Ti-B does not affect significantly the average Pb particle size and number, and neither improves the size distribution. However, the novel inoculant not only increases the number of particles per unit area around 25% but it also reduces and improves the homogeneity of their size.
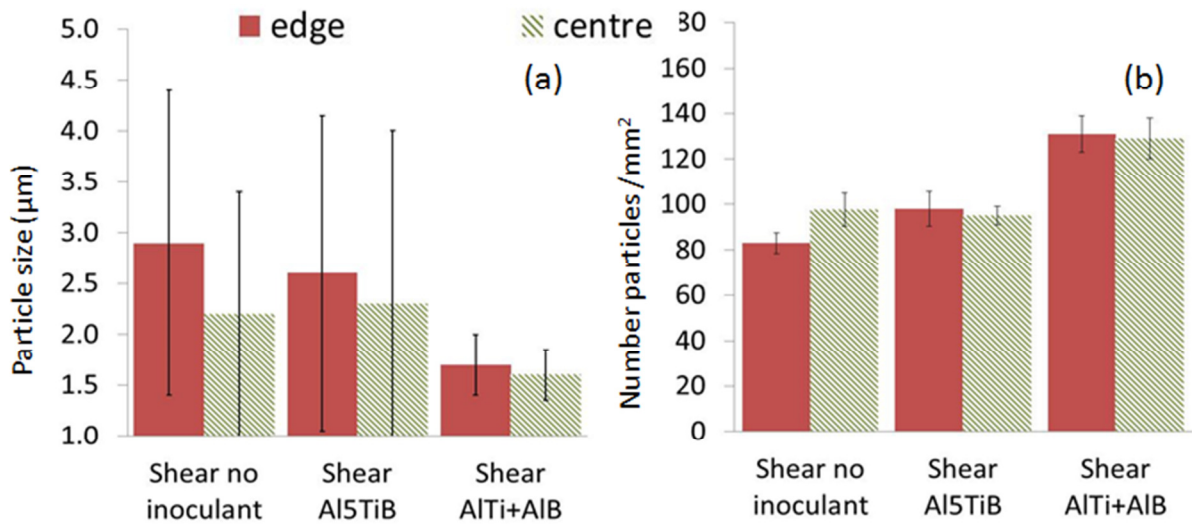
Figure 4-39 Comparison of untreated Al-3Pb alloy melt, and melt sheared and with different inoculant additions (a) Particle size and (b) number of particles from edge to centre of the billet.
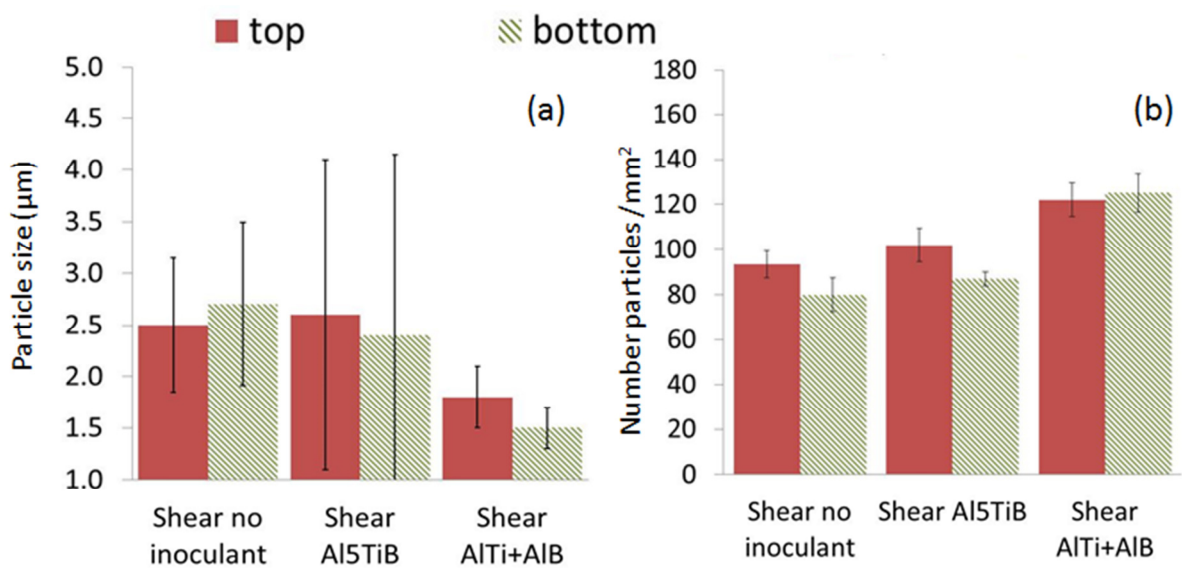
Figure 4-40 Comparison of Al-3Pb DC cast billets with and without inoculant, (a) Particle size and (b) number of particles from top to bottom of the billet.

Table 4-6 confirms not only the effectiveness of the novel inoculant to refine the Pb microstructure within the Al matrix.

Table 4-6 Average number of particles and particle size for Al-3Pb DC cast billet.

	Number particles/mm²	Particle size (µm)
No inoculant	92	2.6
Al5TiB	99	2.4
Al-Ti + Al-B	125	1.6

Figure 4-41 shows the effect of inoculant additions on the Pb content along the cast billet. Without inoculant (a) there is a concentration gradient from top to bottom of the billet, where the Pb content reaches only 1.3 %. Al-5Ti-B additions help to achieve a more homogenous content along the billet, but with values well below the nominal. Severe segregation of Pb towards the central part of the billet is observed in both cases. With the novel inoculant (c) Pb content gets much closer to nominal value and segregation is considerably reduced. The peaks around 300 mm indicate that considerable Pb sedimentation and agglomeration takes place on this particular area of the billet as seen in **Figure 4.12.**
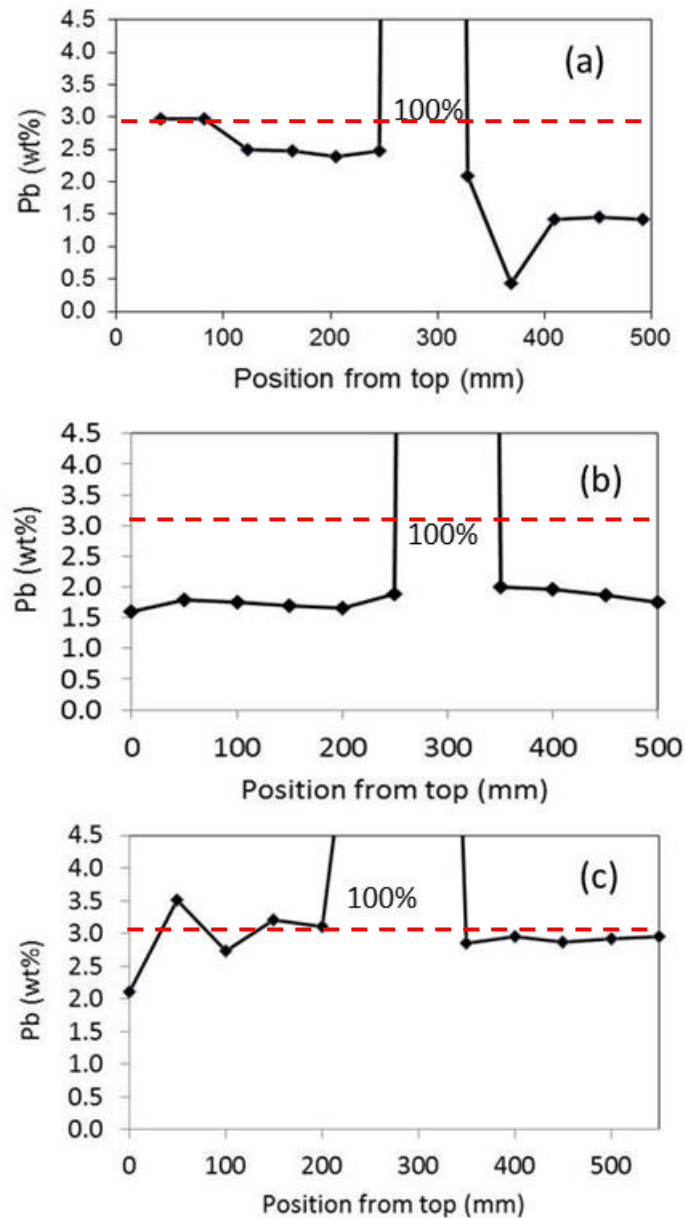
Figure 4-41 Results of the spark analysis, indicating Pb composition in wt% from the top to the bottom of an Al-3Pb billet, for a melt: (a) without inoculant (b) with Al-5Ti-B and (c) with Al-Ti and Al-B.

4.3.1.3 Crucible solidification

Figure 4-42 and **Figure 4-43** comprise SEM back scattered images, of Al-3Pb alloy solidified in a crucible at 1K/min, with synthetic TiB_2 powder additions and Al-Ti Al-B additions, respectively (equivalent to 0.8 % Ti). Comparing both figures it observed that when synthetic TiB_2 is added, all those particles are attached to Pb particles; contrary on the

sample containing TiB_2 obtained from the reaction between Al-Ti and Al-B Pb is found attached only to some of the particles.
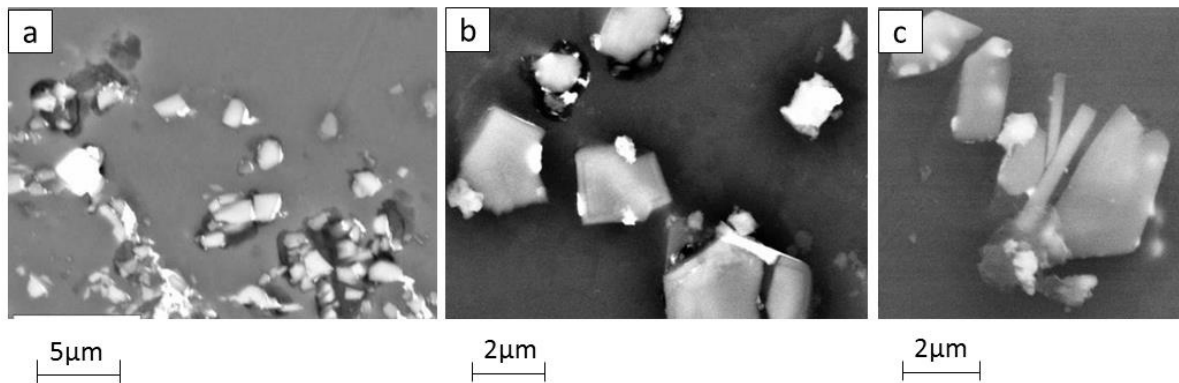
Figure 4-42 SEM images of Al-3Pb alloy solidified in a crucible at 1K/min, containing synthetic TiB_2 particles.
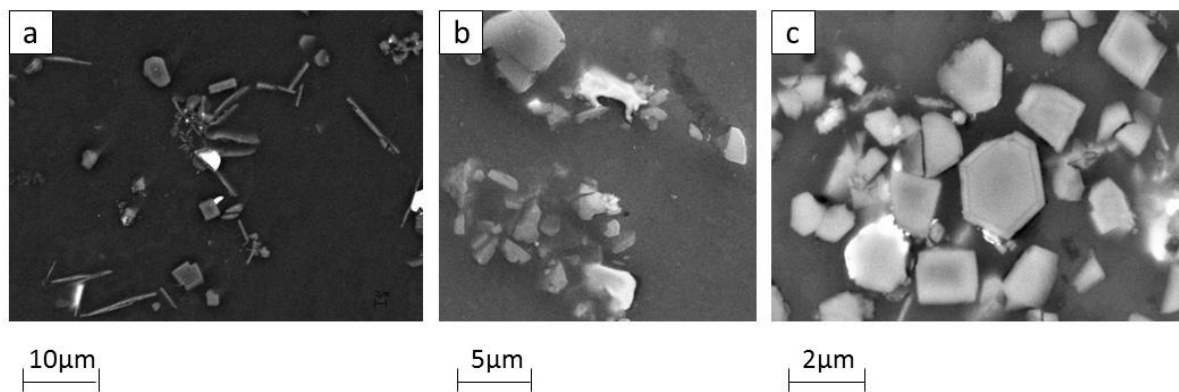
Figure 4-43 SEM images of an Al-3Pb alloy solidified in a crucible at 1 K/min, containing TiB_2 formed from the reaction between Al-Ti and Al-B.

Figure 4-44 Figure 4-45 Figure 4-46 comprise TEM bright field images of the sediment TiB_2 particles obtained from the reaction of Al-Ti and Al-B master alloys. The figures also contain high resolution (HR) images of the particle and a bi-layer on their interface with Al, viewed in the [11-20] TiB_2 and [0-11] Al direction, and the diffraction pattern, where also the d spacing is calculated. The TiB_2 particles collected are faceted, hexagonal with sharp interfaces. No other particles were found in the specimen (see Chapter 9).
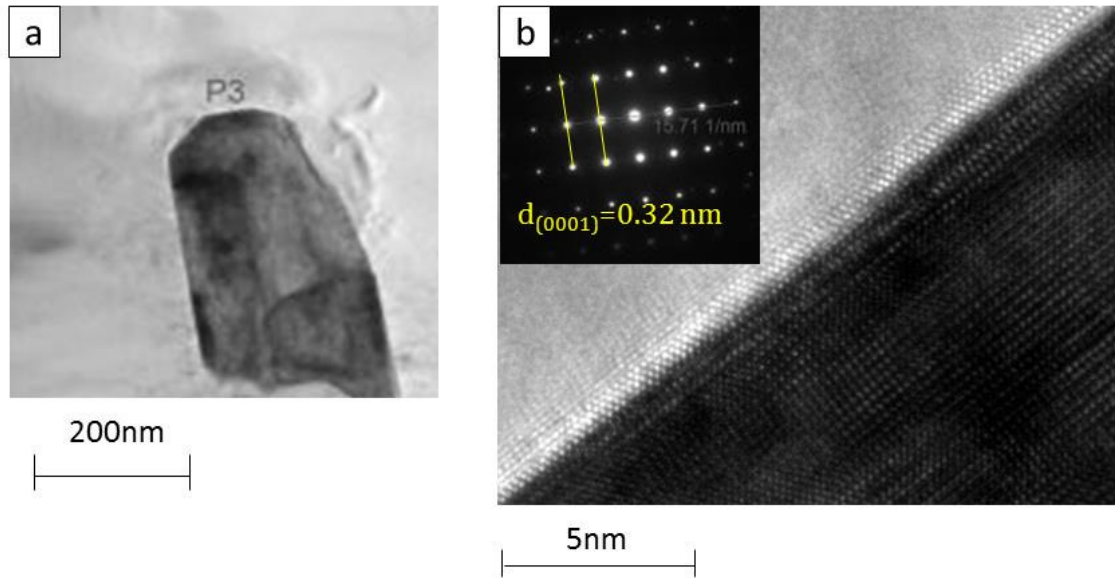
Figure 4-44 TEM images of Al-3Pb solidified in a crucible at 1 K/min, containing TiB₂ particles obtained from the reaction of Al-Ti and Al-B master alloy: (a) lower magnification showing the TiB₂ particles created in situ (b) higher magnification of the particle showing (0001) plane and the diffraction pattern.

Figure 4-45 shows the interface between TiB_2 and Al viewed from the [11-20] TiB_2 and [0-11] Al direction, the atoms on the interface seem to have a different d spacing with respect to the TiB_2 particles. The values of the d spacing for the monolayer were calculated after TEM examination just by comparing the distances obtained for TiB_2, so these results are not reliable. There seem to be a miss-orientation angle on the atoms of the interface in comparison with the orientation of the atoms on the TiB_2 particles.
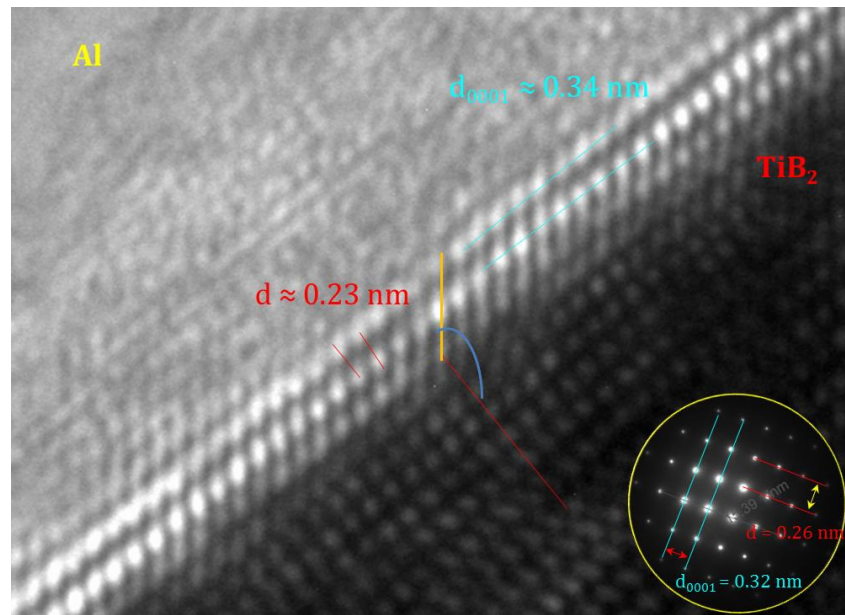
Figure 4-45 HRTEM images of Al-3Pb sample solidified in a crucible at 1K/min, containing TiB₂, obtained from the reaction of Al-Ti and Al-B master alloy: showing the interface between (0001) TiB₂ plane and Al, and the diffraction pattern of TiB₂ with the calculated d spacing.

The interface between the inoculant particles and α-Al is also displayed using HRTEM in **Figure 4-46**. Contrary to previous image, d spacing and orientation of the interface atoms is the same as that of TiB₂ particles. However the difference in contrast between interface and particle is obvious.
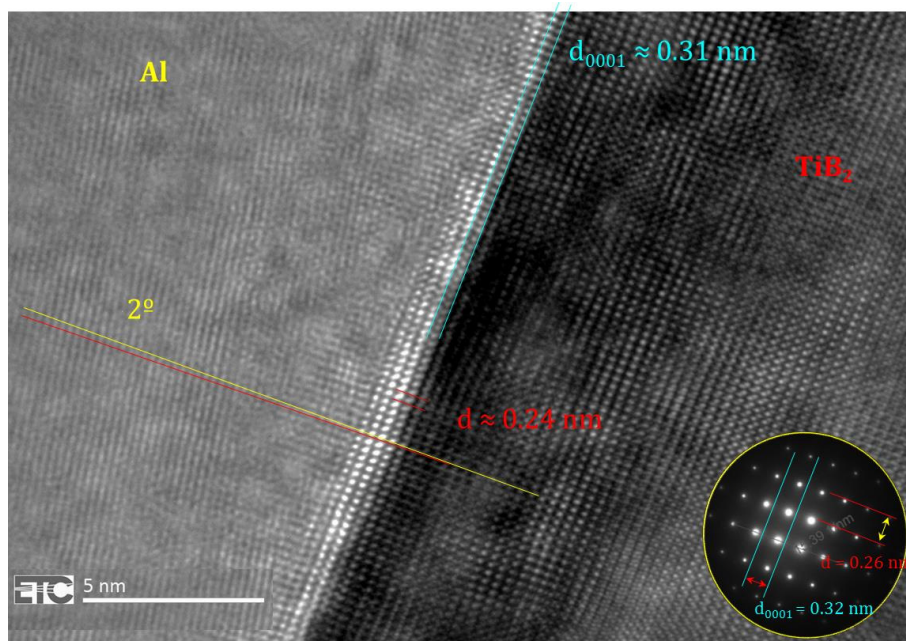
Figure 4-46 HRTEM images of Al-3Pb solidified in a crucible at 1K/min, containing TiB$_2$, obtained from the reaction of Al-Ti and Al-B master alloy: showing (0001) plane of TiB$_2$, the diffraction patter of the particle and intermediate layer between particle and matrix.

4.3.2 Exact Monotectic binary alloy Al-1.2Pb

4.3.2.1 Synchrotron experiments

The microstructural evolution of Pb and its distribution during heating and solidification was studied for both, inoculant free and Al-Ti and Al-B containing samples. Images taken from the live recording of the solidification on the synchrotron were treated with imagej and are presented here. Quantitative information, of particle size evolution during solidification and particle size on the final solidified microstructures, is provided. The amount of inoculant added to the samples was the necessary to get a concentration of 0.1 % of Ti and balanced B for stoichiometric TiB$_2$.

Figure 4-47 comprises imagej treated images of the initial microstructure of both samples (with and without inoculant) before the experiments were initiated. It is clearly seen that Pb particles are coarser for the sample without inoculant additions, and that those particles are always of spherical shapes. On the contrary, on the sample with Al-Ti and Al-B additions, not only the Pb particles are smaller but also present elongated shapes.

132
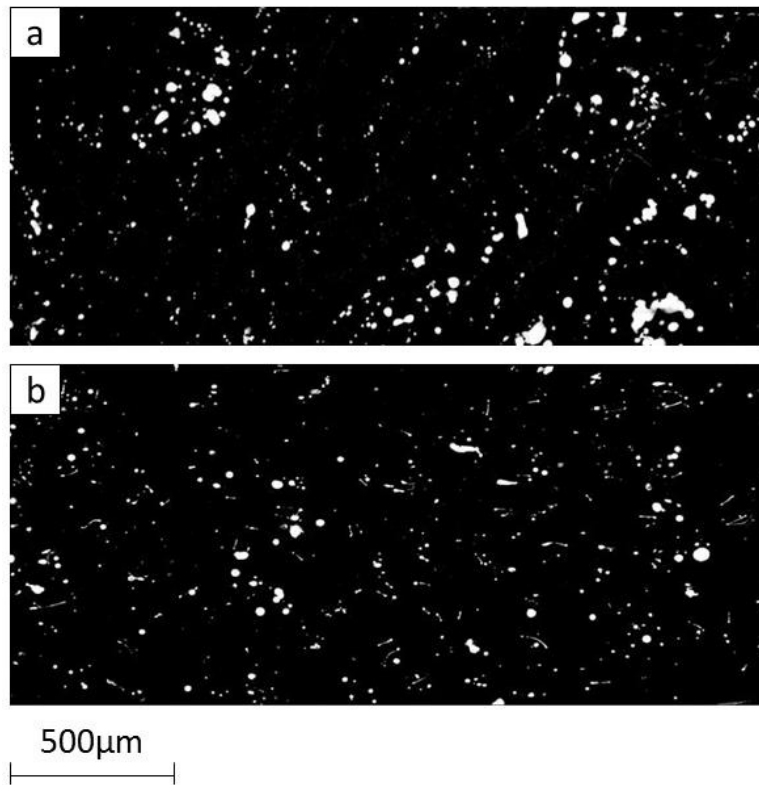
Figure 4-47 Imagej treated synchrotron images, corresponding to the starting microstructure of Al-1.2Pb alloy used in the experiments: (a) sample without inoculant (b) sample with Al-Ti and Al-B additions.

Figure 4-48 shows the microstructure at the end of solidification for both samples, after being heated to 720°C and cool down and solidified at a rate of 2 °C/sec. Contrary to what was observed on **Figure 4-47** the Pb particles are coarser on the sample with inoculant additions and no elongated shapes are observed. As the bottom of the sample is not under the field of view during the life recorded experiments; therefore to be able to understand how much sedimentation was taking place, an SEM post-mortem examination of the samples was required (see **Figure 4-49).** The comparison of the images suggests that much more sedimentation was taking place on the sample without inoculant additions (a). Therefore, the Pb content in the experimental field of view is lower and the particle size consequently smaller.
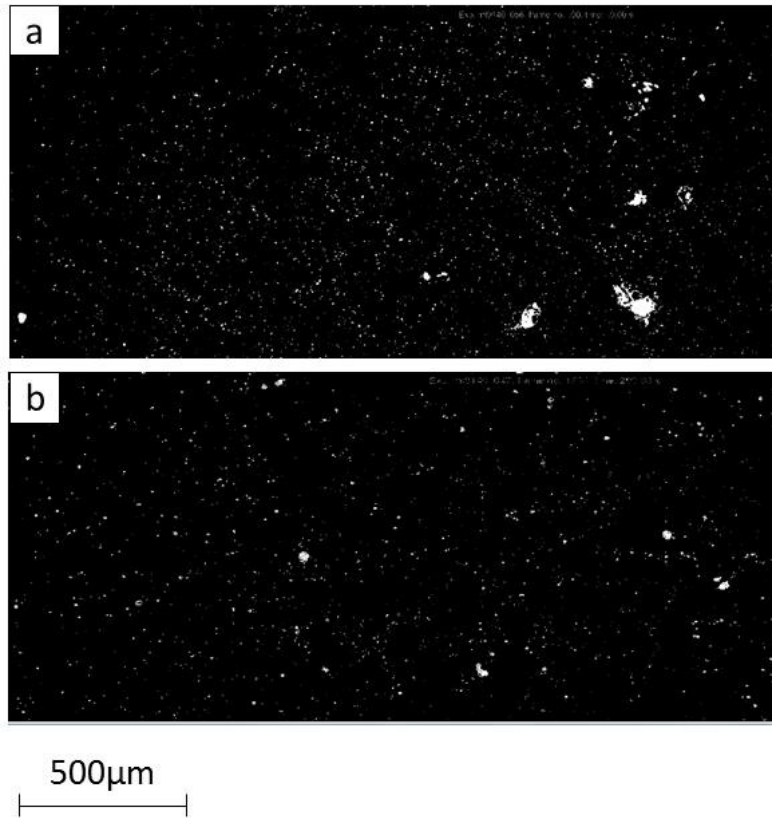
Figure 4-48 Imagej treated synchrotron images, corresponding to the final microstructure solidified at 2 °C/sec after being heated to 720°C: (a) sample without inoculant (b) sample containing Al-Ti and Al-B.
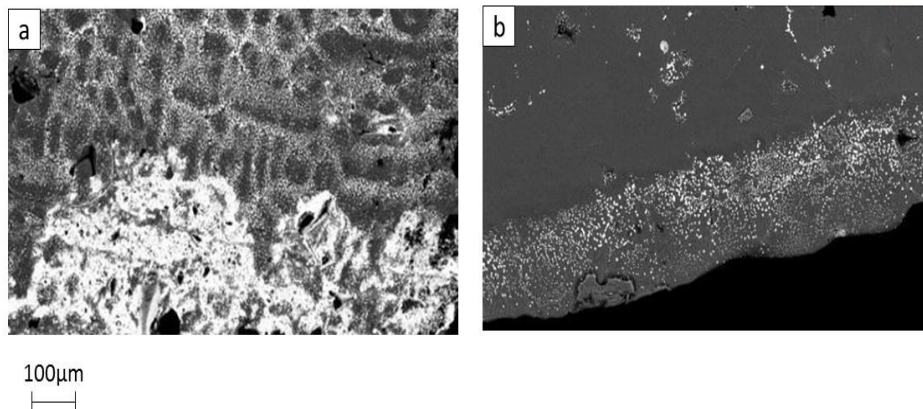
Figure 4-49 Post-mortem SEM images of the samples used in the synchrotron, corresponding to: a) sample without inoculant (b) sample containing Al-Ti and Al-B.

4.3.2.2 Effect of inoculant additions on the DC cast microstructure

The inoculant made from Al-Ti and Al-B master alloys and Al-5Ti-B were the inoculants chosen for the DC cast trials. The inoculant was added to get a concentration of 0.1 % Ti and balanced B for the Al-Ti and Al-B additions. The exact procedure employed for the inoculant additions in described in Chapter 9. The casting temperature was 740°C.

Optical images of the Pb particles on the Al matrix, are shown across the top (**Figure 4-50**) and bottom **(Figure 4-51**) of the billet. The solidified structure obtained from the melt without inoculant (a,b) is compared to that of the melt containing Al-5Ti-B (c,d) and Al-Ti and Al-B (e,f). It is clear that Al-Ti and Al-B provides an increased number of particles of smaller size. However, the effect of Al-5Ti-B is the opposite, providing an heterogeneous distribution and size and a smaller number of particles.
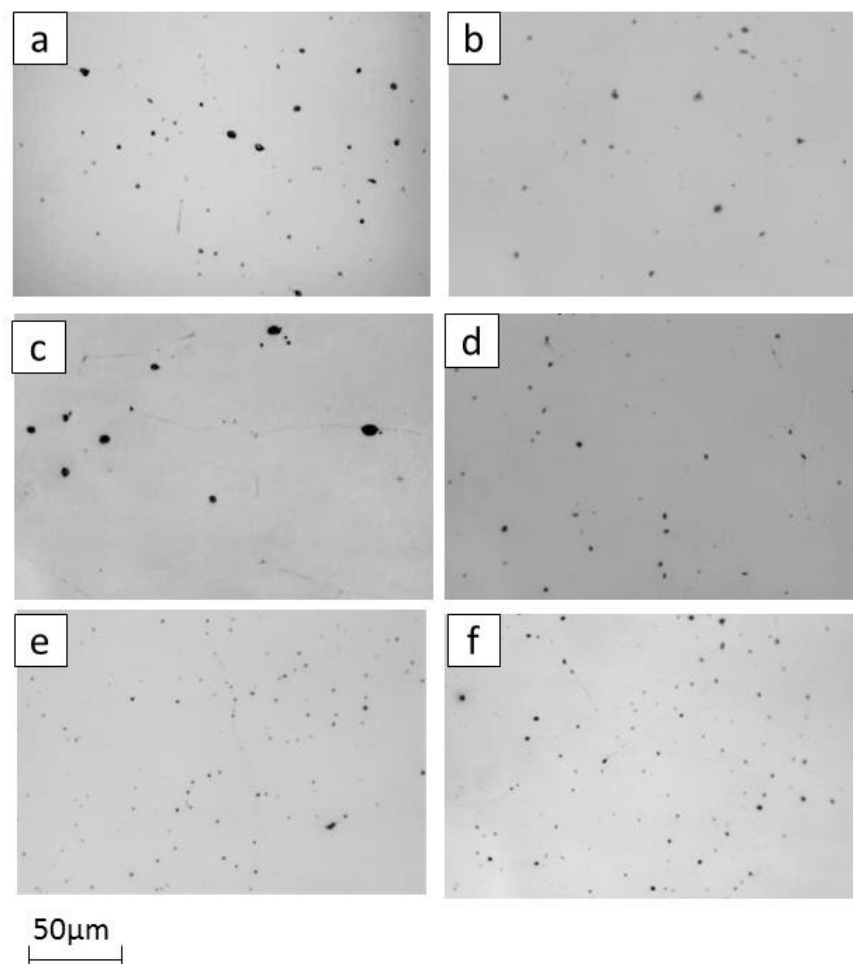
Figure 4-50 Optical micrographs of Al-1.2Pb DC cast billets, cast at 740°C and 140 mm/min, corresponding (a, c, e) to edge and (b, d, f) centre on the top of the billet: (a,b) without inoculant (c,d) with Al-5Ti-B and (e,f) with Al-Ti Al-B.
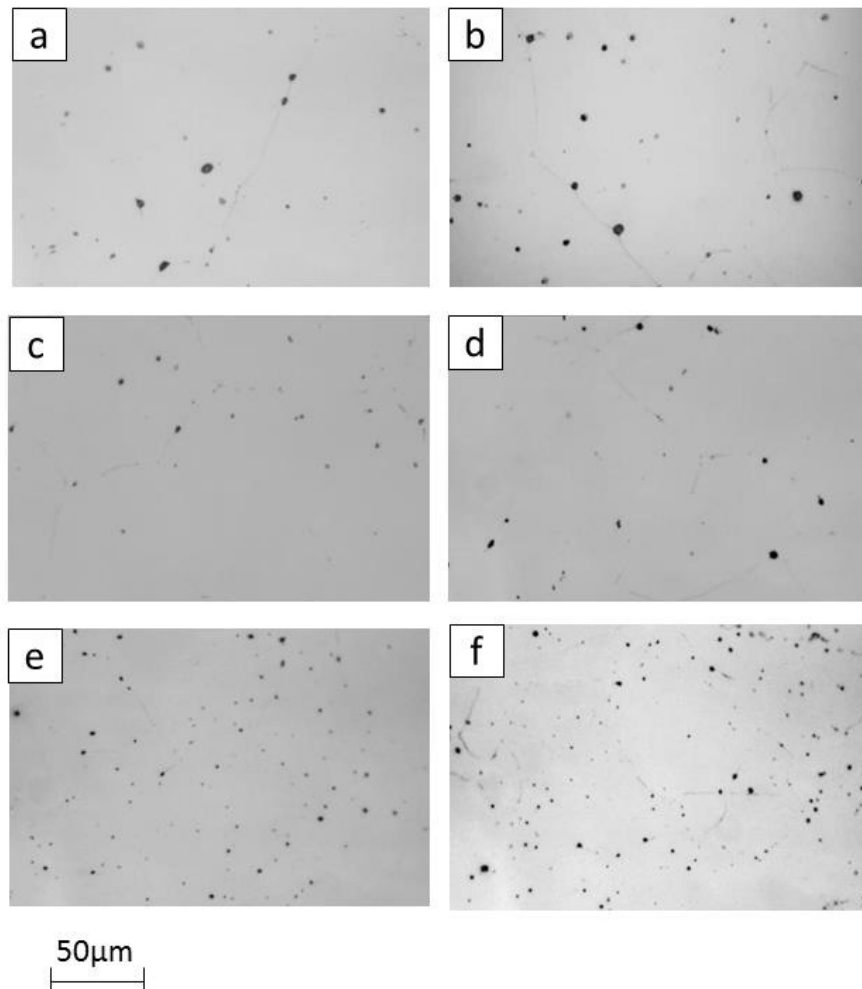
Figure 4-51 Optical micrographs of Al-1.2Pb DC cast billets, cast at 740°C and 140 mm/min, corresponding to (a, c, e) edge and (b, d, f) centre on the bottom of the billet: (a,b) without inoculant (c,d) containing Al-5Ti-B and (e,f) containing Al-Ti Al-B.

Figure 4-52 and **Figure 4-53** provide quantitative information on average particle size and number of particles across and along the billet, respectively. This analysis confirms what is seen on the micrographs, Al-Ti Al-B additions help to produce a homogeneous and fine distribution of Pb in the Al matrix. However, Al-5Ti-B has a small negative effect, decreasing the amount of particles per unit area.

Contrary to the case of hyper-monotectic alloys (see **Figure 4-37 Figure 4-38 Figure 4-39 Figure 4-40**), for alloys of the exact monotectic composition the particle size distribution in the absence of inoculant is more homogenous (smaller standard deviation) and the effect of inoculant additions is less evident.
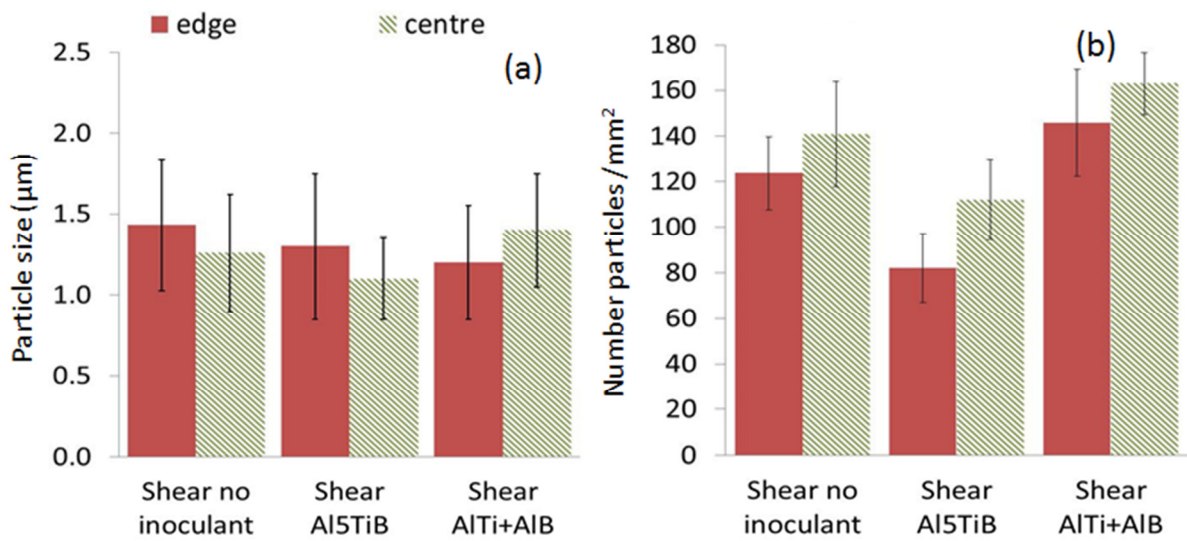
Figure 4-52 Comparison of untreated Al-1.2Pb billet with different inoculant additions (a) Particle size and (b) number of particles from edge to centre of the billet.
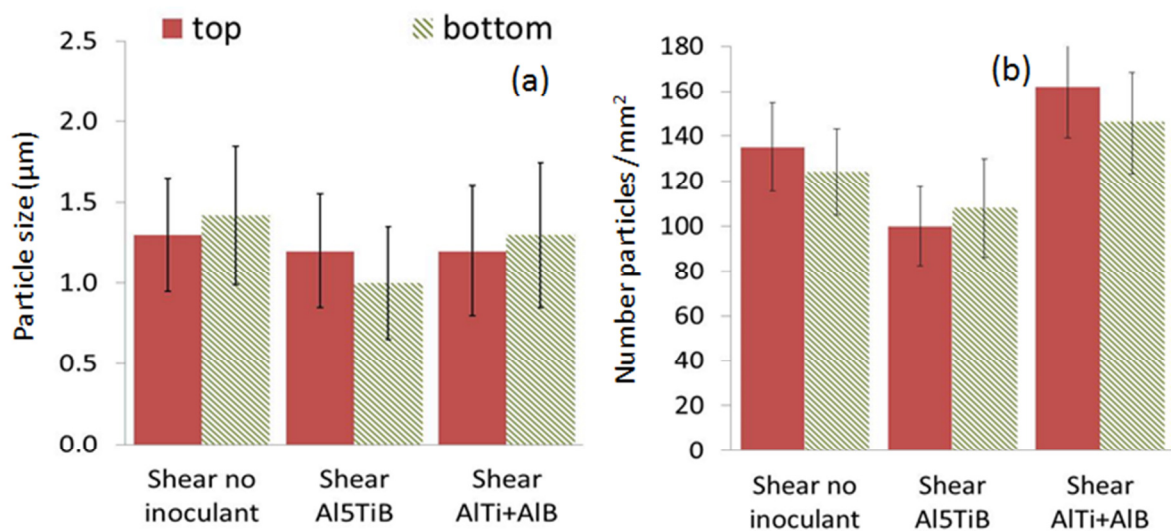
Figure 4-53 Comparison of Al-1.2Pb billet with different inoculant additions (a) Particle size and (b) number of particles from edge to centre of the billet.

Table 4-7 comprises quantitative information of particle size and number of particles for the three castings. Confirming previous results, the number of particles increases considerably

in the presence of Al-Ti and Al-B and decreases when Al-5Ti-B is added to the melt. Furthermore, particle size is not significantly affected by inoculant additions.

Table 4-7 Average number of particles and particle size for Al-1.2Pb DC cast billet.

	Number particles/mm^2	Particle size (µm)
No inoculant	130	1.3
Al5TiB	100	1.2
Al-Ti + Al-B	155	1.2

4.3.4 2011 alloy

For all the billets described in this section, the melt with and without inoculant was heated to 860°C, hold for 1 h before being cool to the casting temperature of 720°C, cast at 140 mm/min and sheared at 6000 rpm. Inoculant was added to obtain a concentration of 0.01 % of Ti and balanced amount of B for stoichiometric TiB$_2$.

Figure 4-54 and **Figure 4-55** show the microstructure of the cast across and along the billet, respectively. Billets cast in the same conditions but without (a,b) and with the novel inoculant (c,d). The images do not show a significant different in particle size and distribution under the effect of the novel inoculant. However, quantitative information of particle size and number, across and along the billet, provided in **Figure 4-56 Figure 4-57** suggest that the novel inoculant has an effect on the particle size and distribution.
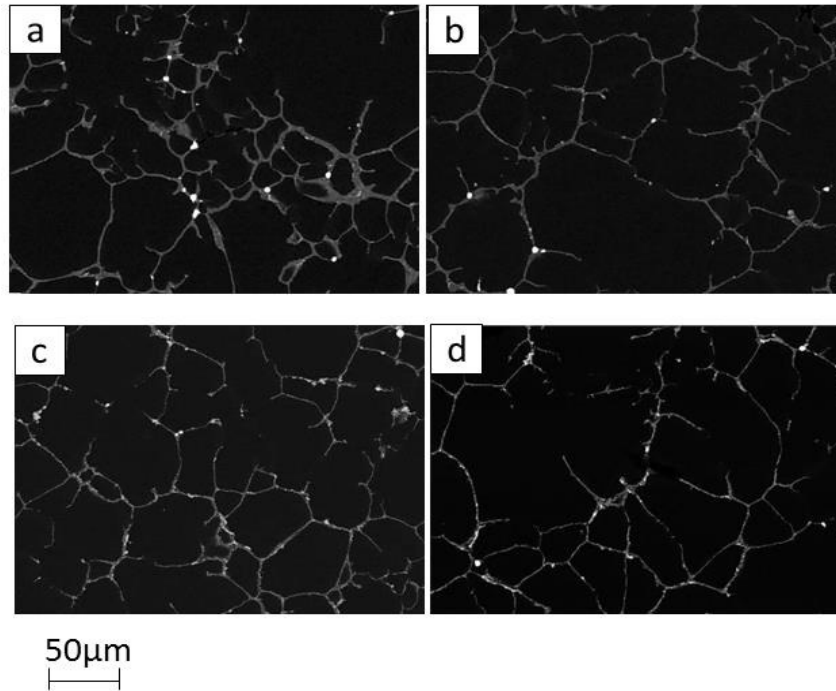
Figure 4-54 Back scattered SEM image of 2011 DC cast billets heated to 860°C, cast at 740°C and 140 mm/min, and sheared at 6000 rpm corresponding to (a, c) edge and (b, d) centre from the bottom of the billet: (a,b) without inoculant (c,d) with Al-Ti and Al-B.
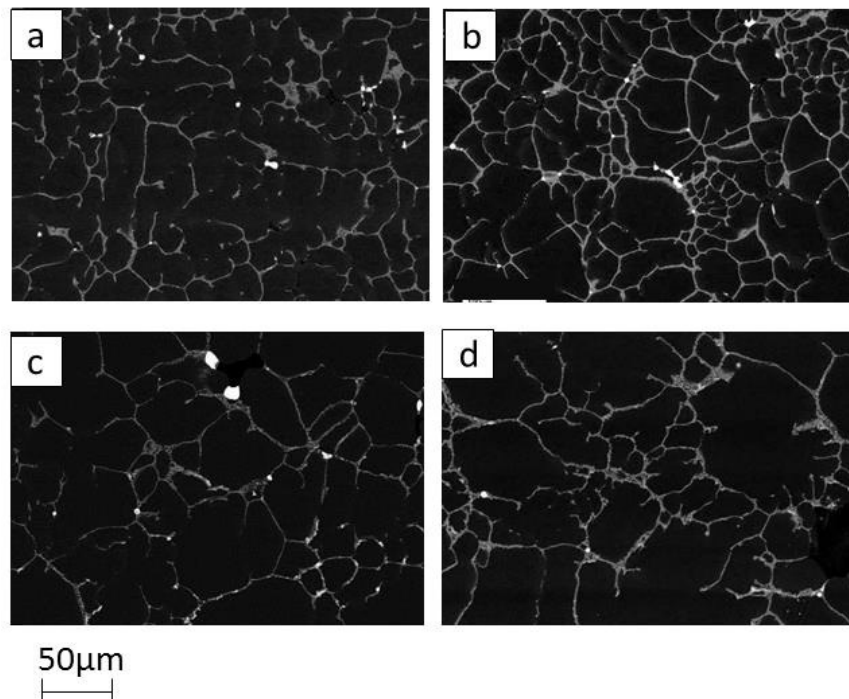
Figure 4-55 Back scattered SEM image of 2011 DC cast billet heated to 860°C, cast at 740°C and 140 mm/min, and sheared at 6000 rpm corresponding to (a, c) edge and (b, d) centre from the bottom of the billet: (a,b) without inoculant (c,d) with Al-Ti and Al-B.

Figure 4-56 shows that the addition of Al-Ti and Al-B can led to an increase in the number of Pb particles and reduce the segregation of particles towards the centre of the billet, resulting in a homogeneous number of particles from edge to centre. Particle size varies considerably across and along the billet, as indicated by the big standard deviation. **Figure 4-57** shows the reduction in particle size and increase in number of particles, in the presence of the novel refiner, from top to bottom of the cast billet.
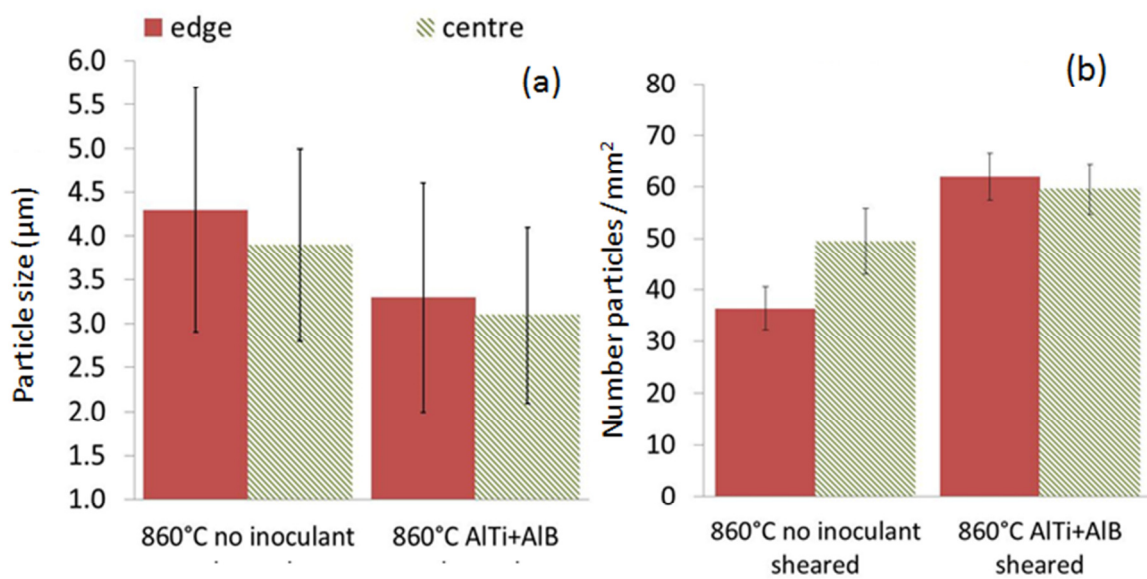
Figure 4-56 Comparison of DC cast 2011 alloys heated to 860°C and sheared at 6000 rpm, without and with inoculant additions: (a) Particle size and (b) number of particles from edge to centre of the billet.
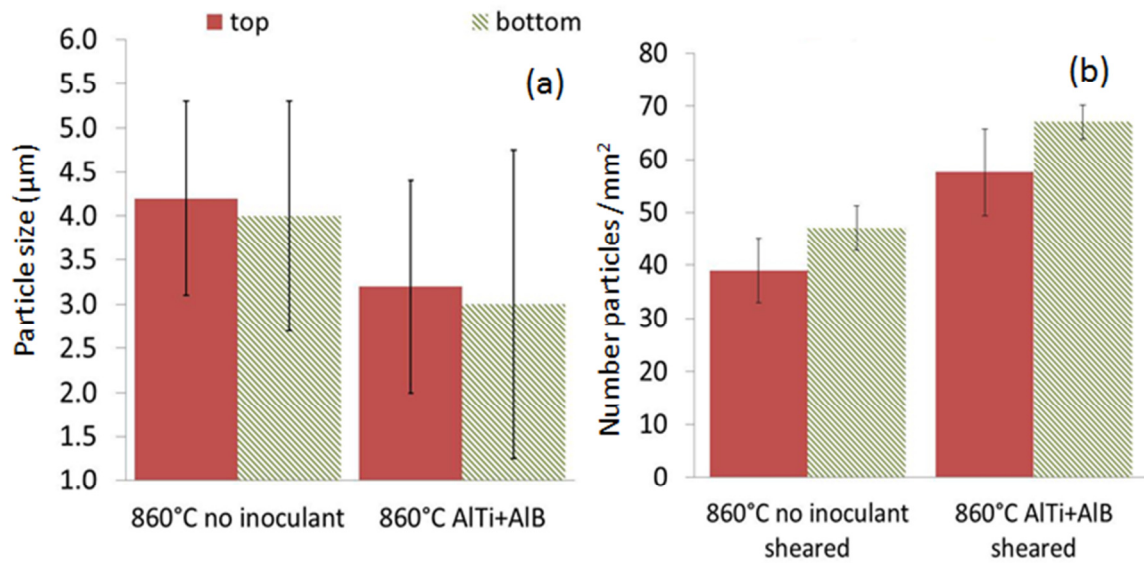
Figure 4-57 Comparison of DC cast 2011 alloys heated to 860°C and sheared at 6000 rpm, without and with inoculant additions: (a) Particle size and (b) number of particles from top to bottom of the billet.

The effect of inoculant on 2011 DC cast billets is summarised in **Table 4-8** and **Figure 4-58**. From **Table 4-8** an average particle size reduction from 4.1 to 3.2 µm an increase in the number of particles from to 60 per unit area, can be observed when Al-Ti and Al-B are present in the melt. **Figure 4-58** shows the effect of the novel inoculant on the particle size distribution for DC cast 2011 billets. The amount of particles between 1 and 3 µm increases, reducing the number of bigger particles.

Table 4-8 Average number of particles and particle size for 2011 DC cast billet.

Cast	Number particles/mm^2	Particle size (µm)
No inoculant	43	4.1
Al-Ti + Al-B	60	3.2
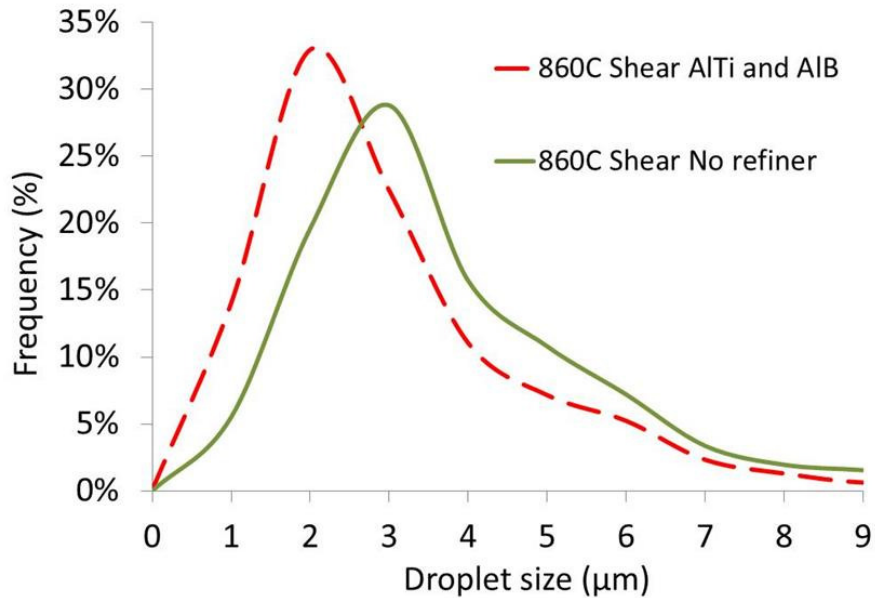
Figure 4-58 Effect of the shearing on particle size distribution for the 2011 DC cast billets without and with Al-Ti and Al-B.

Figure 4-59 and **Figure 4-60** comprise optical images of etched cast structure to reveal the grain morphologies and sizes, across the top and bottom of the billet. The grain morphology of the billets cast without inoculant additions (a,b) are compared to the ones containing the novel inoculant (c,d). Both billets have been produced under the same shearing and superheating conditions. Therefore, as expected, grain sizes and morphologies are equal (rosette) in the centre of the billet. However, small differences are observed on the top edge, comparing images (a) and (c), where the billet without inoculant presents a more dendritic grain morphology.
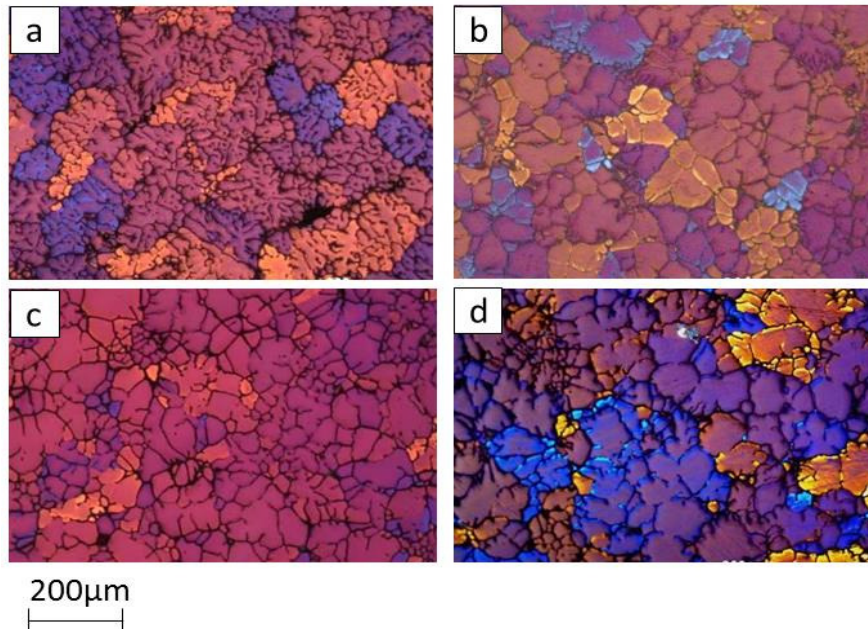
Figure 4-59 Optical images obtained under polarised light, showing the grains of the 2011 DC cast billets corresponding to (a, c) edge and (b, d) centre from the top of the billet: (a,b) without and (c,d) with Al-Ti and Al-B.
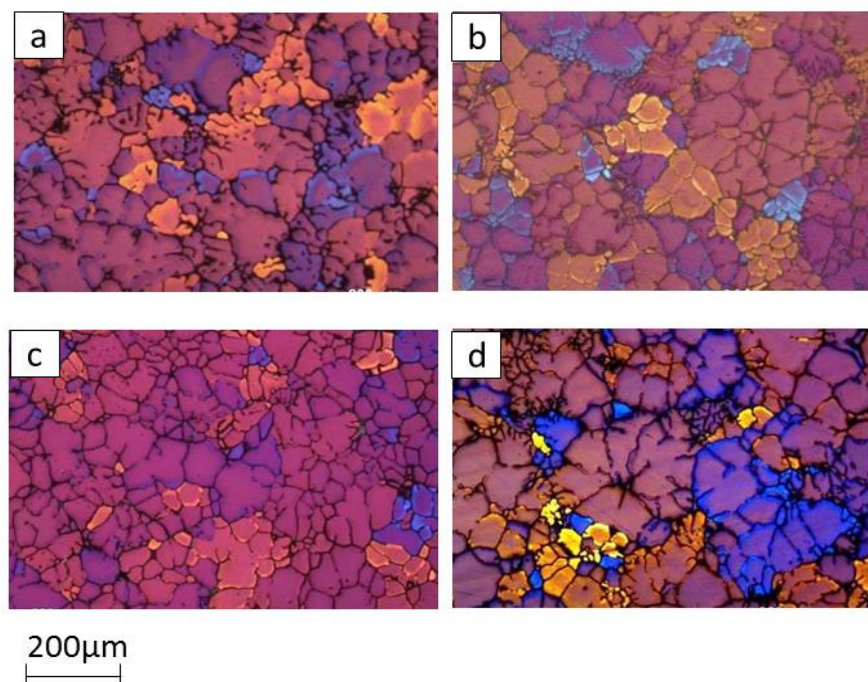
Figure 4-60 Optical images obtained under polarised light, showing the grains of the 2011 DC cast billets corresponding to (a, c) edge and (b, d) centre from the bottom of the billet: (a,b) without and (c,d) with Al-Ti and Al-B.

4.4 Effect of superheat on the cast structure of immiscible systems

Al the billets described in this chapter were cast at 720°C and 140 mm/min and shearing was performed at 6000 rpm. The novel inoculant, created from Al-Ti and Al-B master alloys, was added to the melt. Two different heating and soaking temperatures were chosen before casting, these temperatures will be mentioned individually for each alloy. The casts were repeated 3 times to ensure reproducibility.

4.4.1 Hyper-monotectic binary alloys

The amount of inoculant added was to get a composition of 0.4 % Ti and balanced boron for stoichiometric TiB_2. The casting temperature was 790°C for each individual casting. Similarly all the billets are sheared during DC casting at 6000 rpm.

Figure 4-61 and **Figure 4-62** shows optical images of the Pb particles on the Al matrix across the top (**Figure 4-61**) and bottom (**Figure 4-62**) of the same billet. Both images show that, for the same amount and type of inoculant added, the number of particles increases for the melt superheated to 860°C.
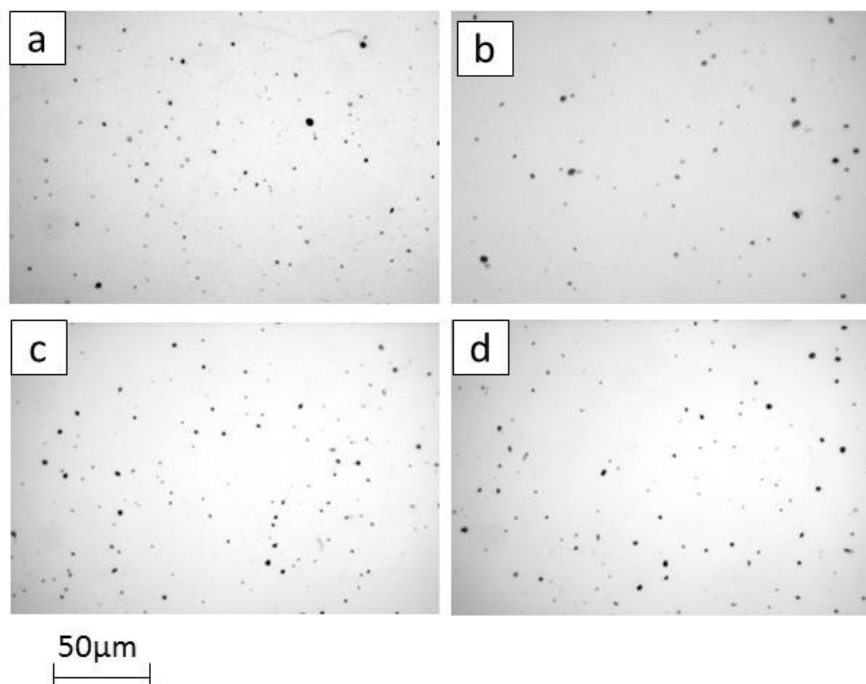
Figure 4-61 Optical micrographs of the Al-3Pb DC cast billets, cast at 790°C and 140 mm/min, sheared at 6000 rpm, corresponding to (a, c) edge and (b, d) centre on the top of the billet: (a,b) melt heated to 800°C and (c, d) melt heated to 860°C.
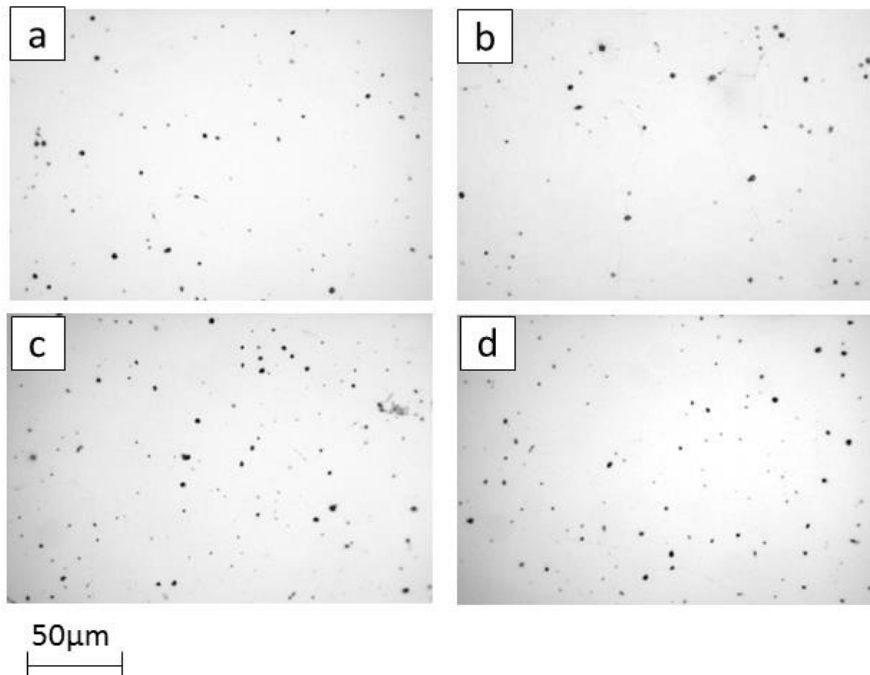
Figure 4-62 Optical micrographs of the Al-3Pb DC cast billets, cast at 790°C and 140 mm/min, sheared at 6000 rpm, corresponding to (a, c) edge and (b, d) centre on the bottom of the billet: (a,b) melt heated to 800˚C and (c, d) melt heated to 860˚C.

Figure 4-63 and **Figure 4-64** display the quantitative analysis with average particle size and number of particles across and along the billet, respectively. This analysis confirm that superheat increases the number of particles from edge to centre on the top and bottom of the billet but it does not seem to affect particle size for hyper-monotectic DC cast alloys (see **Figure 4-65** for more information).
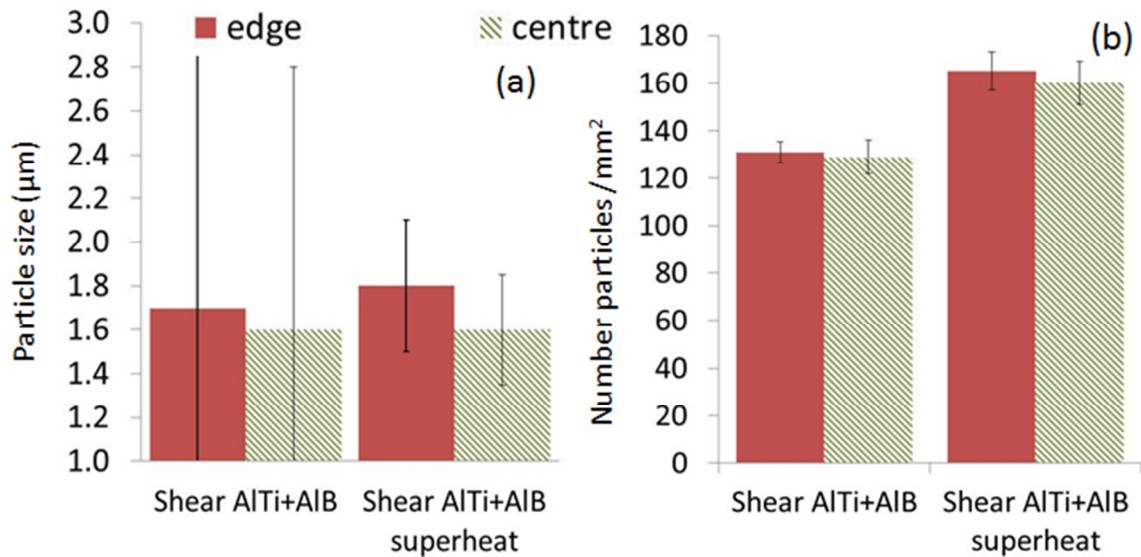
Figure 4-63 Comparison of Al3-Pb DC cast billets heated to 800˚C, and the billet heated to 860˚C: (a) Particle size and (b) number of particles from edge to centre of the billet.
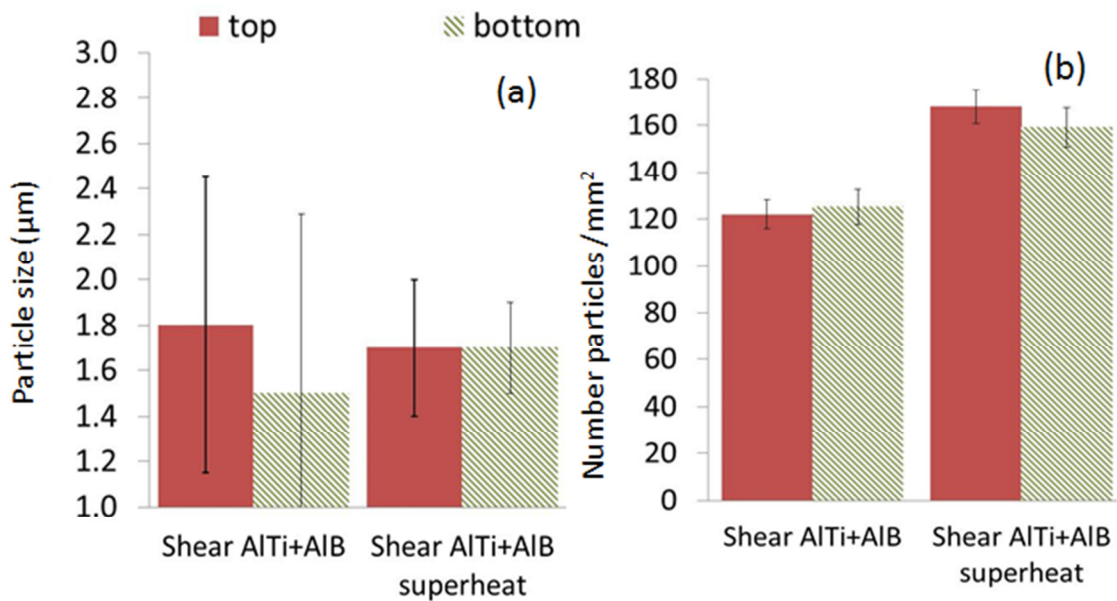
Figure 4-64 Comparison of Al3-Pb DC cast billets heated to 800˚C, and the billet heated to 860˚C: (a) Particle size and (b) number of particles from top to bottom of the billet.

A summary of the average particle size and number of particles is seen on **Table 4-9**. The average particle size keeps a value of 1.6 m for both casts, but the number of particles increases 125 to 158 per unit area, with melt superheat, representing approximately a 21% increase in the number of particles.

Table 4-9 Average number of particles and particle size for Al-3Pb DC cast billet.

	Number particles/mm^2	Particle size (μm)
Al-Ti + Al-B	125	1.6
Al-Ti + Al-B, 860°C superheat	166	1.6

Figure 4-65 shows the effect of superheat on the composition of the alloy along the cast billet. Although the superheat does not provide a completely uniform Pb content along the billet (from 2.5 on the top to 3 % on the bottom), it eliminates the segregation towards the centre of the billet. It is known that the Pb particle size is directly dependent on Pb concentration. The concentration along the billet without superheating treatment is lower than that of the superheated billet, therefore average particle size should be also smaller.
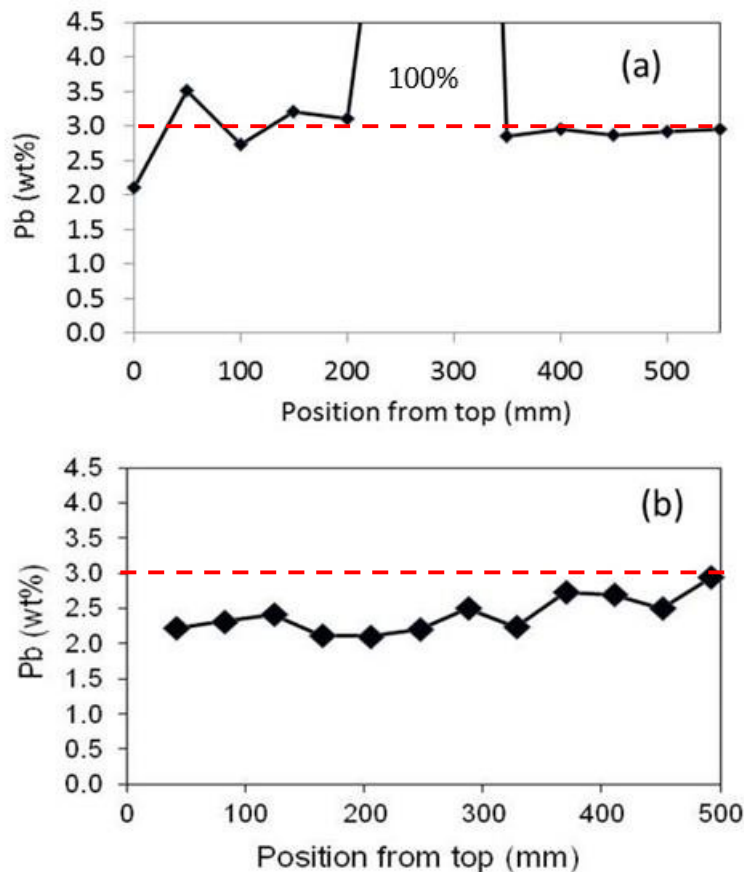
Figure 4-65 Results of the spark analysis, indicating Pb composition in wt% from the top to the bottom of an Al3-Pb DC cast billet, for a melt: (a) containing Al-Ti and Al-B master alloy and (b) containing Al-Ti and Al-B, superheated to 860˚C, before casting.

4.4.2   Monotectic binary alloys

4.4.2.1   Synchrotron experiments

The synchrotron experiments, which were introduced in **Chapter 3 Section 3-6**, will be analysed in more detail considering the effect of superheat for both the alloy without and the alloy with the novel inoculant (obtained from in situ reaction between Ti and B contained in Al-Ti and Al-B master alloys). All the images shown in this chapter are cleaned and treated with imagej. The Pb particles are shown in white and the Al matrix in black, for similitude to back scattered images.

Figure 4-66 shows the imagej treated micrographs of the melt solidified at 2°C/sec, for a sample without (a) and a sample containing the novel inoculant (b), after both being heated to 830°C, which is the maximum permitted by the furnace used in the experiments. It is clear that for the same superheat a more refine and homogenous Pb distribution is obtained for the sample containing the inoculant. **Figure 4-67** shows a quantitative analysis of particle size distribution at the end of solidification **4-67 (a)** and particle size evolution from the beginning to the end of the solidification process **4-67 (b)**, for both samples. As seen in **4-67 (a)** the combination of inoculant and superheat increases the amount of particles smaller than 5 µm, decreasing therefore the number of bigger particles. Figure **4-67 (b)** demonstrates that for the same superheating the final average particle size is reduced from 4.7 to 4.2 µm, for the sample containing the novel inoculant. The combination of inoculant and superheat not only provides a smaller particle size on the final solidified microstructure but it reduces significantly the initial size of the nucleating particles.
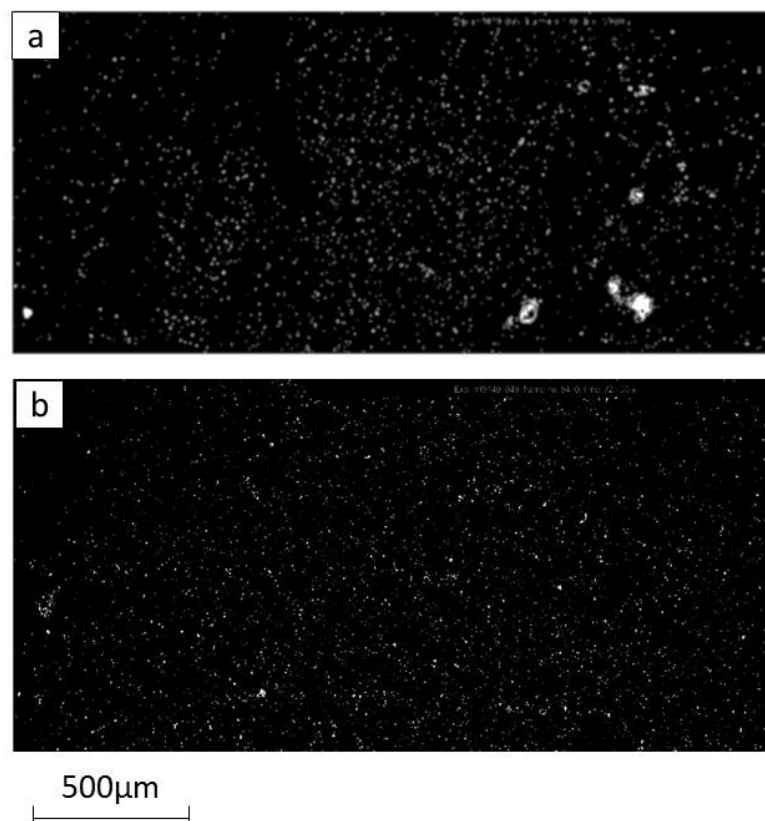
Figure 4-66 Treated synchrotron images, corresponding to the final solidified microstructure after heating Al-1.2Pb samples to 830°C, and cooled down at a rate of 2 °C/sec: (a) without inoculant (b) with novel inoculant.
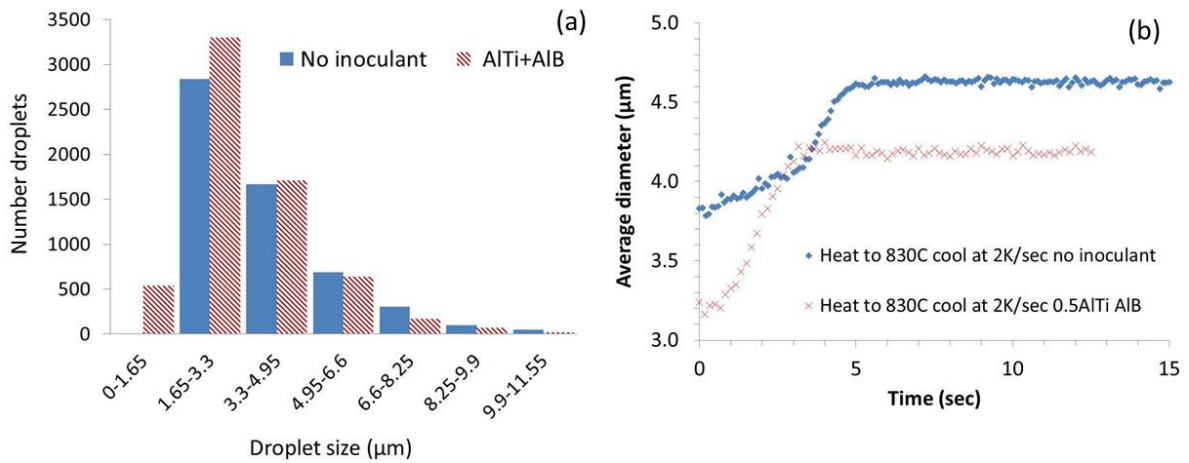
Figure 4-67 Comparison of the sample without and the sample containing the novel inoculant: a) Particle size distribution and b)particle size evolution during the solidification, for Al-1.2Pb samples heated to 830°C, solidified at 2 °C/sec.

Figure 4-68 and **Figure 4-69** show the effect of superheat on the sample without inoculant, and **Figure 4-70** and **Figure 4-71** the effect of superheat on the sample containing the novel inoculant. For that purpose both alloys have been heated to 720°C and 830°C before being solidified at 2°C/sec.

Figure 4-68 shows the solidified microstructure for the Al-1.2Pb alloy heated to 720°C (a) and 830°C (b). Pb particles are smaller for the superheated alloy. A quantitative analysis of particle size distribution at the end of solidification (a) and particle size evolution from the beginning to the end of the solidification process (b) is presented in **Figure 4-69**. Superheating to 830°C, increases the number of particles between 1.5 to 3.3 µm. And as seen on figure **4-69 (b)** reduces not only the final particle size on the solidified microstructure (from 4.6 to 4.85 µm) but the initial size of the nucleated particles; keeping therefore the particle growth rate constant.
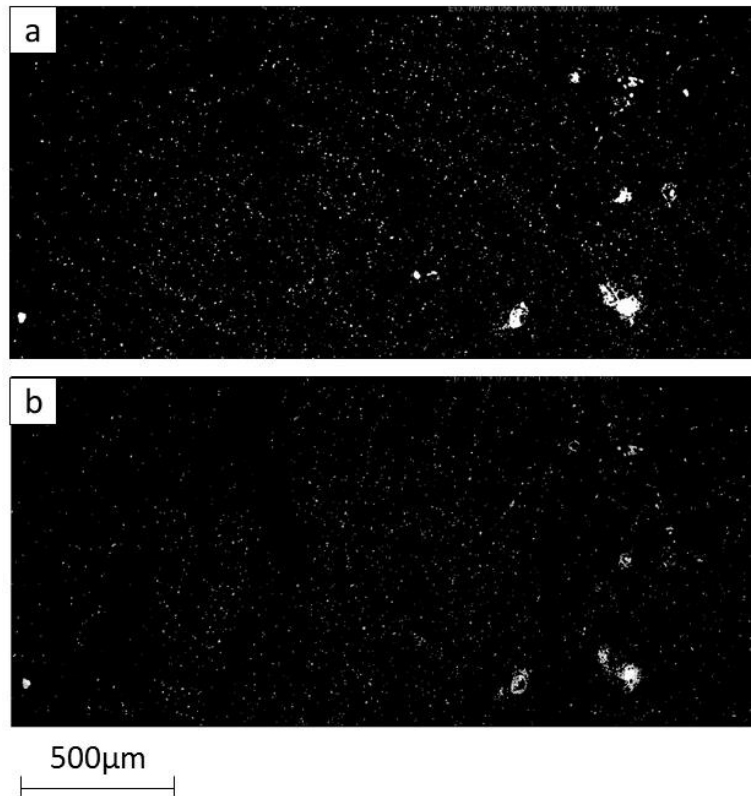
Figure 4-68 Treated synchrotron images, corresponding to Al-1.2Pb samples heated to: (a) 720°C (b) 830°C and solidified at 2 °C/sec.
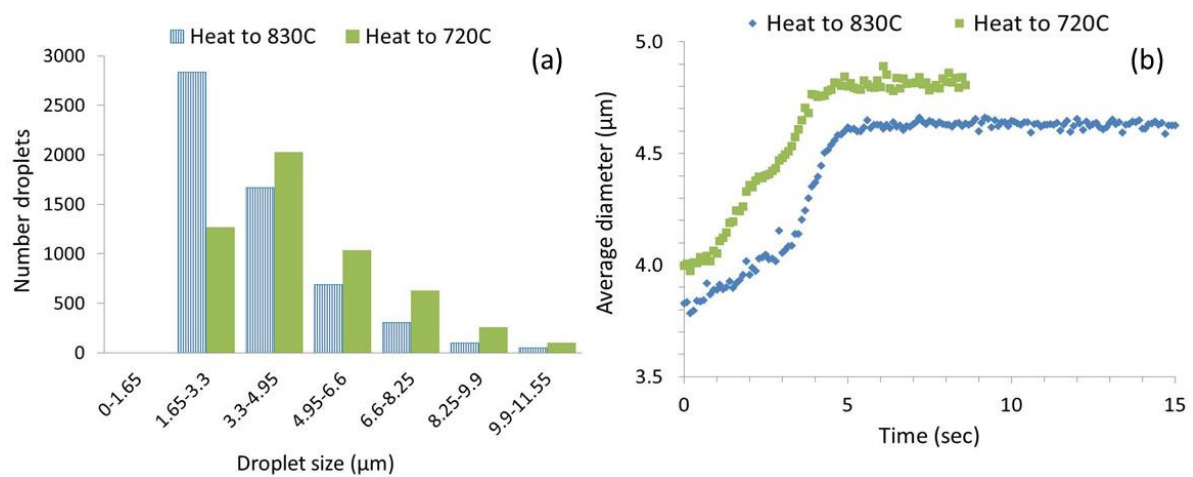
Figure 4-69 Comparison of samples heated to 720°C and to 830°C: a) Particle size distribution and b) particle size evolution during the solidification; for Al-1.2Pb solidified at 2 °C/sec.

Figure 4-70 shows the solidified microstructure of Al-1.2Pb alloy, containing the novel inoculant, heated to 720°C (a) and 830°C (b). Similarly to the sample without inoculant, not only Pb particles are smaller for the superheated alloy but their size is more homogeneous along the observed sample area. A quantitative analysis of particle size distribution at the end of solidification (a) and particle size evolution from the beginning to the end of the solidification process (b) is presented in **Figure 4-71**. Superheat increases the number of particles smaller than 6.6 µm. And as seen on figure **4-71 (b)** superheat reduces not only the final particle size after solidification (from 4.2 to 5.5 µm) but the initial size of the nucleated particles. It is important to notice the increase in particle size with superheating is much more pronounced for the sample containing Al-Ti and Al-B than for the sample without inoculant.
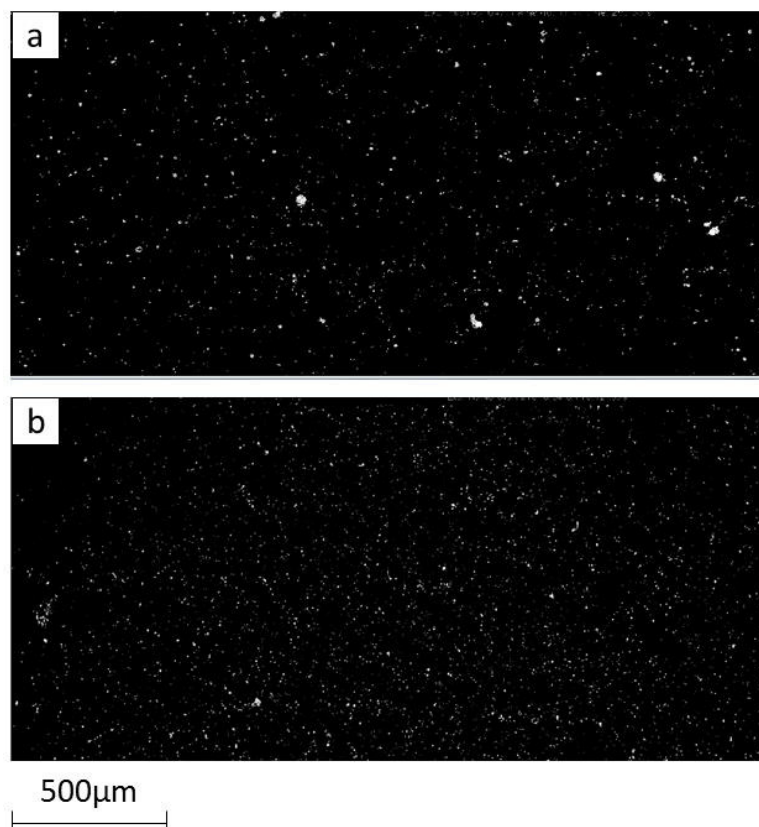
Figure 4-70 Treated synchrotron images, corresponding to Al-1.2Pb samples containing novel inoculant heated to: (a) 720°C (b) 830°C and solidified at 2 °C/sec.
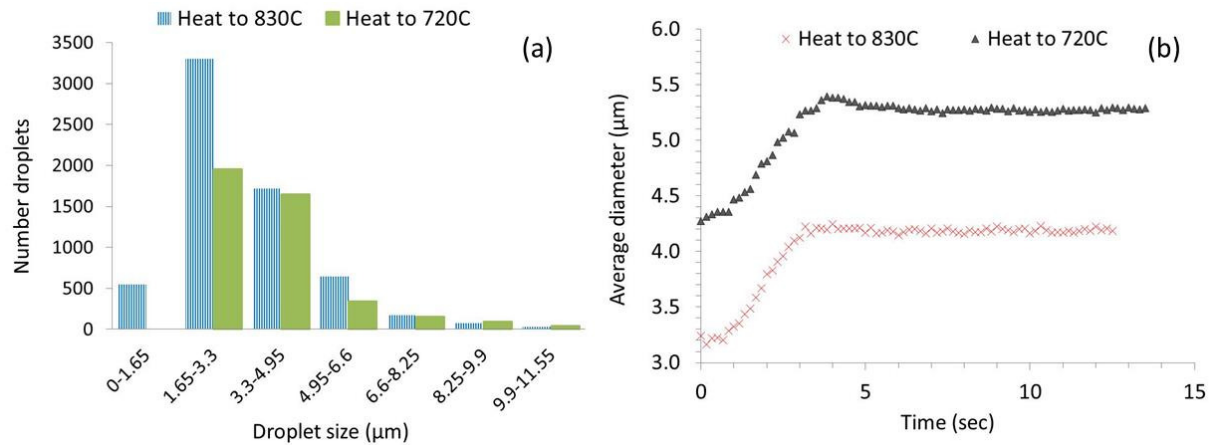
Figure 4-71 Comparison of samples heated to 720°C and to 830°C: a) particle size distribution and b) particle size evolution during the solidification process; for Al-1.2Pb, containing the novel inoculant.

The effect of superheating on alloys with and without inoculant is summarised in **Figure 4-72** and **Figure 4-73**. The smallest particle size is obtained with a combination of superheat and inoculant, nevertheless it presents the highest particle growth rate. Without superheat the sample containing inoculant shows the highest initial and final particle size.
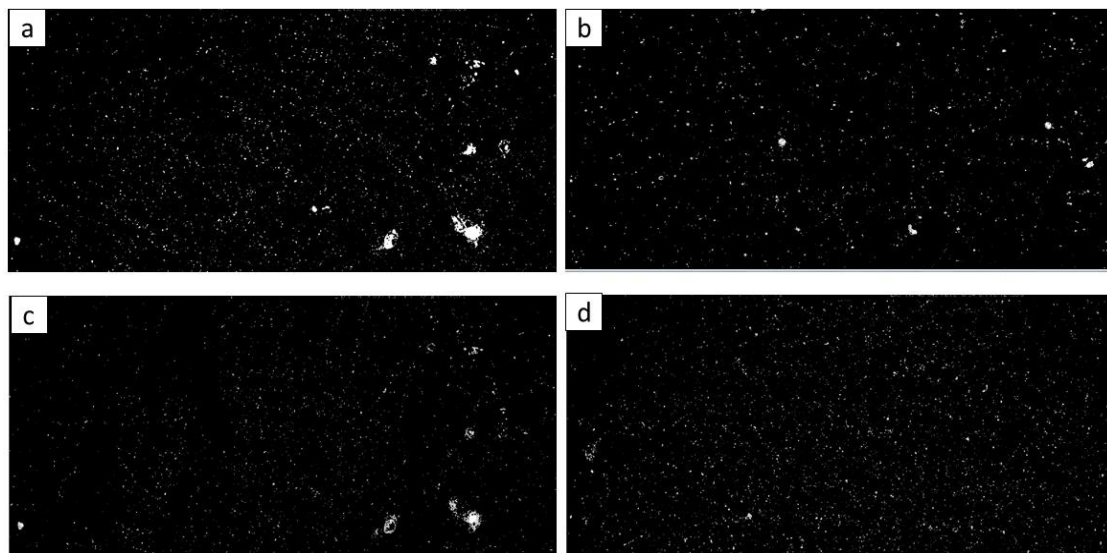
Figure 4-72 Treated synchrotron images, corresponding to the final solidified microstructure for Al-1.2Pb alloy solidified at 2˚C/sec: (a) heated to 720˚C (b) heated to 720˚C with novel inoculant (c) heated to 830˚C (d) heated to 830˚C with novel inoculant.

153
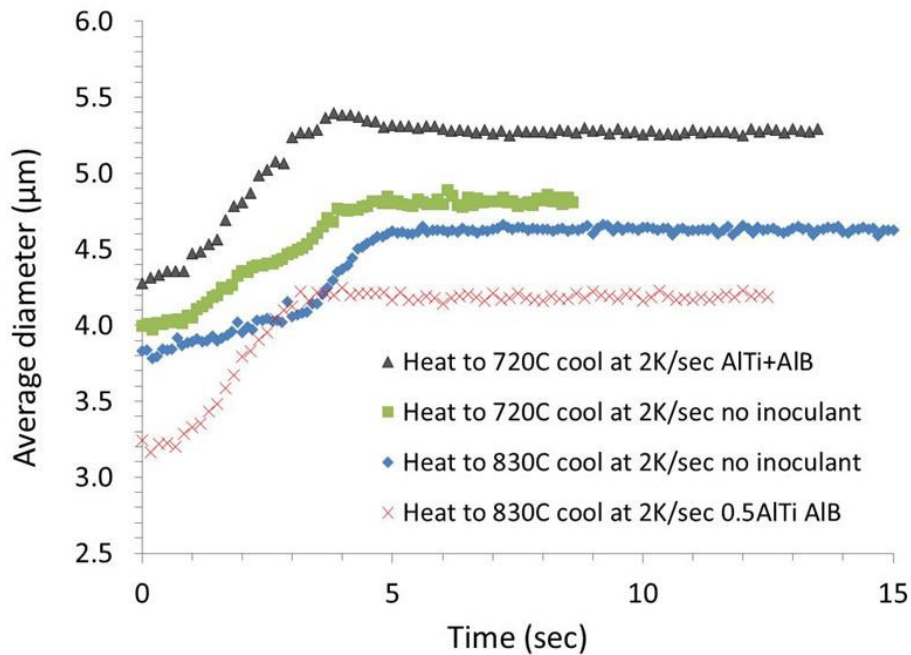
Figure 4-73 Particle size evolution during solidification of the Al-1.2Pb alloy, for the sample without and the sample containing novel inoculant, heated to 720 ℃ and 830˚C.

It has been also observed during the in situ solidification experiments that superheat has an impact on the response of the alloys to cooling rate. These results will be presented from **Figure 4-74** to **Figure 4-77.**

Figure 4-74 compares the final microstructure of the Al-1.2Pb binary alloy, heated to 720°C and solidified at two different velocities, i.e. 0.2°C/sec (a) and 2°C/sec (b). It is obvious by comparing micrographs (a) and (b) that faster cooling rates give place to finer particles on the solidified microstructure. These results are confirmed on **Figure 4-75**, where particle size evolution during solidification is plotted. As cooling rate increases from 0.2 through 0.7 to 2°C/sec, particle size decreases proportionally. It is important to note that the rate of increase changes for different cooling rates, as would be expected.
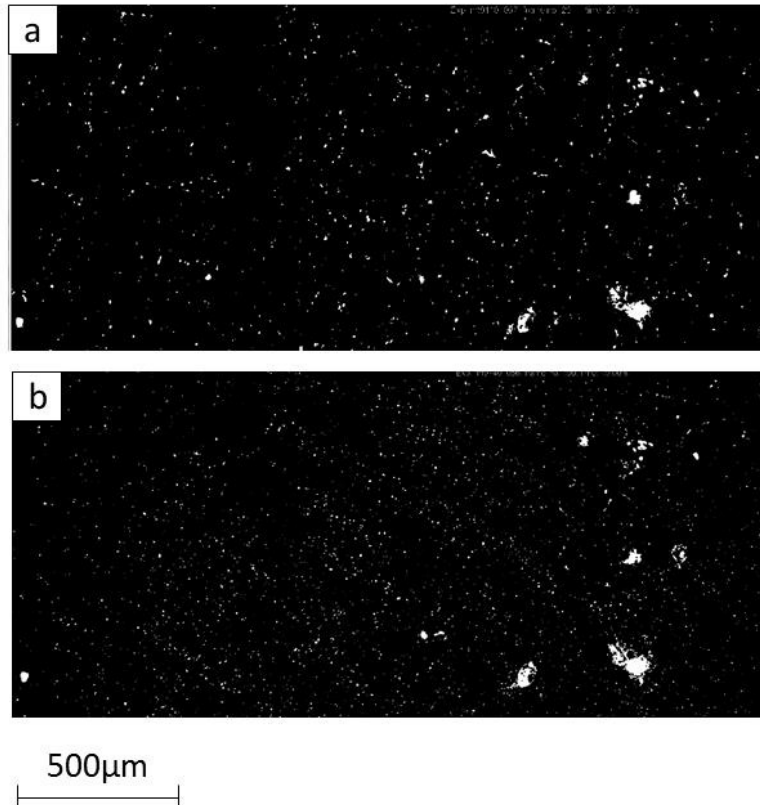
Figure 4-74 Treated synchrotron images, corresponding to the final solidified microstructure for Al-1.2Pb samples heated to 720˚C solidified at: (a) 0.2 ˚C/sec (b) 2°C/sec.
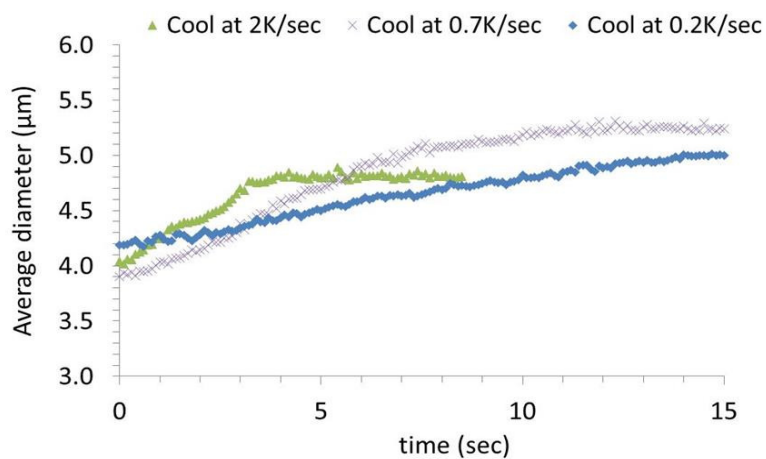
Figure 4-75 Particle size evolution during solidification of the Al-1.2Pb alloy, heated to 720 °C, comparing three different cooling rates 2, 0.7 and 0.2°C/sec.

Figure 4-76 compares the final microstructure of the Al-1.2Pb binary alloy, heated to 830°C and solidified at two different velocities, i.e. 0.2°C/sec (a) and 2°C/sec (b). From the

comparison, of both figures, it is clear that with superheating the particle size is independent on the cooling rate.
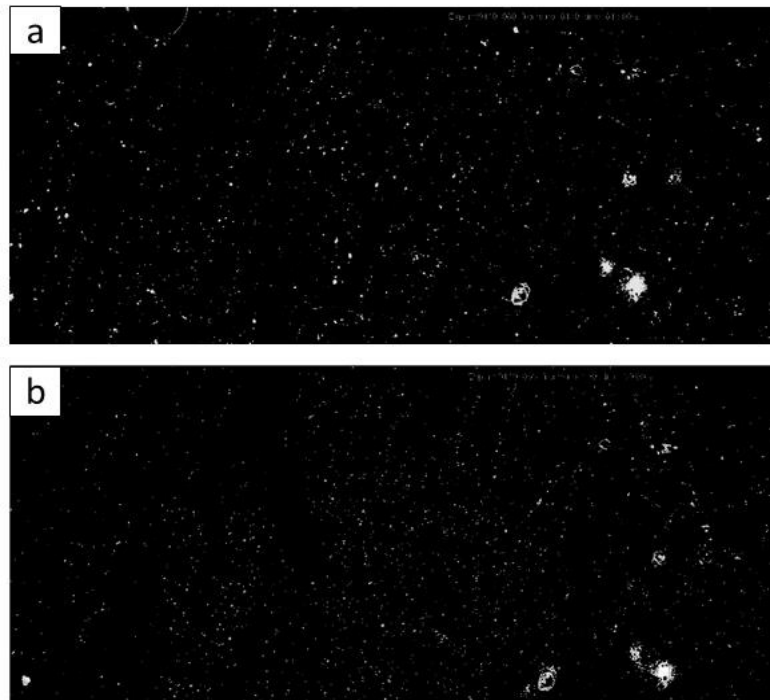
Figure 4-76 Treated synchrotron images, corresponding to the final solidified microstructure Al-1.2Pb samples heated to 830˚C: solidified at (a) 0.2 ˚C/sec and (b) 2°C/sec.

Figure 4-77 summarises the effect of superheat on the samples solidified with the 2 different cooling rates. Samples heated to 720°C are compared to those heated to 830°C, both solidified at two different cooling rates, i.e. 0.2 and 2 °C/sec. It can be seen that superheating not only makes the Pb particle size independent on cooling rate, but it reduces the average particle size compared to the melt heated to 720°C.
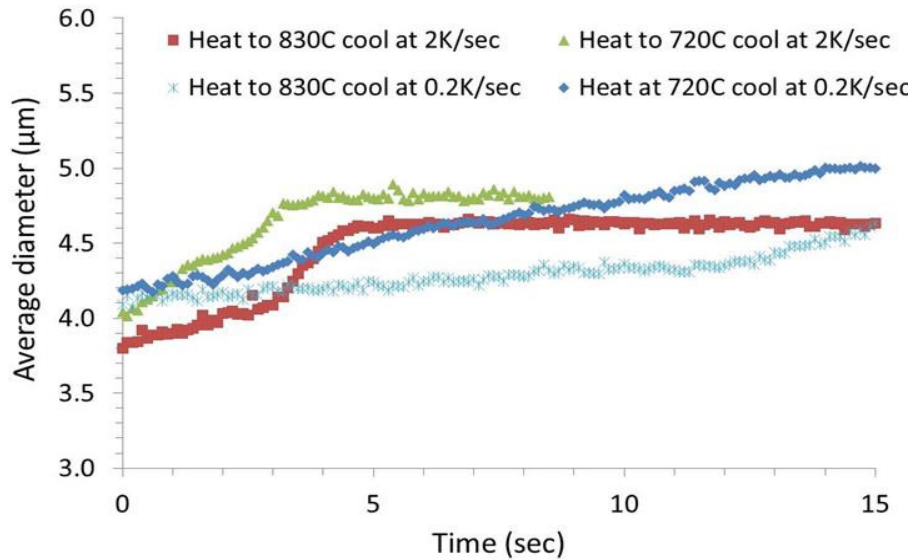
Figure 4-77 Particle size evolution during the solidification process of the Al-1.2Pb samples, heated to 720°C and 830°C and solidified at 2 and 0.2°C/sec.

4.4.2.2 DC casting of monotectic binary alloys

All the billets presented in this section contain Al-Ti and Al-B (novel inoculant), to get a concentration of 0.1 % in Ti and balanced B for stoichiometric TiB$_2$. Similarly all the billets have been sheared at 6000 rpm during DC casting. The casting temperature chosen for the experiments is 720°C.

Figure 4-78 and **Figure 4-79** shows optical images of Pb particles in the Al matrix across the top and bottom of the billet, respectively. The billet cast from the melt heated to 740°C (a,b) is comparted to that from the heated to 860°C (c,d), i.e. superheat. Similar to the Al-3Pb hyper-monotectic alloy, the number of particles, in the final solidified microstructure, increases with melt superheated to 860°C. **Figure 4-80** and **Figure 4-81** display the quantitative analysis of average particle size and number of particles across and along the billet, respectively. The results confirm what is seen on the micrographs, superheat increases the number of particles within the solidified microstructure. However, superheat does not affect average particle size.
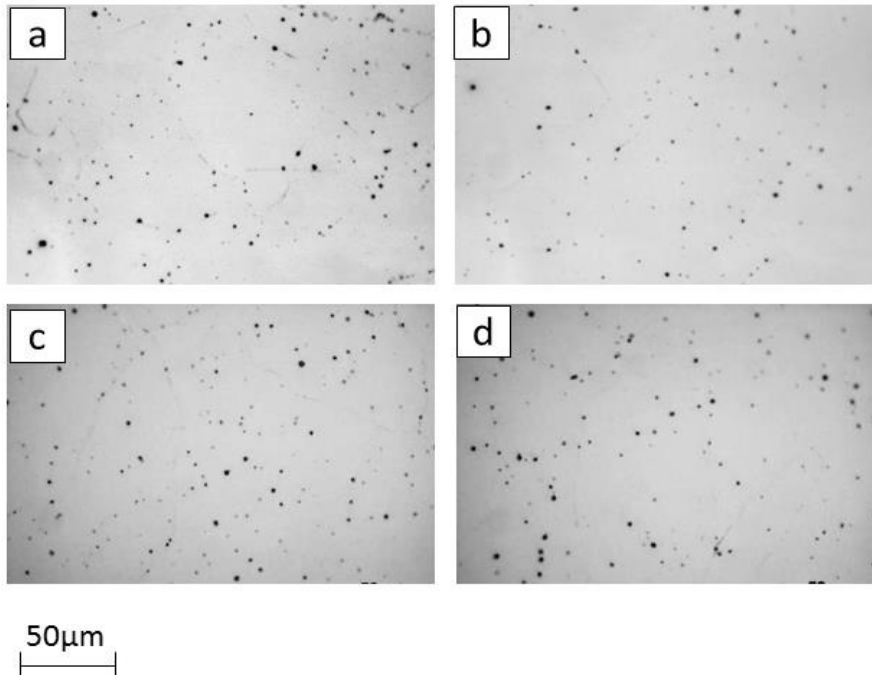
Figure 4-78 Optical micrographs of the Al-1.2Pb DC cast billets, cast at 740°C and 140 mm/min, sheared at 6000 rpm, corresponding to: (a, c) edge and (b, d) centre on the top of the billet: (a,b) melt heated to 740˚C and (c,d) melt heated to 860˚C.
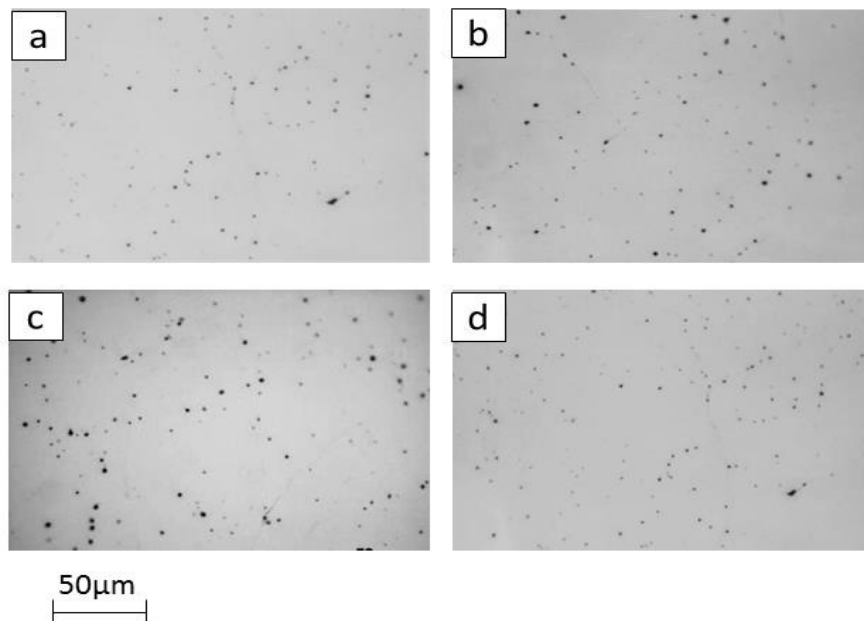
Figure 4-79 Optical micrographs of the Al-1.2Pb DC cast billets, cast at 740°C and 140 mm/min, sheared at 6000 rpm, corresponding to: (a, c) edge and (b, d) centre on the bottom of the billet: (a,b) melt heated to 740˚C (c,d) melt heated to 860˚C.
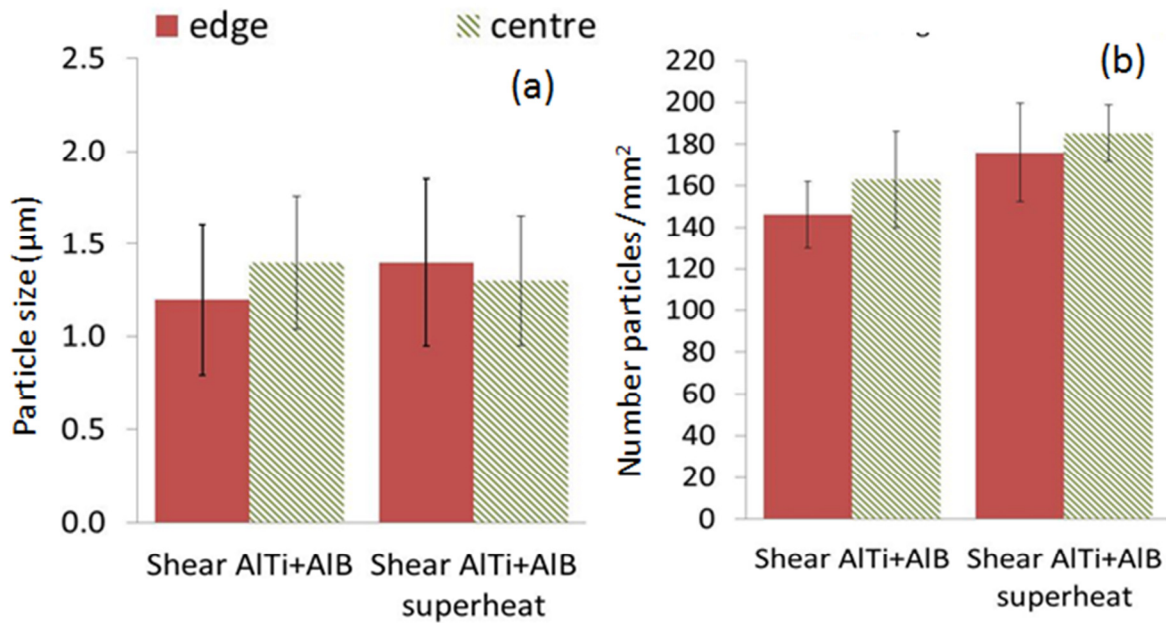
Figure 4-80 Comparison of the Al-1.2Pb DC cast billet heated to 740˚C and the billet heated to 860˚C: (a) Particle size and (b) number of particles from edge to centre of the billet.
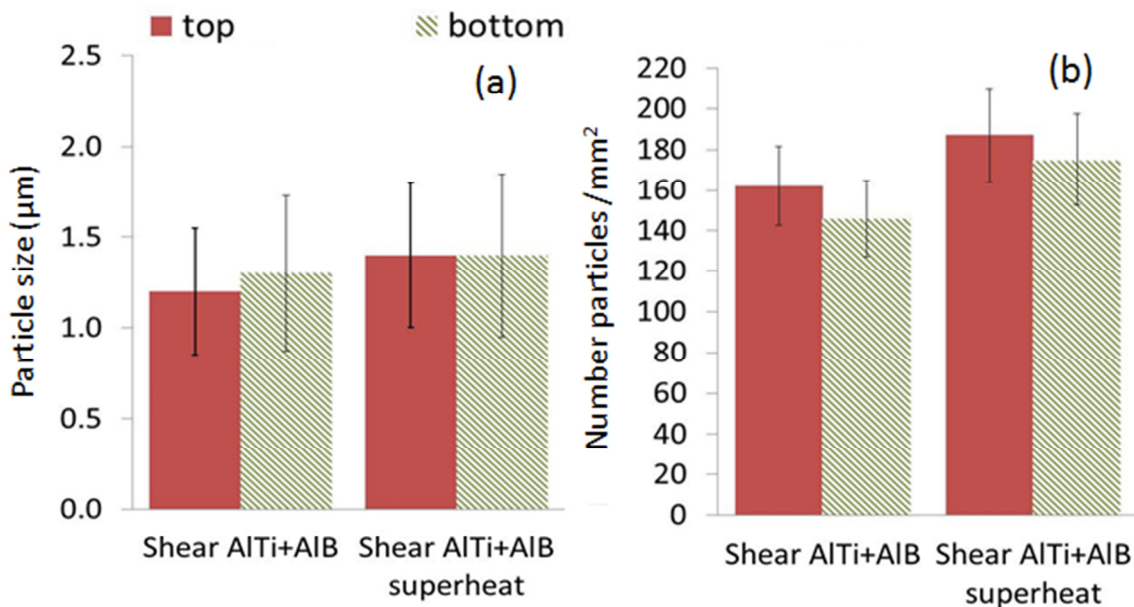
Figure 4-81 Comparison of the Al-1.2Pb DC cast billet heated to 740˚C and the billet heated to 860˚C: (a) Particle size and (b) number of particles from top to bottom of the billet.

Furthermore a summary of the average particle size and number of particles on the whole billet, seen on **Table 4-10**, confirms the observations from previous figures. The average particle size is independent of the alloy heating temperature, but the number of particles increases 155 to 190 per unit area, with melt superheat.

Table 4-10 Average number of particles and particle size for Al-1.2Pb DC cast billet.

Cast	Number particles/mm²	Particle size (µm)
Al-Ti + Al-B	155	1.2
Al-Ti + Al-B, 860˚C superheat	178	1.3

4.4.3   2011 alloy

4.4.3.1   Steel mould casting

To understand the effect of superheat on the microstructure and soft phase distribution of 2011 alloy, initial experiments were performed by solidifying 2011 alloy in a small cylindrical steel mould, as described in Chapter 2, Section 2.2.

In the cases where inoculant was added, its amount corresponds to a concentration of 0.1 % of Ti in the alloy, unless otherwise indicated. Melt conditioning by shearing was not performed in any of the steel mould casting experiments presented here. Samples of 2011 alloy were heated to different temperatures, before being cast at 720˚C.

Figure 4-82 comprises optical images of 2011 etched samples cast at 720˚C, after being heated to 740°C (a,b), 840°C (c,d) and 920°C (e,f). A decrease in secondary dendritic arm spacing (SDAS), as the heating temperature is increased i.e. melt superheat, is evident. When the melt heated to 840˚C (c, d) is compared to the one heated to 740˚C (a, b) a refinement in SDAS is observed. However the structure is not homogeneous and both fine and coarse dendritic arms are present. For the melt heated to 920˚C (e, f) not only the

dendritic arm spacing is finer but completely homogeneous across the cast sample (see also **Figure 4-91**).
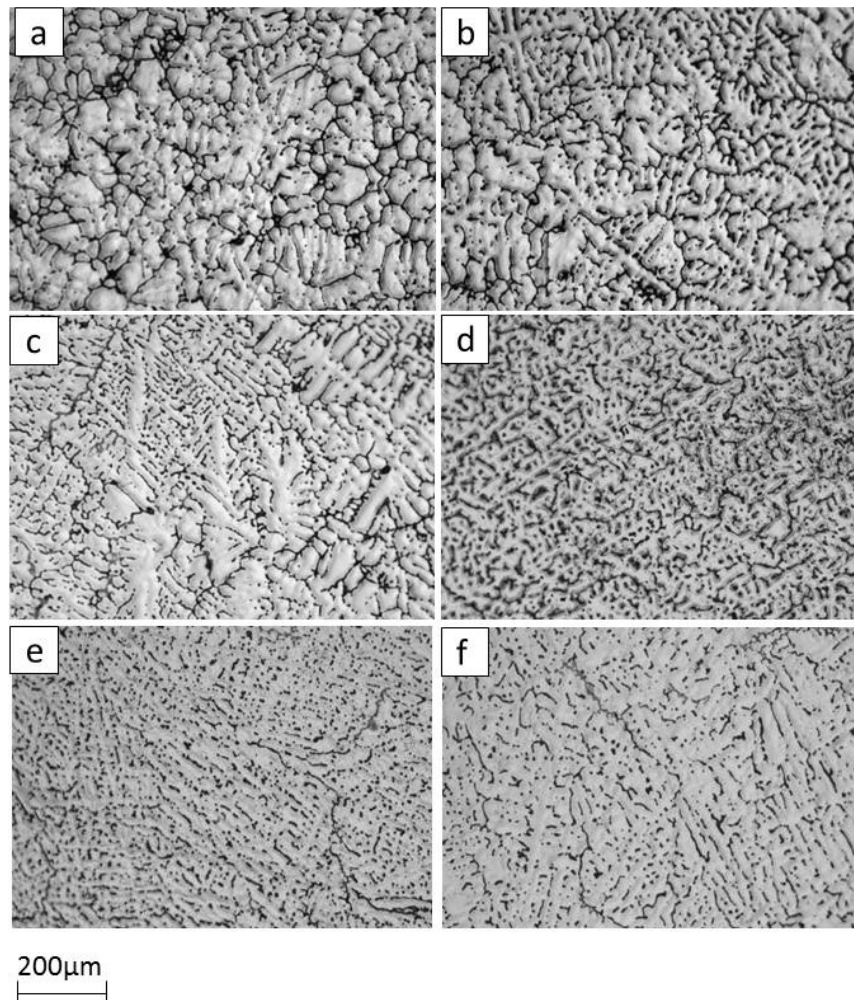
Figure 4-82 Optical images of etched samples of 2011 alloy cast at 720˚C, in a steel mould: (a, b) melt heated to 740˚C (c, d) melt heated to 840˚C and (e, f) melt heated to 920˚C.

Figure 4-83 shows optical images of 2011 alloy containing Al-Ti and Al-B, cast at 720˚C, after being heated to 740°C (a,b), 840°C (c,d) and 920°C (e,f). A minor reduction in SDAS as the heating temperature is increased, i.e. melt superheat. When the melt is heated to 840˚C (c, d) compared to (a,b) the microstructure consist of a mixture of coarser and finer dendrites. When the melt is heated to 920˚C SDAS is slightly finer and more uniform (see also **Figure 4-92**).

161
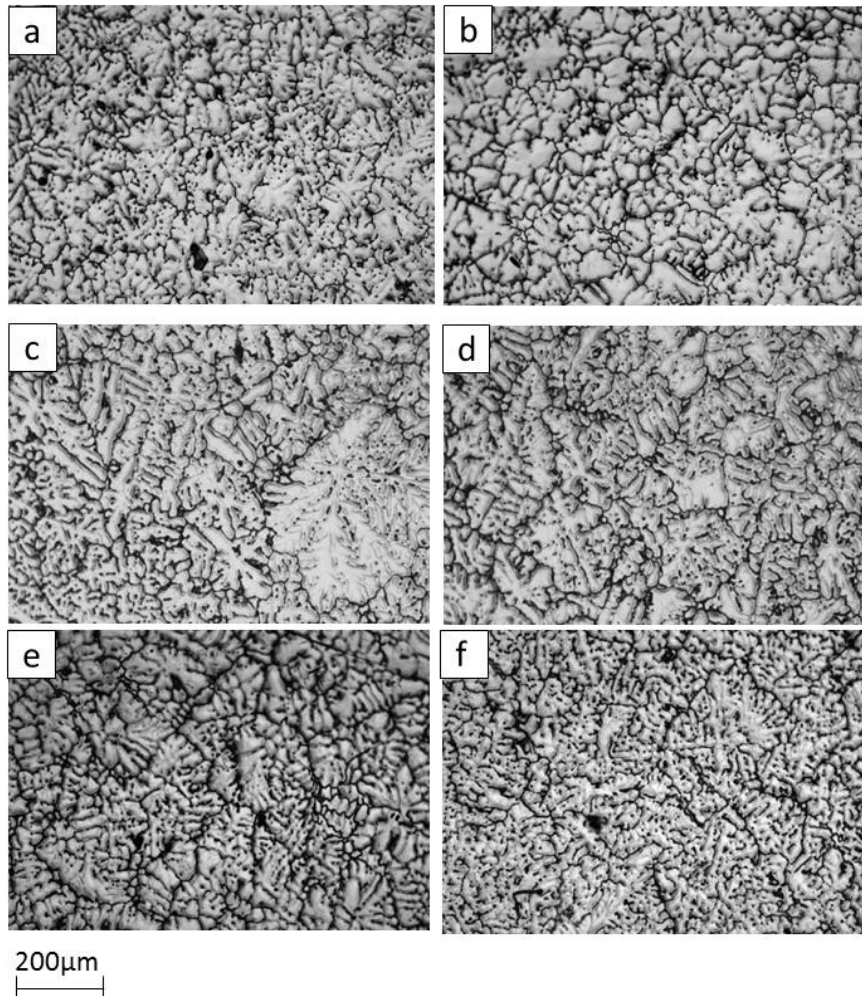
Figure 4-83 Optical images of etched samples of 2011 alloy cast at 720˚C, in a steel mould, containing Al-Ti and Al-B: a) melt heated to 740˚C b) melt heated to 840˚C and c) melt heated to 920˚C.

Figure 4-84 comprises micrographs of the etched samples, observed under polarised light, to reveal the grain sizes and structures. Samples obtained from the melt heated to 740°C (a,b) are compared to those from the melt heated to 840°C (c,d) and 920°C (e,f). As melt superheat increases the grain sizes are reduced; the calculated grain sizes are 621, 421 and 295 µm corresponding to the sample heated to 740˚C, 840˚C and 920˚C respectively.

500μm   200μm
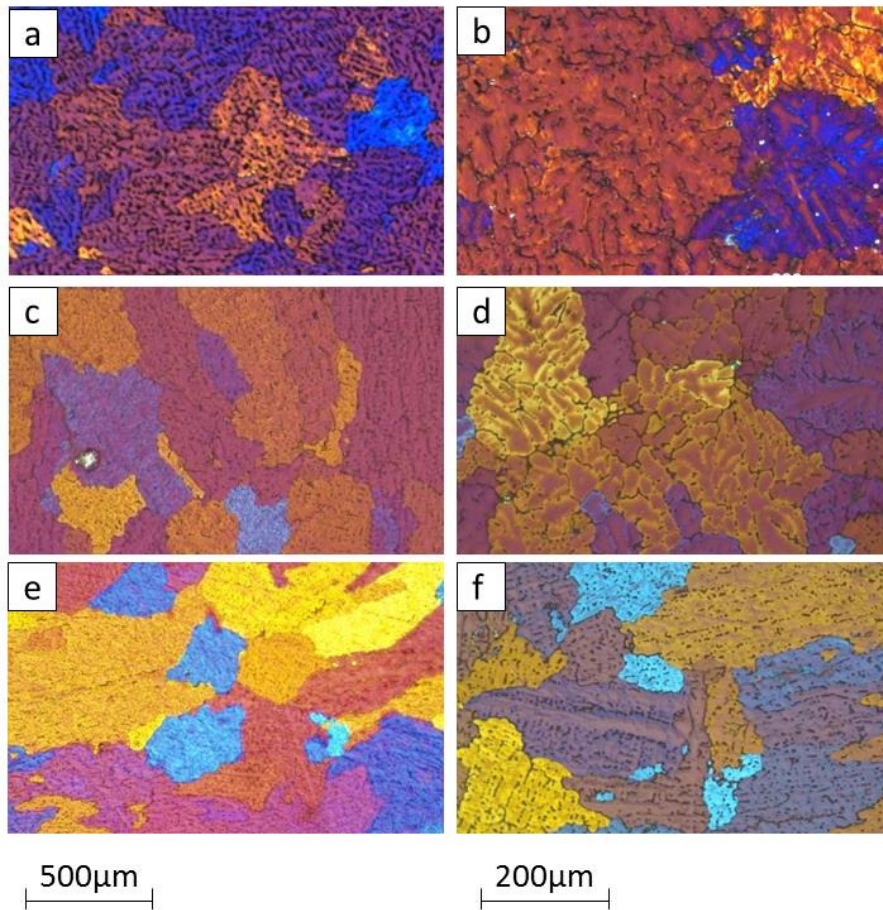
Figure 4-84 Optical images, obtained under polarised light, of etched samples of 2011 alloy cast at 720˚C, in a steel mould: (a, b) melt heated to 740˚C (c, d) heated to 840˚C and (e, f) heated to 920˚C.

Figure 4-85 shows the same micrographs as **Figure 4-84** but for the melt containing the novel inoculant. Contrary to previous, for the melt containing inoculant, the grain size is independent of the heating temperature of the melt. The calculated average grain size for the cast samples is 211, 218 and 207 μm corresponding to the sample heated to 740˚C, 840˚C and 920˚C respectively. This information is summarised in **Figure 4-86.**
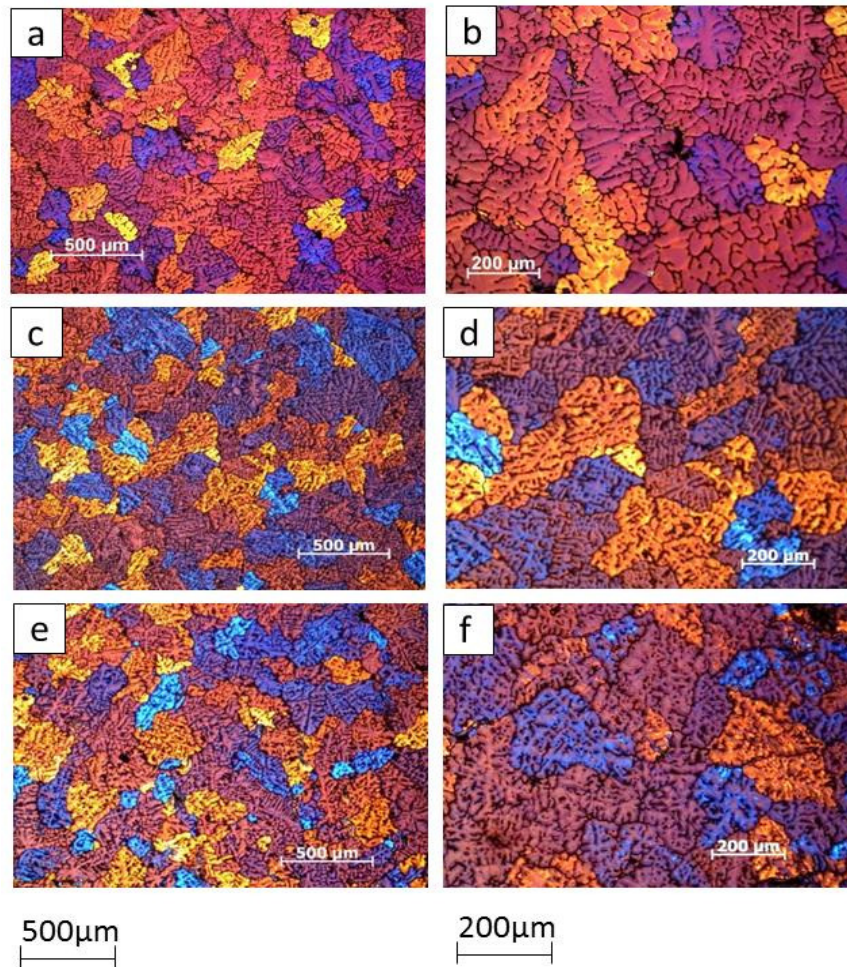
Figure 4-85 Optical images of etched samples of 2011 alloy cast at 720˚C, in a steel mould, containing Al-Ti and Al-B: a) melt heated to 740˚C b) heated to 840˚C and c) heated to 920˚C.
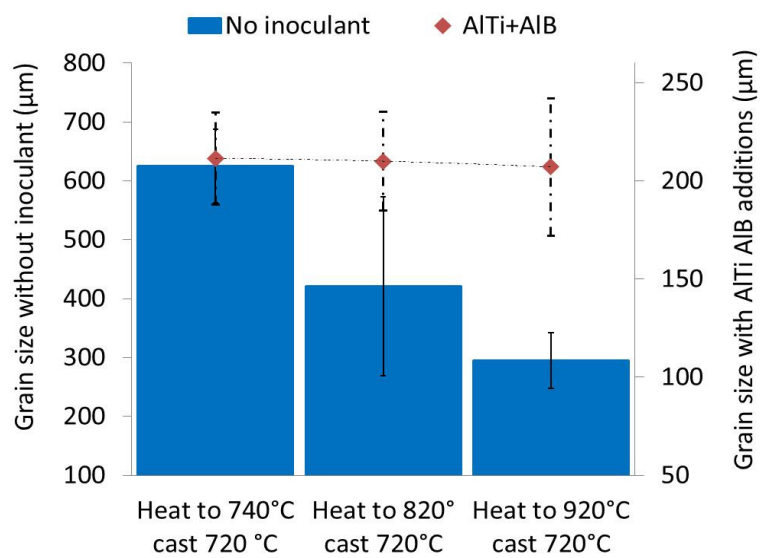
Figure 4-86 Effect of superheat on grain size for 2011 alloy, cast in a steel mould, with and without Al-Ti and Al-B.

The combined effect of the novel inoculant and the industrially used Al-5Ti-B (to get a concentration of 0.02 % Ti), on the solidified microstructure is analysed in **Figure 4-87**. Samples containing Al-Ti and Al-B (a,b) are compared to samples containing also Al-5Ti-B (c,d). By adding the novel inoculant the grain size is reduced from 650 µm to 240 µm, which is bigger than the acceptable grain size for industrial production. On the other hand, the final size of the grain is further reduced to 60 µm after adding Al-5Ti-B. However, Al-5Ti-B have a detrimental effect on the microstructure and distribution of Bi/Pb particles, by increasing the particle size and decreasing the number of particles on the solidified samples. This effect is shown in **Figure 4-88,** where a quantitative analysis of the effect of amount and type of inoculant on Pb particle size is presented. Increasing the amount of novel inoculant reduces the average particle size, and contrary additions of Al-5Ti-B increase the average particle.
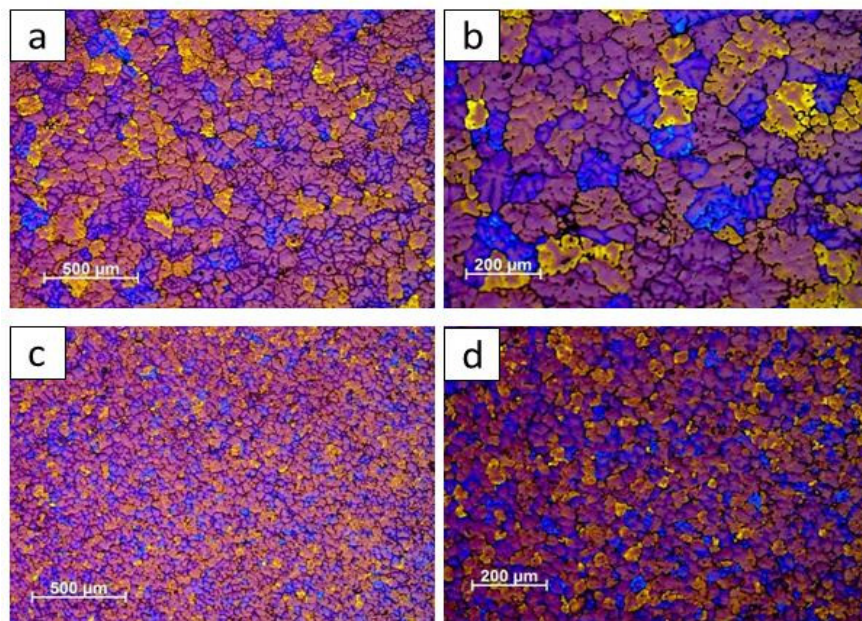
Figure 4-87 Optical image of etched samples of 2011 alloy heated to 860°C and cast at 720˚C, in a steel mould: (a, b) containing Al-Ti and Al-B (c, d) containing Al-Ti, Al-B and Al-5Ti-B.
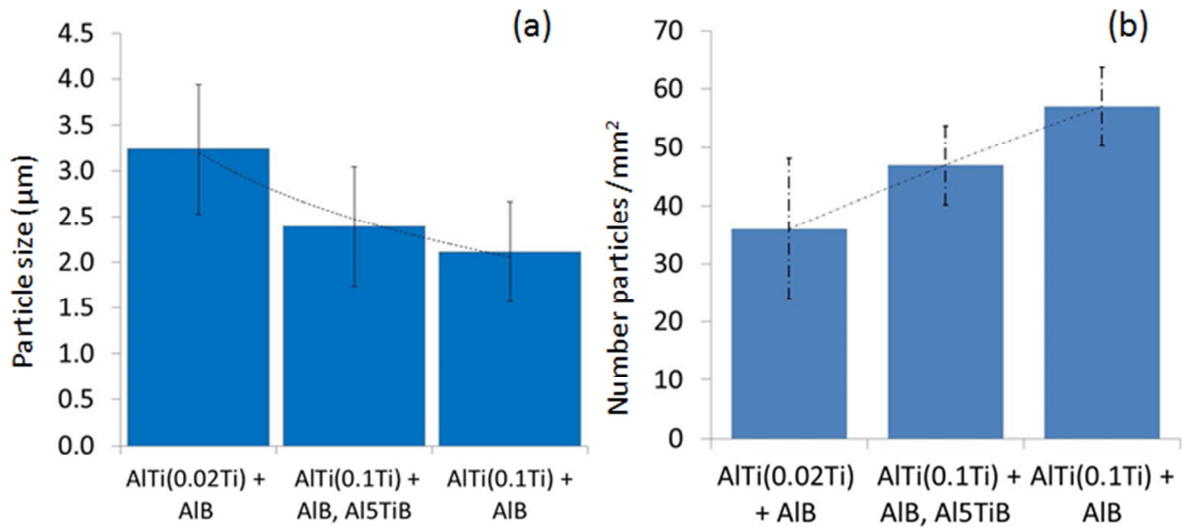
Figure 4-88 Effect of inoculant on: (a) Particle size and (b) number of particles, for 2011 alloy.

Figure 4-89 and **Figure 4-93** comprise SEM images of 2011 samples whose melt has been heated to 740°C (a,b) 840°C (c,d) and 920°C (e,f), for samples without and with Al-Ti and Al-B, respectively. The quantitative analysis of particle size and number of particles for the mentioned castings is shown in **Figure 4-90** and **Figure 4-94**. The size and number of Pb/Bi particles change with increasing melt temperature i.e. the superheat. The higher the melt temperature the smaller the particles size and the more particles are obtained in the solidified microstructure. This microstructural refinement is more significant for the samples free of inoculant.
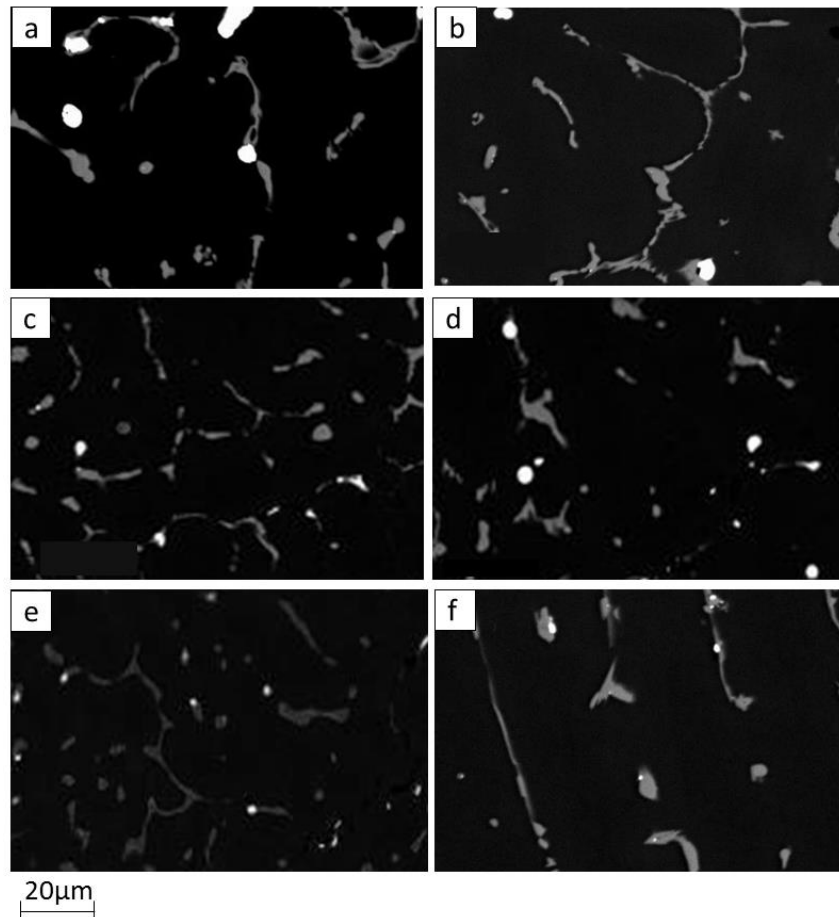
Figure 4-89 SEM images of 2011 samples cast at 720°C, in a steel mould, after being heated to: (a, b) 740°C (c, d) 840°C and (e, f) 920°C.
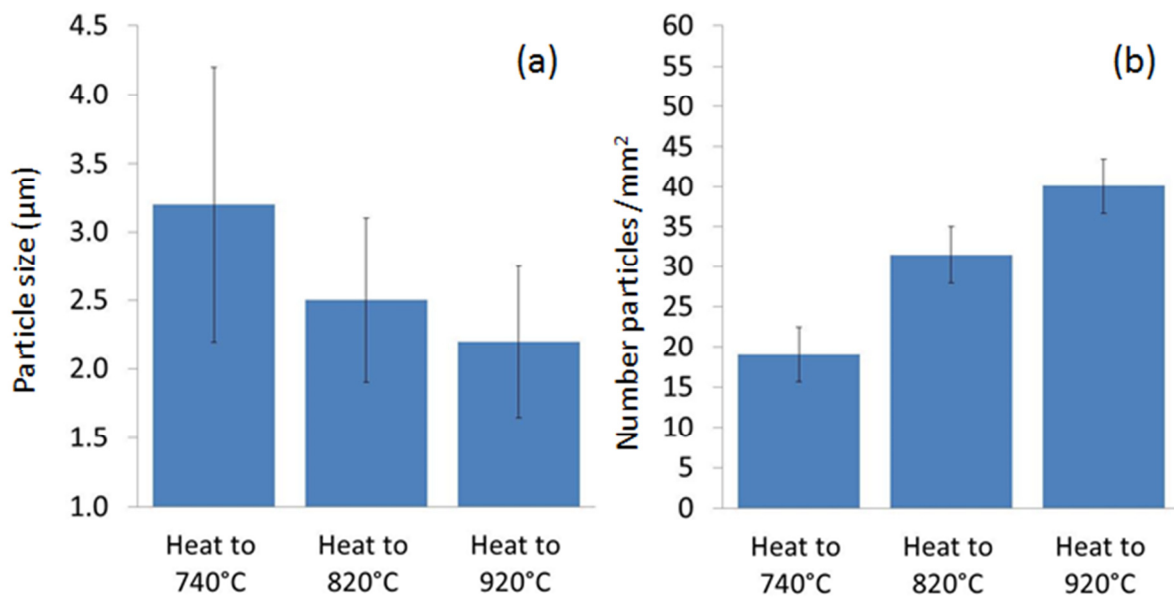
Figure 4-90 Effect of superheat: (a) Particle size and (b) number of particles, for 2011 alloy cast at 720°C.

Figure 4-91 shows a direct correlation between particle size and SDAS, as the SDAS decreases with superheat, the particle sizes decreases proportionally, for samples free of inoculant. The same information as above is displayed in **Figure 4-92**, but for the sample containing the novel inoculant. In this case the change in SDAS with melt superheat is less significant than for samples produced from the inoculant free alloy.
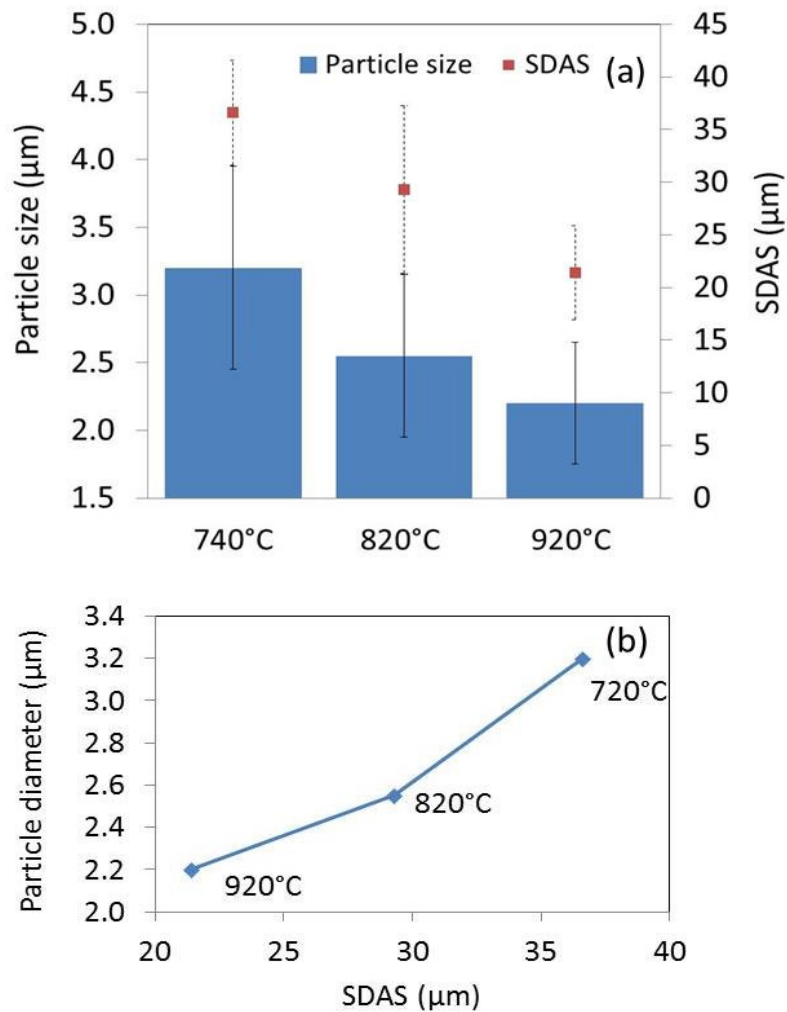
Figure 4-91 Particle size and SDAS for steel mould casting of 2011 without inoculant (a) and correlation between the 2 parameters (b).
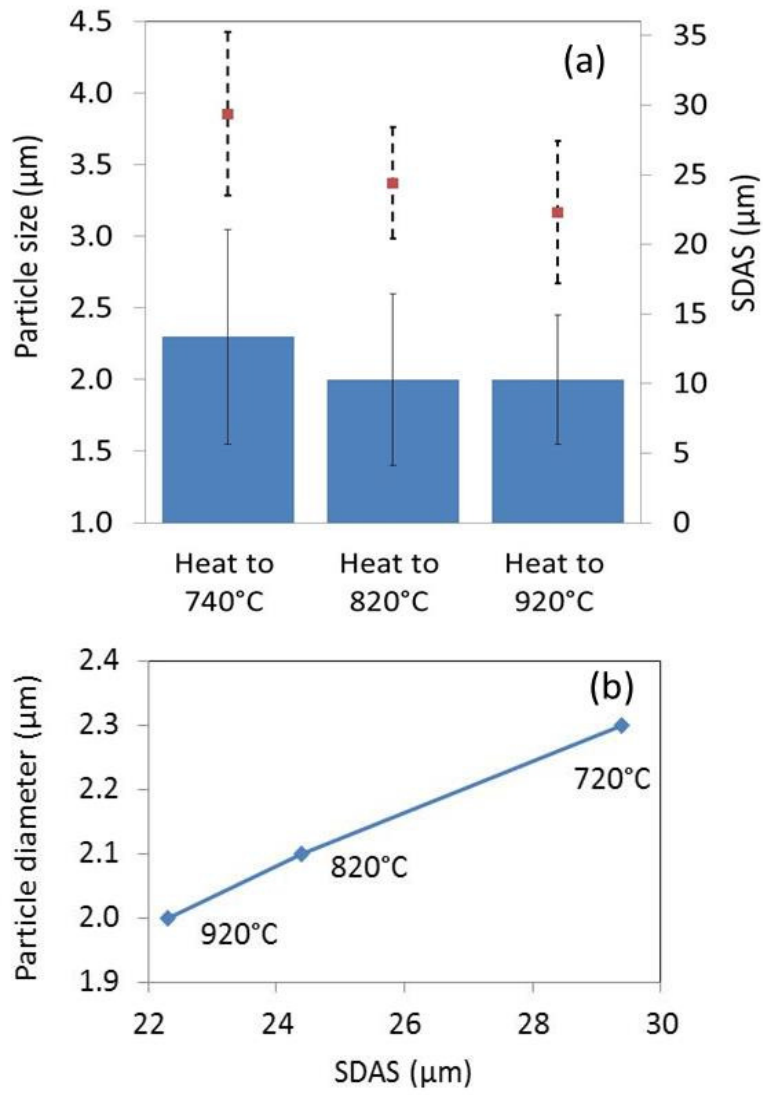
Figure 4-92 Particle size and SDAS for steel mould casting of 2011 with inoculant (a) and correlation between the 2 parameters.
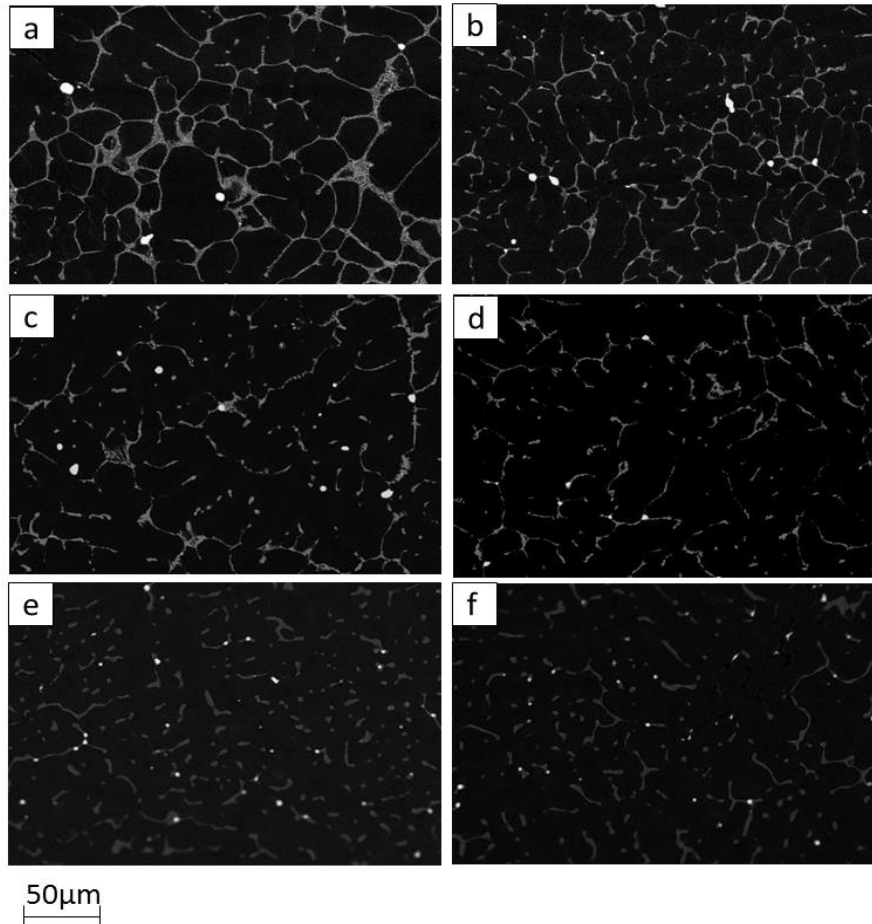
Figure 4-93 SEM images of 2011 samples, cast in a steel mould, containing Al-Ti and Al-B, cast at 720°C after being heated to: (a,b) 740°C (c,d) 840°C and (e, f) 920°C.
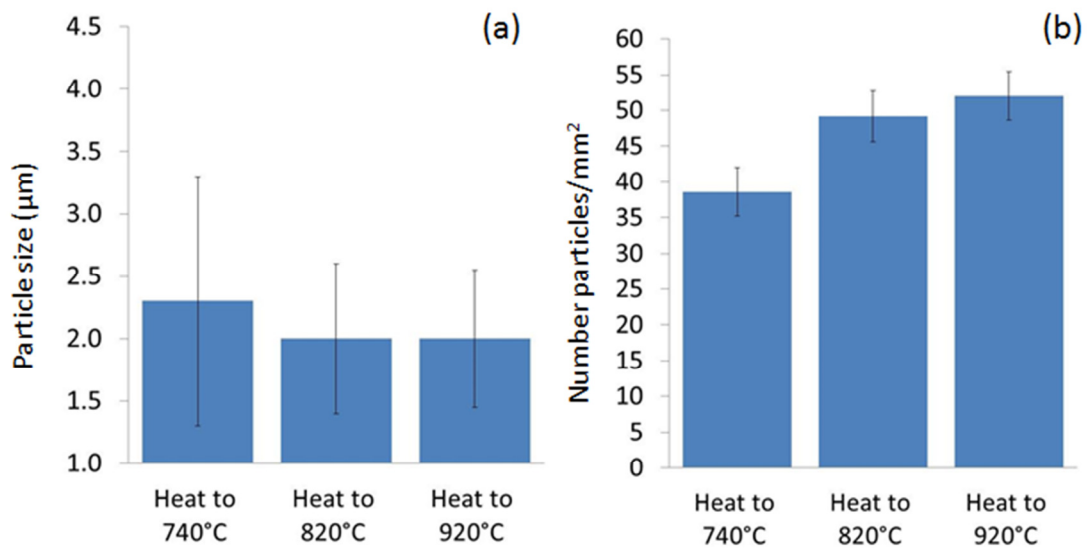
Figure 4-94 Effect of superheat: (a) Particle size and (b) number of particles, for 2011 alloy containing Al-Ti and Al-B, cast at 720°C.

4.4.3.2   DC casting of 2011 alloy

For the two billets described in this section, melt containing Al-Ti and Al-B was heated to 860°C for the first billet and to 740°C for the second, hold for 1 h before being cool to the casting temperature of 720°C, cast at 140 mm/min and sheared at 6000 rpm.

Figure 4-95 and **Figure 4-96** comprises micrographs from the billets whose melt was heated to 740°C (a,b) and 860°C (c,d). Quantitative analysis of particle size and number of particles per unit area is provided in **Figure 4-97** and **Figure 4-98**, where the mentioned data is shown across and along the billet, respectively. It can be seen that superheat reduces the particle size across and along the billet and changes the intermetallic morphology and distribution on the edge of the billet. However this effect is less significant than for alloys of exact of hyper-monotectic compositions.
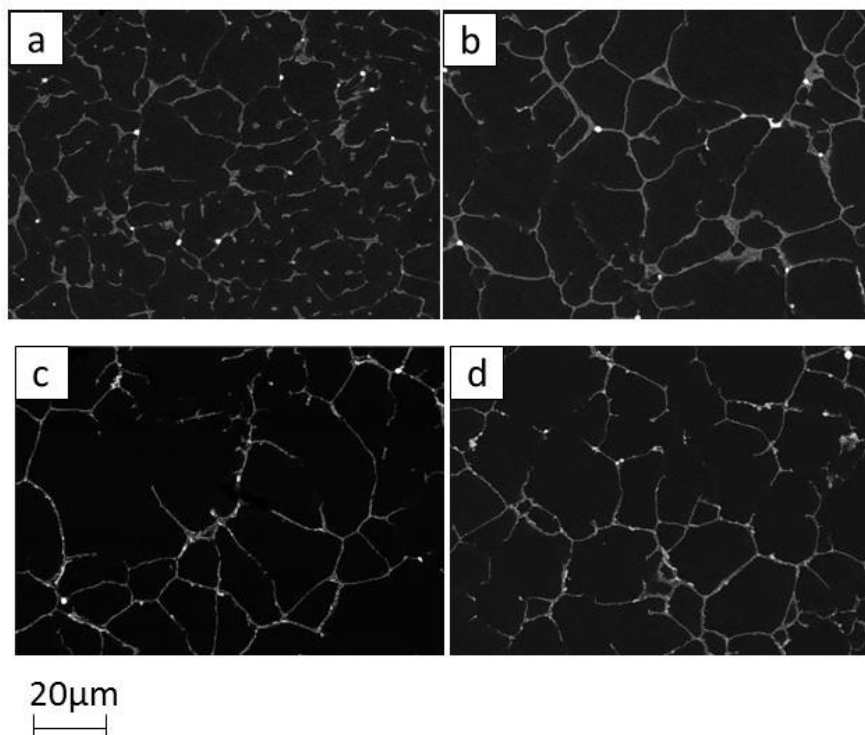
Figure 4-95 SEM images of the 2011 DC cast billets, cast at 740°C and 140 mm/min, sheared at 6000 rpm, corresponding to: (a, c) edge and (b, d) centre on the top of the billet: (a, b) melt heated to 740°C (c, d) melt superheated 860°C.

20µm
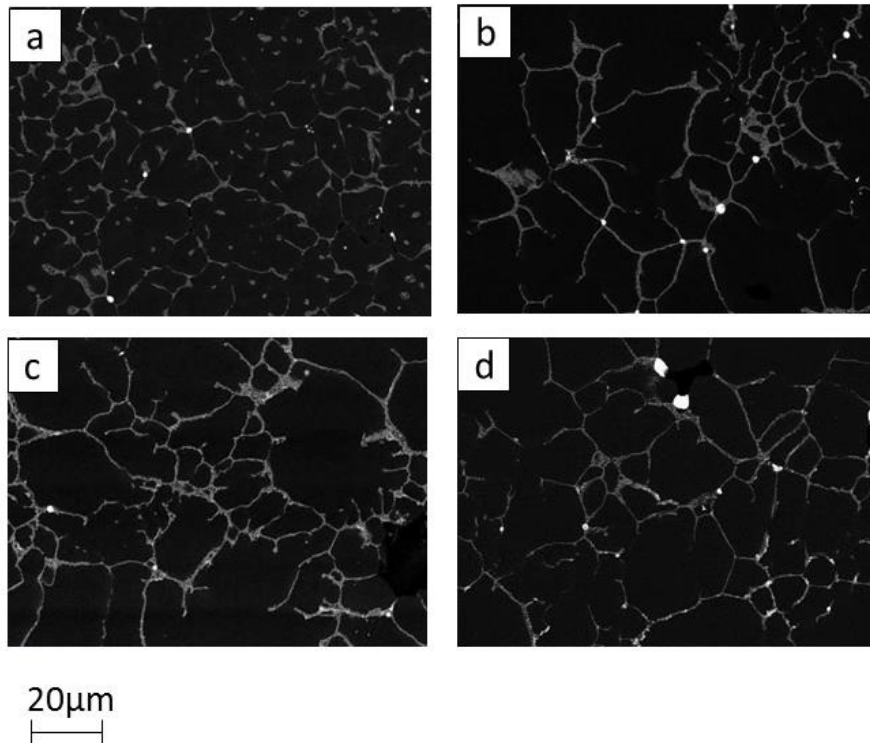
Figure 4-96 SEM images of the 2011 DC cast billets, cast at 740°C and 140 mm/min, sheared at 6000 rpm, corresponding to (a, c) edge and (b, d) centre on the bottom of the billet: (a,b) melt heated to 740°C (c,d) melt superheated 860˚C.
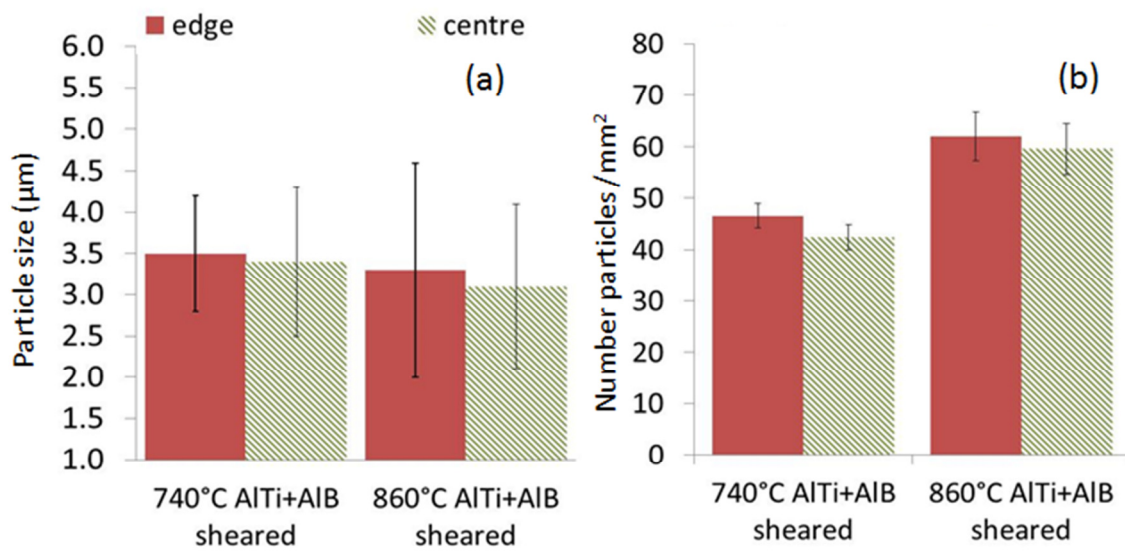
Figure 4-97 Comparison of 2011 DC cast billets, heated to 740°C and 860°C (a) Particle size and (b) number of particles from the top of the billet.
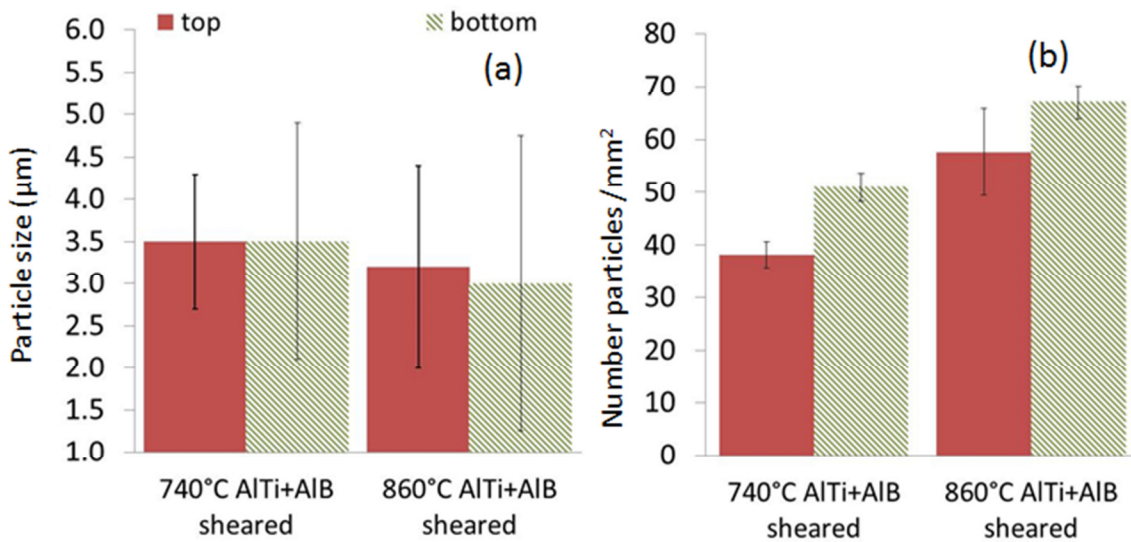
Figure 4-98 Comparison of 2011 DC cast billets, heated to 740°C and 860°C (a) Particle size and (b) number of particles from the bottom of the billet.

Table 4-11 summarizes the average particle size and number of particles comparing billets heated to 740 and 860°C. Superheat increases by 35% the number of particles; however its impact on particle size is less significant, from 3.5 to 3.2 µm.

Table 4-11 Average number of particles and particle size for 2011 DC cast billet.

Temperature	Number particles/mm²	Particle size (µm)
740°C	44.5	3.5
860°C	60	3.2

Figure 4-99 shows the particle size distribution comparing the billets whose melt was heated to 740°C and those heated to 860°C, to the melt. Melt superheat to 860°C, increases the number of particles between 0-1 µm and decreases the number of particles bigger than 4µm.

173
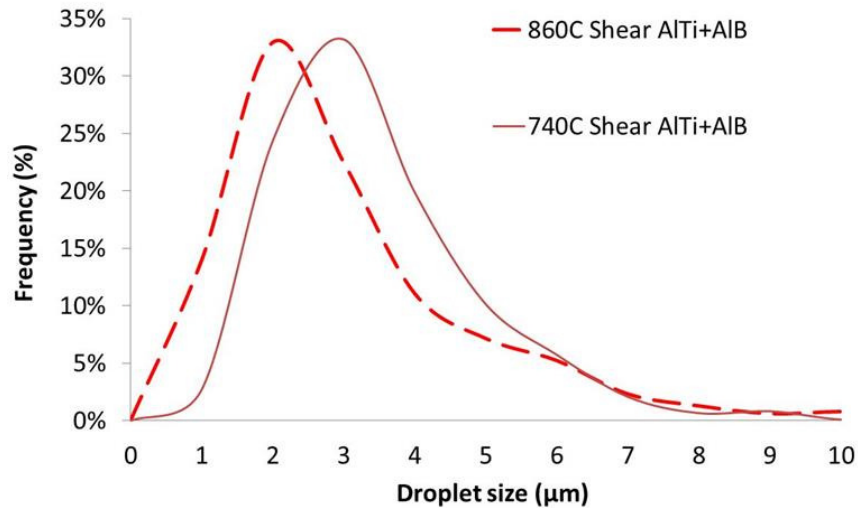
Figure 4-99 Effect of the melt superheat on particle size distribution for 2011 DC cast billets.

Figure 4-100 and **Figure 4-101** comprise optical images of etched cast structure to reveal the grain morphologies and sizes, comparing the billet whose melt was heated to 740°C (a,b) with the billet one to 860°C (c,d). An average grain size of 163 µm for the alloy heated at 740°C and 155 µm for the alloy heated to 860°C, is calculated. The centre of the billet presents the same rosette structure for both billets (compare (b) to (d)). However, the edge of the billet presents a slightly more dendritic for the billet whose melt has been heated to 740°C.
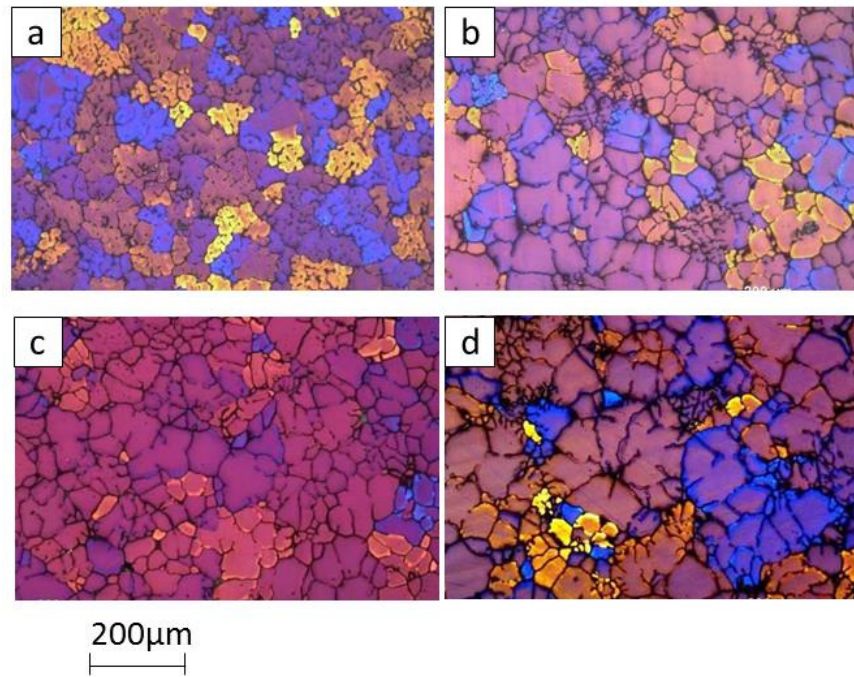
Figure 4-100 Optical images showing the grains of the 2011 DC cast billet, cast at 740°C and 140 mm/min, sheared at 6000 rpm, corresponding to: (a, c) edge and (b, d) centre from the top of the billet: (a,b) heated to 740°C (c,d) heated to 860°C.
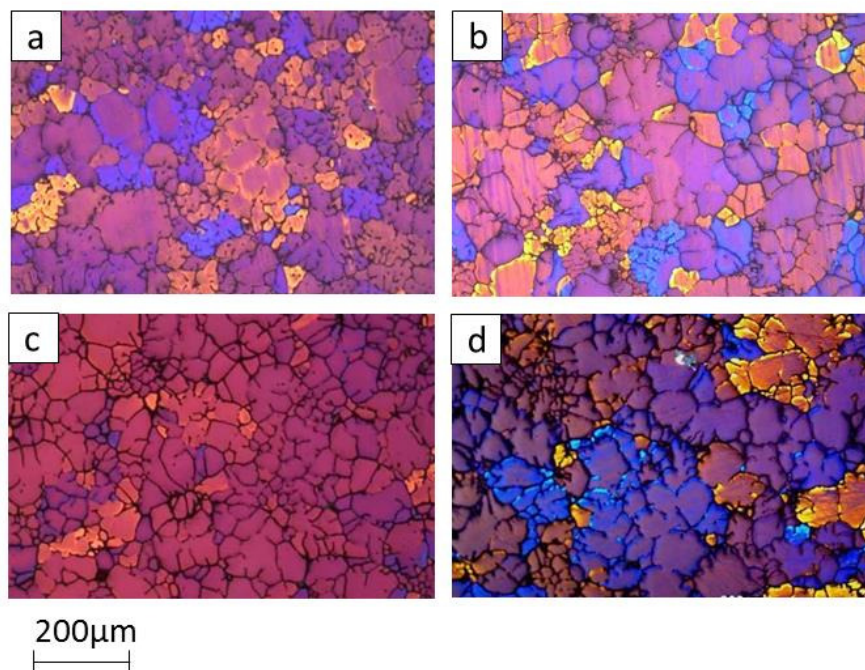
Figure 4-101 Optical images, showing the grains of the 2011 billets, cast at 740°C and 140 mm/min, sheared at 6000 rpm, corresponding to: (a, c) edge and (b, d) centre from the bottom of the billet: (a,b) heated to 740°C (c,d) heated to 860°C.

Figure 4-102 shows the solidification profile of 2011 alloy, comparing the billet whose melt has been heated to 740°C to that heated to 920°C. It is clear that superheating changes the solidification profile of 2011 alloy. **Figure 4-103** shows the solidification profile on the region close to the solidification of the alloy. Temperature at which balance of heat equlas cero (3), temperature at which recalescence finishes (2) and temperature at which latent heat is first released, just bellow the liquidus temperature (1) can be read on the temperature curve. The derivative of temperature with time is also plotted to enable the calculation of the actual liquidus temperature. The calculation of these temperatures is explained in Chapter 3. Superheating treatment of the melt decreases the undercooling, recalescence and liquidus temperature, and increases the temperature difference between undercooling and recalescence.
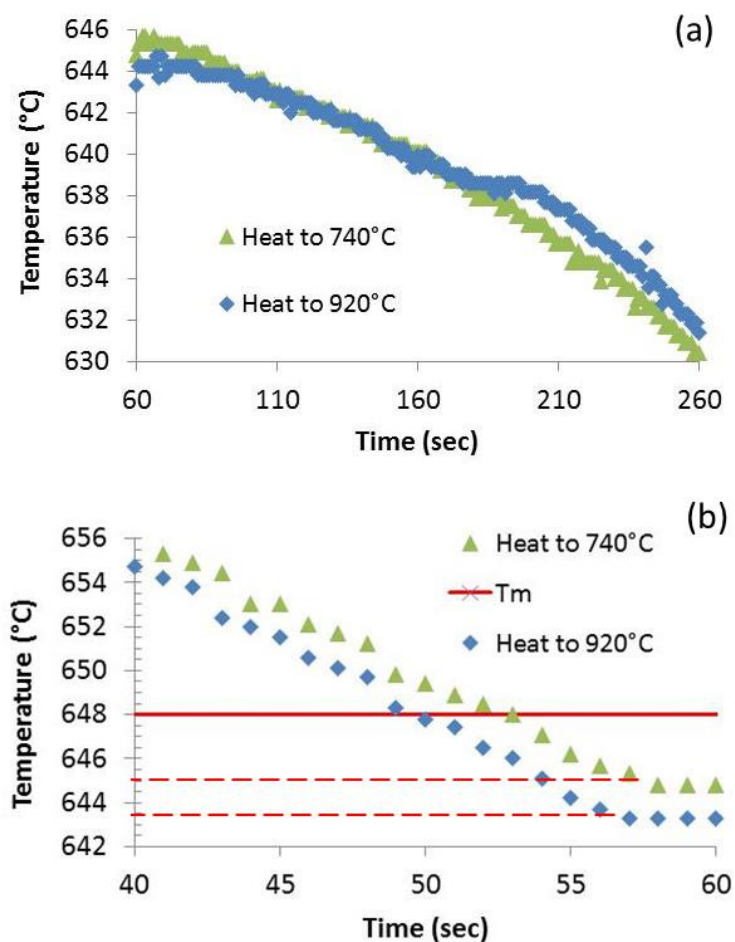
Figure 4-102 Comparison of the solidification temperature profile of 2011 DC cast alloy for the melt heated to 740°C and the melt heated to 860°C.
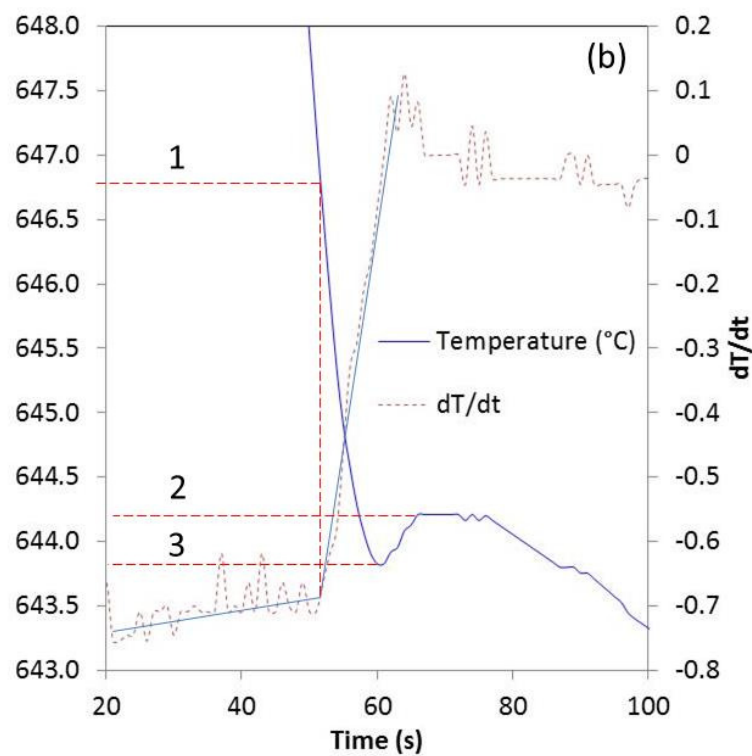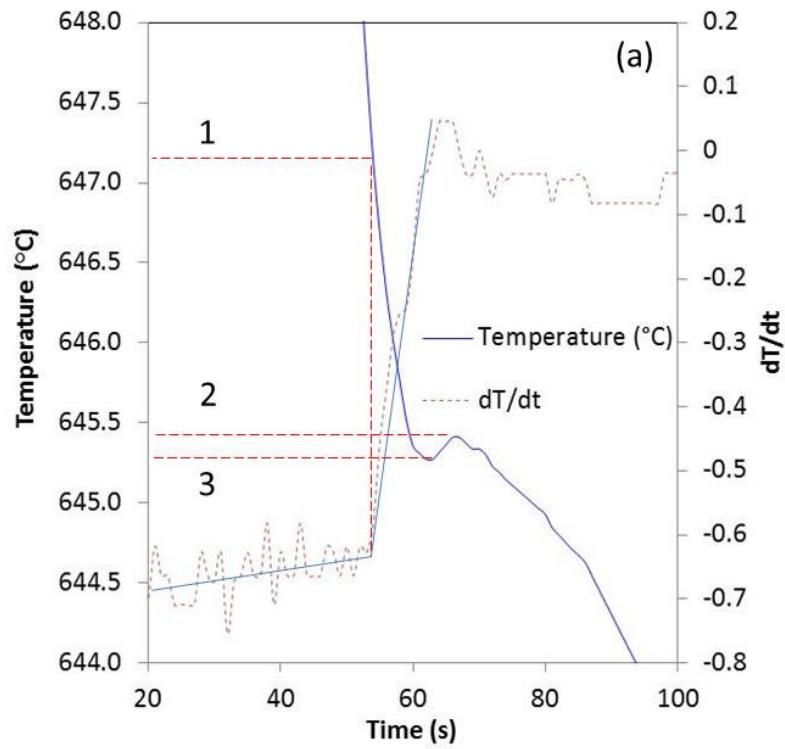
Figure 4-103 Solidification temperature profile of a 2011 alloy sample, measure in a crucible at a cooling rate of 1K/sec, and first temperature derivative, for the alloy heated to 740°C (a) and the alloy heated to 920°C (b): indicating temperature at which latent heat is first released (1) temperature at which recalescence stops(2) and temperature at which the heat balance is 0 (3).

Figure 4-104 shows DSC thermal signal for phase transformation temperatures of 2011 alloy heated to 740°C and 920°C. The cooling rate was 1 k/min. The solidification of the alloy heated to 920°C starts at 1°C of undercooling lower than that of the alloy heated to 740°C.
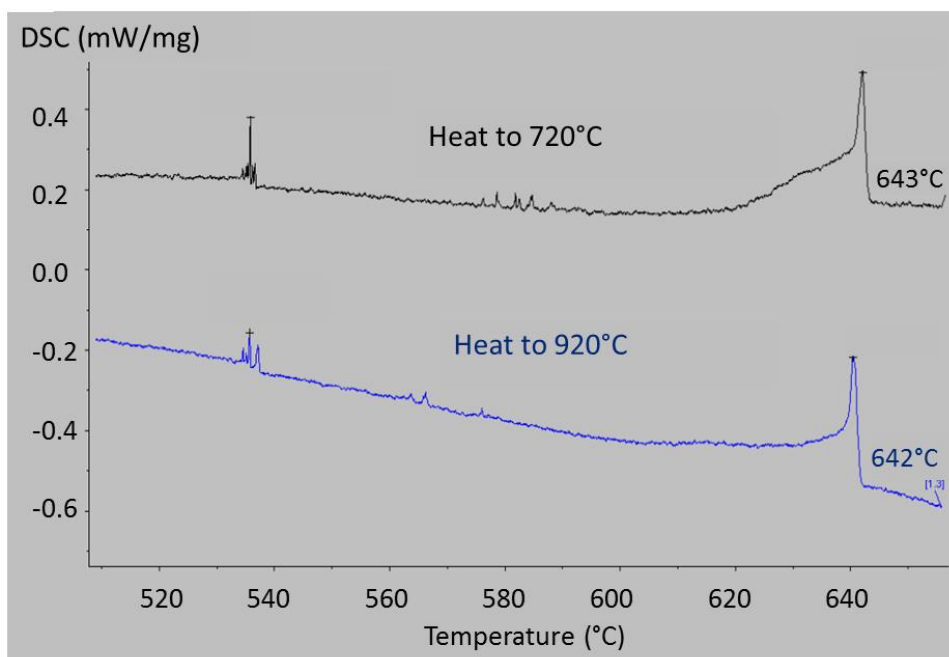
Figure 4-104 DSC trace of 2011 alloy at a cooling rate of 1 K/min for the alloy heated to 740°C and the alloy heated to 920°C.

According to equilibrium calculations (see **Figure 4-105**), at 642.9°C the Al solidifies with a FCC structure, only 0.7 °C lower than the liquidus signal measured on the DSC. However for the alloy whose melt has been superheated the liquidus temperature is reduced by 2.1°C with respect to the equilibrium calculations. Equilibrium calculation predict the formation of $Al_{23}Cu_4Fe$ and Al_7Cu_2Fe at 599°C 592°C, respectively, however from DSC signals indicate that the formation of the phases happens at lower temperatures for the melt heated to 720°C and their corresponding signals much smoother or disappeared when the melt is heated to

920˚C. AlCu, according to equilibrium calculations and DSC signal, is formed at 535.8˚C for both heating temperatures, but the intensity of the peak is smaller with the melt is superheated to 920˚C. This is consistent with SEM EDS analysis, which indicates that in the billets heated to higher temperatures the majority of the compounds found are Al_2Cu, containing small amounts of Fe.
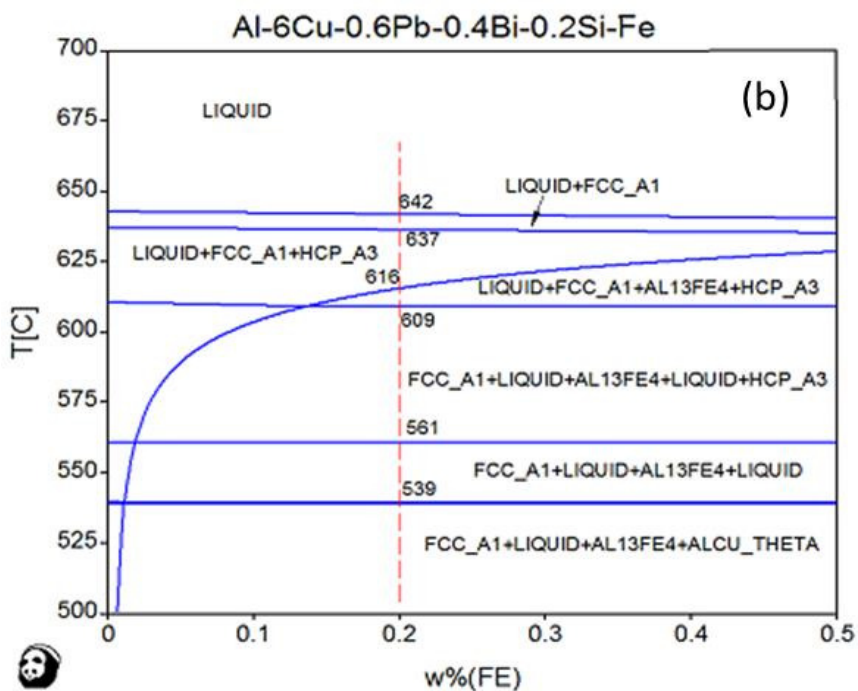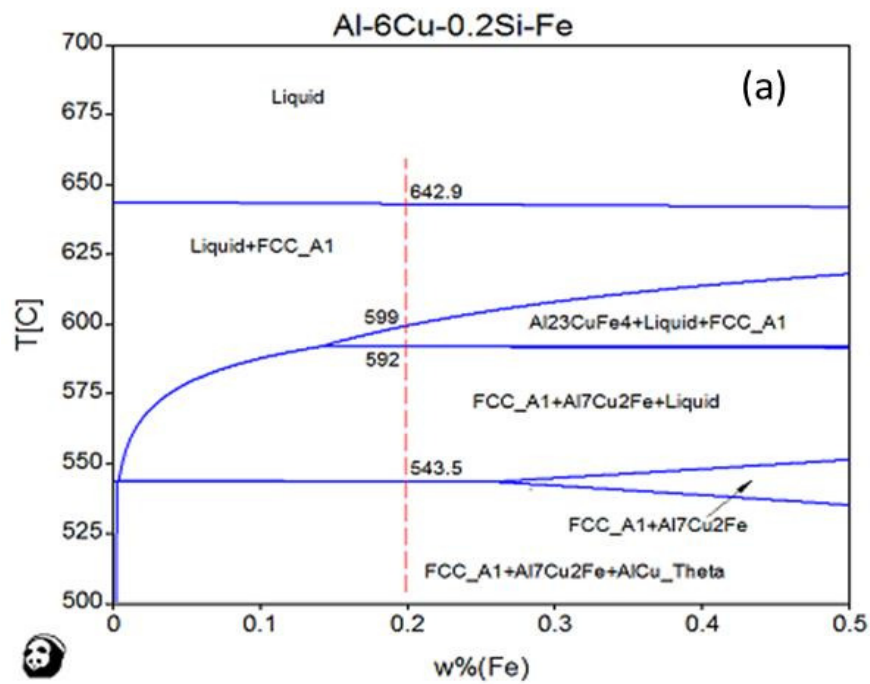
Figure 4-105 Phase diagram of (a) Al-6Cu-0.2Si-0.2Fe calculated from PanAl database and (b) Al-6Cu-0.4Pb-0.6Bi-0.2Fe-0.2Si calculated from SSOL2 database.

4.5 Optimised cast structure

In this chapter the untreated DC cast billets are compared to the optimised casting conditions identified for immiscible monotectic systems though previous sections in this chapter. The combined effect of shearing, superheat and inoculant on the microstructure of immiscible systems Al-Pb is discussed. This section is divided, as previously, in 3 subsections, in which the 3 main regimes of monotectic Al-Pb alloys are covered, i.e. hypo-, exact monotectic and hyper-monotectic compositions. The inoculant added is in the novel inoculant, described in previous sections. The chosen superheat is 860°C, and shearing speed 6000 rpm, as previously mentioned.

4.5.1 Hyper-monotectic binary alloy

The amount of inoculant added is detailed in Section 4.3.1.2. In this section the untreated billet, whose melt is heated to 820°C, is compared to the casting which provides the smallest particle size and the biggest amount of particles per unit area, for which the melt containing Al-Ti and Al-B has been heated to 860°C and sheared at 6000 rpm.

Optical images of Pb particles, in the Al matrix, across the top and bottom of the billet, are shown on **Figure 4-106** and **Figure 4-107** respectively. **Figure 4-108** comprises SEM back scattered images across the bottom of the billet. Untreated billets (a, b) are compared with the optimised microstructure obtained by the combination of shearing, superheat and inoculant additions (c,d). A quantitative analysis of average particle size (a) and number of particles (b) across and along both billets is shown in **Figure 4-109** and **Figure 4-110,** respectively.

It is clear that the combination of the melt treatment processes, not only has a very significant impact on the particle size, distribution and number, but it creates a homogeneous structure from edge to centre and top to bottom, eliminating the Pb segregation and sedimentation.
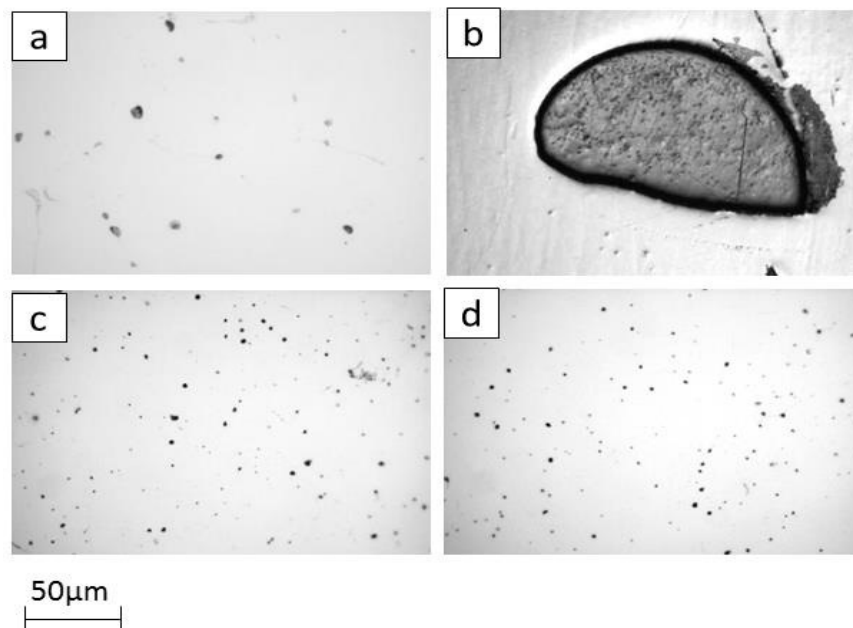
Figure 4-106 Optical micrographs of the DC cast Al-3Pb billets, cast at 790°C at 140 mm/min, corresponding to: (a, c) edge and (b, d) centre on the top of the billet: (a,b) untreated reference billet and (c,d) optimised billet (containing Al-Ti and AlB, heated to 860°C and sheared at 6000 rpm) .
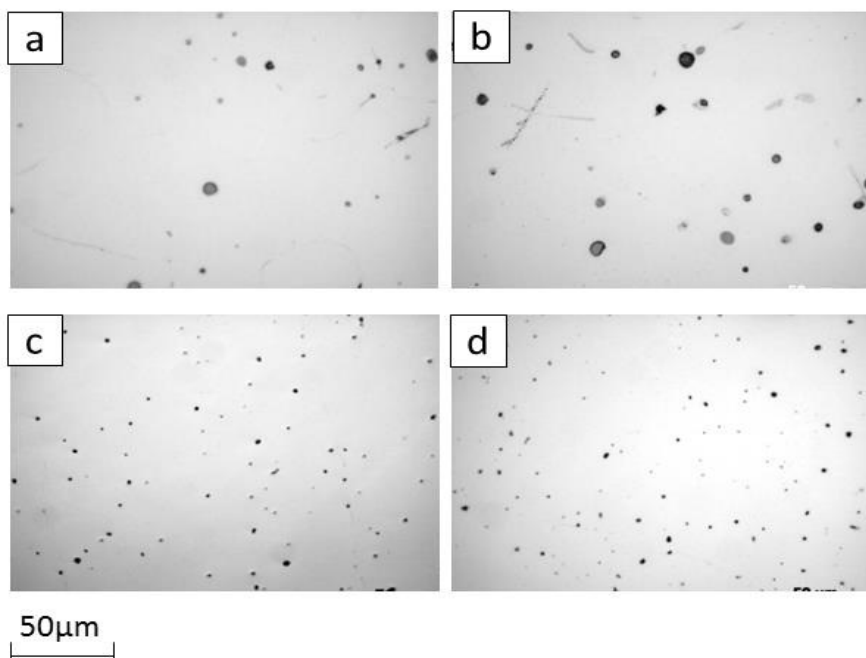
Figure 4-107 Optical micrographs of the Al-3Pb DC cast billets, cast at 740°C and 140 mm/min, corresponding to (a, c) edge and (b, d) centre on the bottom of the billet: (a,b)

untreated reference billet and (c,d) optimised billet (containing Al-Ti and AlB, heated to 860°C and sheared at 6000 rpm).
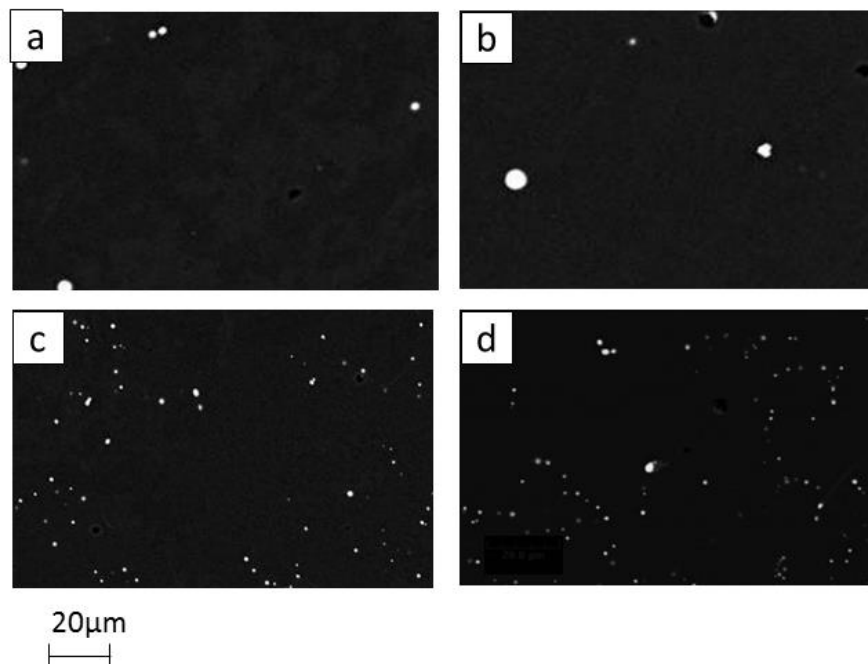
Figure 4-108 SEM images of the Al-3Pb DC cast billets, cast at 740°C and 140 mm/min, corresponding to (a, c) edge and (b, d) centre on the bottom of the billet: (a,b) untreated reference billet (c,d) optimised billet (containing Al-Ti and AlB, heated to 860°C and sheared at 6000 rpm).
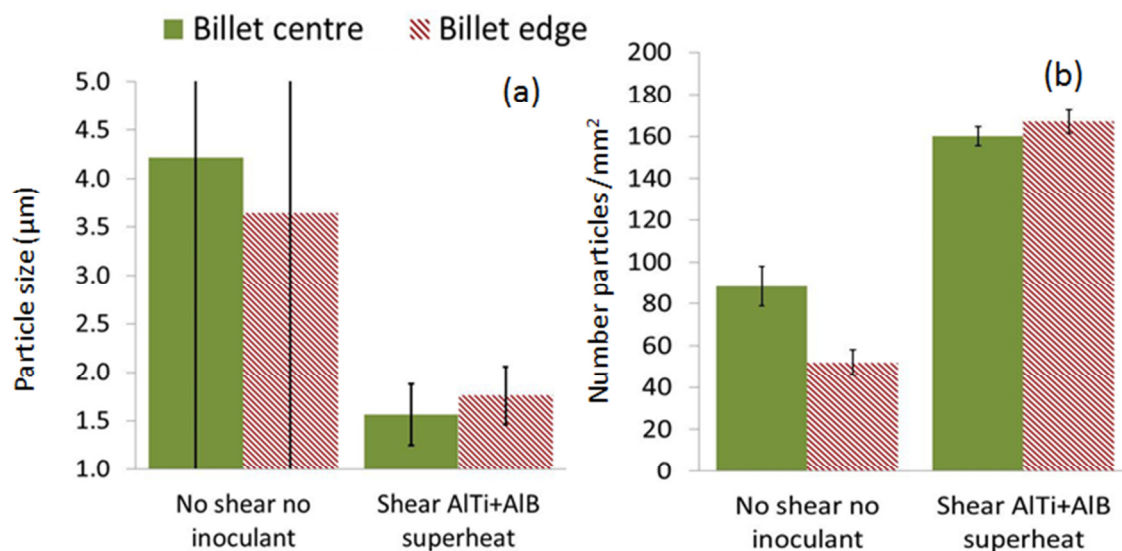
Figure 4-109 Comparison of Al-3Pb DC cast untreated billet with the optimised billet (containing Al-Ti and AlB, heated to 860°C and sheared at 6000 rpm): (a) Particle size and (b) number of particles from edge to centre of the billet.
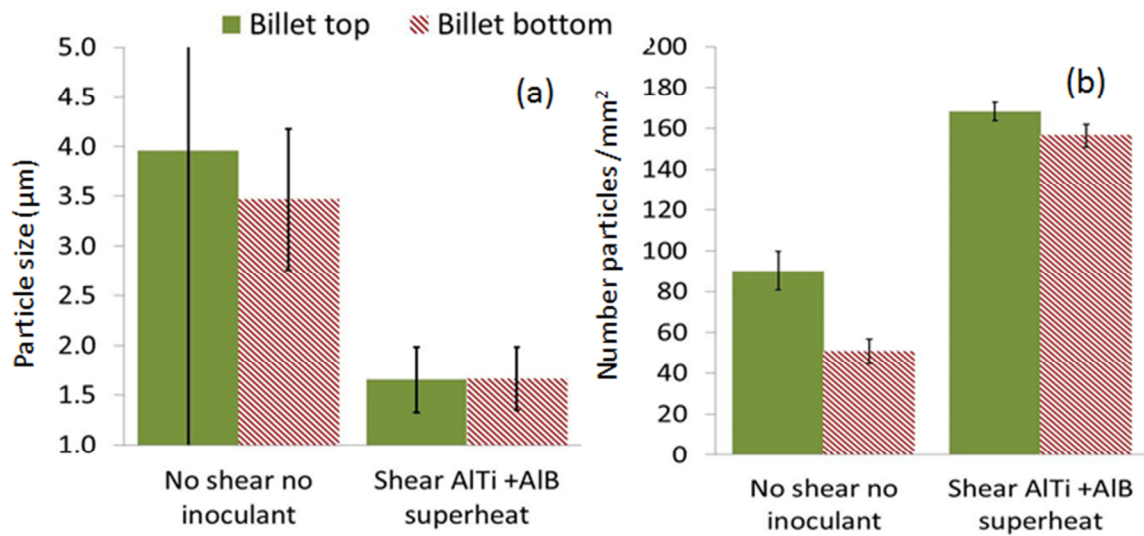
Figure 4-110 Comparison of Al-3Pb DC cast untreated reference billet with the optimised billet (containing Al-Ti and Al-B, heated to 860°C and sheared at 6000 rpm): (a) Particle size and (b) number of particles from top to bottom of the billet.

Figure 4-111 shows the quantitative analysis of the relative of Pb particles, calculated as the area occupied by the Pb particles in the Al matrix, divided by the average particle size. This is not only an indication of the amount of Pb distributed through the billet but, as it is divided by average size, is also an indication of the level of refinement of the soft phase within the matrix. The comparison of untreated and optimised cast is shown across (a) and along the billet (b). With the optimised casting conditions a significant increases in the relative Pb area (indicating a reduction or elimination of Pb sedimentation and segregation and or a reduction in particle size) is obtained.
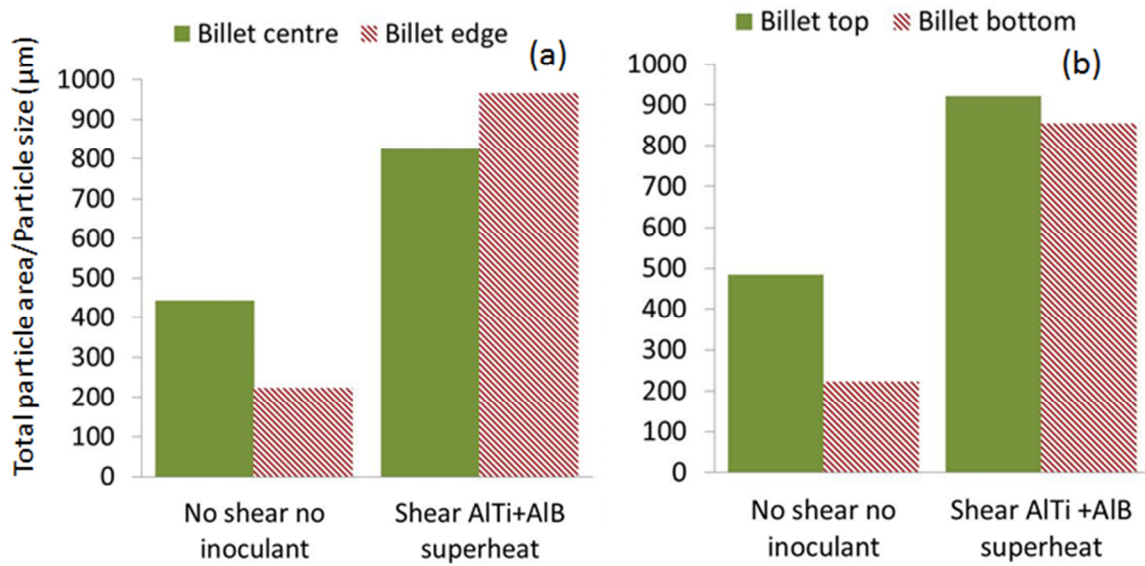
Figure 4-111 Relative particle area occupied by Pb in Al-3Pb DC cast billet, comparing: untreated reference billet and optimised billet (containing Al-Ti and Al-B, heated to 860°C and sheared at 6000 rpm).

The effect of optimised casting conditions on average Pb particle size and number of particles is summarised in **Table 4-12**. A reduction from 3.8 to 1.6 µm (60% reduction) in particle size and an increase of more than 100% in the number of particles can be observed.

Table 4-12 Average number of particles and particle size for Al-3Pb DC cast billet.

Cast	Number particles/mm²	Particle size (µm)
No inoculant, no shear	70	3.8
Al-Ti + Al-B, superheat, shear	166	1.6

The effect of the combination of the 3 melt treatments on Al-3Pb DC cast billets is summarised in **Figure 4-112 Figure 4-113**. In **Figure 4-112** the particle size distribution for untreated billet is compared to the optimised cast. It is clear that the particle size distribution changes significantly with the optimised casting conditions, being the majority

of the particles between 0.9 and 2.4 µm. Contrary to the untreated melt where the majority of the particles have a size between 1.5 and 4.4 µm. Furthermore, as seen on **Figure 4-113** in with the optimised casting conditions Pb segregation and sedimentation is eliminated and a homogeneous Pb content along the billet is obtained. However it was not possible to reach the 3 % nominal.
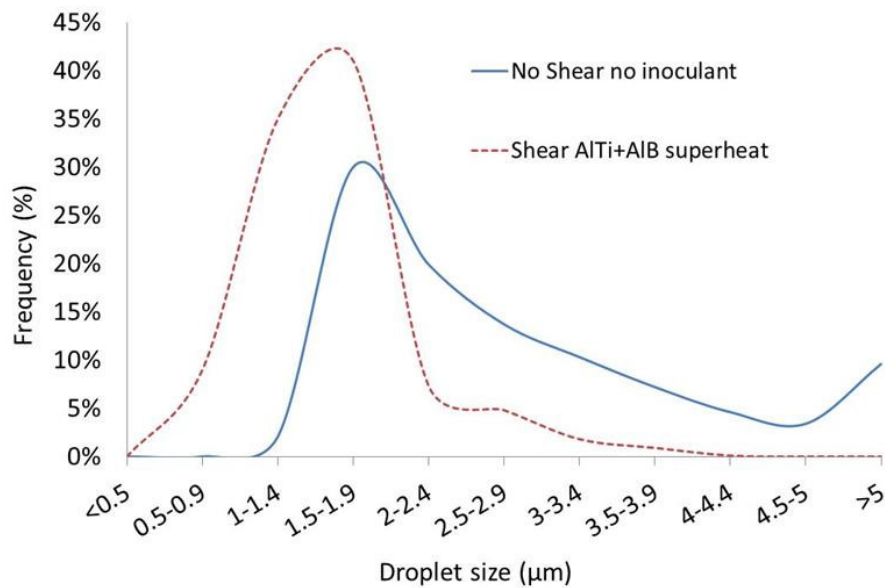
Figure 4-112 Effect of the optimised casting conditions compared to the reference untreated billet on the particle size distribution for the Al-3Pb DC cast billet.
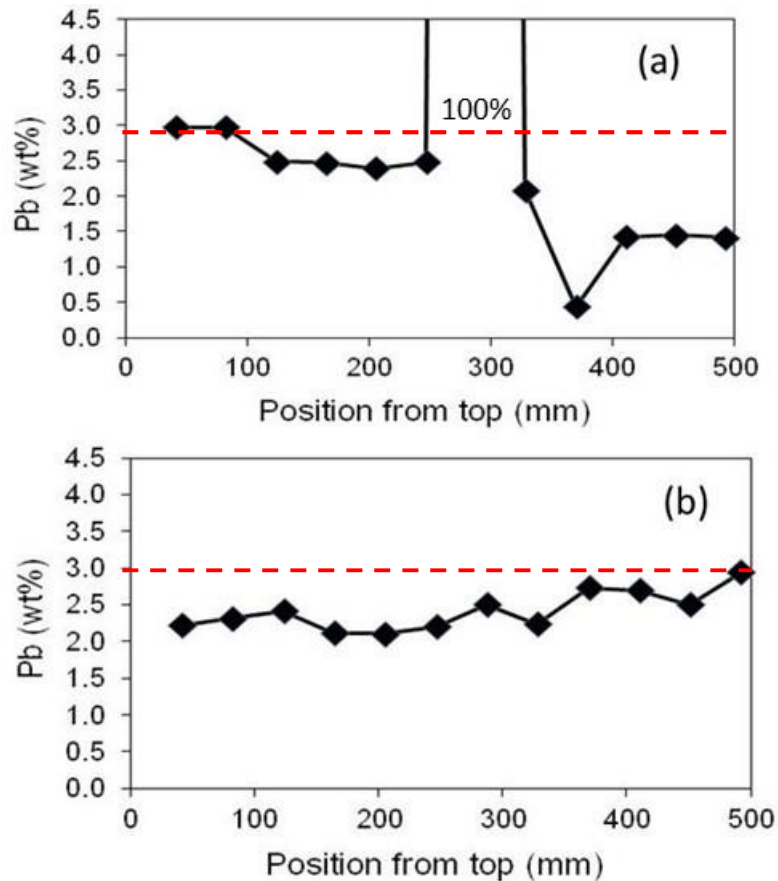
Figure 4-113 Results of the spark analysis, indicating Pb composition in wt% from the top to the bottom of an Al-3Pb DC cast billet, for: (a) the untreated reference billet (b) optimised billet (containing Al-Ti and Al-B, heated to 860°C and sheared at 6000 rpm).

4.5.2 Monotectic binary alloy

The amount of inoculant added is detailed in **Section 4.3.2.2.** In this section the untreated billet, heated to 740°C, is compared to the casting which provides the smallest particle size and the biggest amount of particles per unit area, for which the melt containing Al-Ti and Al-B has been heated to 860°C and sheared at 6000 rpm.

Optical images of Pb particles, in the Al matrix, across the top and the bottom of the billet, are shown on **Figure 4-106** and **Figure 4-107** respectively. The untreated billets (a,b) are compared with the optimised microstructure obtained by the combination of shearing, superheat and novel inoculant additions (c,d). The quantitative analysis of particle size (a) and number of particles (b) is shown in **Figure 4-116** and **Figure 4-117**.

It can be seen that the combination of the 3 melt treatment processes provides a significant increase in the number of particles on the billet. Although the average size from both casts differs considerably, specially in the centre and top of the billet, this is mainly due to the size heterogeneity with the majority of the particles being in the range of 1 to 2 µm, but a very small proportion of them getting values of several millimetres.
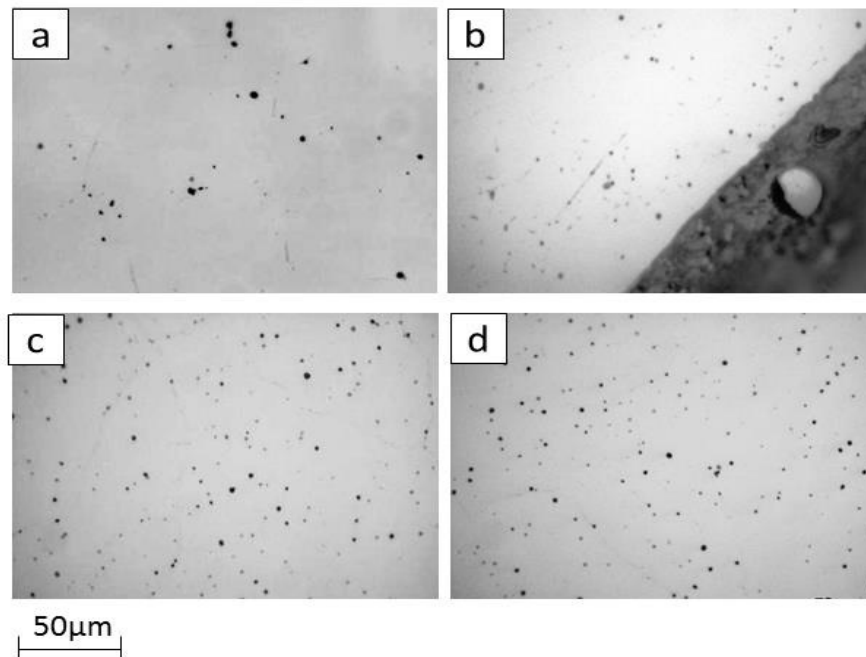
Figure 4-114 Optical micrographs of the Al-1.2Pb DC cast billets, cast at 740°C and 140 mm/min, corresponding to (a, c) edge and (b, d) centre on the top of the billet: (a, b) reference untreated billet and (c, d) optimised billet (containing Al-Ti and Al-B, heated to 860°C and sheared at 6000 rpm).
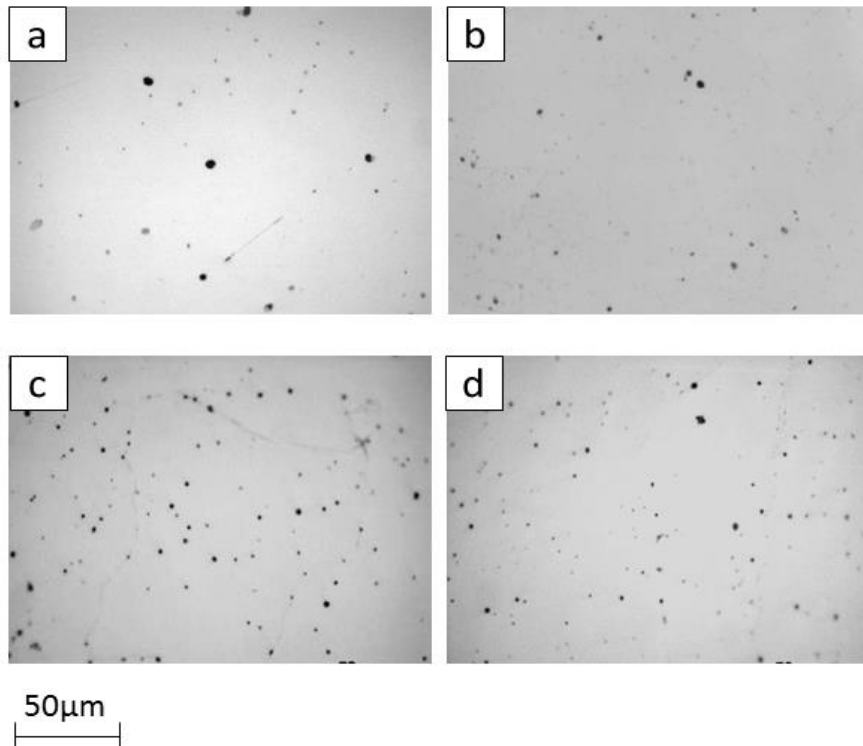
Figure 4-115 Optical micrographs of the Al-1.2Pb DC cast billets, cast at 740°C and 140 mm/min, corresponding to: (a, c) edge and (b, d) centre on the bottom of the billet: (a,b) reference untreated billet and (c,d) optimised billet (containing Al-Ti and Al-B, heated to 860°C and sheared at 6000 rpm).
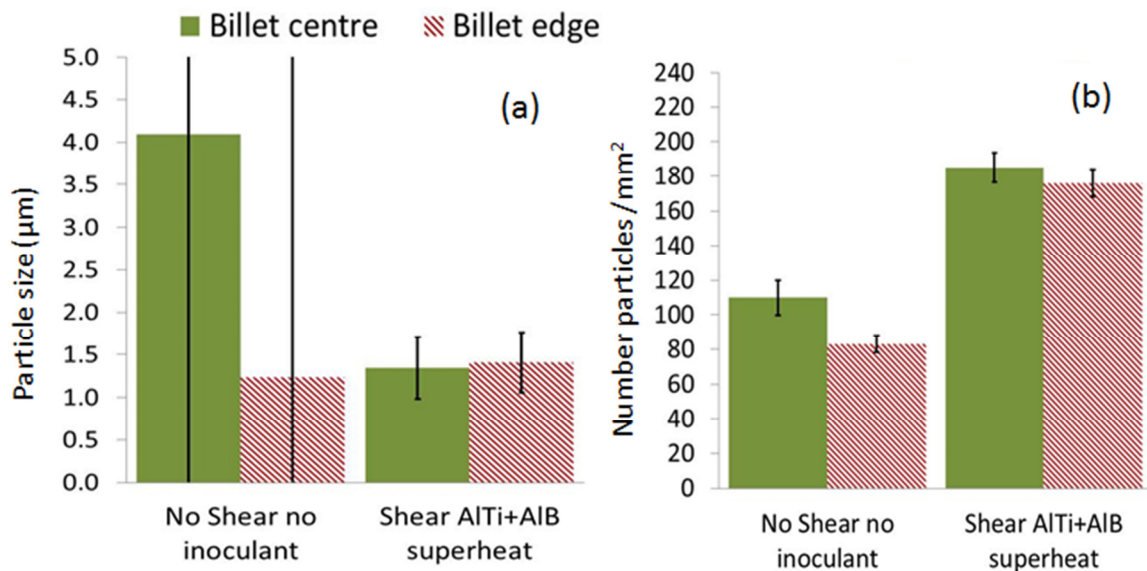
Figure 4-116 Comparison of Al-1.2Pb reference untreated DC cast billet with the optimised billet: (a) Particle size and (b) number of particles from edge to centre of the billet.
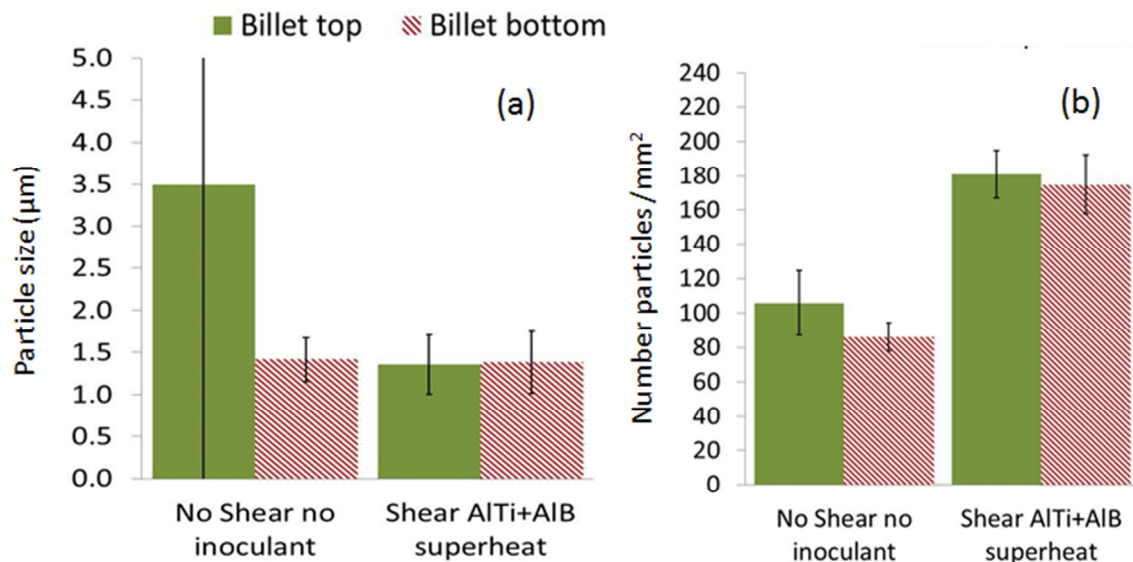
Figure 4-117 Comparison of Al-1.2Pb reference untreated Dc cast billet with the optimised billet: (a) Particle size and (b) number of particles from top to bottom of the billet.

Figure 4-118 shows the quantitative analysis of the relative of Pb particles, calculated as the area occupied by the Pb particles in the Al matrix, divided by the average particle size. The comparison of both casts indicates an increase in the amount of Pb distributed through the billet and refinement of the soft phase within the matrix, for the optimised casting conditions. This improvement is observed across (a) and along (b) the billet of Pb sedimentation and segregation and or a reduction in particle size.
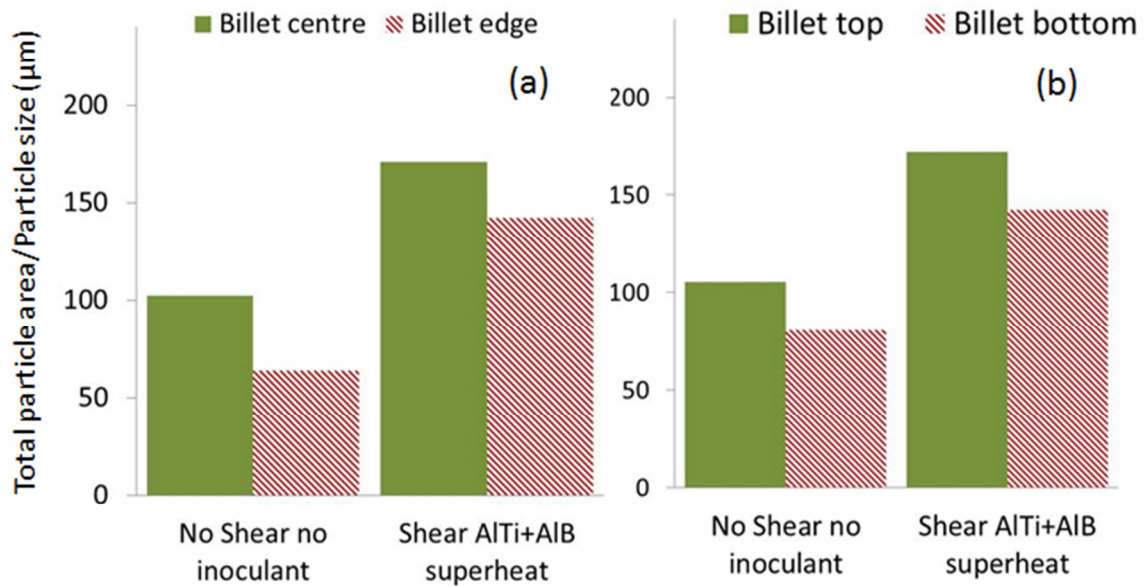
Figure 4-118 Relative particle area occupied by Pb in the Al matrix: comparison of Al-1.2Pb alloy untreated DC cast billet with optimised billet.

For the optimised casting, the average particle size is reduced from 3.8 to 1.6 μm for hyper-monotectic the Al-3Pb hyper-monotectic alloy, and from 2.6 to 1.3 μm for the Al-1.2Pb monotectic composition, as shown in **Table 4-12** compared to **Table 4-13**. The number of particles increases from 70 to 166 per unit area for the hyper-monotectic alloy and from 96 to 178 particles per unit area for the monotectic alloy. The results highlight the dependency of particle size on Pb content for binary immiscible systems Al-Pb.

Table 4-13 Average number of particles and particle size for Al-1.2P DC cast billet.

Cast	Number particles/mm²	Particle size (μm)
No inoculant, no shear	96	2.6
Al-Ti + Al-B, superheat, shear	178	1.3

The effect of the three melt treatments combined on Al-1.2Pb monotectic alloys in DC casting is summarised in **Figure 4-119** and **Figure 4-120**. In **Figure 4-119** the particle size distribution for untreated billet is compared to the optimised DC cast billet. It is clear that

190

the particle size distribution changes significantly with the optimised casting conditions, increasing the number of the particles between 0.5 and 1.7 μm, and decreasing proportionally the particles between 1.7 and 3.5 μm. Furthermore, as seen on **Figure 4-120** for the billet cast in the optimised conditions the Pb sedimentation and segregation is completely eliminated, and a completely homogeneous structure is obtained.
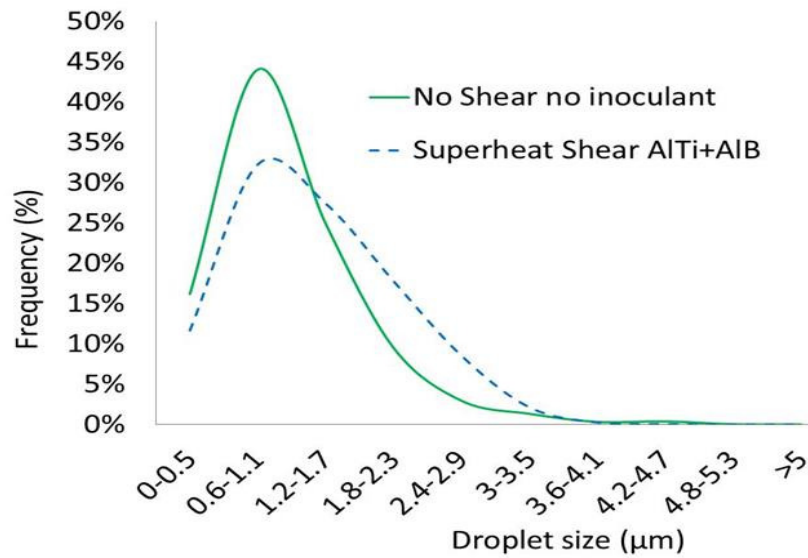
Figure 4-119 Effect of the optimised casting conditions compared to reference untreated billet on the particle size distribution for the Al-1.2Pb DC cast billets.
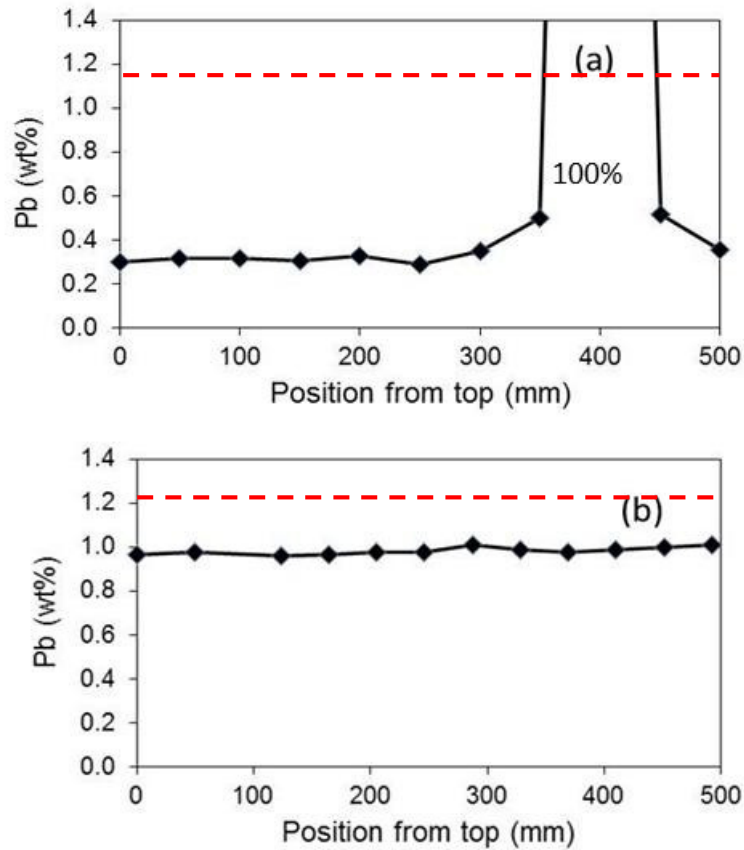
Figure 4-120 Results of the spark analysis, indicating Pb composition in wt% from the top to the bottom of an Al-1.2Pb DC cast: (a) reference untreated billet (b) optimised billet.

By comparing **Figure 4-120** (b) and **Figure 4-113** (b) it is clear that is much easier to get the target content of Pb along the billet for monotectic than for hyper-monotectic systems.

4.5.3 2011 alloy

The amount of inoculant added is detailed **in Section 4.3.3**. In this section the reference cast billet, heated to 740°C, containing Al-5Ti-B is compared to the casting which provides the smallest particle size and the biggest amount of particles per unit area for which the melt containing Al-Ti and Al-B has been heated to 860°C and sheared at 6000 rpm.

SEM back scattered images of Pb particles, in the Al matrix, across the top and bottom of the billet, are shown on **Figure 4-121** and **Figure 4-122** respectively. The untreated billets (a,b) are compared with the optimised microstructure obtained by the combination of

shearing, superheat and novel inoculant additions (c,d). Quantitative analysis of number of particles and particle size for those billets is shown in **Figure 4-123**. The quantitative analysis of particle size (a) and number of particles (b) is displayed in **Figure 4-124**. It is clear that the combination of shear, superheat and novel inoculant, provides a significant decrease in particle size and increase in the number of particles along and across the billet. Although it is important to mention the heterogeneity of particle sizes for both casting conditions as indicated by standard deviation in the graphs.
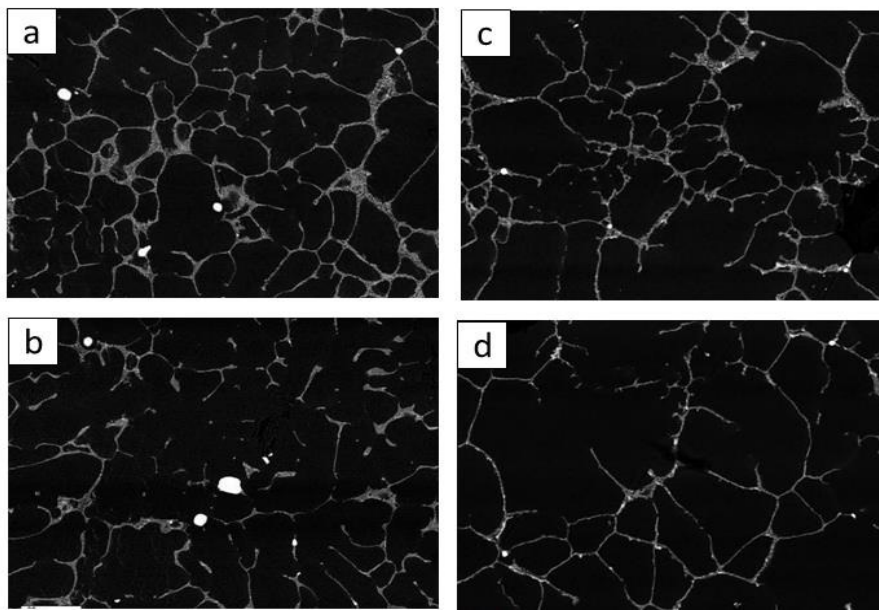
Figure 4-121 SEM images of the 2011 DC cast billets, cast at 740°C and 140 mm/min, corresponding to (a, c) edge and (b, d) centre on the top of the billet: (a,b) reference billet containing Al-5Ti-B (c,d) optimised billet (containing Al-Ti and Al-B, heated to 860°C and sheared at 6000 rpm).
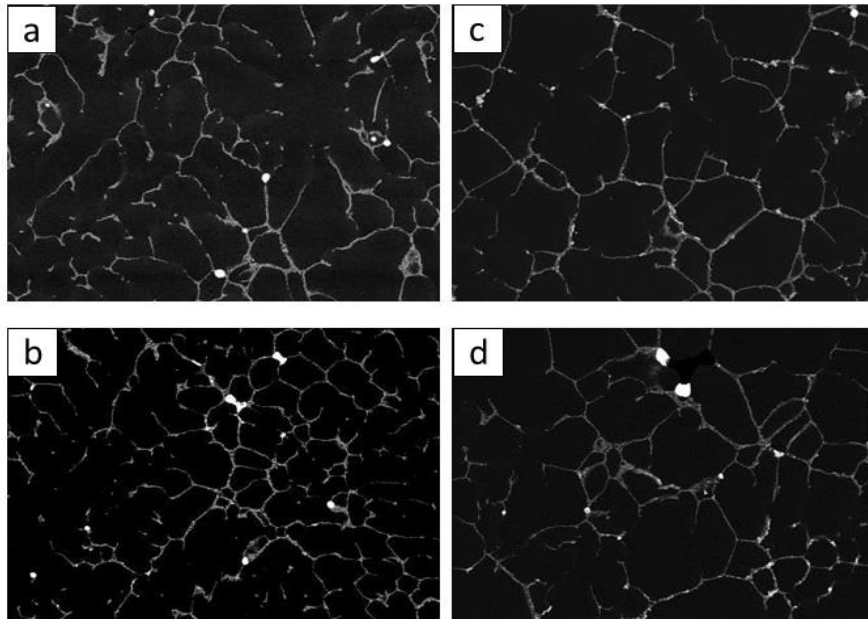
Figure 4-122 SEM images of the 2011 DC cast billets, cast at 740°C and 140 mm/min, corresponding to (a, c) edge and (b, d) centre on the bottom of the billet: (a,b) reference untreated billet containing Al-5Ti-B (c,d) optimised billet (containing Al-Ti and Al-B, heated to 860°C and sheared at 6000 rpm).
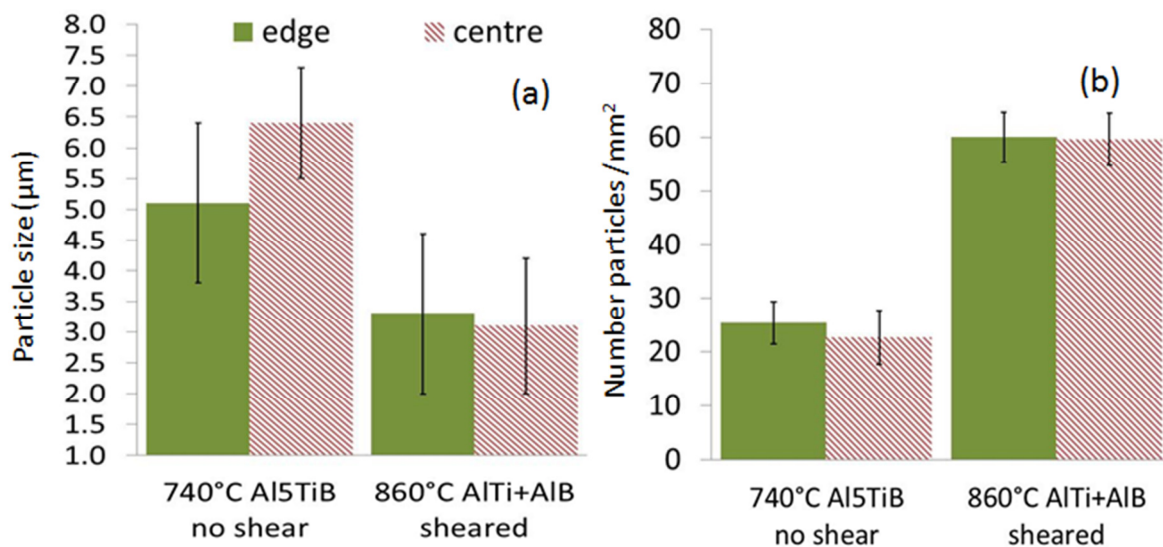
Figure 4-123 Comparison of 2011 reference untreated DC cast billet (containing Al-5Ti-B) with the optimised billet: (a) Particle size and (b) number of particles from edge to centre of the billet.
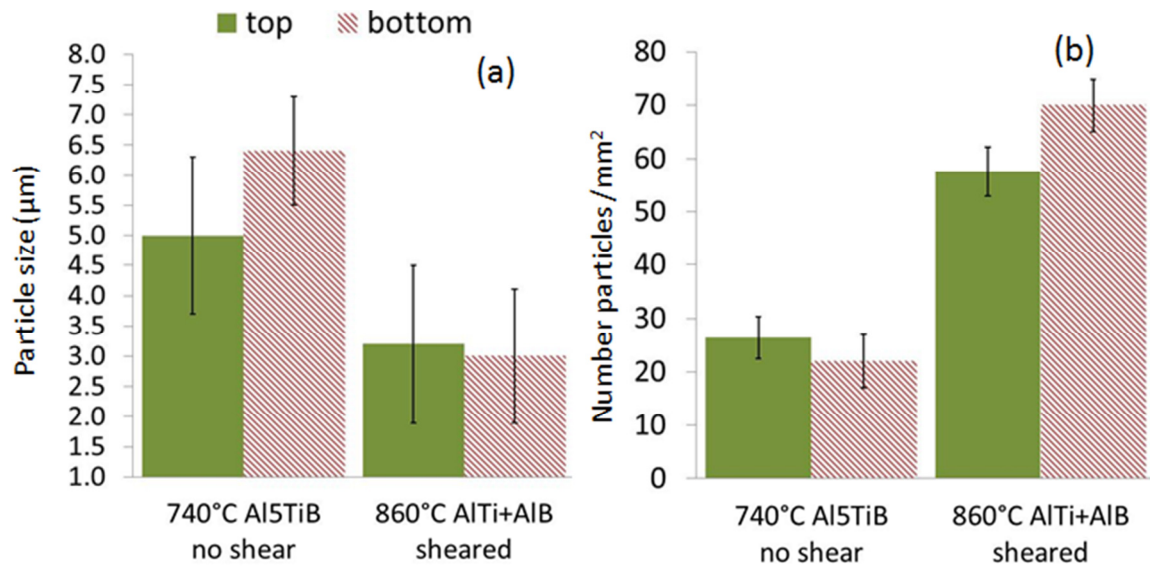
Figure 4-124 Comparison of 2011 reference untreated DC cast billet (containing Al-5Ti-B) with the optimised billet: (a) Particle size and (b) number of particles from top to bottom of the billet.

Figure 4-125 shows the quantitative analysis of the relative of Pb particles, calculated as the area occupied by the Pb particles in the Al matrix, divided by the average particle size. The comparison of both casts indicates an increase in the amount of Pb distributed through the billet and refinement of this soft phase within the matrix, for the optimised casting conditions, for the melt superheated to 860˚C, containing Al-Ti and Al-B and sheared at 6000 rpm. This improvement is observed across (a) and along (b) the billet of Pb sedimentation and segregation and or a reduction in particle size.
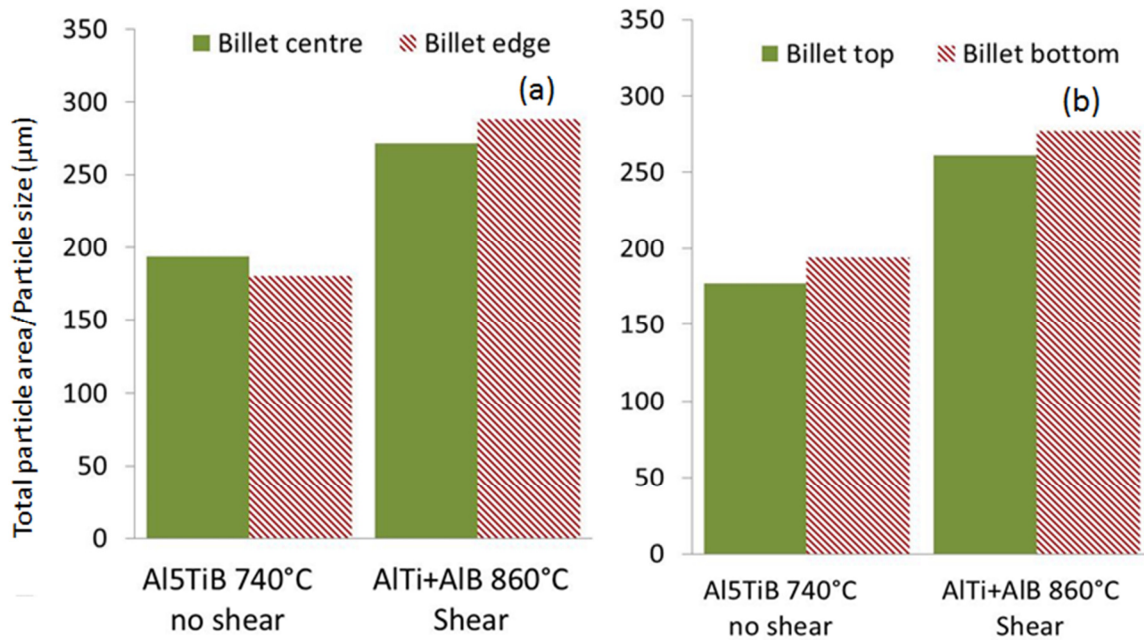
Figure 4-125 Relative particle area occupied by Pb in the Al matrix: comparison of 2011 alloy reference DC cast billet with a sheared billet, with Al-Ti and Al-B and superheat to 860˚C.

For the optimised casting, the average particle size is reduced from 5.7 to 3.2 μm and the number of particles increased from 18 to 61 per unit area, compared to the reference cast, as seen on **Table 4-14**. It is well known that the particle size of the second immiscible phase increases proportionally to its concentration. Nevertheless, contrary to what was expected, the particle size for 2011, which corresponds to hypo-monotectic region of the phase diagram, is bigger than that of the Al-1.2Pb system, as seen by comparing the value of particle size from **Table 4-14** and **Table 4-13.**

Table 4-14 Average number of particles and particle size for 2011 DC cast billet.

Cast	Number particles/mm^2	Particle size (μm)
Al-5Ti-B, 740°C, shear	18	5.7
Al-Ti + Al-B, superheat, shear	61	3.2

196

The effect of shear, superheat and inoculant on the solidified microstructure of DC cast 2011 alloy billets is summarised in **Figure 4-119**. It is clear that the particle size distribution changes significantly with the newly identified casting conditions, increasing the number of the particles between 0.5 and 3 µm, and decreasing proportionally the particles between 3 and 9 µm.
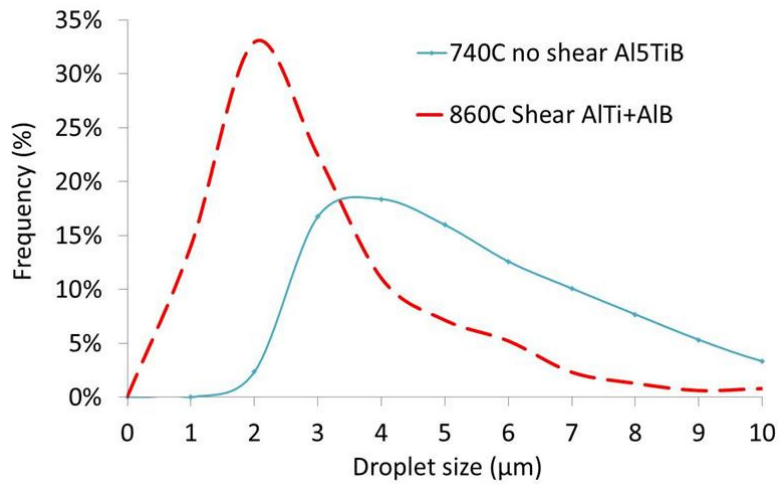
Figure 4-126 Effect of the optimised casting conditions, compared to reference untreated billet, on the particle size distribution for 2011 DC cast billets.

Chapter 5

Discussion

The discussion of the main results, which were presented in the previous chapter, will be covered in detail in the present chapter. The individual contribution of shearing, inoculant, and superheat on the Pb microstructure will be discussed in detail.

As mentioned in **Chapter 2**, the solidification paths for each of the chosen alloys are expected to differ significantly. While the hyper-monotectic Al3-Pb shows demixing of the liquid phase, and therefore nucleation of the Pb droplets, before the commencement of solidification. For the monotectic composition Al-1.2Pb and for alloy 2011, the demixing or nucleation of Pb droplets takes place at the same time as the aluminium starts to precipitate. Therefore, considerable differences in the solidified microstructures would be expected.

The most significant difference is the distribution of the minority phase within the ingot, and therefore the level of sedimentation and macrosegregation, which finally affects the composition of Pb along the casted ingot. For the hyper-monotectic Al-Pb alloy a strong uneven phase distribution leads to a strong macrosegregation **Figure 4-12** and **Figure 4-18.** The segregation cannot be completely eliminated (composition of the ingot is approximately 2.5 % in the upper region to 3 % in the bottom region), even under the combined effect of inoculant, superheat and shearing (see **Figure 4-113**).

It is generally known that at low superheat temperatures and short holding times localised temperatures can originate compositional heterogeneities within the melt. These compositional heterogeneities can induce in the melt localised areas with Pb contents in the hyper-monotectic region. Therefore, due to the phase separation that was taking place in the crucible during the pouring (see **Figure 4-24**), considerable macrosegregation towards the central part of the ingot is observed for the binary alloy of exact monotectic composition (**Figure 4-120 (a)**).

By contrast, for 2011 alloy, which contains only 0.4 % Pb and 0.6 % Bi, the soft immiscible phase distribution along the ingot is homogeneous even for the untreated melt, cast under conventional conditions. The soft phase particles are more regularly distributed between the Al-Cu and Al-Cu-Fe phases on the microstructure. This clearly indicates that the liquid separation occurred during primary solidification. However, small variations on droplet size between the top and bottom part of the ingots are observed from **Figure 4-30** and **Figure 4-31**.

The second difference is the droplet size distribution, which is affected by the joint contribution of nucleation and growth. Therefore this phase distribution will be affected by diffusion, melt convection, and droplet motion. Furthermore, it is generally known that the average droplet size of the minority soft phase in immiscible systems, is directly related to its concentration in the alloy. For conventional DC casting, it is observed experimentally that the average droplet of the alloy of exact monotectic composition is 32% lower than the average droplet for the hyper-monotectic alloy. The values are taken from **Table 4-3** and **Table 4-4,** where quantitative information about average particle size and number of particles is displayed, for hyper- and exact monotectic compositions, respectively.

However, droplet sizes of eutectic Pb/Bi in 2011 alloy are bigger than those in any of the binary systems (**Table 4-5** compared to **Table 3-3** and **Table 4-4**). This is believed to be related to the addition of 6 % Cu, known to increase the liquid-liquid interfacial tension and reduce further the miscibility of Pb in aluminium (Kaban et al., 2008; Kaban et al., 2007). A Gaussian distribution relates frequency to droplet size for each of the studied alloy systems, for both the conventional and optimised casting conditions, as seen from **Figure 4-32**, **Figure 4-58**, **Figure 4-99**, **Figure 4-112** and **Figure 4-119** in **Chapter 4**.

A tendency for segregating to the central region of the ingot, with more and slightly bigger particles, is observed in DC casting of monotectic and hyper- compositions (**Figure 4-16**, **Figure 4-17**, **Figure 4-22** and **Figure 4-23** respectively).

As seen in **Chapter 4**, under conventional DC casting conditions, immiscible alloys exhibit significant segregation of the solidified microstructure. However, under optimised casting conditions, i.e. by using the combination of shearing, superheat and adequate inoculant additions, it was possible to alter each of the individual factors, which contribute to droplet

coalescence, and restrict therefore the droplet growth and sedimentation. Consequently, a final solidified microstructure in which Pb particles are finely and uniformly distributed was obtained under the optimised casting conditions. The newly obtained microstructure represents a very significant improvement in the refinement of Pb particles in an Al matrix, and Pb/Bi eutectic particles in an Al-6Cu alloy.

Inoculant additions, shearing and superheat can improve the solidified microstructure for the 3 alloys systems studied in this work, despite the different solidification paths which characterise each of these alloys. The main effect of each of the individual melt treatments can be summarised as follows:

- Shearing creates a more uniform size distribution both along the length and across the width of the ingot, provides a minor refinement on average size of the particles and increases their number per unit area. However, it does not eliminate the compositional segregation of Pb in the centre/bottom of the ingot, and therefore does not achieve the nominal Pb composition on the cast ingot.

- Combination of shearing with Al-Ti and Al-B additions (to form TiB_2 particles in the melt) can significantly refine and improve the distribution of Pb particles not only for hyper- and exact monotectic compositions, as seen on **Table 4-6** and **Table 4-7**, but for 2011 alloy (**Table 4-8**). Although the combination of shearing and TiB_2 particles cannot eliminate completely the Pb compositional segregation and achieve nominal composition values along the ingot length, for hyper- and monotectic concentrations, it reduces segregation/sedimentation considerably.

- Superheat to 860°C, after the inoculant (Al-Ti and Al-B) has been added to the melt and before it has been sheared, creates the finest and most uniform distribution of Pb on the microstructure. It produces changes in the solidified microstructure of α–Al and Al-Cu matrixes and eliminates the Pb compositional segregation along the ingot length for hyper- and exact monotectic alloy systems (see **Chapter 4, Section 4.4**).

1.45.1 Effect of shearing

The effect of shearing on the size and distribution of the soft immiscible phases in binary and ternary aluminium alloys was studied. Shearing decreases the average size of the particles and increases their number density, for both Pb droplets in Al and Pb/Bi eutectic particles in the Al-6Cu alloy (2001 alloy). The high shear device is the key element in the MC-DC process to deliver several advantages to the DC casting process. The high shear device and the advantages of its use for melt conditioning are described in **Chapter 2, Section 2.3**. One of the major functions of the high shear device is its dispersive mixing action: the centrifugal force created by the rotation of the rotor generates a negative pressure inside the stator, which in turn sucks the melt below the high shear device into the stator and forces it to escape at high speed through the openings in the wall of the stator. This process subjects the melt to a high shear action in the gap between the rotor and the stator, and in the openings in the stator wall. The shear rate achieved can be many orders of magnitude higher than that provided by electromagnetic stirring. As a consequence shearing has 2 main effects on immiscible alloys systems, i.e. it not only promotes droplet break up and emulsification but also reduces considerably the Marangoni and Stokes motion of the droplets.

It was determined that for droplet break up, under the effect of shearing, the Capillary number (K) has to be larger than a critical value, which in turn determines the minimum droplet size that can be ruptured (Fan et al., 2001). This critical capillary number depends on the viscosity ratio, as represented in **Figure 5-1**. The following formulas were employed to calculate those parameters (Duan et al., 2003):

$$k = \frac{2\mu_m r \dot{\gamma}}{\sigma_{L1L2}} \qquad\qquad (5\text{-}1)$$

where K is the *capillary number*, σ_{L1L2} is the interfacial tension between two liquids (Jm^{-2}), $\dot{\gamma}$ is the shear rate (s-^{1}). The shear rate is calculated dividing the shearing velocity (m/sec) by the size of the gap in m, r is the droplet radius (m) and μ_d and μ_m are the viscosities of the droplets and matrix respectively (Pas).

$$\Lambda = \frac{\mu_d}{\mu_m} \qquad\qquad (5\text{-}2)$$

Where Λ is the viscosity ratio, μ_d is the viscosity of the liquid droplets (Pas) and μ_m is the viscosity of the matrix (Pas).

The parameters of the equations are described in **Chapter 2, Section 2.3.**
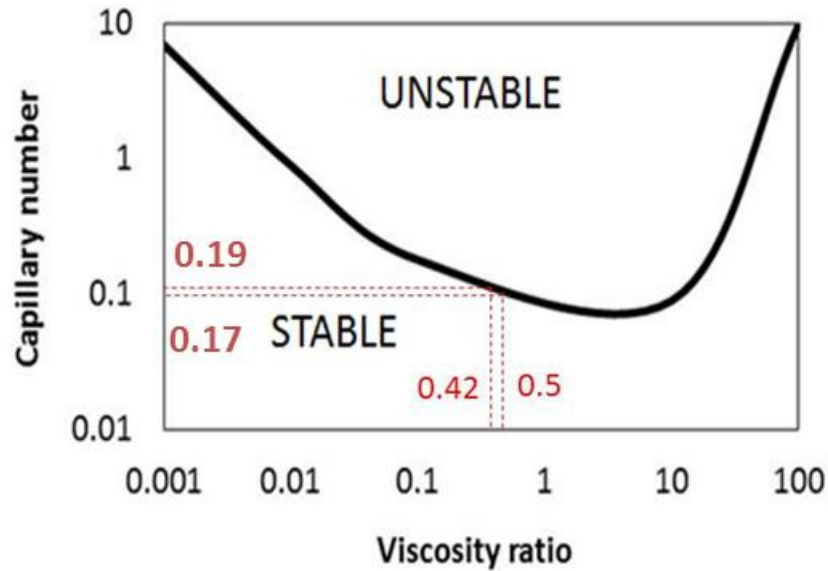
Figure 5-1 Capillary number and viscosity ratio: Droplet stability under shearing.

For the binary systems Al-Pb, considering the viscosity of aluminium and Pb droplets at 660°C to be 0.003 and 0.0015 Pa.s, respectively, the calculated viscosity ratio, using **Equation 5-2** is 0.5 at 660°C for binary alloys Al-Pb. At the same time, the viscosity values were calculated with the following equations:

$$\mu_m = C\,exp\left(\frac{E}{RT}\right) \qquad\qquad (5\text{-}3)$$

$$\mu_d = 0.0001492exp\left(\frac{1986.9}{T}\right) \qquad\qquad (5\text{-}4)$$

Where μ is the viscosity (Pa s), C (Pa s) and E (Jmol^{-1}) are constants and R the ideal gas constant (Jmol^{-1}K^{-1}).

Taking the value calculated for viscosity ratio to **Figure 5-1**, it is possible to determine the critical Capillary number *(K)* to get to an area of droplet instability. In this case the value for binary Al-Pb alloys is 0.17, as seen in **Figure 5-1**.

The values obtained of the critical Capillary number should be linked to the minimum droplet size above which rupture can take place. In **Figure 5-2** the critical *K* values are plotted as a function of droplet size. For that, values of interfacial tension need also to be calculated, using the following equation:

$$\sigma = \sigma_0 \left(1 - \frac{T}{T_c}\right)^{1.26}$$ *(5-5)*

Where σ is the interfacial tension (Jm^{-2}), σ_0 is a constant (Jm^{-2}), T is the absolute temperature of the system (K), T_c the critical temperature (K), which for the Al-Pb binary system was calculated from the phase diagram with a value of 1695.4K.

Using the previous equation a value of 0.12 J/m^2 has been obtained, for the interfacial tension Al-Pb at 660°C. Shear rate $\dot{\gamma}$ provided by the high shear device at 6000 rpm is 623818 s^{-1}.

Taking the critical Capillary number as an input to **Figure 5-2**, it can be seen that the size at which the droplets become unstable and therefore break under the effect of shear is 5.4 µm. In other words, for droplets smaller than 5.4 µm will not break under the current shearing conditions.
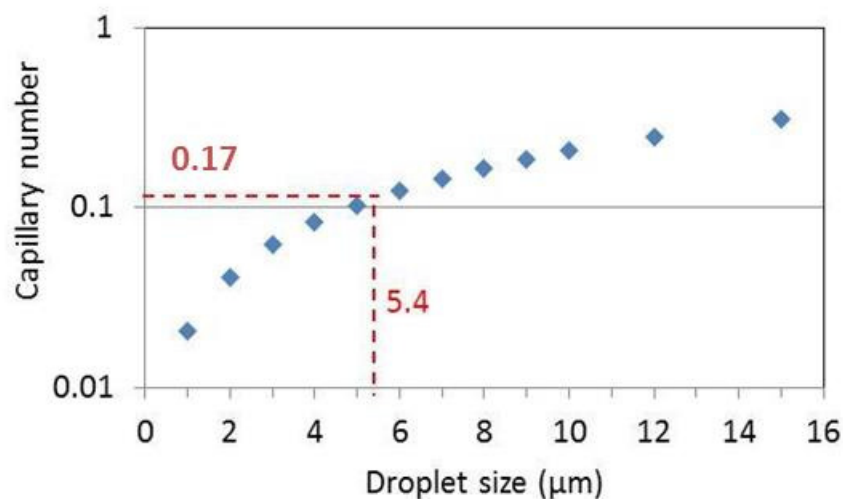
Figure 5-2 Capillary number as a function of droplet size for Al-Pb alloys.

For 2011 alloy, if we consider the viscosity of aluminium and Pb droplets at 647°C to be 0.0034 and 0.0014 Pa.s, respectively, the calculated viscosity ratio, using Equation 5.2 is 0.42 at 647°C for 2011 alloy. Those viscosity values were calculated with the following equations:

$$\mu_{dd\prime} = 0.000494 exp\left(\frac{754.1}{T}\right) \qquad (5\text{-}6)$$

$$\mu_m = 0.0004636 exp\left(\frac{1036.7}{T}\right) \qquad (5\text{-}7)$$

Where $\mu_{dd\prime}$, μ_m are the viscosities of the soft phase droplets (Pa S) and T is the absolute temperature (K).

For the calculated viscosity ratio of 0.42, the critical Capillary number *(k),* to get to an area of droplet instability is 0.19, as seen on **Figure 5-1.**

Taking the value calculated for viscosity ratio to **Figure 5-1**, it is possible to determine the critical value of K to get to an area of droplet instability. In the case of 2011 alloy the critical Capillary number takes a value of 0.19.

In **Figure 5-3** the calculated value of *K* values are plotted against droplet size. To calculate *k* is necessary to determine first the values of interfacial tension and shear rate. Interfacial tension for Al-Cu/Pb-Bi is calculated using **Equation 5-5,** and for the employed conditions takes a value of 0.104 J/m^2.

Taking the critical capillary number as an input in **Figure 5-3**, it can be seen that the size at which the droplets become unstable and therefore break under the effect of shear is 4.5 μm. In other words, for droplets smaller than 4.5 μm the rupture will not be initiated under the current shear conditions.
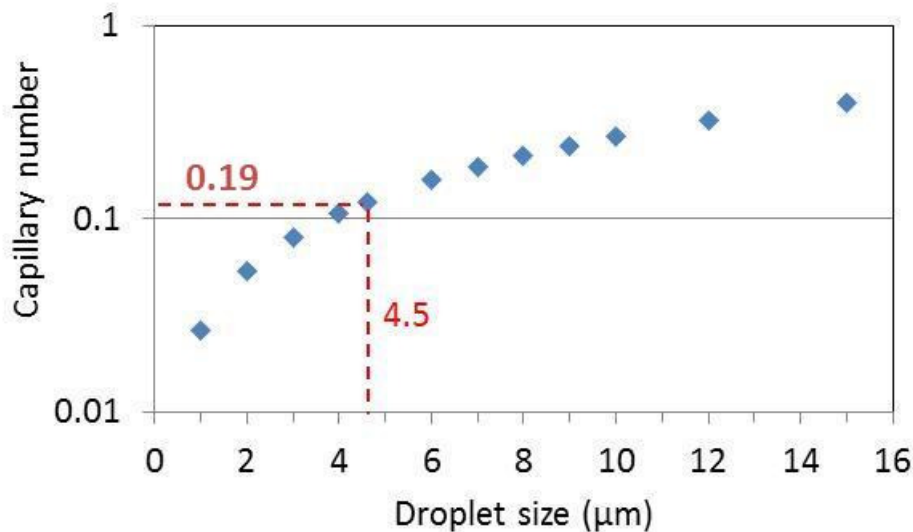
Figure 5-3 Capillary number as a function of droplet size for 2011 alloy.

Both alloys have viscosity ratio values within 0.3<Λ<1.5, therefore it is expected that droplet break up will be easily induced (Fan et al., 2001).

The importance of affecting the phase separation from its initial stage, i.e. the nucleation of the Pb droplets is highlighted in this study. Therefore, the melt temperature during shearing is critical for the effectiveness of the shearing process.

Results from the DC simulator experiments demonstrate that, for the hyper-monotectic Al-3Pb alloy, a considerably improved distribution of the soft phase in the final solidified microstructure, is achieved when the melt is sheared from above the decomposition (binodal) temperature to the monotectic reaction temperature (see **Figure 4-5** to **Figure 4-9**).

 The temperature at which the melt is sheared is determined by the cast temperature, the position of the shear and the shearing speed. The position of the shear is fixed with respect to the sump (see **Figure 5-4**), for all the DC casting experiments. This position provides a shearing temperature that is just below the liquidus temperature of the alloy. Not only reducing/eliminating the time available for coalescence, but also increases the viscous forces as well as slows down diffusion and reduces agglomeration.

As a consequence, shearing will affect each of the three alloys at different stages during their solidification paths: for hyper-monotectic Al-3Pb alloy the shearing will act on the already nucleated Pb droplets, and for the monotectic and hypo-monotectic (2011 alloy) it will be affecting the droplets as demixing occurs, during their nucleation process. Therefore, during the DC casting experiments it was not possible to shear from above the decomposition temperature of 780°C. The efficiency of shearing was, hence reduced for the hyper-monotectic Al3-Pb alloy, compared to the alloy of exact monotectic composition. This can be seen by comparing the quantitative results in **Table 4-3** to those in **Table 4-4**, where the effect of shearing, on droplet size and distribution, is summarised for alloys of hyper- and exact monotectic composition. For the alloy of exact monotectic composition shearing decreases the droplet size by approximately 50%, however for the Al-3Pb hyper-monotectic alloy tehr educiton in droplet size under the effect of shear is only around 30%.
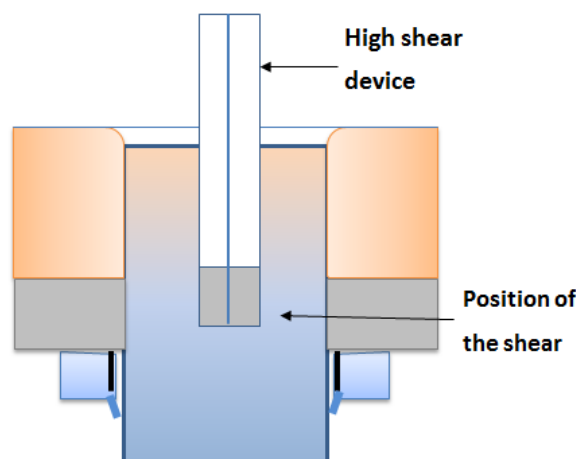
Figure 5-4 Drawing indicating the position of the shear with respect to the graphite mould in the DC cast unit.
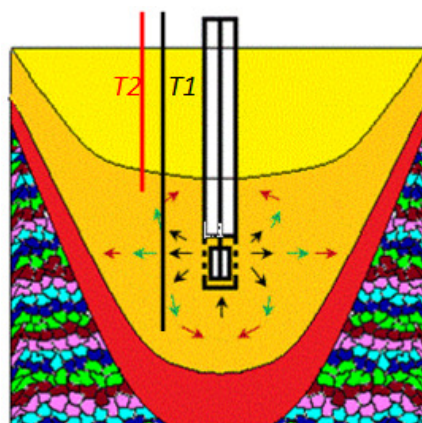
Figure 5-5 Position of the thermocouples in the sump.

It can therefore be concluded that the rupture and dispersion of the droplets is one of the effects of shearing on immiscible systems. However, it is generally known that the fine liquid suspension, created by shearing, will become unstable and will demix rapidly under the effect of Stokes and Marangoni motions once the shear deformation field is removed (Briscoe et al., 1999). Hence, the importance of reducing not only the time available for coalescence but the Marangoni and Stokes velocities of the droplets, which is another important microscopic effect created by shearing on immiscible systems. The reduction of Marangoni of Stokes velocity under the shearing effect is a consequence of the uniform temperature created in the sump, as explained in the following paragraphs.

Figure 5-6 shows the solidification profile of 2011 alloy, comparing sheared and non-sheared melt, and **Figure 5-5** comprises a schematic representation of the position of the thermocouples with respect to the sump. Initially the melt is casted without shearing, then the shear is introduced in the position previously indicated, and the shearing process starts, after a transition period (**Figure 5-6**), the temperature in the sump becomes uniform. The liquid rapidly escaping from the openings on the stator will create a macroscopic flow pattern in the sump. This macroscopic flow provides a distributive mixing action in the sump, which homogenizes not only the temperature but the chemical composition of the melt.

Due to this temperature uniformity within the sump, the calculated thermal gradient *(G)*, for sheared melt is only 0.012 °C/mm. The value of G, for sheared melt is more than 50 times lower than that calculated considering the temperature difference in the sump before the shearing commences. The effect of this temperature gradient on the Marangoni velocity is plotted in **Figure 5-7. Figure 5-7 (**a) shows the Marangoni velocity as a function of droplet size for both the non-sheared and sheared melt, and it clearly highlights the effect of shearing to significantly reduce the Marangoni motion of the droplets. The values of the Marangoni velocity for the sheared melt are plotted in **Figure 5-7 (b**), considering an average droplet size of 5 μm, the Marangoni velocity will take a value of 0.002 mm/sec.

Therefore, it is clearly seen, that shearing can reduce the Marangoni velocity of the droplets by nearly 3 orders of magnitude compared to the untreated melt.
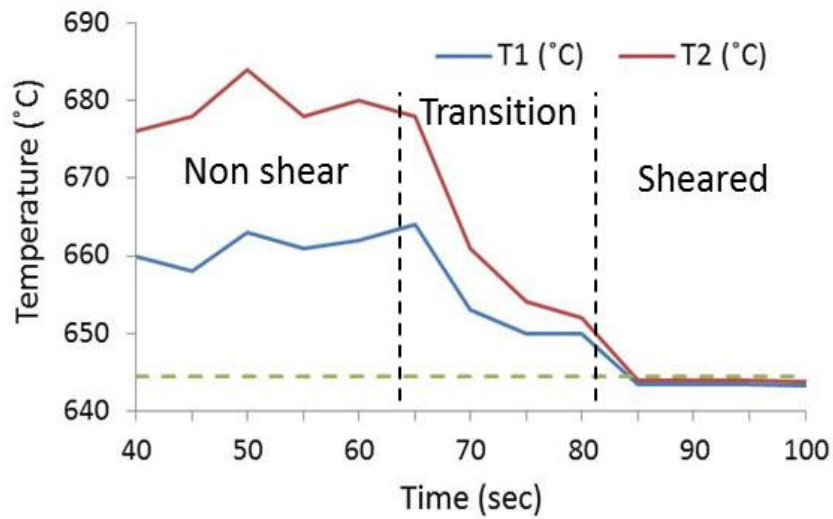
Figure 5-6 Temperature recorded in 2 different positions in the sump during DC casting of 2011 alloy.
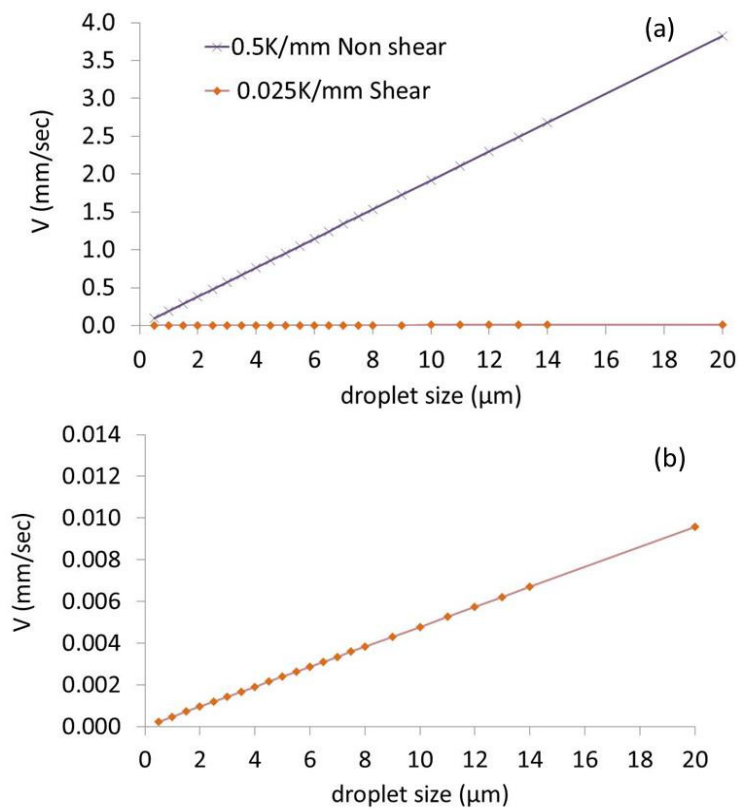
Figure 5-7 Marangoni velocity as a function of the droplet size: (a) for both sheared and non-sheared ingot and (b) smaller scale to show the values of Marangoni velocity for the non-sheared ingot.

The effect on Stokes motion is a secondary effect coming from the reduction of the average droplet size as Marangoni velocity is reduced. As seen from **Equation 5.8**, the Stokes velocity depends on droplet size, therefore the smaller the droplet the smaller the Stokes forces.

$$V_s = \frac{2g\Delta\rho r^2}{3\mu_m} \cdot \frac{\mu_d + \mu_m}{3\mu_d + 2\mu_m} \qquad (5\text{-}8)$$

Where V_s is the *Stokes sedimentation velocity (ms^{-1})*, g is the gravity force (N) and $\Delta\rho$ is the density difference between both phases (Kgm^{-3}).

To conclude, shearing improves the distribution of the immiscible Pb droplets in the aluminium matrix. Shearing has two effects on immiscible alloys systems, i.e. it not only promotes droplet break up and emulsification but it also creates a macroscopic flow, providing a distributive mixing action in the sump, which homogenizes the temperature and chemical composition of the melt, consequently reducing considerably Marangoni and Stokes motion of the droplets.

1.5 5.2 Effect of particle additions

The refinement and uniform distribution of Pb droplets in the presence of particular inoculant particles have been discussed in several publications (Ratke and Diefenbach, 1995) (Kotadia et al., 2009; Scadovelli et al., 1999). The present study shows the effect of inoculant additions on the size distribution of Pb particles in the immiscible system Al-Pb. The chosen alloys represent three different regions on the phase diagram Al-Pb, that is Hypo-, Hyper- and monotectic compositions, and therefore three different solidification paths have been considered. Theoretically, for alloys of completely homogenous and exact monotectic (or hypo-monotectic) composition, the solidification path will dictate that Pb nucleation takes place at the same time as the α-Al starts to form and therefore the inoculant additions will have no or very limited effect. Therefore it was initially believed that the effect of inoculant

additions would only be relevant for the alloy presenting demixing of the liquid phase and nucleation of the Pb droplets before the onset of solidification, i.e. Al-3Pb.

It is generally known that at low superheat temperatures and short holding times localised temperatures can originate compositional heterogeneities within the melt. These compositional heterogeneities can induce in the melt localised areas with Pb contents in the hyper-monotectic region. This would explain why inoculant additions have an effect on alloys of exact monotectic composition, as demonstrated in the present work (see **Figure 4-50** to **Figure 4-58**).

The precise moment at which the droplets nucleate and the unset of the nucleation to the formation of α–Al could not be stablished. The resolution from the in situ solidification experiments of Al-1.2Pb samples (**Chapter 4, Section 4.1**), only allows accounting for droplets larger than 2 μm. However, when droplets start to nucleate they have a much smaller size and therefore the nucleation process and the identification of the stage at which it takes place cannot be experimentally determined. The results from those experiments show that just the addition of the inoculant particles reduces considerably the sedimentation of the Al-Pb alloy of monotectic composition (**Figure 4-49**), while maintaining a very similar size distribution and average size of Pb particles (see **Figure 4-48**).

Evidence suggesting an enhanced heterogeneous nucleation of Pb on those potent inoculant TiB_2 particles, is found in the present work. It is strongly believed that the presence of certain particles (TiB_2 in this case) can affect the initial stage of phase separation, by enhancing the heterogeneous nucleation of the liquid soft phase droplets in the aluminium matrix (Kaban et al., 2009) .From **Figure 5-8** Pb can be seen on the interface of particular planes on the TiB_2 particles. Similarly to the nucleation of aluminium in the presence of suitable grain refiners, the droplets will nucleate on the surface of the inoculant particles, thus considerably increasing the number density of nucleated droplets and decreasing proportionally their sizes. However, contrary to the case of aluminium solidification, the lattice misfit between the nucleating solid substrate and the nucleated liquid droplet cannot be taken into consideration, as the nucleated phase remains liquid and therefore it does not have a crystal structure.
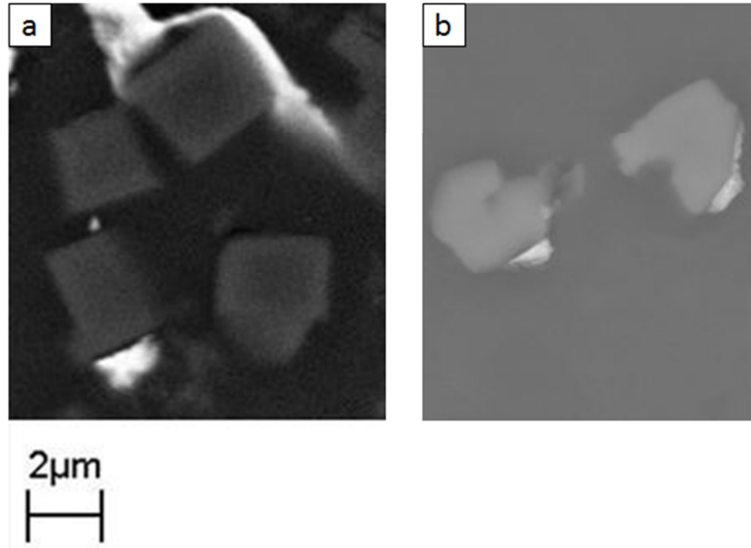
Figure 5-8 SEM back scattered images of Pb covering particular faces of the TiB₂ particles. The images are obtained from the Al-3Pb filtered samples.

According to the classical nucleation theory, the energy barrier for homogeneous and heterogeneous nucleation can be calculated as follows:

$$\Delta G_{hom} = \frac{16\pi}{3} \frac{\sigma_{L1L2}^3}{\Delta G_v^2} \qquad (5\text{-}9)$$

$$\Delta G_{het} = \Delta G_{hom} f(\theta) \qquad (5\text{-}10)$$

$$f(\theta) = (2 - 3cos\theta + cos^3\theta)/4 \qquad (5\text{-}11)$$

ΔG_v is the Gibbs free energy change per unit area associated with formation of the L_2 phase (in the case of nucleation for immiscible systems) or between the undercooled liquid and the solid in the case of aluminium solidification. $\sigma^3{}_{L1L2}$ is the interfacial tension (Jm^{-2}) between the liquid and liquid in nucleation of Pb in aluminium and between solid and liquid in the solidification of aluminium, $f(\theta)$ is the catalytic factor and θ is the contact angle between the inoculant and the droplets of the minority phase.

As seen from **Equation 5-10** the barrier for heterogeneous nucleation is obtained by multiplying the homogeneous barrier for nucleation by the catalytic factor. To reduce the

barrier for nucleation and act as inoculants, these particles should provide an appropriate contact angle (θ) for the nucleation of the liquid Pb droplets, and therefore a catalytic factor lower than 1.

It is generally known that contact angles smaller than 90˚ correspond to high wettability, and they are observed when the liquid spreads on the surface (**Figure 5-8** shows the Pb spreading on the surface of the TiB_2 particles, indicating a good wettability), while large contact angles (>90˚) correspond to low wettability, and they are observed when the liquid beads on the surface, trying to minimise its contact with the surface and forming a compact liquid droplet.

As described by Young's equation, the contact angle of a liquid drop is defined by the mechanical equilibrium of the drop under the action of three interfacial tensions, between the solid nucleating particle and liquid 1, between the solid particle and liquid 2, and between liquid 1 and liquid 2:

$$\gamma_{l1l2}\cos\theta = \gamma_{sl1} - \gamma_{sl2} \qquad (5\text{-}12)$$

Where γ_{L1L2} is the interfacial tension between the 2 immiscible liquids, γ_{SL1} is the interfacial tension between the solid inoculant particles and liquid 1 and γ_{SL2} the interfacial tension between the solid and liquid 2 (Jm^{-2}).

The contact angle between Pb and TiB_2 was measured elsewhere (Kaban et al., 2011), employing a tensiometric technique. For the working temperature conditions, the calculated contact angles were between 22-25˚.

Considering those values for the contact angle, the catalytic factor takes the value calculated below:

$$f(\theta) = \frac{(2 - 3\cos 22 + \cos^3 22)}{4} = 0.004$$

$$f(\theta) = \frac{(2 - 3\cos 25 + \cos^3 25)}{4} = 0.006$$

$$\Delta G_{het} = \Delta G_{hom} 0.004$$

Giving the value of the contact angle and the small catalytic factor obtained, TiB_2 can be considered as a very potent inoculant, thus reducing considerably the barrier for heterogeneous nucleation of Pb droplets in the aluminium matrix, in the presence of, and therefore TiB_2 could.

From theoretical calculations, Al_2O_3 provides a better contact angle than TiB_2 for nucleation of Pb in an aluminium matrix. However, during experimental observation either ZrO_2 or TiB_2 particles proved more efficient (Kavan et al., 2010). Therefore the practical efficiency of both TiB_2 and ZrO_2 was tested experimentally during the current research. As seen from **Figure 4-35** and **Figure 4-36** both reduce the size and increase the number of particles on the final solidified microstructure.

 Evidence of the interaction between TiB_2 and Pb is provided in **Figure 4-42** and **Figure 4-43.** By comparing both figures it can be seen that more Pb particles are attached to pure TiB_2 particles, indicating that pure synthetic TiB_2 is more effective than the TiB_2 obtained from the reaction between Ti and B, contained in the Al-10Ti and Al-5B master alloys (see Appendix). However, inducing wettability of pure TiB_2 by aluminium has been proven very difficult during experimental trials, and therefore pure synthetic TiB_2 was inefficient and of low applicability, especially considering future industrial development.

Optimum results were therefore obtained with the inoculant made in situ by the reaction between Ti and B. This novel inoculant provides a reduction in droplet size of approximately 50% and an increase of 70% in the number of particles in the final solidified structure (**Figure 4-36**). The efficiency of the new inoculant is tested on DC cast ingots of hyper- (**Figure 4-37** to **Figure 4-41**) monotectic (**Figure 4-50 to Figure 4-53**), and hypo- Pb contents (**Figure 4-54** to **Figure 4-58).**

Fan (Fan et al., 2015; Fan, 2012) suggested that at the atomic level, the process of heterogeneous nucleation on a potent substrate can be considered as to occur by building the initial solid phase atom-by-atom Therefore, high resolution TEM observation of the interface between the TiB_2 particles, is crucial to determine if the absorption at atomic level is taking place as an initial stage of nucleation. **Figure 4-44**, **Figure 4-45** and **Figure 4-46** show an interface layer on the surface of the TiB_2 particles on the (0001) surface. By examining the electron diffraction (SAED) image in **Figure 4-45** a deviation in orientation

between (0001) TiB$_2$ and the layer on its surface is observed. The calculated d spacing, for the arrangements of atoms on the interface of the TiB$_2$ particles, differs from that of TiB$_2$. However, further analysis is required at higher resolution to confirm these results (see **Chapter 7**).

Contrary **Figure 4-46** shows no misorientation or difference in d spacing between the TiB$_2$ particles and the layer on its surface. These differences between the interfaces in both images could be an indication that not all particles present in the melt are acting as inoculants. Suggesting therefore, that nucleation of Pb on TiB$_2$ particles could only occur when absorption of a particular layer of atoms (believed to be a layer of Pb atoms) takes place on the surface of the TiB$_2$ particles. Furthermore for that absorption to take place the TiB$_2$ particles should be clean of remaining of aluminium borides and titanium aluminides.

On the other hand, it is proposed in several publications that certain solid insoluble particle can be absorbed on the interface of the minority phase droplets. This will result in a reduction in the interfacial energy (exposed surface is reduced), helping to stabilize metallic emulsions and avoiding, therefore, the droplet coalescence and growth (Budai and Kaptay, 2009).

The interfacial energy will retain the particles on the interface as long as the energy required to remove the particles is considerably larger than the energy of Brownian motion of these particles (Chen et al., 2014):

$$\Delta G_{remov} = \pi r^2 \sigma (1 - cos(\theta))^2 \qquad (5\text{-}13)$$

$$E_b = \frac{kT}{2} \qquad (5\text{-}14)$$

Where ΔG_{remove} is the *energy to remove the particle from the interface of the droplet (J)*, r is the average radius of the particles (μm), σ is the interfacial tension (Jm^{-2}) and θ is the wetting angle. E_b is the *brownian motion of the droplets (J)*, K is the Boltzmann constant which has a value of 1.38065 10^{-23} m^{2}kgs^{-2} K^{-1} and T is the absolute temperature of the liquids (K).

Considering an average radius of the particles of 2 μm, a value of the Boltzmann constant *(K)* of 1.38 10-23 $m^2kgs^{-2} K^{-1}$, a contact angle (θ) is 22˚, and using **Equation 5-5** to calculate interfacial tension as a function of the melt temperature, and **Equation 5-13**, **Equation 5-14** we can obtained the values of ΔG and E_b provided in **Table 5-1**.

As seen in **Table 5-1** the energy that keeps the particles attached to the Pb droplets is 6 orders of magnitude higher than their energy of Brownian motion, in the temperature range from 660 to 920˚C. Therefore, it is expected that the droplets and the particles will remain attached to each other.

Table 5-1 Energy to remove the particle from the interface and Brownian motion, calculated at different temperatures, assuming an average size of the particles of 2 μm.

Temperature (˚C)	AG (J)	E_b (J)
920	4.7 E-15	8.2 E-21
820	5.9 E-15	7.6 E-21
720	7.2 E-15	6.9 E-21
660	8.0 E-15	6.4 E-21

Figure 5-9 (a) shows the energy necessary to remove the particles from the droplet interface, as a function of the contact angle between the immiscible phase droplets and the particles; **Figure 5-7 (b)** shows the same energy but for small values of the contact angle. However, the contact angle that provides a higher energy interaction between the droplets and the particles is around 180˚.

However, evidence from the present work shows that the Pb appears always on the interface of the tested inoculant particles and no the particles around Pb, even when employing the nano-scaled ZrO_2 particles.
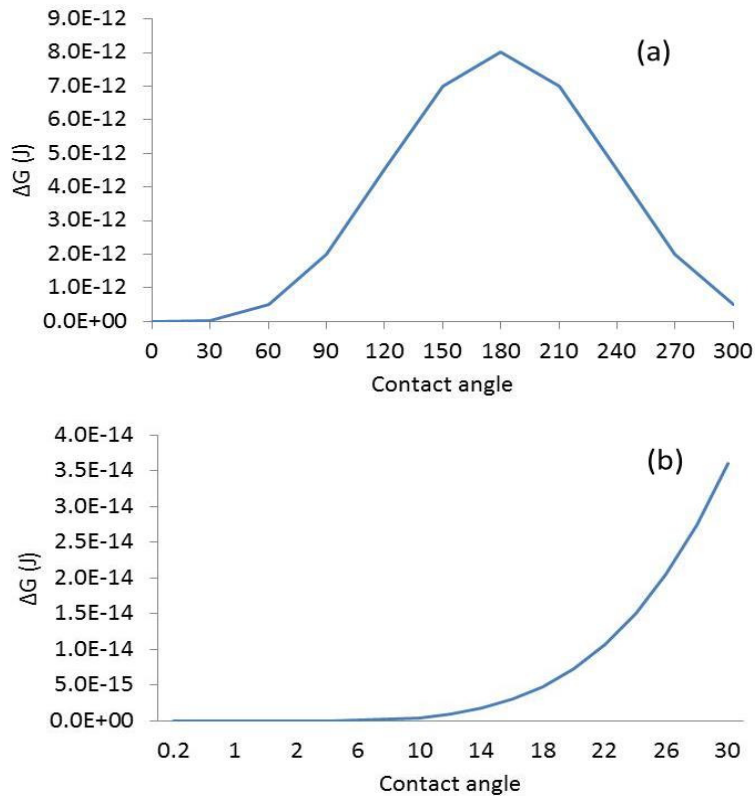
Figure 5-9 Energy to remove the particle from the interface, as a function of the contact angle, for (a) all angles (b) low contact angles, where TiB_2 is included.

To summarise, the combination of shearing and additions of TiB_2 reduces the size of the immiscible phase droplets, increases their number, and reduces considerably the compositional macrosegregation on the ingots. It is strongly believed that the mechanism responsible for this refinement is that of an enhanced heterogeneous nucleation of liquid Pb droplets on TiB_2 particles. However, further high resolution STEM examination is required as proposed in **Chapter 7**.

1.6 5.3   Effect of superheat

The effect of melt superheat can be divided into two effects:

- Direct effect provided by the superheat on the nucleation of the soft phase (Pb, Bi) in the aluminium matrix, which will affect the binary monotectic Al-1.2Pb and hyper-monotectic Al-3Pb alloys.

- Secondary effect as the superheat affects the nucleation and growth of aluminium, which in turn will affect the process of droplet coalescence and growth.

In the present work, after superheating the melt is cooled down to standard casting temperatures, therefore the ingots will be solidified under the same temperature gradient *(G)* and cooling rate *(R)* conditions. Consequently the effect of solidification conditions can be disregarded.

5.3.1   Effect of melt superheat on aluminium nucleation and growth

As the Pb/Bi content in 2011 alloy correspond to that of hypo-monotectic composition, their solidification paths will dictate that the droplets will nucleate when the α-Al starts to form, and therefore it is expected that their sizes and distribution will be linked to the dendritic arm spacing and the grain size. From **Figure 4-91** and **Figure 4-92**, a direct dependency between droplet size and secondary dendritic arm spacing is observed for 2011 alloy, casted in the steel mould. Droplet size is found to decrease linearly with secondary dendritic arm spacing (SDAS).

It is generally known that 2 factors significantly affect the refinement of grain structures of as-cast metals: insoluble suitable substrates and soluble solute elements. Insoluble substrates are in-homogeneities of different kinds existing in the melt, which act as heterogeneous nucleation sites, and solutes, like Fe and Cu, segregate at the growing solid/liquid interface to restrict the growth, providing more undercooling for nucleation (Zhou, 2015).

Multiple insoluble substrates, ranging from oxides to spinel and other impurities, are contained in liquid aluminium alloys. Hence, nucleation can occur practically at any temperature below the liquidus (Venkatarami et al., 1994). The maximum number of sites available for nucleation, no, has been reported to be in the range of 1.02×10^8 to 1.05 x

$10^8 m^{-3}$. With grain refinement, it has been reported to increase to a value in the range of 10^{11} to $10^{12} m^{-3}$.

For aluminium alloys high temperature, in the melt, promote the formation of α-Al_2O_3, instead of the γ-Al_2O_3 that normally forms when the melt is heated to around 700°C. γ-Al_2O_3 has a fcc structure with the following lattice parameters a, b, c = 0.79240 and between the (111)[110]//(111)[110] the lattice misfit Al/γ-Al_2O_3 has a value of 3.38. However, α-Al_2O_3 has a rhomboidal crystal structure with the following lattice parameters: a = 0.47587, c = 1.29929 and between the (0001)[10-10]//(100)[001] the lattice misfit Al/α-Al2O3 has a value of -0.48. This much lower value of the lattice misfit indicates that α-Al_2O_3 is a much more favourable substrate for aluminium nucleation. Furthermore due to the enhanced diffusion when the alloy melt is treated by high temperature superheat, the constituent atoms oxides might diffuse in the melt and the size of these alumina particles reduced (Wang et al., 2012, 2013; Li, 2011).

100 µm
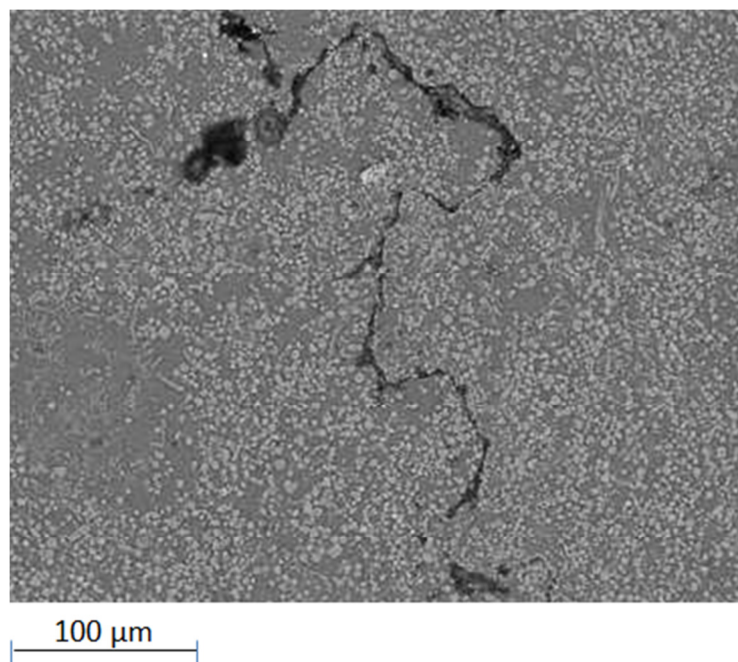
Figure 5-10 Low magnification SEM micrograph showing the continuous oxide layer in the aluminium matrix in Al, containing 0.1 % TiB₂, heated to 740°C and then pressure filtered.

When aluminium is melted, a thin protective amorphous film is formed. This amorphous film is thermodynamically unstable when compared to its crystalline counterpart and will transform (Men and Fan, 2010), after an incubation period of 5-10 min at 750°C. **Figure 5-10**

and **Figure 5-11** show the morphology of those oxides formed at 740°C. It can be seen that the dominant oxide formed at 740°C in CPAl are thin and continuous oxide films.
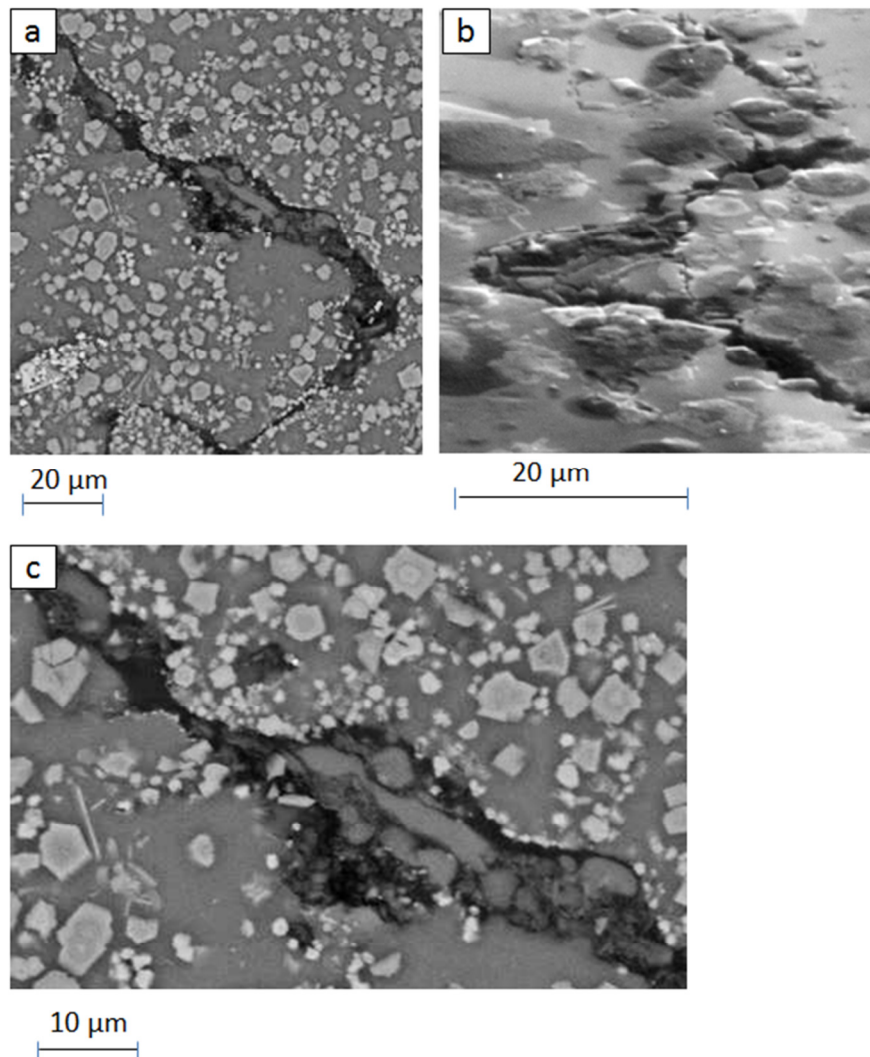
Figure 5-11 High magnification SEM micrograph showing the continuous oxide (Al$_2$O$_3$) layer in different positions in the aluminium matrix in CPAl, containing 0.1 % TiB$_2$, heated to 740°C and then pressure filtered.

Figure 5-12 shows the EBSD mapping on the oxides formed in CPAl melt heated to 740°C, containing 0.1 % TiB$_2$, which was concentrated by the pressure filtration technique. It has been previously suggested that some of them will be consisting of plate like γ-Al$_2$O$_3$ particles. Furthermore, it was suggested that the faceted γ-Al$_2$O$_3$ can act as potent heterogeneous nucleation substrates for Al (Li, 2011). However, it was not possible to index

the oxides under any crystal structure (indicated as oxygen rich areas in **Figure 5-12 (a)**. This might indicate that part of the oxides formed at that temperature are still present as a continuous amorphous layer and therefore cannot act as substrates for the nucleation of α-Al. However, it can also indicated that the particles are too small to be indexed. I tis therefore important to mention that clear kikuchi patterns were not obtained during EBSD analysis on the oxide particles.
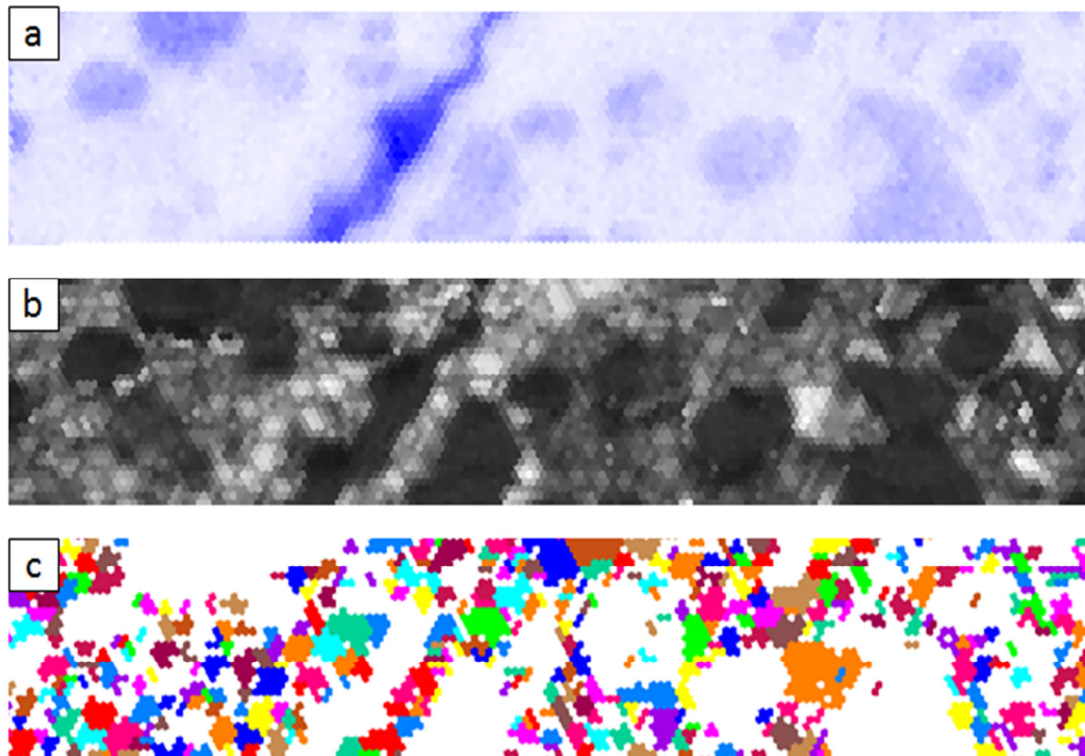
Figure 5-12 Analysis of the oxides obtained in CPAl heated to 740°C and then pressure filtered (a) EDS mapping highlighting the oxygen rich areas (b) EBSD mapping showing in black the areas that could not be indexed (non-crystalline structures) (c) EBDS mapping showing the orientation of the aluminium indexed crystals.

Figure 5-13 shows the XRD pattern of the identifying the oxides collected by the pressure filtration technique, from the melt heated to 740°C. The patterns identify the γ-Al_2O_3 phase. However the curve at around 10° indicates that the structure of some of the oxides is still amorphous or between crystalline and amorphous. It is important to mention that the peaks from α-Al_2O_3 were not present in this sample.
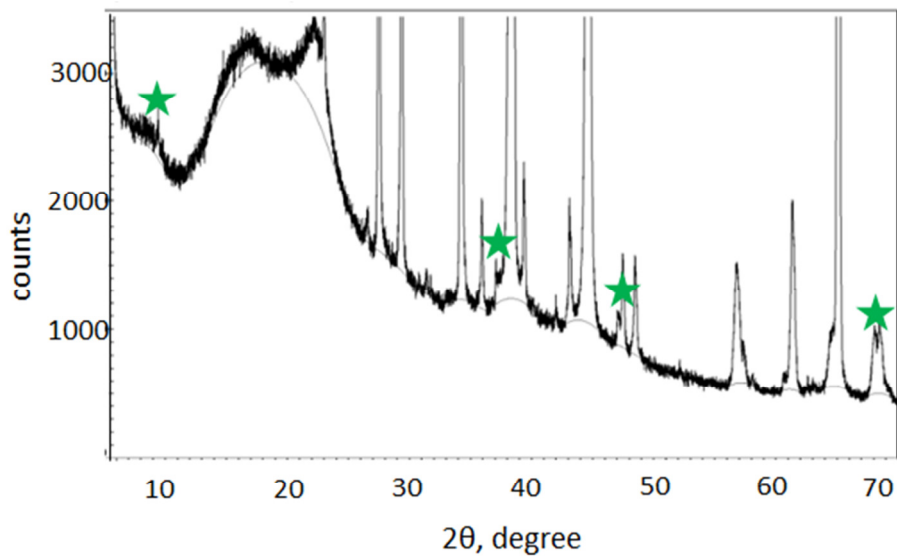
Figure 5-13 XRD pattern of oxides formed in CPAl melt heated to 740°C collected by the pressure filtration technique.
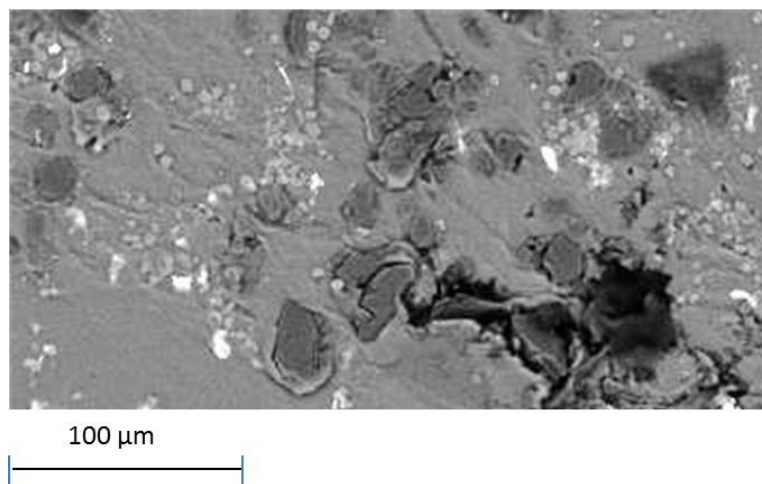
Figure 5-14 Low magnification SEM micrograph showing the continuous oxide layer in the aluminium matrix in CPAl, containing 0.1 % TiB_2, heated to 920°C, hold at that temperature for 1h and then pressure filtered.
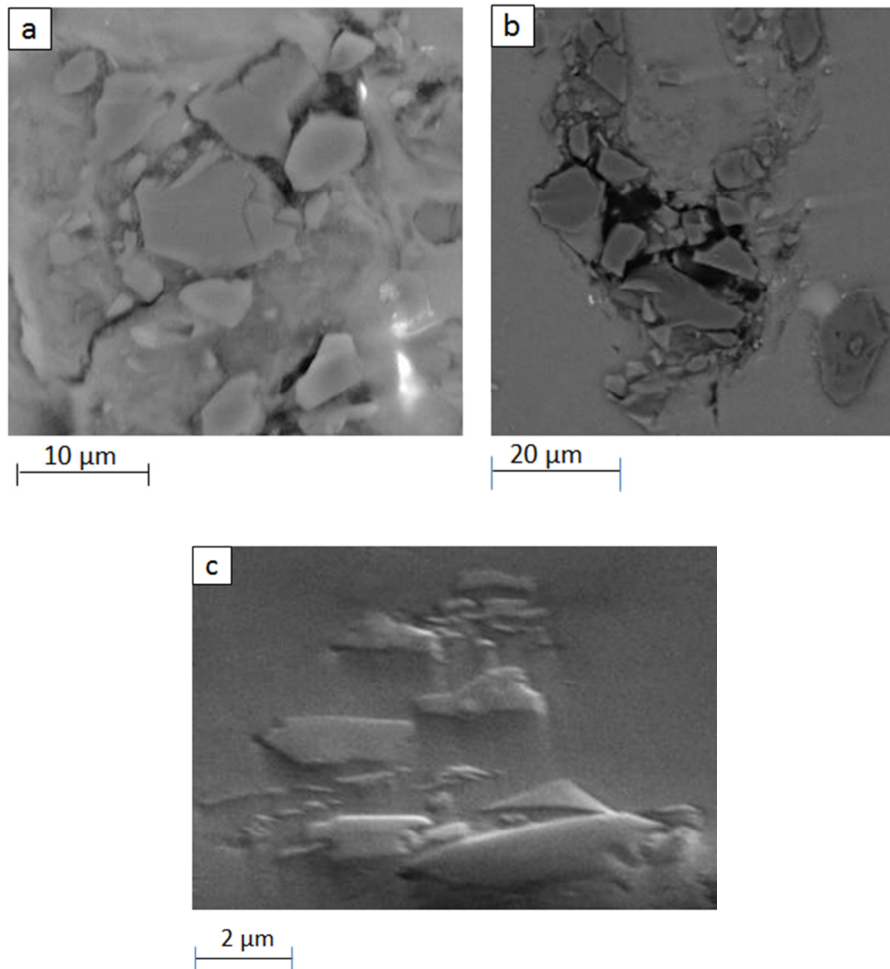
Figure 5-15 High magnification SEM micrograph showing the continuous oxide layer in the aluminium matrix in CPAl, containing 0.1 % TiB$_2$, heated to 920°C, hold at that temperature for 1h and then pressure filtered.

Figure 5-14 and **Figure 5-15** show the morphology of the Al$_2$O$_3$ oxides particles contained in CPAl heated to 920°C. The different morphology of the oxides formed at both temperatures, i.e. 740°C and 920°C, is highlighted by comparing the micrographs in **Figure 5-10** and **Figure 5-11** to those **in Figure 5-14** and **Figure 5-15**. Instead of continuous oxide films, clusters of very small Al$_2$O$_3$ particles are the oxides formed at 920°C.
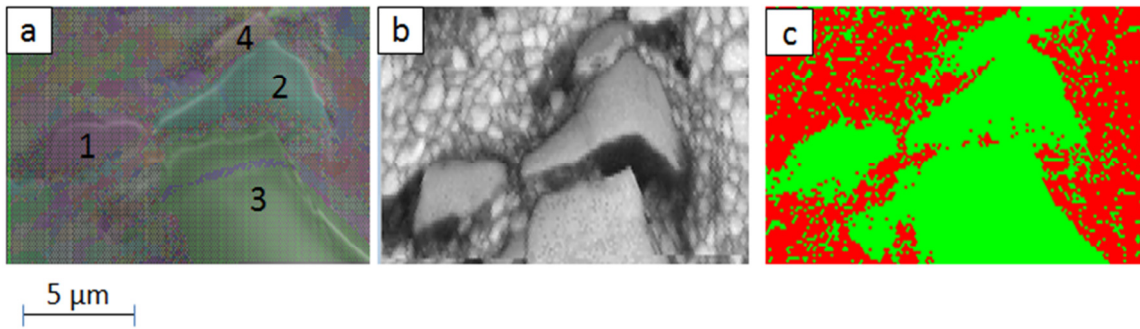
Figure 5-16 SEM analysis of the oxides obtained at 920°C (a) EBSD mapping showing crystal orientations of the Al and α-Al₂O₃ superposed on the SEM image (b) EBSD showing in grey and white the indexed particles and black the areas that could not be indexed and (c) EBSD map showing in green the areas indexed as α-Al₂O₃ and in red the areas indexed as α–Al.
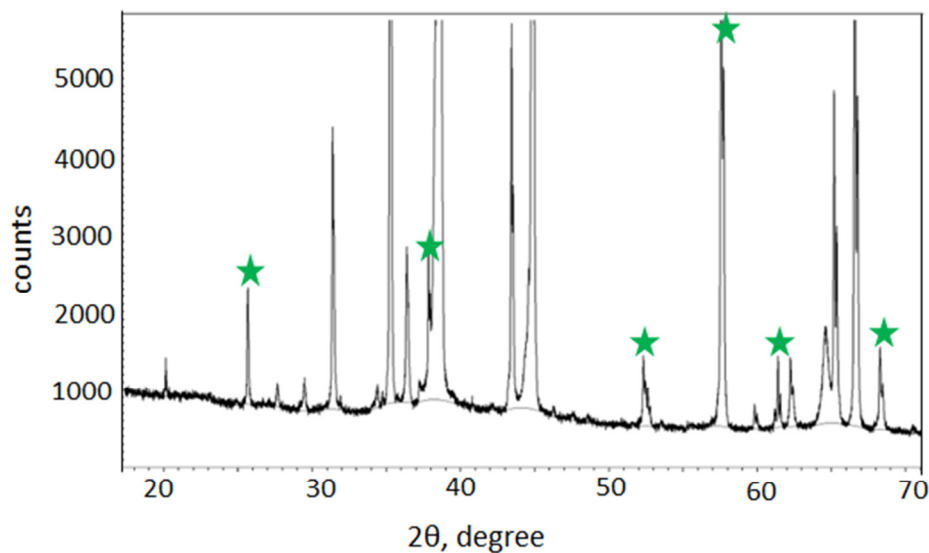
Figure 5-17 XRD pattern of oxides formed in CPAl melt heated to 920°C collected by the pressure filtration technique.

EBSD analysis (**Figure 5-16**) confirms that the oxides formed in the CPAl melt at 920°C, are α-Al₂O₃. The thermodynamically stable α-Al₂O₃ structure possesses trigonal symmetry with rhombohedra centring (space group R3c). The unit cell contains10 ions (6 O^{2-} Al $^{3+}$) per unit cell. The oxygen anions in this structure are approximately in hcp packing and the Al cations are located in octahedrally coordinated interstitial sites in the anion sub-lattice (Yang et al., 1998; Wefers and Misra, 1987).Furthermore, **Figure 5-17** shows the XRD pattern of the

identifying the oxides collected by the pressure filtration technique, from the melt heated to 920°C. The patterns identify the α-Al_2O_3 phase.

Lee and co-workers (Lee and Kim, 2011) performed experiments with Al and α–Al_2O_3, under electron irradiation in a high voltage electron microscope. They observed nucleation of liquid Al droplets in α–Al_2O_3. Ordering in the liquid at the Al/α-Al_2O_3 was observed; as an indication of epitaxial growth. Furthermore, they observed that when increasing the temperature from 800 to 1100°C the system undergoes a transition from a contact angle of 90° to a contact angle bellow 90°, related probably to a decrease in the solid/liquid interface.

Other possible effects of superheat on the aluminium solidification need to be considered. It has been previously demonstrated that the thermal history of the melt determines the diffusion process and therefore has a great influence on the nucleation process of aluminium. The melt solidified microstructure will be therefore closely related to its thermal history, even if the thermal gradient, withdrawal velocity and alloy composition remain unchanged.

According to diffraction studies the structural transformation occurring in liquid iron when the melt is heated above a particular temperature, which has been named "anomalous temperature of change", is accompanied by an increase in the mean interatomic distances and in the number of nearest neighbours in the liquid state. The anomalous temperature is defined as the temperature at which the melt structure becomes completely homogeneous, and is identified due to the unexpected change in some of the melt properties and short-range order parameters of liquid. When the melt is not heated above the anomalous temperature of change the solidification will occur without significant undercooling. The results obtained by Sidorov, in combination with diffraction data, suggest that the metastable melt forms upon melting of Fe and the short range order in the melt retains some characteristic features of the initial phase. The features of structural transformations were also repeatedly noted in the study of the structure and properties of liquid aluminium (Brodova et al., 2001). Moreover, Bian (Bian et al., 2000) investigated the structures in the melt of Al-13Si alloy heated up in a wide temperature range. The high temperature X-ray diffractometer showed that with increasing the temperature up to 775 °C, the atomic

density and the coordination number of the alloy slowly increased, then a sudden change in those parameters occurs in the temperature range from 775 °C to 875 °C, suggesting that the liquid structure changed, as a consequence of the Si-Si clusters dissolving into the Al bulk melt. Calvo-Dahlborg and co-workers (Calvo-Dahlborg et al., 2013) investigated the effect of superheat on the microstructure of Al-Si alloys by Small Angle Neutron Scattering (SANS) during thermal cycles above the liquidus temperature. They showed that for all compositions, the melt is more homogeneous after being heated to the highest temperatures (Li et al., 2002). Furthermore, it was demonstrated for Ni-based super-alloys that clusters contained in the melt decrease in size considerably when the melt temperature reaches critical temperature (Yin et al., 2003).

An increase on nucleation undercooling, for the melt heated to high superheat temperatures, was observed on **Figure-4.103**. The temperature at which recalescence begins is 1.5°C lower for the melt treated to the higher temperature of 920°C, compared to that of the melt heated to only 740°C. Considering that from this point (3) no more particles will be activated as nucleation sites, for the alloy whose melt has been heated to 920°C more particles and smaller can be activated as nucleation sites. This larger undercooling before the beginning of recalescence could be explained both by the changes in the melt structure (as previously mentioned) or to the nucleation of Al on the α-Al$_2$O$_3$:

- Owing to this resemblance of the melt heated to low temperature (i.e. 740°C) with the initial solid phase, such melt does not experience significant difficulties in solidification into the parental structure. Upon heating above the anomalous temperature, the metastable state of the liquid iron is destroyed irreversible and the short range order losses its similarity to the original phase. On further cooling the initial state of the melt is not restored and, as a consequence, the nucleation of the crystals with bcc structure is hindered and needs a deeper undercooling to be initiated (Brodova et al., 2001).
- It is known that the lattice misfit with Al is -0.48 % for α–Al$_2$O$_3$ and 0.09 % for Al$_3$Ti. This indicates that, in terms of lattice misfit at the interface, the oxides are less potent than the Al3Ti. Undercooling can be affected by other factors including the size of the nucleant particles, the smaller the particle size the larger the

undercooling. It is observed that the size of the oxides particles is in general smaller than that of the TiB$_2$ particles.

For both homogeneous and heterogeneous nucleation, the nucleation rate is sensitive to undercooling and increases with the increase of undercooling. At the same time, as indicated in the free growth model, the increase in undercooling is an indication of the reduction of the critical nucleating radius. In other words, atom clusters which are less than critical nucleation radius can become stable nucleation site with increasing undercooling.

Furthermore, for diffusion-controlled spherical growth at an isothermal condition, the growth velocity of solid increases in inversion proportion to the radius of the spherical nucleating particle (Hellawell et al., 1975).

The dependency of nucleation rate with undercooling can be explained as follows. The transformation from a highly disordered liquid to an ordered solid is accompanied by a lowering of the energy state of the metal and therefore the release of thermal energy (latent heat). The driving force for solidification is the difference in bulk chemical free energy between the liquid and solid phases, i.e. the transformation from liquid to solid is driven by a decrease in this free energy. For an undercooled melt the Gibbs free energy of the solid phase will be much lower and therefore the nucleation barrier for heterogeneous nucleation (**Equation 5-10**) will be reduced and the driving force for solidification increased. Thus, the increase in undercooling will benefit for nucleation providing an enhanced nucleation rate and increased growth velocity. This enhanced nucleation will give place to finer dendrites. However, it is important to consider that if the inoculant is less potent (α-Al$_2$O$_3$ compared to Al$_3$Ti) its efficiency will be lower and grain size can be increased as the number of nucleation sites can be reduced.

The temperature difference between 2 and 3, as seen in **Figure 4-103**, is an indication of the temperature increase during recalescence, when the first crystals start to solidify. During the solidification of the melt heated to 920°C (**Figure 4.103 (b)**) the temperature increase during the formation of these first crystals is bigger compared to the melt heated to 740°C (**Figure 4.103 (a)).** However, the temperature at which recalescence finishes decreases by 1.2˚C, i.e. from 645.4˚C to 642.2˚C with melt superheat, allowing for a larger undercooling

during the begining of the solidification process, increasing the possibilities of an enhanced heterogeneous nucleation.

The solidification profile, presented in **Figure 4-103** as well as the DSC trace analysis in **Figure 4-104** for alloy 2011 without and with inoculant additions, respectively, shows a reduction in the liquidus temperature of the alloy, after the alloy has been superheated to temperature sin the range of 900°C. The liquidus slope, and therefore the solidification onset temperature, decreases as a consequence of the melt superheat. This effect has been previously observed in Ni-based alloys (Yin et al., 2003).

The increased diffusion coefficient in the presence of superheat will have a significant effect on the solidification process, affecting not only the insoluble elements and the structural state of the liquid metal but also the solid-liquid interface. The diffusion coefficient is one of the important physical properties in liquid metal and alloy, which has an obvious effect on the distribution of elements, crystal growth rate and segregation in solidification process. The factors influencing the diffusion coefficient are temperature and composition.

Diffusion coefficient increases exponentially with temperature, following and Arrhenius type distribution, as indicated by the following formula:

$$D = D_0 exp\left(-\frac{Q_d}{RT}\right) \qquad (5\text{-}15)$$

Where D is the diffusion coefficient (m^2s^{-1}), D_0 is the pre-exponential constant (m^2s^{-1}), Qd is the activation energy ($J\ mol^{-1}$), R the gas constant (8.314 $Jmol^{-1}K^{-1}$) and T the absolute temperature of the melt (K).

From **Equation 5-15**, it can be calculated that diffusivity increases approximately 2 orders of magnitude for the melt heated to 920°C compared to the lower heating temperature of around 660-700°C. Some atoms will atoms will diffuse faster than others, depending on the values of D_0 and Q_d. This increased diffusivity at high temperatures provides a much uniform distribution of the additions and impurities within the melt. However, the diffusivity will decrease as the temperature is reduced to the final solidification temperature.

Factors such as the reduced solidification interval (due to the reduction in liquidus temperature), and the increased growth velocity (v) with increasing melt superheat has been found to have a direct influence on SDAS, as seen **Equation 5-19** (Wang et al., 2003). One can find that the dendritic arm spacing will be considerably reduced when superheat is applied to the melt, under the individual contribution of each of the factors or the combination of them.

$$\lambda_2 = 4.3 \left(\frac{D \beth \Delta T_0}{k}\right)^{0.25} G^{-0.5} v^{-0.25} \qquad (5\text{-}17)$$

Where λ_2 is the *SDAS calculation based on the model developed by Kurz and Fisher,* $\beth$ is the Gibbs-Thomson coefficient, ΔT_0 is the difference between the liquidus and solidus temperature (K), G is the temperature gradient (Km^{-1}), which will be constant in this study and, v is the growth velocity (ms^{-1}).

From the experiments on steel mould (see **Figure 4-84**, **Figure 4-85** and **Figure 4-86**), it was proven that for alloys containing inoculant the grain size is constant regardless of the heating temperature of the melt, having a value of around 200 μm. However, for the inoculant-free 2011 alloy, the grain size is reduced considerably as melt superheat temperature is increased from 740°C to 920°C. Furthermore, SDAS decreases as the melt preheating temperature increases, with and without inoculant additions, as seen in **Figure 4-91** and **Figure 4-92**, where a direct relationship between SDAS and soft phase droplet size has been found. Confirmation of this in found in **Figure 4-89** and **Figure 4-93.**

As seen in **Figure 4-91** the reduction in dendritic arm spacing, associated with the effect of melt superheat, is found to be directly related to the reduction in droplet size for immiscible 2011 alloy without refiner additions. When the dendrite tip radius is small enough the spheres are entrapped by the dendrite, and therefore remain much smaller than the droplets rejected by dendrite tips which present a bigger radius curvature. With big radius of the dendrite tip the repulsion of the droplets is much higher, and all the rejected droplets will accumulate and grow (Yin et al., 2003). The effect of superheat on SDAS for alloy 2011 containing Al-Ti and Al-B is shown in **Figure 4-92**, from which it can be concluded that superheat has only a minor effect on SDAS when refiner is added to the melt, indicating that the final structure is mainly, but not solely, governed by the refiner particles.

5.3.2   Effect of melt superheat on nucleation of Pb/Bi droplets

For alloys of monotectic and hyper-monotectic compositions the superheat affects directly the nucleation of the minority immiscible phase droplets. For the alloy of exact monotectic composition, in-situ solidification experiments support the findings from DC casting. Two different samples of Al-1.2Pb alloy were chosen for the experiments, i.e. with and without inoculant additions.

For the samples containing Al-Ti and Al-B, superheat to 830°C reduces the droplet size and the sedimentation in comparison with the sample heated to 720°C (**Figure 4-48, Figure 4-66**, **Figure 4-67**, **Figure 4-70** and **Figure 4-71).** For the samples without inoculant, superheat reduces the size of the particles on the final solidified microstructure, the sedimentation (see **Figure 4-70** and **Figure 4-71**) and the sensitivity of the alloy to cooling rate, as seen from **Figure 4-74 to Figure 4-77.**
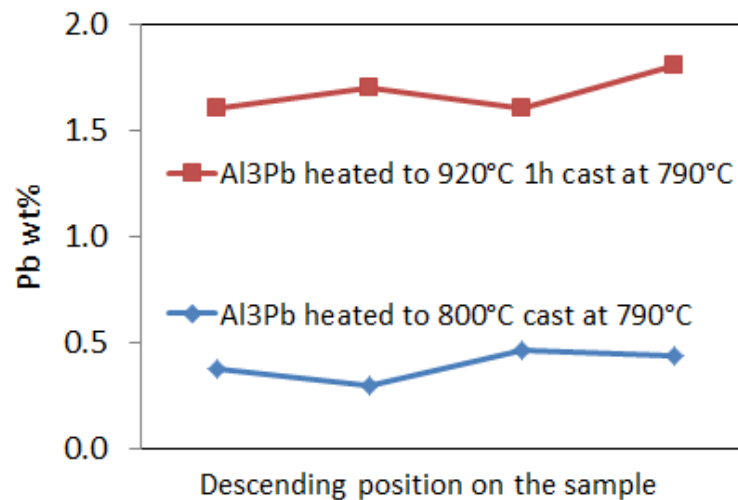
Figure 5-19 Effect of superheat on Pb content of the Al-3Pb samples (measured from top to bottom of the sample).
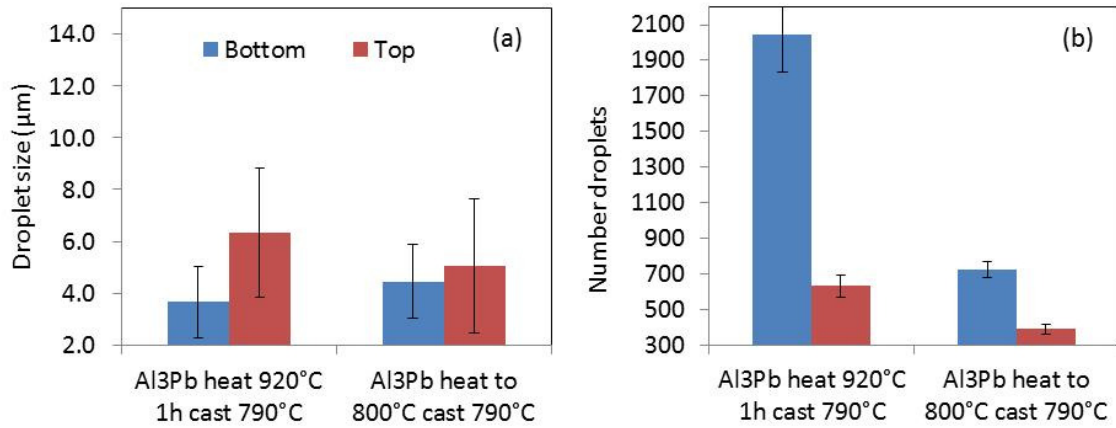
Figure 5-20 Effect of superheat on (a) particle size and (b) number of particles for Al-3Pb alloy casted in a steel mould.
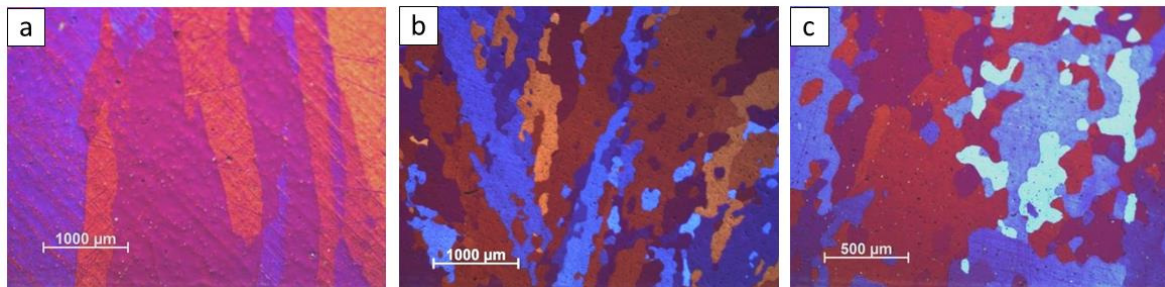
Figure 5-21 Optical images showing the grains of Al-3Pb for samples casted at 790°C in a cylindrical steel mould: (a) heated to 810°C hold for 20 min before casting, (b) heated to 920°C, hold for 1h before casting.
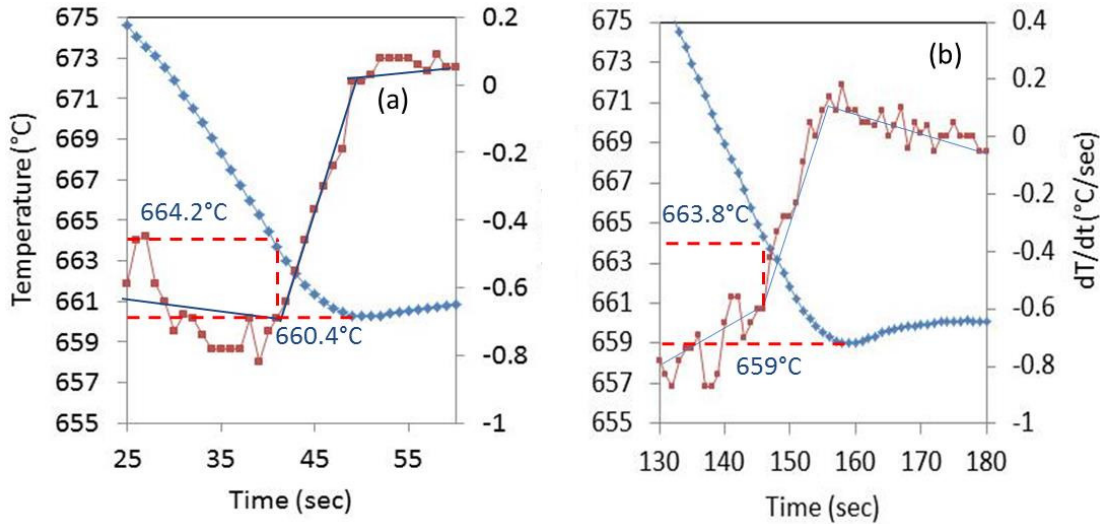
Figure 5-22 Solidification temperature profile of an Al-3Pb alloy sample, measure in a crucible at a cooling rate of 1K/sec, and first temperature derivative: indicating the liquidus (1) recalescence (2) and undercooling (3) temperature. For the melt heated to 740°C (a) and the melt heated to 920°C (b).

From the analysis in **Figure 5-19** and **Figure 5-20** it can be seen that superheat to 920°C reduces Pb sedimentation on the crucible, increasing therefore considerably the number of particles distributed in the casted microstructure. **Figure 5-19** proves that the separation of the 2 liquid phases and the Pb sedimentation takes place mainly in the crucible. Furthermore, under the effect of superheat the droplet size does not increase proportionally to the Pb content of the alloy. Grain morphologies of the casted samples change considerably with superheat, as seen in **Figure 5-21**. This can be explained considering the solidification profile of the Al-3Pb whose melt has been heated to 920°C and the melt heated to 740°C are represented in **Figure 5-22**. It can be seen that the temperature at which recalescence begins is 1.4°C lower for the sample whose melt has been previously heated to 920°C, which account for the differences observed in the solidified maicrostructures in **Figure 5-21.**

The solidification path of Al-3Pb hyper-monotectic alloy dictates that the liquid-liquid separation process happens before the formation of the α–Al, the changes in the solidified microstructure cannot be responsible for the improvement in the Pb distribution within the

casted sample. The effect of superheat on the nucleation and final solidified microstructure of alloys with a Pb content of 1.2 % or higher is explained in the following paragraphs.

The decomposition of the liquid with the initial concentration C_0, just after quenching, will lead to a continuous change of the supersaturation, which depends on the average concentration of the soft phase atoms in the matrix surrounding the nucleated and growing droplets. As the alloy starts to cool from the binodal line the nucleation rate will start to increase rapidly after a certain incubation time to its stationary value, and after a short period of time it drastically decreases by several orders of magnitude due to the mentioned decrease in supersaturation (Ratke and Alkemper, 1995).

It is generally known that the metastable zone width can be greatly affected by the thermal history of the melt. A melt that has been kept long enough, at a temperature sufficiently higher than the saturation temperature, will be found to have a wider metastable zone than if it had only been kept slightly above the saturation temperature (Ratke and Diefenbach, 1995; Schauffer et al., 2009; Ratke, 1988). The higher the preheating and the longer the melt is maintained at that temperature the higher the saturation level at which nucleation starts. Therefore the level of undercooling, at which the nucleation of the minority immiscible phase takes place, would be larger the higher the superheat temperature at which the melt has been hold. The larger nucleation undercooling will allow for a reduction in the time available for droplet coalescence and growth.

Furthermore, as indicated previously (5.3.1) and considering **Equation 5-9**, for an undercooled melt the Gibbs free energy of the nucleating droplets will be much lower and therefore the nucleation barrier for heterogeneous nucleation (**Equation 5-10**) will be reduced and the driving force for solidification increased. Hence the increase in number of nucleated droplets and the corresponding decreases in their size (Kaban et al., 2011).

To summarise, superheat after the inoculant additions and before shearing, improves the efficiency of the inoculant, improving size distribution of Pb (and eutectic Pb/Bi) particles. Furthermore, it creates an even phase distribution by eliminating the compositional heterogeneities within the melt. The effect of superheat can be attributed to changes in the nucleation process for both Al and liquid Pb droplets, mainly by increased nucleation undercooling and the driving force for nucleation. Enhancing diffusion of solute elements together with irreversible changes in the liquid structure of the melt and increasing the level of super saturation at which nucleation starts; for the aluminium matrix and Pb droplets respectively. For aluminium the growth velocity is increased, and the solidification interval reduced, giving place to finer dendrites and smaller grains, which will trap smaller Pb droplets and for Pb decreasing the size of the nucleated droplets, increasing their number and reducing the miscibility gap and therefore the time available for coalescence and growth.

Chapter 6

Conclusions

1. Theoretically, for alloys of hypo- and exact monotectic composition, their solidification paths dictate that sedimentation cannot take place. However, in practice, sedimentation was observed also on alloys of exact monotectic composition. Both exact and hyper-monotectic alloys present strong uneven phase distribution leading to a strong macrosegregation and sedimentation during solidification.

2. **Shearing** improves the distribution of the immiscible Pb/Bi droplets in the aluminium matrix. The most important shearing parameters are:
   - Shearing temperature: Shearing affects the phase separation from its initial stage, i.e. the nucleation of the Pb droplets. For hypo- and monotectic compositions the melt should be sheared as close as possible to the monotectic temperature, and for hyper-monotectic alloys shearing should be initiated at a temperature just above the binodal line and continued to the monotectic temperature.
   - Shear rate: High shear rates are more efficient to disperse and break the droplets. Optimum results were obtained for the shear rates obtained at 6000 rpm.

3. **Shearing** not only promotes droplet break up and emulsification but it creates a macroscopic flow, providing a distributive mixing action in the sump. The more homogeneous temperature and chemical composition of the melt in the sump considerably reduces velocity of droplet coalescence and sedimentation.

4. **A new inoculant** is created from the in situ reaction between Ti and B and not only reduces the size of the Pb droplets, while increasing therefore their number, but it also improves macrosegregation of the ingots. The inoculant is more efficient for –hyper monotectic alloys.
   - The amount of inoculant required increases with Pb composition and as cooling rate decreases.

- The inoculant should be added as soon as the aluminium melts. The alloy containing the inoculant should be heated to a temperature above the binodal line.

5. The TiB_2 particles contained in the **inoculant** act as substrates for the liquid Pb droplets, enhancing their heterogeneous nucleation, decreasing consequently the size distribution of nucleated droplets.

6. **Superhea**t (heating of the melt to 920°C) improves the size distribution of Pb droplets, and creates an even phase distribution. It eliminates therefore the compositional heterogeneities within the melt. SDAS and grain size decrease linearly with superheat temperature, while a mixed structure is present in intermediate states. The effect of superheat can be attributed to changes in the nucleation process for both Al and liquid Pb droplets, mainly by increased nucleation undercooling and the driving force for nucleation.

7. The sizes and homogeneity of distribution of the soft immiscible phase droplets are a strong function of the solidification conditions and melt treatment. Combination of shearing, superheat and inoculant can create a microstructure consisting of finely and uniformly distributed Pb droplets, with an even phase distribution, in which macrosegregation is eliminated.

Chapter 7

Recommendation for future work

7.1 Effect of microstructure on machinability of 2011 alloy

The 2011 alloy casted ingots have been homogenised, extruded into a 16 mm diameter solid bar. The bars have been thermo-mechanically treated to T6 temper, and machined as explained in **Chapter 2, Section 2.5**.

Three casts were selected to assess machinability. The selection was based on the belief that machinability depends on Pb/Bi droplet size and distribution, therefore two casts with very different droplet size and distribution across the ingot were selected. The first was the reference cast (**Chapter 4**) which provides the coarsest Pb droplet size. The second one contained Al-Ti and Al-B, in a melt heated to 860°C and sheared at 6000 rpm, producing the biggest amount of droplet of the smallest size. A third cast was chosen, without inoculant, heated to 860°C and sheared at 6000 rpm which produces also very small droplet size and increased number of droplets for reproducibility.

Hence the results from the machining (on primary vertical axis) tests for three selected castings are presented in **Figure 7-1**, together with average, minimum and maximum droplet size from the DC cast microstructure (on secondary vertical axis) to understand a possible correlation between them. The reason to choose cast microstructure is because it is believe that the soft phase droplet size and their distribution is determined by the casting process and it will not change during subsequent extrusion and thermo-mechanical treatment. In general, it can be said from the analysis of **Figure 7-1** that better machining response is linked to smaller droplets in the casted structure. However, despite having similar droplet sizes the 2nd and 3rd cast present difference response in machinability. It is therefore necessary to investigate other factors that might contribute to the change in machining response.
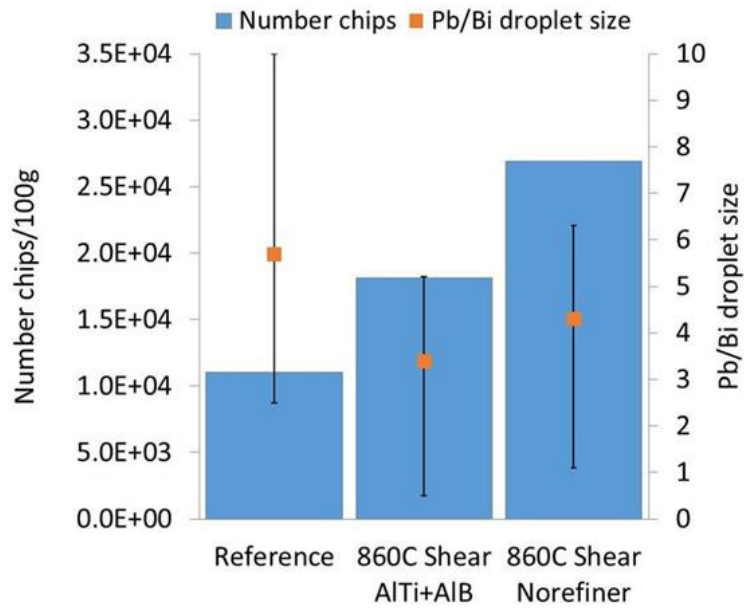
Figure 7-1 Machinability measured as number of chips per 100g, for 3 different 2011 ingots and its relationship with droplet size.

The mechanical properties of the mentioned castings are displayed in Error! Reference source not found.. The best combination of Yield Stress and Ultimate Tensile Strength (UTS) is obtained for the cast, which provides an 11% increase in Yield Stress and a 2% increase in UTS compared to the reference cast. Furthermore, the cast with the best machinability presents the smallest difference between the value of UTS and that of yield strength.
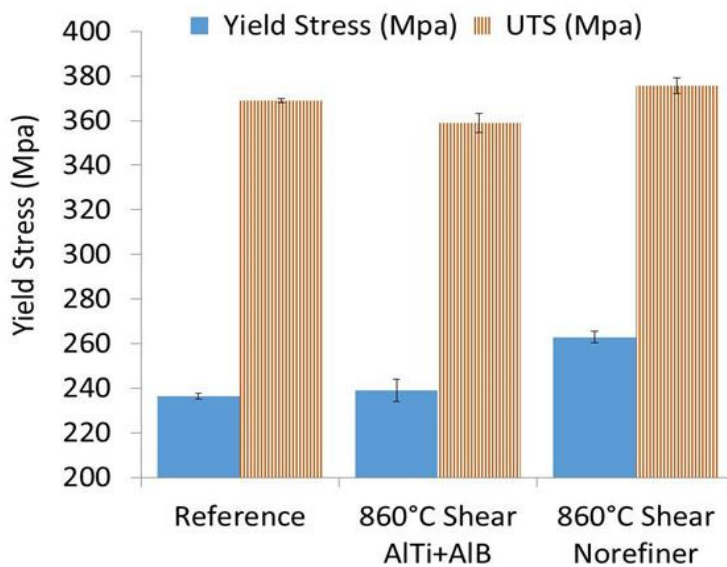
Figure 7-2 Mechanical properties for the 3 selected castings.

Figure 7-3 and **Figure 7-4** show SEM back scattered images of the extruded and thermo-mechanically treated bars, corresponding the extrusion direction and direction normal to extrusion, respectively. A different distribution and size of Al_2Cu intermetallic is obtained under the different casting conditions; corresponding the smallest size, and better distribution to the cast with best machining properties. Imagej was used on the SEM images to calculate the size and number of intermetallics. The results of this analysis is shown in **Figure 7-5**, and confirm what is seen on the micrographs, the highest number of intermetallics is obtained for the melt with best machinability, i.e. melt free of inoculant, superheated to 860°C and sheared. The increased number of intermetallics could be linked to the improved machinability, although there is no conclusive evidence.
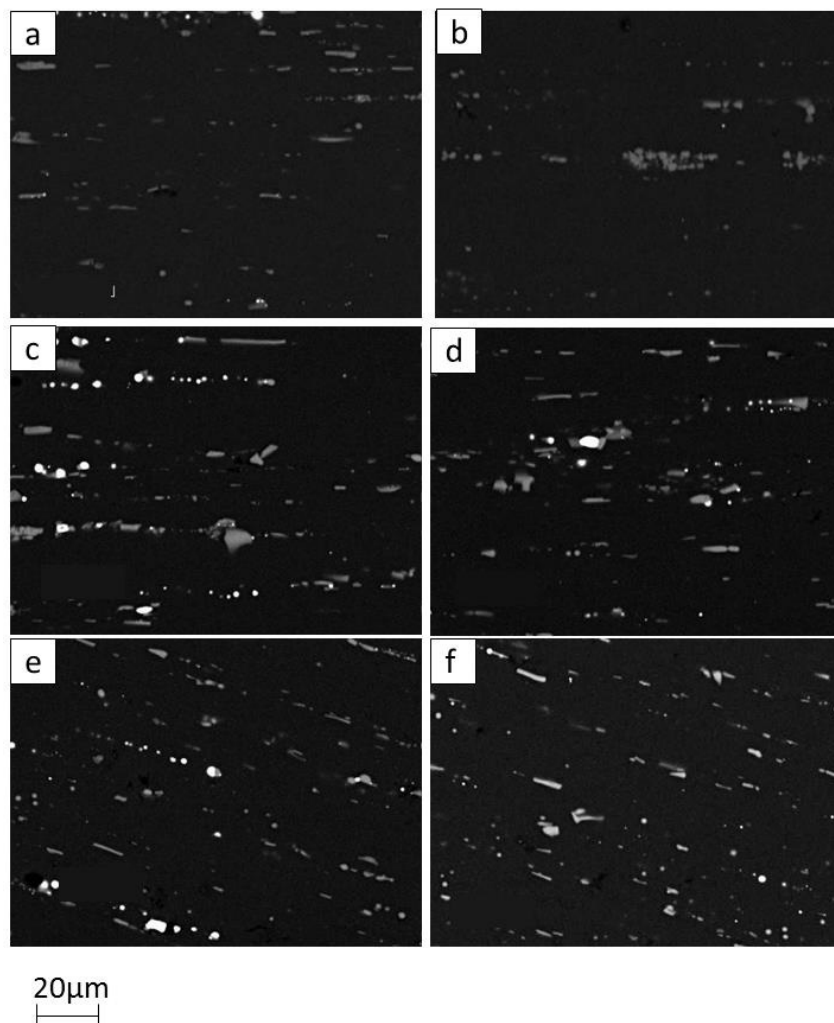
Figure 7-3 SEM back scattered images of the extruded sections, on the longitudinal direction, coming from the following casts: (a, b) reference untreated containing Al-5Ti-B (c, d) containing Al-Ti and Al-B, heated to 860˚C and sheared and (e, f) ingot heated to 860˚C and sheared at 6000 rpm.
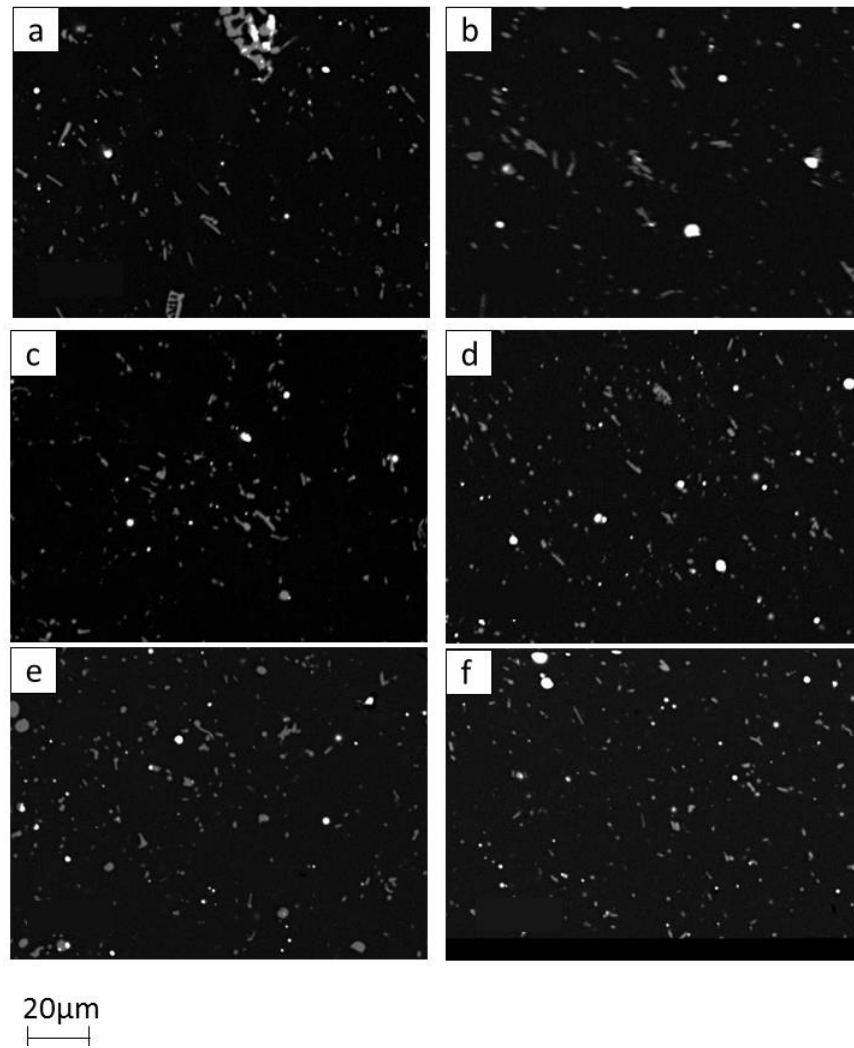
Figure 7-4 SEM back scattered images of the extruded sections, on the normal direction, coming from the following casts: (a, b) reference untreated containing Al-5Ti-B (c, d) containing Al-Ti and Al-B, heated to 860˚C and sheared and (e, f) heated to 860˚C and sheared at 6000 rpm.
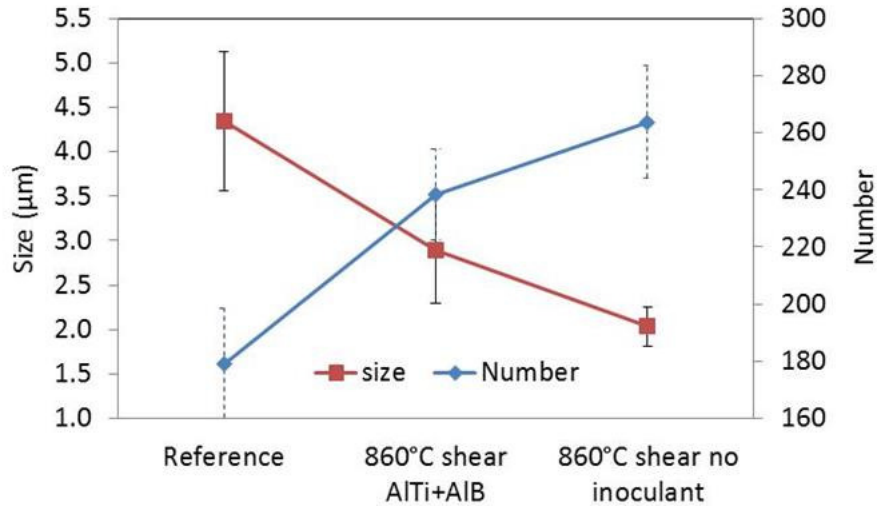
Figure 7-5 Individual area and number of each Al₂Cu intermetallic for the three selected conditions.

The grain sizes for the extruded bars are shown in **Figure 7-6. A**ll bars present very similar grain sizes after extrusion, with a value of 508, 491 and 540 μm for the reference, melt heated to 860˚C, sheared and containing Al-Ti and Al-B and melt heated to 860˚C, sheared and without inoculant, respectively.
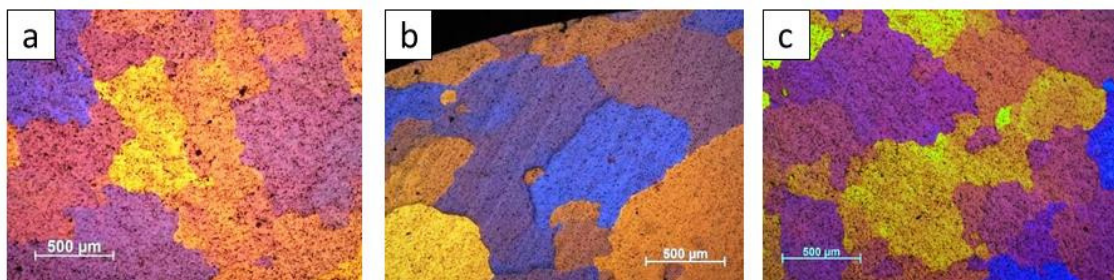
Figure 7-6 Optical images, obtained under polarised light, showing the grain structure of the extruded bars from the following casts: (a) reference untreated (b) containing Al-Ti and Al-B, heated to 860˚C, sheared and (c) heated to 860˚C and sheared at 6000 rpm.

Pictures of the chips obtained from the machining process for the three casts are shown in **Figure 7-7**, and show clearly the difference in machinability between the bars obtained from

the reference untreated cast and the cast whose melt has been heated to 860˚C, sheared and without inoculant.

Figure 7-7 Photographs of the chips obtained during machining for the extruded and heated bars of the following casts: (a) reference untreated cast, containing Al-5Ti-B(b) containing Al-Ti and Al-B, heated to 860˚C, sheared and (c) heated to 860˚C, sheared.

Additional work is required to understand the effect of the extruded and thermo-mechanically treated microstructure in machinability. It is important to identify what exactly is the contribution of the soft phase droplet size and distribution and that of the Al_2Cu intermetallics, as well as an understanding the effect of mechanical properties in machinability:

- Further characterisation of the extruded bars in different tempers, to identify the type and morphology of intermetallics obtained under the different casting conditions and tempers and their correlation to mechanical properties.
- Continue TEM/SEM analysis of the chips and machined surface is essential to get a better understanding of the chip braking and what aids it.
- Further casting trials on 2011 alloy without soft phase additions. To obtain new bars for machining and determine the individual contribution of Al-Cu-Fe intermetallics to machinability.

7.2 Improved 2011 alloy keeping the current machining properties with reduced levels of soft phase additions (Bi/Pb)

- Further casting trials on 2011 alloy with reduced contents of soft phase additions, following the casting conditions that provided the optimum machining results.

7.3 STEM analysis of the TiB$_2$/Al interface

It is expected that the atom absorptions at the TiB$_2$/Al interface will be investigated using the STEM. This would help to identify the bi-layer observed on the interface between TiB$_2$/Al and prove whether the mechanism responsible for the Pb refinement in the presence of TiB$_2$ is that of the enhanced heterogeneous nucleation. And in any case to further understand the affinity between Pb and TiB$_2$.

Chapter 8

Bibliography

A

- Akagwu, I.P., Quested, P.N., Brooks, R.F., and Fan, Z. (2000): Immiscible alloys for automotive applications, Proceedings of the Engineering Doctorate in Environmental Technology, Annual Conference.

- Al-Helal, K. W. A. (2013): New Approaches to Casting Hypereutectic Al-Si Alloys to Achieve Simultaneous Refinement of Primary Silicon and Modification of Eutectic Silicon. Brunel Centre for Advanced Solidification Technology (BCAST), Brunel University.

- Aluminium alloys: Their Physical and Mechanical Properties, vol 3, Some ideas to improve machinability without Pb, Bi particles, page 2029-2034, Proceedings of the 6th International Conference on aluminium alloys, ICAA-6.

- Andrews, J. B., Schmale, A. L., Dwyer, Z. B., Moss, C. B., and Hayes L.J. (1993): Solidification in immiscible alloy. Adv. Space Res. Vol. 13, No. 7, pp. (7)229—(7)234.

- Asano, K., Fujiwara, A. (1971): Quantitative evaluation of free-machining properties of 2011 alloy, Journal of Japan. Institute of Light Metals 21 579–588.

- ASM Metal Handbook (*1990)*: Volume 2. Properties and Selection: Nonferrous Alloys and Special-Purpose Materials.

B

- Bian, X., Wang, W. (2000): Thermal-Rate Treatment and Structure Transformation of Al-13 % Si Alloy Melt. Mater. Lett. 44(1): p. 54-58.

- Binder, K. (1976): "Statistical Mechanics of Nucleation and Phase Separation" (invited review for the IUPAP International Conference on Statistical Physics, Budapest, August 25-29, 1975; p. 219-244.

- Binder, K., Stauffer D. (1976): "Statistical Theory of Nucleation, Condensation and Coagulation", Advances of Physics 25 p. 343-396.

- Briscoe, B.J., Lawrence, C.J., Mietus, W.G.P. (1999): A review of immiscible fluid mixing. Adv Colloid Interface Sci. 81(1):1–17.

- Brodova, I.G., Popel, P.S., Eskin, G.I., (2001): Liquid metal processing: Applications to Aluminium alloy production. CRC Press.

- Budai, I. (2014): Intermetallic phase stabilized Al/Pb metallic emulsion. Int J Mater Res. 105(12):1230–1.

- Budai, I., Kaptay, G. (2009): A new class of engineering materials: particles stabilized metallic emulsions and monotectic alloys, Metall. Mater Trans A , vol.40A, pp.1524-1528.

- Budai, I., Kaptay, G. (2010): Wettability of SiC and alumina particles by liquid Bi under liquid Al. J Mater Sci; 45(8):2090–8.

C

- Callister, W.D. (2007): Materials science and engineering an introduction. 7th ed. New York, NY: Wiley; 721 p.

- Calvo-Dahlborg, M., Popel, P.S., Kramer, M.J., Besser, M., Morris, J.R., and Dahlborg, U. (2013): Superheat-dependent microstructure of molten Al–Si alloys of different compositions studied by small angle neutron scattering. Journal of Alloys and Compounds 550 9–22.

- Campbell, C.E., Bendersky, L.A., Boettinger, W.J., Ivester, R. (2006): Microstructural characterization of Al-7075-T651 chips and work pieces produced by high-speed machining. Mater Sci Eng A. 430(1-2):15–26.

- Campbell, J., Butterworth-Heinemann (2003): The New Metallurgy of Cast Metals: Castings. Second Edition, (Chapter 5: Solidification Structure).

- Cao, P., Qian, M., St. John, D.H. (2007): Mechanism for grain refinement of magnesium alloys by superheating. Scr Mater. 56(7):633–6.

- Chadwick, G.A. (1965): Monotectic solidification. Br J Appl Phys. 16(8):1095.

- Chen, L-Y., Xu, J-Q., Choi, H., Konishi, H., Jin, S., and Li, X-C. (2014): Rapid control of phase growth by nanoparticles. Nat Commun.

- Chen, L., Xu, J-Q., Choi, H., Konishi, H., Jin, S., and Li, X-C. (2014): Rapid control of phase growth by nanoparticles. Nature Communications 5, Article number: 3879 doi: 10.1038/ncomms4879.

- Coriell, S.R., Mitchell, W.F., Murray, B.T., Andrews, J.B., and Arikawa, Y. (1997): Analysis of monotectic growth infinite diffusion in the L2 phase. Journal of Crystal Growth 179 647 657.

D

- Dahlborg, U., Kramer, M.J., Besser, M., Morris, J.R., Calvo-Dahlborg, M. (2013): Structure of molten Al and eutectic Al–Si alloy studied by neutron diffraction. J Non-Cryst Solids. 361:63–9.

- Dai, R., Zhang, S.G., Li, Y.B., Guo, X., and Li, J.G. (2011): Phase separation and formation of core-type microstructure of Al–65.5mass% Bi immiscible alloys. J Alloys Compd. 509(5):2289–93.

- Dantzig, J.A., and Rappaz, M. (2009): Solidification, EPFL Press, 1st Edition.

- Das, A., Fan, Z. (2002): Non dendritic structural evolution in stirred Sn-15% Pb alloy melts. In: II Processing of 7th International Conference on Semi-solid Processing of Alloys and Composites, Japan. p. 449–4.

- Das, A., Ji, S., and Fan, Z. (2002): Morphological development of solidification structures under forced fluid flow: a Monte-Carlo simulation. Acta Mater.50(18):4571–85.

- Dieter, G.E. Mechanical Metallurgy. 3rd Edition. MacGraw Hill International Editions. Material Science and Engineering series. Page 679.

- Doherty, R.D., et al. (1984): Microstructure of stir cast metals, Materials Science and Engineering, 65 181-189.

- Duan, X., Sheppard, T. (2003): Simulation and control of microstructure evolution during hot extrusion of hard aluminium alloys. Mater Sci Eng A. 351(1):282–92.

- Duplančić, I., Prgin, J., Bračić, Z., Junaković, S. Properties of 2xxx aluminium extruded rods in T3 and T8 tempers. Faculty of Electrical Engineering, Mechanical Engineering and Naval Architecture, University of Split, Ruđera Boškovića bb, 21000 Split, Croatia.

E

- Elgallad, E.M., Samuel, F.H., Samuel, A.M., and Doty, H.W. (2010): Machinability aspects of new Al–Cu alloys intended for automotive castings. J Mater Process Technol. 210(13):1754–66.

- Enright, P. G., Hughes, I. R., Pickering, J. (2003): Characterisation of Molten Metal Quality Using the Pressure Filtration Technique. American Foundry Society.

- Eskin, D. (2008): Physical Metallurgy of Direct Chill Casting of Aluminium, Advances in Metallic Alloys. A Series edited by J.N. Fridlyander and D.G. Skin.

- Eskin, D.G., Savran, V.I., Katgerman, L. (2005): Effects of melt temperature and casting speed on the structure and defect formation during direct-chill casting of an Al-Cu alloy. Metall Mater Trans A. 36(7):1965–76.

F

- Fang, X., Fan, Z. (2006): Rheo-diecasting of Al–Si–Pb immiscible alloys. Scr Mater. Mar;54(5):789–93.

- Fan, Z., Ji, S. and Zhang, J. (2001): Processing of immiscible metallic alloys by rheomixing process. Materials Science and Technology July 2001 Vol. 1.

- Fan, Z., Wang, Y., Zhang, Y., Qin, T., Zhou, XR. (2015): Thompson GE, et al. Grain refining mechanism in the Al/Al–Ti–B system. Acta Mater. Feb; 84:292–304.

- Fan, Z., Xia, M., Zhang, H., Liu, G., Patel, J.B., and Bian, Z. (2009): Melt conditioning by advanced shear technology (MCAST) for refining solidification microstructures. Int J Cast Met Res. 22(1-4):103–7.

- Fan, Z.Y., Zuo, Y.B., Jiang, B. (2011): A new technology for treating liquid metals with intensive melt shearing. In: Materials Science Forum. Trans Tech Publ

- Z. Fan (2012): An Epitaxial Model for Heterogeneous Nucleation on Potent

Substrates. The Minerals, Metals & Materials Society and ASM International DOI: 10.1007/s11661-012-1495-8.

G

- Grum, J., Kisin, M. (2003): Influence of microstructure on surface integrity in turning—part II: the influence of a microstructure of the work piece material on cutting forces. Int J Mach Tools Manuf. 43(15):1545–51.
- Grum, J., Kisin, M. (2003): Influence of microstructure on surface integrity in turning—part I: the influence of the size of the soft phase in a microstructure on surface-roughness formation. Int J Mach Tools Manuf. 43(15):1535–43.

H

- He, J., Zhao, J., Li, H-T., Zhang, X., Zhang, Q. (2008): Directional Solidification and Microstructural Refinement of Immiscible Alloys. Metall Mater Trans A. May; 39(5):1174–82.
- Helawell, A., Kirkwood, D.H., Kapranos, P. (Eds.): Proceedings of the 4th International Conference on Semi-Solid Processing of Alloys and Composites, The University of Sheffield, Sheffield, UK, 1996, p. 60.
- Hey, J., Xing, Zhao, J., and Zhao, J. (2010): Microstructure formation Al Bi Co immiscible alloys directionally solidified with diff melt superheat. Mater. Sci. Technol., 26(2), 136-140.

J

- Jamaly, N., Phillion, A., Cockcroft, S., Drezet, J-M. (2012): Hot Tearing Susceptibility in DC Cast Aluminum Alloys. In: Supplemental Proceedings: Volume 2: Materials Properties, Characterization, and Modeling TMS (The Minerals, Metals & Materials Society).
- Jaradeh, M. (2006):The effect of processing parameters and alloy composition on the microstructure formation and quality of DC cast aluminium alloys.

- Jarry, P. (2009): Analysis and tentative interpretation of the first solidification results obtained from a highly sheared aluminium melt.

K

- Kaban, I., Köhler, M., Ratke, L., Hoyer, W., Mattern, N., Eckert, J. (2011): Interfacial tension, wetting and nucleation in Al–Bi and Al–Pb monotectic alloys. Acta Mater. 59(18):6880–9.

- Kavan, I., Kohler, M., Hoyer, W., and Ratke, L. (2010): Catalytic efficiency of oxide particles on heterogeneous nulceation with miscibility gap. High Temperatures-High Pressures, Vol. 39, pp. 347–355.

- Kaban, I., Köhler, M., Ratke, L., Nowak, R., Sobczak, N., Mattern, N. (2012): Phase separation in monotectic alloys as a route for liquid state fabrication of composite materials. J Mater Sci. 47(24):8360–6.

- Kaban, I., Hoyer, W., Kehr, M. (2007): Liquid–Liquid Interfacial Tension in Ternary Monotectic Alloys Al–Bi–Cu and Al–Bi–Si. Int J Thermophys. 28(2):723–31.

- Kaban, I., Mhiaoui, S., Hoyer, W., Gasser, J-G. (2005): Surface tension and density of binary lead and lead-free Sn-based solders. J Phys Condens Matter. 17(50):7867–73.

- Kamiya, M., Yakou, T. (2008): Role of second-phase particles in chip breakability in aluminum alloys. Int J Mach Tools Manuf. 48(6):688–97.

- Kapranos, P., Kirkwood, D.H. (1996): Conference proceedings: 4th International Conference on Semi-Solid Processing of Alloys and Composites, the University of Sheffield, England, Department of Engineering Materials.

- Kaptay, G. (2006): On the temperature gradient induced interfacial gradient force, acting on precipitated liquid droplets in monotectic liquid alloys. In: Materials Science Forum. Trans Tech Publ.

- Koch, S., Antrekowitsch, H. (2008): Free-cutting aluminium alloys with tin as substitution for lead. BHM Berg- Hüttenmänn Monatshefte. 153(7):278–81.

- Koch, S. and Antrekowitsch, H. (2010): Alloying Behaviour of copper, magnesium and Manganese in Lead-free Al-Cu Based Alloys Intended for Free Machining. Nonferrous Metallurgy, Montanuniversität Leoben.

- Kostorz, G. (2001): Phase Transformations in Materials. WILEY-VCH Verlag GmbH, Weinheim. ISBN: 3-527-30256-5.

- Kotadia, H.R., Das, A., Doernberg, E., Schmid-Fetzer, R. (2011): A comparative study of ternary Al–Sn–Cu immiscible alloys prepared by conventional casting and casting under high-intensity ultrasonic irradiation. Mater Chem Phys. 131(1-2):241–9.

- Kotadia, H.R., Patel, J.B., Fan, Z., Doernberg, E., Schmid-Fetzer, R. (2009): Solidification and processing of aluminium based immiscible alloys. Brunel Cent Adv Solidif Technol.

- Kotadia, H.R. (2010): Solidification behaviour of Al-Sn-Cu immiscible alloys and Al-Si cast alloys processed under intensive shearing. Brunel University.

- Kotadia, H.R., Doernberg, E., Patel, J.B., Fan, Z. and Schmid-Fetzer, R. (2009): Solidification of Al-Sn-Cu based immiscible alloys under intense shearing. The Minerals, Metals & Materials Society and ASM International. DOI: 10.1007/s11661-009-9918-x.

- Kouam, J., Zaghbani, I., Songmene, V., Parson, N., and Maltais, A. (2012): Factors affecting Machinability of Al-Mg-Si Extrusions.

- Kumar, S., Hari, Babu N., Scamans, G.M., and Fan, Z. (2011): Influence of Intensive Melt Shearing on the Microstructure and Mechanical Properties of an Al-Mg Alloy with High Added Impurity Content. Metall Mater Trans A. 42(10):3141–9.

L

- Lee, S.B. and Kim Y-M. (2011): Direct observation of in-plane ordering in the liquid at a liquid Al/α-Al$_2$O$_3$(1 1 0 2) interface. Acta Materialia 59 1383 – 1388.

- Li, H-T. (2011): Enhanced Heterogeneous Nucleation on Oxides in Al Alloys by Intensive Melt Shearing. BCAST (Brunel Centre for Advance Solidification technology).

- Li, H-T., Wang, Y., Fan, Z. (2012): Mechanisms of enhanced heterogeneous nucleation during solidification in binary Al–Mg alloys. Acta Mater. 60(4):1528–37.

- Li, HT., Ji, S., Wang, Y., Xia, M., and Fan, Z. (2012): Effect of intensive melt shearing on the formation of Fe-containing intermetallics in LM24 Al-alloy. IOP Conf Ser Mater Sci Eng. 27:012075.

- Li, H-T., Wang, Y., Fan, Z. (2012): Enhanced heterogeneous nucleation on oxides in Al alloys by intensive shearing. IOP Conf Ser Mater Sci Eng. 27:012047.

- Li, H-T., Xia, M., Jarry, P., Scaman, G.M., and Fan, Z. (2011): Grain refinement in a AlZnMgCuTi alloy by intensive melt shearing: A multi-step nucleation mechanism. J Cryst Growth. 314(1):285–92.

- Li, P., Nikitin, V.I., Kandalova, E.G., Nikitin, K.V. (2002): Effect of melt overheating, cooling and solidification rates on Al–16wt.% Si alloy structure. Mater. Sci. Eng. A. 332(1):371–4.

- Li, P., Nikitin, V.I., Kandalova, E.G. and Nikitin, K.V. (2002): Effect of melt overheating, cooling and solidification rates on Al–16wt.%Si alloy structure. Materials Science and Engineering A332 371–374.

- E. Liotti, A. Lui, R. Vincent, S. Kumar, Z. Guo, T. Connolley, I.P. Dolbnya, M. Hart , L. Arnberg, R.H. Mathiesen, P.S. Grant. (2014): Synchrotron X-ray radiography study of dendrite fragmentation induced by a pulsed electromagnetic field in an Al 15Cu alloy Acta Materialia 70 228-239.

- Lu, W.Q., Zhang, S.G., Li, J.G. (2014): Depressing liquid phase separation and macrosegeregation of Fe–Sn immiscible alloys by Cu alloying. Mater Sci Technol. 30(2):231–5.

M

- Maxwell, I., and Hellawell, A. (1975) A simple model for grain refinement during solidification. Acta Metall., 23, 229-237

- Men, H., and Fan, Z. (2010) Transition of amorphous to crystalline oxide film in initial oxide overgrowth on liquid metals. Mater. Sci. Tech., in press.

- Men, H., Jiang, B., & Fan, Z. (2010): Mechanisms of grain refinement by intensive shearing of AZ91 alloy melt. Acta Mater., 58, 6526-6534.

- Mohamed, A., Samuel, F.H., Samue,l A.M., Doty, H.W. (2009): Effects of Individual and Combined Additions of Pb, Bi, and Sn on the Microstructure and Mechanical Properties of Al-10.8Si-2.25Cu-0.3Mg Alloy. Metall Mater Trans A. 40(1):240–54.

- Mondolfo, L.F. (1976): Aluminium alloys: Structures and properties, Butter Worths.

- Moritz, G.E. (1965, filed 1962): US Patent 3212142.

- Mullis, A.M., (1999): Growth Induced Dendrite Bending and Rosette Formation During Solidification in a Shearing Flow. Acta Mater., Vol. 47, 1783-1789).

N

- Nadella, R., Eskin, D.G., Du, Q., Katgerman, L. (2008): Macrosegregation in direct-chill casting of aluminium alloys. Prog Mater Sci. Mar; 53(3):421–80.

- Nestler, B., Wheeler, A.A., Ratke, L., Stöcker, C. (2000): Phase-field model for solidification of a monotectic alloy with convection. Phys Nonlinear Phenom. 141(1):133–54.

- OECD Nuclear Energy Agency, Nuclear Science Committee (2007). Handbook on lead-bismuth eutectic alloy and lead properties, materials compatibility, thermal-hydraulics and technologies. Issy-les-Moulineaux, France: OECD Nuclear Energy Agency.

P

- Polmear, I.J. (2005): Light Alloys, Fourth Edition. Chapter 3: Wrought Aluminium Alloys.

- Porter, D.A. (2009): Easterling K.E., Sherif M. Phase transformation son Metals and Alloys.

- Predel B. (1997): Constitution and thermodynamics of monotectic alloys—A survey. J Phase Equilibria. 18(4):327–37.

R

- Rack A., Weitkamp T., Riotte M., Grigoriev D., Rack T., Helfen L. (2010): Comparative study of multilayers used in monochromators for synchrotron-based coherent hard X-ray imaging. J Synch Rad;17:496–510.

- Ratke, L. (1988): Immiscible alloys under microgravity conditions. F. R. G. Adv. Space Res. Vol. 8, No. 12, pp. (12)7—(12)16.

- Ratke, L. and Alkemper, J. (1995): Modelling of Phase separation in liquids with a miscibility gap. Advances in Colloid and Interface Science, 58 151-170 151.

- Ratke, L. and Diefenbach S. (1995): Liquid Inmiscible alloys, Material Science and Engineering, R15 263-347.

- Ratke, L., Drees, S., Diefenbach, S., Prinz, B., Ahlborn, H. (1996): Microstructure evolution in immiscible AlSiBi alloys under reduced gravity conditions. In: Materials and fluids under low gravity, Springer.

- Rocha, L., Siqueira, C. and Garcia, A. (2003): Heat flow parameters affecting dendritic spacing during unsteady state solidification of Sn-Pb and Al-Cu alloys Metallurgical and Material transactions, April 2003 Metallurgical and Materials Transactions Volume 34, Issue 4, pp 995-1006.

S

- Sato, S., Kumai, T., Kobayashi, and Murakami, Y. (1998): Aluminium alloys: their Physical and Mechanical properties, vol 3, page 2009-2034. T. Proceeding of the 6th international Conference on aluminium alloys.

- Sawhney K.J.S., Dolbnya I.P., Tiwari M.K., Alianelli L., Scott S.M., Preece G.M., (2010): A test beamline on diamond light source. In: AIP conference proceedings of the 10th international conference on synchrotron radiation instrumentation, vol. 1234; p. 387.

- Scamans, G., Li, H-T., Fan, Z. (2012): Melt Conditioned Casting of Aluminum Alloys. In: ICAA13: 13th International Conference on Aluminum Alloys.

- Scardovelli, R., Zaleski, S. (1999): Direct numerical simulation of free-surface and interfacial flow. Annu Rev Fluid Mech. 31(1):567–603.

- Schaffer, P.L., Mathiesen, R.H., Arnberg, L. (2009):L2 droplet interaction with α-Al during solidification of hypermonotectic Al–8 wt.% Bi alloys. Acta Mater. (10):2887–95.

- Silva, A.P., Spinelli, J.E., Garcia, A. (2009): Thermal parameters and microstructure during transient directional solidification of a monotectic Al–Bi alloy. J Alloys Compd. 475(1-2):347–51.

- Smallman, R.E., Bishop, R.J., (1999): Modern Physical Metallurgy and Materials Engineering: Metals and Materials.

- V. Songmene, R. Khettabi, I. Zaghbani, J. Kouam, and A. Djebara: Machining and Machinability of Aluminum Alloys.

- Spillard, C. (1998): Alloy 6020: A Lead-Free Aluminum Alloy Featuring "A" Rated Machinability, SAE Technical Paper.

- Stauffer, D., Binder, K. and Wildpaner, V. (1974): "Structure of Binary Solution Droplets: Continuum Theory and Monte Carlo Simulation", Water-Air Soil Pollution 3 p. 515-525.

- Stöcker, C., Ratke, L. (1999): A new Jackson–Hunt' model for monotectic composite growth. J Cryst Growth. 203(4):582–93.

- Stöcker, C., Ratke, L. (2000): Monotectic composite growth with fluid flow. J Cryst Growth. 212(1):324–33.

- Suyitno, Eskin, D.G., Savran, V.I. and Katgerman, L. (2004): Effects of Alloy Composition and Casting Speed on Structure Formation and Hot Tearing during Direct-Chill Casting of Al-Cu Alloys. Metallurgical and Material Transactions. Volume 35A—3551.

T

- Taha, M.A., El-Mahallawy, N.A., Assar, A-W., Hammouda, RM. (1992): Effect of melt superheat and chill material on interfacial heat-transfer coefficient in end-chill Al and Al-Cu alloy castings. J Mater Sci. 27(13):3467–73.

- Tang, H., Wrobel., L.C. (2005): Modelling the interfacial flow of two immiscible liquid mixing processes. International Journal of Engineering Science 43 1234–1256.

- Tang, H., Wrobel, L.C., Fan, Z. (2005): Hydrodynamic analysis of binary immiscible metallurgical flow in a novel mixing process: rheomixing. Appl Phys A. 81(3):549–59.

- Tang, H., Wrobel, L., Fan, Z. (2004): Numerical evaluation of immiscible metallic Zn–Pb binary alloys in shear-induced turbulent flow. Mater Sci Eng A. 365(1-2):325–9.

- Tang, H., Wrobel, L.C., Fan, Z. (2006): Numerical analysis of the hydrodynamic behaviour of immiscible metallic alloys in twin-screw rheomixing process. Mater Des. 27(10):1065–75.

- Tash, M., Samuel, F.H., Mucciardi, F., Doty, H.W., VAl-Tierra, S. (2006): Effect of metallurgical parameters on the machinability of heat-treated 356 and 319 aluminum alloys. Mater Sci Eng A. 434(1-2):207–17.

- Tegze, G., Pusztai, T., Gránásy, L. (2005): Phase field simulation of liquid phase separation with fluid flow. Mater Sci Eng A. 413-414:418–22.

V

- Venkatarami, R., Simpson, R. and Ravindran, C. (1994). Effect of melt superheat on maximum nuclei density in A356 alloy. Presented at the International Metallographic Society Symposium on "Microstruchual Characterization of Lightweight Materials for Transportation," Montreal.

- C. Vives, (1989): Hydro-dynamic, thermal and crystallographical effects of an electromagnetically driven rotating flow in solidifying aluminium alloy melts. International journal of heat and mass transfer 0017-9310 Volume: 33 Issue: 12 Page: 2585-2598.1990.

W

- Wang, W.L. Chen F.Y. and Chen W.H. Effect of Process Metallurgical Factors on the Properties of 2011 Free Cutting Aluminium Alloy.

- Wang, Y., Li, H-T., Fan, Z. and Scamans, G. (2013): Characterisation of Oxide Films in Al-Mg Alloy Melts. Materials Science Forum Vol. 765 pp 220-224.

- Wang, C., Zhangy, J., Liu L. and Fu H. (2011): Effect of melt superheat on directional solidification interface morphology.

- Wang, Y., Li, H-T. and Fan, Z. (2012): Oxidation of Aluminium Alloy Melts and Inoculation by Oxide Particles. Conference Proceedings. Trans Indian Inst Met DOI 10.1007/s12666-012-0194.

- Wang, J., Zhong, Y.B., Fautrelle, Y., Zheng, T.X., Li, F., and Ren, Z.M. (2013): Influence of the static high magnetic field on the liquid–liquid phase separation during solidifying the hyper-monotectic alloys. Appl Phys A. 112(4):1027–3

- Wang, W.L., Chen, F.Y., and Chen, W.H. (1987): Effect of process metallurgical factors on properties of 2011 free cutting alloy: On the size and distribution of Pb/Bi particles.

- Wang, F., Zou, J., Wang, X., and Fan Z. (2009): Effect of melt superheat on microstructure of Al4Fe2Mn1.5 Monel alloy. Trans Nonferrous Met Soc China. 19(1):19–25.

- Wang, J., Heb, S., Sunb, B., Guoa, Q. and Nishioa, M. (2003): Grain refinement of Al–Si alloy (A356) by melt thermal treatment. Journal of Materials Processing Technology 141 29–34.

- Wefers, K., and Misra, C. (1987) Oxides and hydroxides of aluminium. Alcoa, USA: Alcoa Laboratories.

- Wilson, P.W., Kattamis, T.Z., Shiohara, Y. (1988): Coarsening during solidification of Aluminium-copper alloys. J Mater Sci. 23(8):2882–92.

X

- Xia, M.X., Prasadd Rao, A.K., and Fan, ZY. (2013): Solidification Mechanisms in Melt Conditioned Direct Chill (MC-DC) Cast AZ31 Billets. Mater Sci Forum. 765:291–5.

Y

- Yamada, H. and Tanaka, T. (1977): Combined Effect of Copper and Manganese on the Machinability of Aluminum Casting Alloys, Journal of Japan Institute of Light Metals, Vol. 27 (11), pp. 542-547.

- Yang, J. C., Schumann, E., and Ruhle, M. (1998) Transient oxidation of NiAl. *Acta Mater.*, 46, 2195-2201.

- Yin, F.S., Sun, X.F., Li, J.G., Guan, H.R., and Hu, Z.Q. (2003): Effects of melt treatment on the cast structure of M963 superalloy. Scr Mater. 48(4):425–9.

- Yoshihara, S. and Osaki, S. Research on Mechanism of chip-breaking of developed lead-free 6061 based aluminium alloy under 2 dimensional cutting. Kobe Steel Limited, Shiminoseki, Japan.

- Yoshihara, S. and Hirano, M. The influence of additional elements of aluminium on machinability. Aluminium alloys volume 3, page 2029.

- Yuan, Y. and Randall Lee, T. (2013): Surface Science techniques. Chapter 1, Contact angle and Wetting properties, Surface Science Tecniques. Bracco, G. Holst, B (Eds.) XXVIII, 663 p.

Z

- Zhang, M., Fan, Z. and Zhen Z.(2006): Direct Chill Rheocasting (RDC) of AZ32 Mg-Alloy, Materials Science and Technology, Vol 22, N 12, p1489-1498

- Zhao, J., Ratke, L., .Jia, J. and Li, J. Q. (2002): Modeling and Simulation of the Microstructure Evolution during a Cooling of Immiscible Alloys in the Miscibility Gap. Mater. Sci. Technol., vol 18 No 3.

- Zhao, J.Z., Gao, L.L., He, J. (2005): Effect of Brownian coagulation on the microstructure evolution in rapidly solidified immiscible alloys. Appl Phys Lett. 87(13):131905.

- Zhao, J.Z., Ratke, L., Feuerbacher, B. (1998): Microstructure evolution of immiscible alloys during cooling through the miscibility gap. Model Simul Mater Sci Eng. 6(2):123.

- Zhao, J.Z., Ratke L. (2004): A model describing the microstructure evolution during a cooling of immiscible alloys in the miscibility gap. Scr Mater. 50(4):543–6

- Zhou, L. (2015): The Role of Solute Elements on Grain Refinement of Al Alloys with Al-Ti-B inoculations. BCAST (Brunel Centre for Advance Solidification Technology), Brunel University.

- Zolotorevskij, V.S., Belov, N.A., Glazoff, M.V. (2007): Casting aluminum alloys. 1. ed. Amsterdam [u.a.]: Elsevier; 530.

- Zuo, Y.B., Jiang, B., Zhang, Y., and Fan, Z. (2012): Grain refinement of DC cast magnesium alloys with intensive melt shearing. IOP Conf Ser Mater Sci Eng. 27: 012043.

- Zuo, Y.B., Jiang, B., and Fan, Z. (2011): Microstructures of DC cast light alloys under the influence of intensive melt shearing.

Chapter 9

Appendix: Crucible experiments

Those experiments were perform, as explained in **Chapter 3**, firstly to obtain samples for TEM and secondly determine the optimum adding conditions for inoculant in hyper-monotectic alloys.

Figure 9-1 shows the results of the solidification in the crucible with a cooling rate of 0.5 °C/min. It can be observed by comparing images a, b and c that Al-5Ti-B rod additions do not avoid the sedimentation of the Pb as a continuous layer on the bottom of the sample. The amount of Pb that sediments is the same without inoculant and with Al-5Ti-B. However, when Al-Ti and Al-B master alloys are added Pb sedimentation is nearly supressed. **Figure 9-2** shows images the sample containing Al-Ti and Al-B, including optical images at lower magnification in **Figure 9-2(a)** and SEM images at higher magnification in **Figure 9-2(b).** EDS chemical analysis shows that the light grey particles have the following composition: 23 % Al, 46 % B and 30 % Ti. The white phase within these particles is Pb.
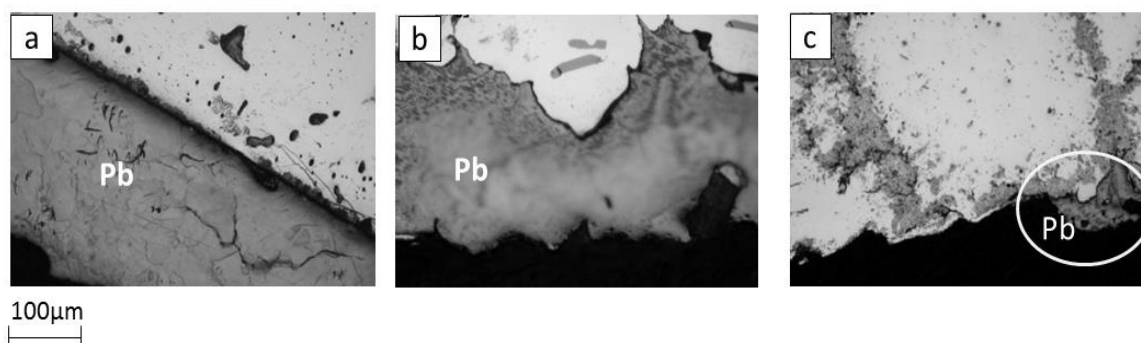
Figure 9-1 Optical micrographs of an Al-3Pb alloy solidified in the crucible: a) without inoculant b) with Al-5Ti-B (0.4 %Ti) c) with Al-Ti (0.4 %Ti) and Al-B (0.2 % B) additions. Both added at 720°C, heated to 860C and hold at temperature for 30 min.
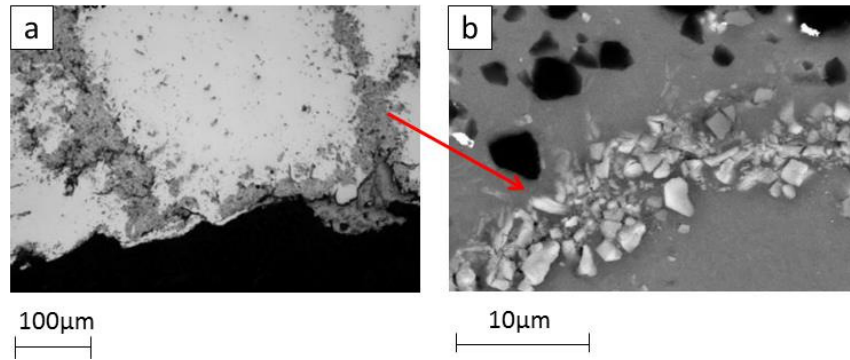
Figure 9-2 Micrographs of an Al-3Pb alloy solidified in the crucible, with Al-Ti (0.4 %Ti) and Al-B (0.2 % B) additions: a) optical image at lower magnification b) SEM image on the same area with a higher magnification.

Figure 9-3 highlights the importance of adding the inoculant at the correct temperature. Both micrographs show samples containing Al-Ti and Al-B. However for the sample represented in micrograph in **Figure 9-3 (a)** the particles have been added at 860°C, temperature at which the alloy constitutes a single uniform phase; and for the sample represented in micrograph in **Figure 9-3 (b)** the particles were added at 720°C, temperature at which both metals are immiscible in each other. It is clearly seen that a much smaller amount of Pb was found to sediment when the inoculant is added at 860°C.
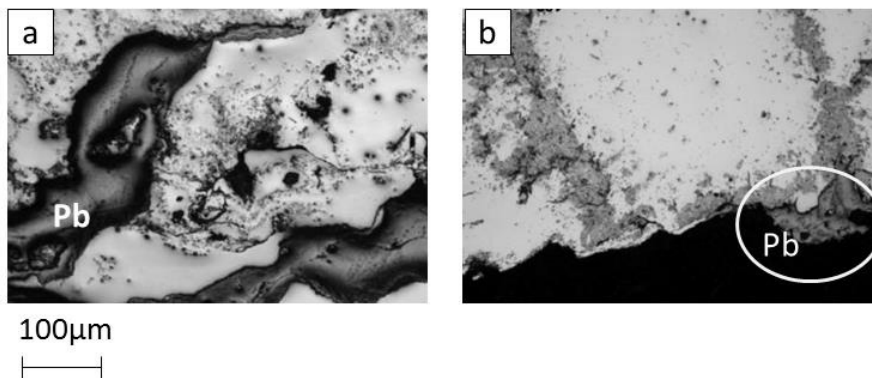
Figure 9-3 Optical micrographs of an Al-3Pb alloy solidified in the crucible containing Al-Ti (0.4 %Ti) and Al-B (0.2 % B): a) added at 860°C and hold for 30 min, b) added at 720°C, heated to 860°C and hold for 30 min.

Figure 9-4 comprises SEM images of the TiB$_2$ particles obtained by mixing the Al-Ti and Al-B master alloys. Micrographs from **Figure 9-4 (a)** and **Figure 9-4 (b)** correspond to SEM images on the same area of the sample, but at lower and higher magnification. **Figure 9-4 (c)** shows an EBSD mapping of the area showed in **Figure 9-4 (b)**, where the crystal structure of the different metals and compounds present in the sample will be identified. The green areas are indexed as TiB$_2$, red Aluminium and yellow and blue Pb oxide and Pb respectably (both have the same crystal structure).
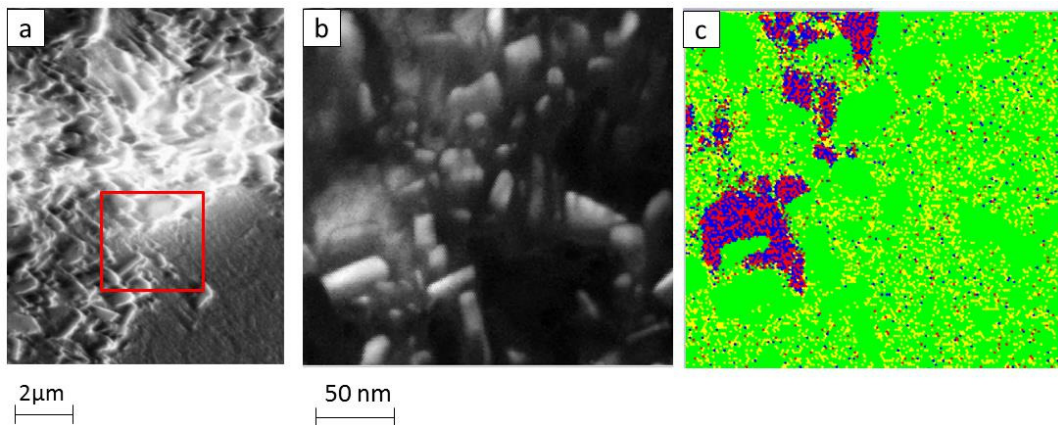
Figure 9-4 SEM images of an Al-3Pb alloy solidified in the crucible a) area showing TiB$_2$ particles covered in a thin layer of Pb, as identified by EDS analysis b) higher magnification of the area in the red square in a and c) EBSD mapping of the area showed in b.

Further analysis was done on the bottom of the Al-3Pb crucible samples. **Figure 9-5** shows EDS analysis proving the particles created by adding Al-Ti and Al-B master alloys are titanium borides in the necessary weight proportion for TiB$_2$. These results are also supported by the EBSD mapping showed on **Figure 9-6**, in which the crystal structures of Al, Pb and TiB$_2$ have been indexed.
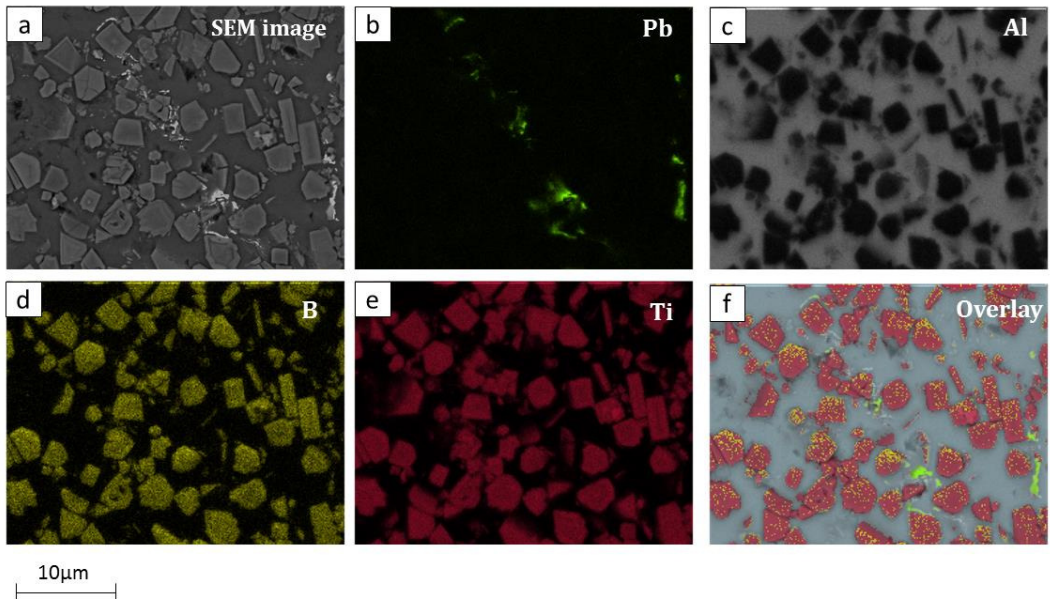
Figure 9-5 SEM images of the Al-3Pb alloy solidified in the crucible: a) back scattered image b)EDS map showing the Pb in green, c) EDS map showing the aluminium in grey, d) EDS map showing the boron in yellow, e) EDS map showing the titanium in red and f) EDS map showing the overlay of all the elements.
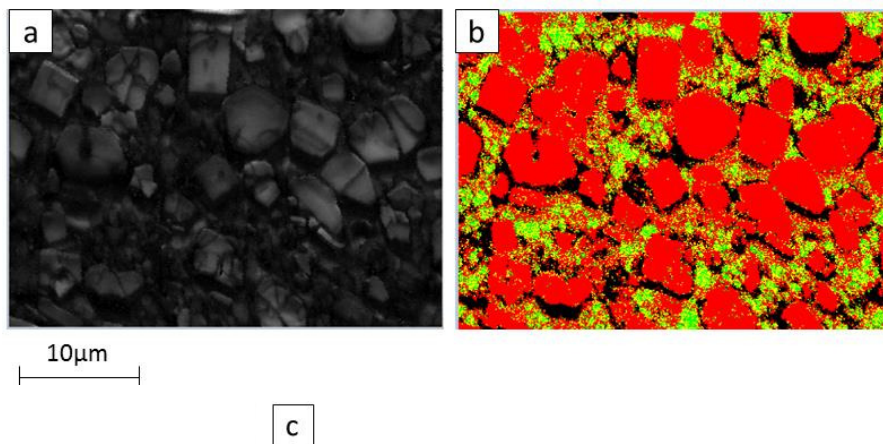
Phase	Fraction	colour
TiB$_2$	0.72	red
Al	0.09	green
Pb	0.19	yellow

Figure 9-6 SEM images of the Al-3Pb alloy solidified in crucible: a) secondary electron image b) EBSD in which the crystal structures of Pb, Al and TiB$_2$, are identified as indicated in c)

Table 9-1 shows the lattice parameters used in the EBSD program to identify the crystal structure of the elements and compounds found on the crucible sample. Although the chemical composition analysis does not identify Al-B_2 (see **Figure 9-5**), it has been added to **Table 9-1** to highlight that its crystal structure is very similar to that of TiB_2.

Table 9-1 Crystal structures and lattice parameters of the elements found on the Al-3Pb alloy solidified in the crucible.

Phase name	Structure	Spacegroup	a (Å)	c (Å)
Aluminum	Cubic	Fm-3m	4.050	
Lead	Cubic	Fm-3m	4.948	
TiB_2	Hexagonal	P6/mmm	3.018	3.234
AlB_2	Hexagonal	P6/mmm	3.022	3.238

Furthermore TiB_2 particles were found with TEM EDS analysis, as seen on **Figure 9-7**. Due to its low atomic number boron is on the limit of detection, therefore the % of boron detected is very low. **Figure 9-8** shows the diffraction pattern of the particle seen on **Figure 9-8**, which is that corresponding of TiB_2.

Element	Net counts	Weight	Atom	Atom error
B K	2776	1.2 %	4.9 %	± 0.2%
Al K	121021	9.5 %	15.1 %	± 0.1%
Ti K	1204323	89.3 %	80.0 %	± 0.3%
Total		100 %	100 %	
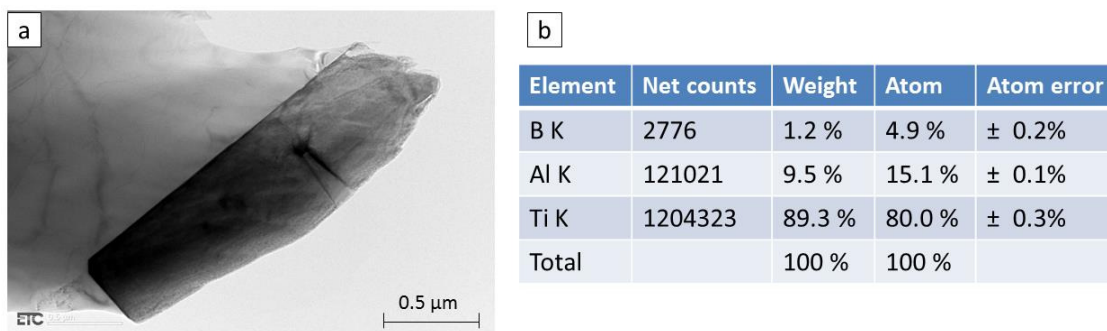
Figure 9-7 a) TEM bright field image of a TiB_2 particle b) chemical composition of the identified particle.
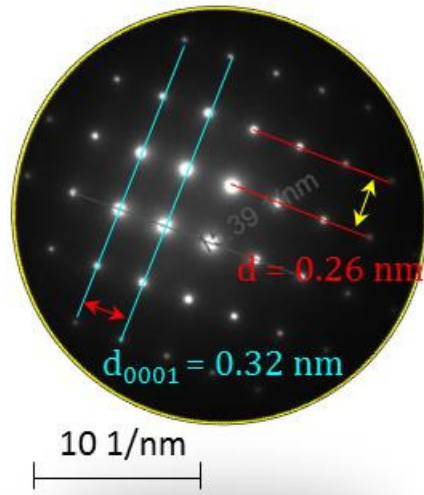
Figure 9-8 Diffraction pattern of the particle in Figure 9-7.

Figure 9-9 Figure 9-10 and **Figure 9-11** comprises EDS mapping, with their corresponding composition tables which display weight and atomic % and the corresponding spectrum indicating peaks for the identified metals. Three different layers are identified, on the particles formed from the in situ reaction between Al-Ti and Al-B. All those layers consist of Al, B, and Ti; however, different proportions of each of the elements are identified in each of the three layers. Figure 9-9 represents the central layer, and the 3 layers can be seen in **Figure 9-11**. From the comparison of the 3 figures it is clear that the aluminium content increases as we get closer to the aluminium matrix, being the composition on the middle (blue) much closer to that of TiB_2. These results are contradictory with previous, were the particles were identified as pure TiB_2 particles. This difference could be explained from the uncontrolled conditions during the reaction of the borides and titanium aluminides in the melt.

(Ti$_{0.8}$Al$_{0.2}$)B$_2$
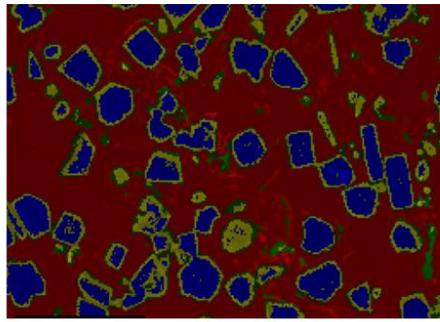
Element	Weight %	Atomic %
B K	34.31	67.75
AlK	8.66	6.85
PbM	0.04	0.00
TiK	56.99	25.39
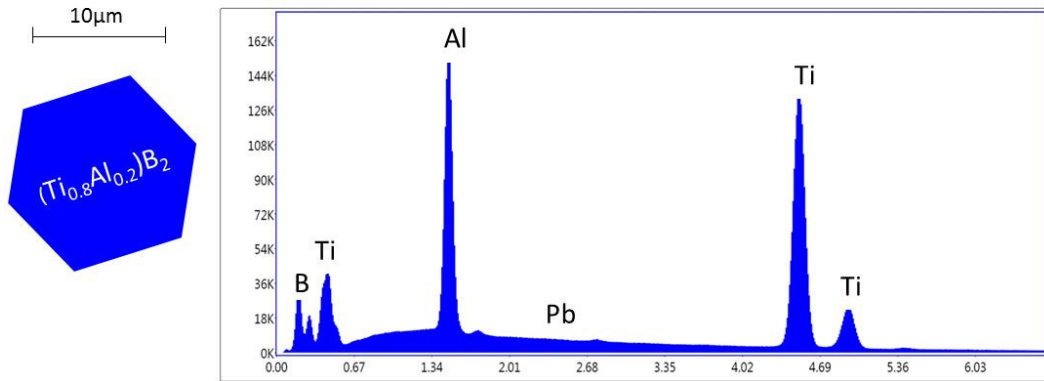
Figure 9-9 EDS mapping showing the composition in weight and atomic % for the phase marked in blue, for the Al-3Pb alloy solidified in the crucible.
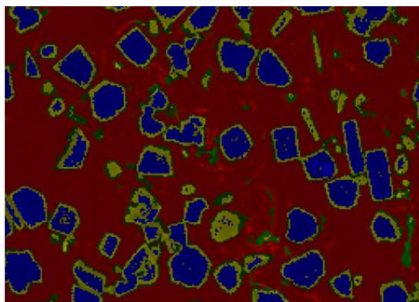
Element	Weight %	Atomic %
B K	36.28	67.47
AlK	17.86	13.31
PbM	0.10	0.01
TiK	45.76	19.21
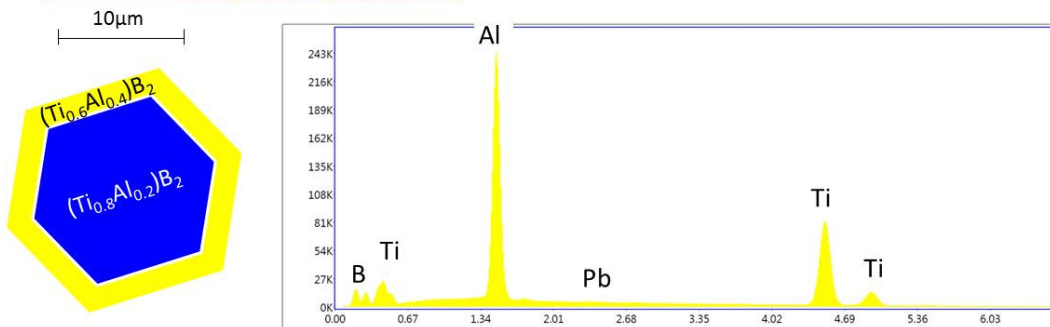
Figure 9-10 EDS mapping showing the composition in weight and atomic % for the phase marked in yellow, for the Al-3Pb alloy solidified in the crucible.

263

$(Ti_{0.4}Al_{0.6})B_2$

Element	Weight %	Atomic %
B K	35.61	64.38
AlK	31.33	22.69
PbM	1.78	0.17
TiK	31.27	12.76
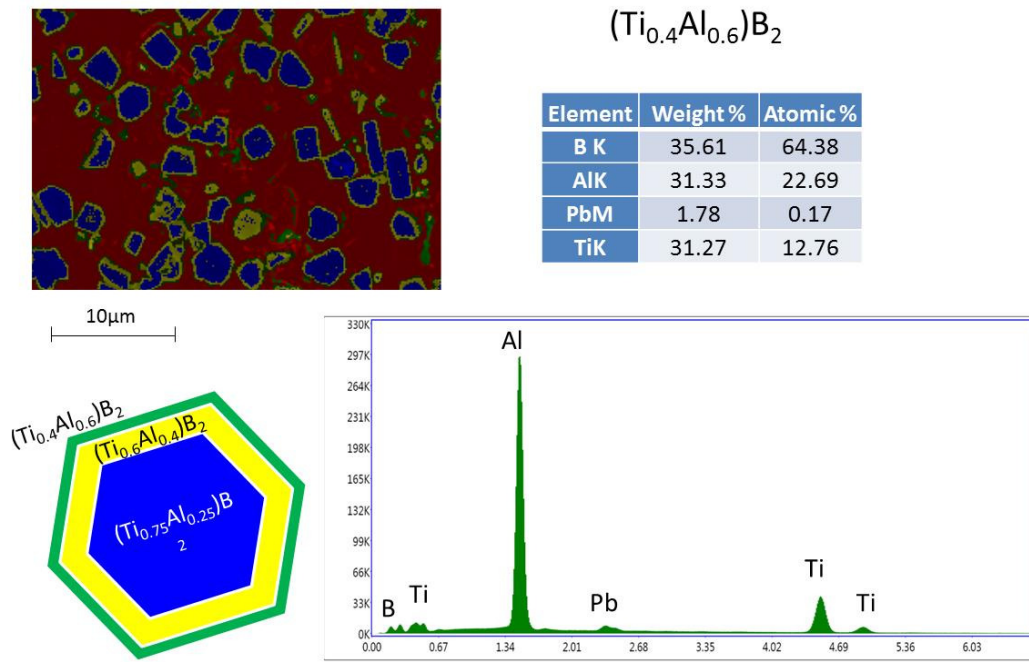
Figure 9-11 EDS mapping showing the composition in weight and atomic % for the phase marked in green, for the Al-3Pb alloy solidified in the crucible.